STRENGTH, STABILITY, AND MICROSTRUCTURE OF SIMULATED CALCITE FAULTS SHEARED UNDER LABORATORY CONDITIONS SPANNING THE BRITTLE-PLASTIC TRANSITION

B. A. Verberne

Utrecht Studies in Earth Sciences
No. 90

Members of the dissertation committee:

Prof. Dr. Einat Aharonov
Earth Science Institute, The Hebrew University of Jerusalem
Jerusalem, Israel

Prof. Dr. Frederick M. Chester
Dept. of Geology and Geophysics, Texas A&M University
College Station (Texas), United States of America

Prof. Dr. Martyn R. Drury
Dept. of Geosciences, Utrecht University
Utrecht, The Netherlands

Prof. Dr. Brian Evans
Earth Resources Laboratory, Massachusetts Institute of Technology
Cambridge (Massachusetts), United States of America

Prof. Dr. Changrong He
Institute of Geology, China Earthquake Administration
Beijing, People's Republic of China

This research was carried out at:

High Pressure and Temperature Laboratory
Dept. of Geosciences, Utrecht University
Budapestlaan 4, 3584 CD, Utrecht
The Netherlands

State Key Laboratory of Earthquake Dynamics
Institute of Geology, China Earthquake Administration
Yard #1, Huayanli, Chaoyang district, Beijing
P. R. of China.

ISBN/EAN: 978-90-6266-402-3

Printed by: CPI Koninklijke Wöhrmann

Cover image: Fibrous (mirror-like) slip patch formed at 1 μm/s. SE micrograph, HFW = 10.2 μm.

Strength, stability, and microstructure of simulated calcite faults sheared under laboratory conditions spanning the brittle-plastic transition

Sterkte, stabiliteit, en microstructuur van calciet breukgesteenten, gedeformeerd onder laboratorium condities die de overgang van bros naar ductiel bestrijken
(met een samenvatting in het Nederlands)

Proefschrift

ter verkrijging van de graad van doctor aan de Universiteit Utrecht op gezag van de rector magnificus, prof.dr. G.J. van der Zwaan, ingevolge het besluit van het college voor promoties in het openbaar te verdedigen op vrijdag 18 september 2015 des ochtends te 10.30 uur

door

Berend Antonie Verberne

geboren op 18 juli 1984
te Halsteren

Promotor: Prof. dr. C. J. Spiers

Copromotoren: Dr. J. H. P. de Bresser
Dr. A. R. Niemeijer

Dit proefschrift werd(mede) mogelijk gemaakt door financiële steun via beurs #2011-75 toegekend door het Netherlands Research Centre for Integrated Solid Earth Sciences (ISES).

“Sabba danam dhamma danam jinati
sabbam rasam dhamma raso jinati
sabbam ratim dhamma rati jinati
tanhakkhayo sabba dukkham jinati”

- Verse 354, Dhammapada (Tanhavagga)

Contents

Summary

Destructive earthquakes are commonplace in tectonically-active carbonate-bearing terrains, often leading to major loss of life and severe economic damage. Recent examples include the 2012 Emilia and 2009 L'Aquila sequences in Italy, as well as the devastating 2008 Wenchuan earthquake in China and the 2005 Kashmir earthquake in Pakistan. Efforts to improve seismic risk assessment in such regions require a quantitative understanding of the failure, slip, and healing behaviour of faults in carbonate rocks. However, few relevant data exist. In this thesis, I report the results of an experimental study aimed at filling this knowledge-gap, through experimental investigation of the mechanisms controlling the shear behaviour of simulated fault gouges composed of calcite ($CaCO_3$). To quantify the mechanical behaviour of these materials, saw-cut, direct-shear, as well as rotary-shear experiments were conducted at sub-seismic sliding velocities, under pressure and temperature conditions relevant to earthquake nucleation in the upper and middle crust. To identify the controlling deformation processes, the deformed samples were submitted to correlative microstructural study, across scales ranging from the cm/ mm range down to the nanoscale, using state-of-the-art microscopy methods.

In **Chapter I**, an outline of the motivation and scope of this study is given, including a brief overview of seismicity in limestone and carbonate terrains, and of the phenomenology of fault friction and seismogenesis. Key definitions are summarized, and relevant previous work is discussed. I close by listing the aims of this thesis.

Chapter II investigates the frictional properties of samples collected from the region hit by the 2008 Wenchuan earthquake, i.e. from the Longmenshan Fault Zone (LFZ), Sichuan, China. The samples consisted of simulated gouges prepared from limestone (the Xujiahe Limestone), clay-rich clastic sediments, and a clay-rich natural fault gouge recovered from a trenched surface rupture. Friction experiments employed a simulated gouge layer embedded in a saw-cut assembly. This was sheared in an Argon-gas medium, triaxial deformation apparatus, under water-saturated conditions using a pore ware pressure of 20 MPa, at a confining pressure of 53 MPa, at temperatures of 25° to 150°C, and at sliding velocities of ~0.1 to 1 μm/s. While the clay-rich samples were frictionally

relatively weak (friction coefficient μ = 0.4-0.6) and consistently velocity strengthening, the simulated limestone gouge was strong (μ = 0.6-0.7), and showed a transition from velocity strengthening behaviour at 25° and 50°C to velocity weakening at ~100° and 150°C. When applied to faulting in the LFZ region, this implies that the presence of clay-rich sediments may have a damping effect upon ruptures propagating from depth, whereas limestones at 5 to 8 km depth may accelerate propagation, producing significant stress drops. The presence of large masses of limestone in the upper-crust may thus enhance seismic hazard.

Chapter III focuses exclusively on the frictional properties of simulated gouge prepared from limestone and pure calcite, and on the microscale processes controlling the transition from velocity strengthening to velocity weakening behaviour reported in Chapter II, i.e. at temperatures between 50° and 100°C. The experiments consist of direct shear tests performed in a silicone-oil confining medium, triaxial deformation apparatus, under nominally dry and water-saturated conditions, at 18° to 150°C, at an effective normal stress of 50 MPa, and sliding velocities of 0.1 to 10 μm/s. Wet tests were conducted using a pore water pressure of 10 MPa. Regardless of whether dry or water-saturated, the results resemble the data on simulated limestone gouge presented in Chapter II, though the wet samples showed lower frictional strengths then the dry samples (μ = 0.6-0.7 vs. 0.7-0.8). Both wet and dry runs showed a transition from velocity strengthening to velocity weakening behaviour above ~80° to 100°C. All samples developed narrow boundary and inclined, Riedel-type shear bands characterized by a crystallographic preferred orientation (CPO) and an ultrafine grain size of only ~5 to 20 nm in the shear band core. Through-going boundary shear bands accommodated the bulk of the imposed displacement, and thus represent the principal slip zone (PSZ). When split after an experiment, the PSZ becomes exposed, revealing striated, highly-reflective (shiny) surface patches developed within the PSZ shear plane, resembling the 'mirror slip' surfaces recently reported to form at co-seismic slip rates (>0.1 m/s). Contrary to recent claims, these results suggest that nanocrystalline, 'mirror-slip' surfaces in faults cutting carbonates are not unambiguously indicative of paleoseismic slip. By comparison with previous work it is argued that the observed frictional behaviour is controlled by a mechanism of dilatant granular flow operating in competition with creep-controlled compaction which increases in importance with increasing temperature. Assuming a geotherm of 20-25°C/km, it is argued that the upper cut-off in seismogenesis

in limestone terrains occurs at a depth of ~4 km, consistent with fore- and aftershock hypocentre distributions reported for e.g. the Apennines (Italy).

Chapter IV continues with a micro- and nanostructural study of the PSZs reported in Chapter III, including a detailed investigation of the striated, shiny or 'mirror-like' slip-surface patches. Imaging of the PSZ micro-/ nanostructure was achieved using focused ion beam - scanning electron microscopy (FIBSEM) and transmission electron microscopy (TEM). Atomic force microscopy (AFM) was used for roughness characterization of the shiny surfaces. The PSZ is shown to consist of a relatively porous, 10 to 50 μm thick, sheet-like volume, composed mainly of rounded, ~100 nm-sized particles or nanospherules that show widespread interparticle neck growth or sintering. The shiny surface patches, on the other hand, consist of dense, planar films composed of aligned chains of nanospherules, or fibres, about 100 nm in width, embedded within the PSZ volume. At the sub-nanospherule scale, the nanofibres consist of ~5 to 20 nm sized calcite crystallites, with their (104) rhomb planes aligned sub-parallel to the shear plane, consistent with the shear band CPO reported in Chapter III. It is argued that a thin (~1-2 nm) aqueous film adsorbed to the ~100 nm nanospherules facilitated intergranular diffusive-mass transfer and neck growth in the PSZ. On this basis, a mechanism of dilatant nanogranular or nanofibre flow with partial accommodation by diffusive mass transport, resembling Ashby-Verrall superplasticity and consistent with the model discussed in Chapter III, is put forward to explain the transition from velocity strengthening to velocity weakening slip seen in simulated calcite gouge above ~80°C. The implication is that nanocrystalline PSZs in calcite faults can produce seismogenic fault friction through a mechanism involving diffusive mass transfer, even at depths in the upper crust where temperatures are generally considered too low to support diffusion at active fault slip rates. In view of numerous recent reports of nanogranular fault surfaces in tectonically-active terrains, I suggest that the proposed mechanism may be generally relevant to upper-crustal seismogenesis.

In an attempt to gain equivalent insight into what controls the lower limit of the seismogenic zone in limestone terrains, **Chapter V** explores the shear behaviour of simulated calcite gouge over temperatures expected to embody the full frictional-to-viscous or brittle-plastic transition. Experiments were conducted in a hydrothermal ring-shear apparatus at 20° to 600°C, under water-saturated conditions using pore fluid

pressures (P_f) in the range 10 ≤ P_f ≤ 100 MPa. Velocity stepping experiments, performed at an effective normal stress of 50 MPa and employing sliding velocities in the range 0.03 ≤ v ≤ 100 μm/s, showed that the velocity weakening behaviour observed in the preceding chapters at temperatures above 80° to 100°C is maintained up to temperatures of ~550°C. This was frequently associated with regular stick-slip behaviour, showing major stress drops, especially at the higher temperatures and lower sliding velocities employed. A transition back to velocity strengthening behaviour was finally seen at ~600°C. Across the full temperature range explored, the gouge shear strength, measured after ~11 mm of displacement at v = 1 μm/s, varied from ~28 MPa ($\mu \approx 0.6$) at 20°C, 19 to 23 MPa ($\mu \approx$ 0.4-0.5) at 100° to 550°C, and 29 to 32 MPa ($\mu \approx 0.6$) at 600°C. Meanwhile, combined velocity-stepping and effective normal stress-stepping tests, conducted using 1 ≤ v ≤ 100 μm/s and 30 ≤ σ_n^{eff} ≤ 100 MPa, consistently showed a linear increase of shear stress upon increasing effective normal stress. The microstructure of samples sheared at 20° to 200°C showed the same localized shear band pattern reported to form in samples sheared at 20° to 150°C in Chapter III. However, the microstructures developed at 400° to 600°C show that pervasive, intracrystalline plastic deformation and dynamic recrystallization of the gouge grains also played role, alongside localized boundary slip involving dilatant flow. Continuing the comparison of the shear behaviour observed in simulated calcite gouges with the predictions of the granular flow versus compaction creep model discussed in Chapters III and IV reveals a striking phenomenological consistency. It follows from the experimental data that the base of the seismogenic zone in overpressurized limestones occurs at 13 to 24 km depth, depending on geothermal gradient and degree of pore fluid overpressure. This depth range is consistent with observations of seismicity attributed to the suspected presence of carbonate rocks at depth in the southern Apennines as well as in the Zagros Mountains (Iran).

Chapter VI further investigates the processes operating in simulated calcite gouge sheared at conditions near the transition, at 550° to 600°C, from velocity weakening to velocity strengthening behaviour, as established in Chapter V. The experiments reported consist of ring-shear tests performed under water-saturated conditions, at a temperature of ~550°C, at a pore fluid pressure of 100 MPa, at constant sliding velocities of 0.1, 1, 10 and 100 μm/s, and at an effective normal stress that was either fixed at 50 MPa or else sequentially stepped in the range 20 ≤ σ_n^{eff} ≤ 140 MPa. When sheared at 0.1 μm/s, gouge strength was found to be insensitive to effective normal stress, and the corresponding

microstructure points to shear dominated by distributed, ductile flow. By contrast, samples sheared at a relatively high sliding velocity (1, 10, or 100 μm/s) all showed a linear increase in shear strength with effective normal stress, verifying frictional behaviour, plus a strongly localized microstructure consisting of a single boundary-parallel shear band cutting a relatively undeformed bulk gouge. Interestingly, the shear band, formed at 100 μm/s at 550°C, showed a similar optical CPO to that formed in samples sheared at 0.1 to 10 μm/s at 20° to 150°C (Chapter III), pointing to a common deformation process inferred to involve oriented attachment of ultrafine (<300 nm) calcite grains. The experimental and microphysical work combined point to a strain rate dependent, frictional-to-viscous transition in simulated calcite fault gouge, and show that localization is crucial in controlling fault strength and stability, especially at pressure-temperature conditions close to the base of the seismogenic zone.

Finally, in **Chapter VII**, the main findings of this research are summarized, and a synopsis of the main implications for seismogenesis in tectonically-active carbonate terrains is given. Major overall conclusions concern the nanogranular nature of the fault rock that forms in calcite gouge sheared at sub-seismic sliding velocities, the role that physical processes on the nanoscale play in controlling the nucleation of earthquakes in carbonates, as well as the frictional-to-viscous transitions seen with temperature and with slip rate. I close the thesis by providing a list of the main unsolved issues, as well as new problems, which follow directly from this research.

Samenvatting

Aardbevingen vinden vaak plaats in gebieden die gekenmerkt worden door grote hoeveelheden carbonaatgesteenten, zoals kalksteen en dolomiet. Voorbeelden van recente, zeer destructieve aardbevingen in dergelijke gebieden zijn de 2012 Emilia en 2009 L'Aquila bevingen in Italië, de 2008 Wenchuan beving in China en de 2005 Kashmir beving in Pakistan. Om beter inzicht te krijgen in de frequentie, locatie en magnitude van toekomstige aardbevingen is een algemeen begrip van de wrijvingseigenschappen van breukgesteenten, en de microfysische processen die hierbij van belang zijn, essentieel. Er is hier echter vooral wat betreft carbonaatgesteenten nog weinig over bekend. In dit proefschrift presenteer ik de bevindingen van een onderzoek dat zich ten doel stelt om dit gebrek aan kennis op te vullen, alsmede om een beter algemeen begrip van het aardbevingsfenomeen te verkrijgen.

Het onderzoek berust op een experimenteel programma rondom het wrijvingsgedrag van ca. 1 mm dikke laagjes gesimuleerd breukgesteente, of 'breukmeel', voornamelijk bestaand uit calciet ($CaCO_3$) ofwel de hoofdcomponent van kalksteen. Voor deze experimenten maak ik gebruik van verscheidene typen, unieke deformatieapparatuur, die het mogelijk maken om de druk- en temperatuurcondities van toepassing op breuken in de aardkorst te simuleren. Om een begrip te krijgen van de microfysische processen die een rol spelen tijdens wrijving van het breukmeel worden de gedeformeerde laagjes na een experiment onderworpen aan een correlatieve, microstructurele studie, waarbij gebruik gemaakt wordt van de nieuwste technieken in de (elektronen) microscopie. Veel aandacht gaat uit naar de wrijvingssnelheidsafhankelijkheid van de breukmeellaagjes, omdat deze materiaaleigenschap een cruciale rol speelt in het bepalen van de wrijvingsstabiliteit, en dus, in het geval van natuurlijke breuken, in de nucleatie van aardbevingen.

In **Hoofdstuk 1** begin ik met een uiteenzetting van de motieven voor deze studie, en geef ik een overzicht van essentiële literatuur aangaande seismiciteit in kalk- en carbonaatgesteenten, alsmede de fenomenologie van frictie en seismogene breuken. Belangrijke definities worden toegelicht en relevant eerder werk wordt bediscussieerd. Ik

sluit af met een opsomming van de specifieke doelstellingen van dit proefschrift.

In **Hoofdstuk II** presenteer ik de resultaten van een onderzoek naar de wrijvingseigenschappen van gesteenten afkomstig uit het Longmengebergte in China, uit de directe omgeving van de breuk waarop de extreem destructieve 2008 Wenchuan aardbeving is genucleëerd. De monsters bestaan uit natuurlijk, klei-rijk breukmeel en gesimuleerd breukmeel, vervaardigd van kalksteen (de Xujiahe kalksteen) en klei-rijke klastische gesteenten. Laagjes van dit breukmeel zijn gedeformeerd in de zogenaamde 'saw-cut' of 'zaagsnede' constructie, in een Argon-gas-gemedieerd, triaxiaal deformatie-apparaat, onder een alzijdige druk van 50 MPa, een poriëndruk van 10 MPa, een temperatuur van 25°C tot 150°C, gebruikmakend van een wrijvingssnelheid van ~0.1 tot 1 μm/s. Waar de klei-rijke monsters relatief zwak zijn (frictiecoëfficiënt μ = schuifspanning / normaalspanning ≈ 0.4-0.6) en consistent snelheidsversterkend, is het gesimuleerde kalkbreukmeel sterk (μ ≈ 0.6-0.7), en snelheidsverzwakkend op temperaturen van ~100°C en 150°C. In het geval van een aardscheuring langs een breuk op diepte in het Longmengebergte, betekenen deze resultaten dat de klei-rijke sedimenten de scheuring kunnen dempen, terwijl de kalkgesteenten op 5 tot 8 km diepte het kunnen versnellen, met een groot verval in spanning als gevolg. Met andere woorden, de resultaten van dit onderzoek suggereren dat de aanwezigheid van grote volumes kalksteen op diepte het gevaar van destructieve aardbevingen vergroot.

Hoofdstuk III concentreert zich volledig op het wrijvingsgedrag van gesimuleerde breukgesteenten van kalksteen en puur calcietgruis, met een nadruk op de microfysische processen die het snelheidsverzwakkende gedrag op temperaturen boven ca. 100°C, zoals gezien in hoofdstuk II, kunnen verklaren. De experimenten bestaan dit keer uit zowel droge als natte tests in zogenaamde 'direct-shear' of 'directe-verschuiving', uitgevoerd in een siliconenolie-gemedieerd, triaxiaal deformatie-apparaat, onder een effectieve normaalspanning van 50 MPa, op temperaturen van 18°C tot 150°C, gebruikmakend van wrijvingssnelheden van 0.1 tot 10 μm/s. Natte experimenten gebruiken een poriëndruk van 10 MPa, terwijl de droge tests in contact staan met de atmosfeer zoals in het laboratorium aanwezig. Alhoewel de natte breukmeelmonsters iets zwakker zijn dan de droge (μ ≈ 0.6, vs. 0.7-0.8), laat de data min of meer hetzelfde gedrag zien als gerapporteerd in Hoofdstuk II voor de Xujiahe kalksteen. Zowel de droge als de waterverzadigde runs laten een transitie zien van snelheidsversterkend naar

snelheidsverzwakkend gedrag rond een temperatuur van 80° tot 100°C. De microstructuur van alle gedeformeerde monsters wordt gekenmerkt door de aanwezigheid van nauwe, grensparellelle alswel schuine schuifzones, indicatief voor inhomogene deformatie ofwel lokalisatie. De schuifzones doorsnijden een matrix van relatief groffe (10 tot 30 μm) breukmeelkorrels gelijkend op het startmateriaal, terwijl ze zelf bestaan uit extreem fijne korrels, dat wil zeggen tot een grootte van ca. 5 tot 20 nm. Ook worden de schuifzones ook gekenmerkt door een kristallografische voorkeursoriëntatie. Omdat het overgrote deel van de verplaatsing wordt geaccommodeerd door een grensparallelle schuifzone nabij het raakvlak van het monster met de stalen blokken van de directe-verschuiving configuratie, is dit de belangrijkste schuifzone of hoofdschuifzone, ook wel de 'principal slip zone' (PSZ) genoemd. Als de PSZ intern wordt gespleten bij het ontmantelen van de directe-verschuiving configuratie, wordt het schuifvlak herkend door gestrieerde, sterk reflecterende vlakjes, vergelijkbaar met welke vormen in experimenten op kalkbreukgesteenten op co-seismische snelheden (wrijvingssnelheden >0.1 m/s). Met behulp van eerder werk beredeneer ik dat het wrijvingsgedrag waarschijnlijk bepaald wordt door een mechanisme van dilatante korrelstroming, simultaan opererende met tijdsafhankelijke compactie van het korrelaggregaat. Omdat dit laatste steeds sneller gaat, en dus belangrijker wordt, met verhogende temperatuur, kan een transitie van wrijvingssnelheidsversterking naar wrijvingssnelheidsverzwakking zich voordoen. Voor een typische geothermische gradiënt van 20-25°C/km, impliceren de resultaten dat de bovengrens van de seismogene zone in kalkgesteente op een diepte van zo'n 4 km ligt. Dit is in overeenstemming met observaties van seismische activiteit in tectonisch-actieve gebieden die rijk zijn aan carbonaatgesteenten, zoals bijvoorbeeld in de Apennijnen (Italië).

In **Hoofdstuk IV** ga ik door met een micro- en nanostructureel onderzoek van de hoofdschuifzones of PSZs zoals gerapporteerd in hoofdstuk III, inclusief een detailstudie van de gestrieerde, sterk reflecterende vlakjes. De PSZ is onderzocht met behulp van een gecombineerde ionen/ electronenmicroscoop (een 'focused ion beam - scanning electron microscope'), een transmissie-elektronenmicroscoop, en een atoomkrachtmicroscoop. De observaties maken duidelijk dat de PSZ een relatief poreus, 10 tot 50 μm dik, plaat-achtig volume vormt, wat voornamelijk bestaat uit geronde, ~100 nm grote deeltjes of 'nanobolletjes' die onderling vaak gesinterd zijn. Binnen het PSZ volume worden de gestrieerde vlakjes aangetroffen, als dichte films van gelijkgerichtte, ca. 100 nm brede,

ketting-achtige vezels. Intern bestaan de nanobolletjes, en dus de nanovezels, uit ~5 tot 20 nm kleine calciet kristallieten, die met hun (104) kristalvlak (hexagonaal kristalsysteem) min of meer gelijkricht liggen aan het algemene schuifvlak. Aan de hand van de observaties stel ik voor dat massatransport in de PSZ gefaciliteerd is door diffusie via een 1-2 nm dikke, aan het oppervlak van de nanobolletjes geadsorbeerde waterfilm. Aan de hand hiervan wordt vervolgens een conceptueel model gepresenteerd die de transitie van wrijvingssnelheidsversterkend naar wrijvingssnelheidsverzwakkend gedrag van calcietbreukmeellaagjes boven ~80°-100°C, zoals geconstateerd in de voorgaande hoofdstukken, kan verklaren. Het model berust op dilatante stroming van nanobolletjes en –vezels, vergelijkbaar met het model zoals bediscussieerd in hoofdstuk III, en met het klassieke model voor superplastische deformatie van Ashby-Verrall. Een belangrijke implicatie is dat nanokristallijne schuifzones in calcietbreukmeel seismogeen kunnen zijn als gevolg van een diffusieproces, zelfs op diepten waar de temperatuur normaliter te laag is om dit te kunnen activeren. In het licht van talloze recente publicaties die het voorkomen en belang van nanokristallijne breukvlakken in een verscheidenheid van gesteenten in de bovenkorst onderschrijven, suggereer ik dat het voorgestelde mechanisme een toepassing heeft op seismogeen gedrag in het algemeen.

Vervolgens, in een poging om een soortgelijk inzicht te krijgen in de processen die een rol spelen rondom de onderlimiet van de seismogene zone in kalkgesteente, onderzoek ik in **Hoofdstuk V** het wrijvingsgedrag van gesimuleerde calcietbreukmeellaagjes op temperaturen waarvan redelijkerwijs verwacht mag worden dat ze de bros-ductiel transitie bestrijken. Experimenten worden uitgevoerd in een hydrothermale ringwrijvingsmachine (ofwel 'ring shear'), op temperaturen van 20° tot 600°C, onder waterverzadigde omstandigheden met een poriëndruk van 10 tot 100 MPa. Experimenten waarbij de wrijvingsnelheid systematisch en stapsgewijs wordt gevarieerd, uitgevoerd bij een effectieve normaalspanning (σ_n^{eff}) van 50 MPa en gebruikmakend van wrijvingssnelheden tussen 0.03 en 100 µm/s, laten zien dat het snelheidsverzwakkende gedrag boven temperaturen van ca. 80°C zich doorzet tot een temperatuur van ~550°C. Een transitie naar snelheidsversterkend gedrag wordt uiteindelijk gevonden op ~600°C. De schuifsterkte van de laagjes breukmeel, gemeten na ca. 11 mm verplaatsing op een snelheid van 1 µm/s, varieerde van ~28 MPa ($\mu \approx 0.6$) op 20°C, 19 tot 23 MPa ($\mu \approx 0.4$-0.5) op 100° tot 550°C, en 29 tot 32 MPa ($\mu \approx 0.6$) op 600°C. Experimenten waarin zowel stappen in wrijvingssnelheid (v) als in effectieve normaalspanning worden toegepast,

gebruikmakende van $1 \leq v \leq 100$ µm/s en $30 \leq \sigma_n^{eff} \leq 100$ MPa, laten zien dat de schuifsterkte lineair toeneemt met toenemende effectieve normaalspanning, en dus een frictie-proces vertegenwoordigd. De microstructuur van de breukmeellaagjes gedeformeerd op 20°C tot 200°C word gekenmerkt door een vergelijkbaar patroon van lokalisatie in nauwe schuifzones, zoals gezien in monsters gedeformeerd op 20°C tot 150°C in hoofdstuk III. Echter, op 400°C tot 600°C zijn naast dilatante korrelstroming in een gelokaliseerde, grensparallelle schuifzone ook tekenen van meer homogene deformatie zichtbaar, waaronder intrakristallijne plastische vloei en dynamische rekristallisatie van de grovere breukmeelkorrels. De resultaten laten een opvallende gelijkenis zien met voorspellingen van het eerder aangehaalde model omtrent dilatante korrelstroming met tijdsafhankelijke deformatie, d.w.z. hoofdstuk III en IV. Verder impliceren de resultaten dat de seismogene zone in kalkgesteenten, in een staat van overdruk, zich uitstrekt tot een diepte van ca. 13 tot 24 km. Dit komt overeen met seismiciteit zoals geobserveerd in de zuidelijke Apennijnen, en het Zagrosgebergte in Iran, op diepten waarvan verwacht wordt dat er carbonaatgesteenten aanwezig zijn.

Hoofdstuk VI omvat een onderzoek naar de wrijvingseigenschappen en microstructuur van gesimuleerde calcietbreukmeellaagjes gedeformeerd op condities rondom de transitie van snelheidsverzwakkend naar snelheidsversterkend gedrag rondom ~550°C tot 600°C, zoals geconstateerd in hoofdstuk V. De experimenten zijn wederom uitgevoerd in de ringwrijvingsmachine, onder waterverzadige omstandigen met een poriëndruk van 100 MPa, op een temperatuur van 550°C, gebruikmakende van constante wrijvingssnelheden van 0.1, 1, 10 en 100 µm/s. De effectieve normaalspanning is constant gehouden op 50 MPa, dan wel gestapt in een bereik van $20 \leq \sigma_n^{eff} \leq 140$ MPa. Bij relatief lage snelheid (0.1 µm/s) is de gemeten schuifspanning in minder mate, dat wil zeggen niet-lineair, afhankelijk van de effectieve normaalspanning, indicatief voor ductiliteit, en wordt de microstructuur gekenmerkt door homogene deformatie, typisch voor ductiele vloei. Ter vergelijking, in experimenten op relatief hoge snelheid (1, 10, of 100 µm/s) is de schuifspanning lineair afhankelijk van de effectieve normaalspanning, indicatief voor frictie, terwijl de microstructuur op 100 µm/s gekenmerkt wordt door lokalisatie in één grensparallelle schuifzone. Opmerkelijk genoeg heeft deze schuifzone optische eigenschappen vergelijkbaar met die van de breukmeellaagjes gedeformeerd op 0.1 tot 10 µm/s, bij 20°C tot 150°C, zoals gerapporteerd in hoofdstuk III. De resultaten impliceren ondermeer dat de bros-ductiel transitie in calcietbreukmeel afhankelijk is van

de vervormingssnelheid. Verder laten ze zien dat lokalisatie cruciaal is voor breuksterkte en -stabiliteit, in het bijzonder nabij de ondergrens van de seismogene zone.

Tenslotte wordt in **Hoofdstuk VI** een synopsis gepresenteerd van de voornaamste bevindingen in dit proefschrift en geef ik een overzicht van de implicaties voor seismiciteit in kalksteenrijke gebieden. Voorname conclusies betreffen het nanokristallijne karakter van gelokaliseerde zones in calcietbreukmeel, de rol die fysische eigenschappen op de nanoschaal spelen in het nucleëren van aardbevingen, en de bros-naar-ductiel transitie die is geconstateerd met temperatuur en met wrijvingssnelheid. Ik sluit af met een opsomming van onopgeloste problemen, en formuleer ook nieuwe problemen, welke direct volgen uit het gepresenteerde werk.

Chapter I

General introduction and aims

1.1. Motivation and scope of this study

Earthquakes are the result of a sudden release of energy during rapid slip ($v > 1$ m/s) along geologic fault zones in the Earth's crust or upper mantle, resulting in the generation of seismic waves that can be highly destructive at Earth's surface. Throughout history, earthquakes and associated tsunamis have claimed countless lives and caused severe material and economic damage. It is therefore of utmost importance to improve prognoses on the frequency, location, and magnitude of future events. However, this requires sophisticated modelling of earthquake nucleation and dynamic rupture propagation, which in turn requires a fundamental understanding of the failure, slip, and healing mechanisms operative in geologic faults, i.e. of fault rock sliding mechanisms active under in-situ conditions in the Earth.

Despite several decades of research on fault friction, our understanding of the material properties of fault rocks and how they control the nucleation of earthquakes, remain poor. Tectonically loaded faults, such as those present along plate boundaries or in depleted gas reservoirs, can exhibit aseismic "creep" without producing earthquakes, or exhibit unstable motion, resulting in slow-slip events or catastrophic failure as the case for earthquakes (see e.g. Scholz, 1998, 2002; Peng & Gomberg, 2010). Seismic fault motion of this type can occur at the lithosphere-scale, such as along megathrust faults in subduction zones (e.g. Hyndman et al., 1997), on a regional scale as is the case for reservoir-induced seismicity (e.g. Talwani, 1997), but also within mm- to cm-scale samples in the laboratory (e.g. Passelègue et al., 2013). The fault zones involved typically show evidence for multi-scale, self-similar behaviour (e.g. Tchalenko, 1970; King, 1983), characterized by strain localization into extremely narrow zones (e.g. Sibson, 2003) composed of nanogranular fault rocks (Power & Tullis, 1989; Chester & Chester, 1998; Chester et al., 2005; Ma et al., 2006; Siman-Tov et al., 2013; Kuo et al., 2014; Collettini et al., 2014). This suggests that the physical properties of fault rocks at the nano-scale may exert a major control on the macroscopic fault sliding properties. To achieve a better understanding of earthquake nucleation processes it is therefore crucial to unravel the key processes that control multi-scale fault slip, starting with a fundamental understanding of the nano- to micro-scale, material physical processes active within fault zones.

In this thesis, motivated by the frequency of destructive earthquakes in tectonically-active carbonate-bearing terranes, I report the results of an experimental study designed to determine the mechanisms controlling the sliding behaviour of fault rocks composed

of the dominant carbonate mineral, calcite ($CaCO_3$). Experiments were conducted using unique triaxial deformation equipment as well as a unique ring shear apparatus, at low sliding velocities (0.01 to 100 μm/s) and under in-situ conditions of pressure and temperature pertaining to upper-crustal seismogenesis. Correlative observations from the visual, cm-scale to the nano-scale, using state-of-the-art methods in microscopy, allowed for imaging and subsequent interpretation of the relevant physical mechanisms active during fault slip. Alongside providing new data, and new insights into the processes leading to seismogenesis, the results lend support to the validity of recent mechanistic models for fault gouge friction.

1.2. Seismicity in carbonate terrains and deformation processes in calcite rocks

Carbonate rocks are a class of rock types that are primarily composed of minerals characterized by a divalent cation plus a carbonate anion (CO_3^{2-}), such as calcite and aragonite [$CaCO_3$], siderite [$FeCO_3$], or dolomite [$CaMg(CO_3)_2$]. The major rock groups of sedimentary origin include limestones and dolostones, which are respectively composed mainly of calcite and dolomite. These rocks typically form as bioclastic calcite deposits, which may later be dolomitized by Mg-rich fluids (e.g. Machel, 2004), or as biochemical calcite or dolomite precipitates in marine or lacustrine environments (e.g. Nichols, 2004). The largest occurrences are platform carbonates, which form as vast marine, mainly calcareous deposits at the margins of the continental shelf (e.g. Wilson, 1975; Nichols, 2004). After diagenesis, and uplift and erosion in the orogenic cycle (see e.g. Twiss & Moores, 2007), such platform carbonate bodies frequently come to form a dominant lithology in tectonically-active terrains such as rifts and the external zones of orogens. It is for this reason that seismicity in carbonate or carbonate-bearing terrains is commonplace.

Recent, devastating examples of highly destructive earthquakes in tectonically-active carbonate terrains include the M_w 5.9 2012 Emilia event (Italy – Pizzi & Scisciani, 2012), the M_w 6.1 2009 L'Aquila event (Italy – Chiaraluce, 2012), the M_w 7.9 2008 Wenchuan event (China - Xu et al., 2009; Chen et al., 2013a, b) and the M_w 7.6 2005 Kashmir event (Pakistan – Hussain et al., 2009). Some of these earthquakes have relatively shallow hypocentres, as is the case for the first main shock in the Emilia sequence (6.3 km, Pizzi & Scisciani, 2012), or are associated with numerous shallow aftershocks, as observed following the 2009 L'Aquila event (~2 km, Chiaraluce, 2012; Valoroso et al., 2013). Their shallow nature means that they are often particularly damaging, even when the moment

magnitude is relatively moderate (Boatwright & Choy, 1986; Ma, 2008; Lee et al., 2009). Knowledge of the lithology of the earthquake host rock at greater hypocentral depths is often challenging, however, in some cases seismicity at ≥15 km depth has been specifically attributed to the presence of carbonate rocks. Examples include earthquakes at 15 km depth in the Zagros mountains of Iran (Nissen et al., 2011, 2014), but also in the southern Apennines, where seismicity at depths of ~18 km is inferred to be due to the stacking of carbonate rocks of the Apulia platform (Boncio et al., 2007).

Despite the frequency of destructive earthquakes in tectonically-active carbonate terrains, previous work on the frictional behaviour of carbonate fault rocks is limited (see also Mirabella et al., 2008; Scuderi et al., 2013). Experimental data show that (simulated) calcite(-rich) fault rocks exhibit unusual frictional properties compared with other common sedimentary rock types such as clay stones and sandstones (Ohnaka, 1975; Scuderi et al., 2013; Carpenter et al., 2014; Tesei et al., 2014), and have a tendency to exhibit potentially seismogenic behaviour at relatively shallow, upper-crustal conditions of pressure and temperature (Drennon & Handy, 1972; Olsson, 1974; Ohnaka, 1975). At the same time, calcite(-rich) rocks are well-known to exhibit ductile deformation by mechanisms such as pressure solution and crystal plasticity, at lower pressures and temperatures than generally required for these mechanisms to operate in other upper crustal rock types, such as granite (e.g. Burkhard, 1990; De Bresser, 1991; Spiers et al., 2004; see also Paterson & Wong, 2005). From microphysical modelling and analogue experiments, it is well-known that such time-dependent deformation mechanisms can play an important role in the processes controlling gouge frictional sliding, including those leading to seismogenic fault slip (Chester, 1994; Sleep, 1997; Nakatani, 2001; Bos & Spiers, 2002a, b; Niemeijer & Spiers, 2006, 2007; Den Hartog & Spiers, 2013, 2014). Crystal plasticity or pressure solution processes may therefore offer the key to explaining the unusual frictional behaviour of calcite-rich fault rocks compared with other sedimentary rocks.

Combining a) the frequency of seismicity in the carbonate cover of regions such as the Apennines (e.g. Chiarabba et al., 2005, 2014) and Corinth Rift (e.g. Bernard et al., 2006), with b) the atypical, readily unstable frictional character of calcite fault rocks, with c) their tendency to exhibit ductile deformation at shallow crustal conditions, suggests that faults in carbonates may be particularly prone to seismogenic slip at upper crustal depths (e.g. <10 km) compared with other common crustal rock types. The implication is that the mechanical properties of limestones may render carbonate terrains in active orogens

especially susceptible to seismicity and to seismic risks. To improve our understanding of the seismic cycle in tectonically-active carbonate terrains and for progress in modelling the dynamics of, and hazards posed by, seismogenesis in such regions, a much better understanding of the mechanical behaviour of carbonate fault systems, and of the controlling microphysical mechanisms, is needed.

1.3. The earthquake instability and the seismogenic zone

Field and drilling studies of active and inactive natural fault zones frequently demonstrate the presence of a mm- to cm-wide principal slip zone (PSZ) that accommodates, or has accommodated, the bulk of displacement along the fault (e.g. Sibson, 1986, 2003; Chester & Chester, 1998; Stewart et al., 2000; Wibberley & Shimamoto, 2003; Ma et al., 2006; Barth et al., 2013; Li et al., 2013; Kuo et al., 2014). The presence of such long-lived, localized zones in the crust implies that the fault rocks within are weaker than the surrounding country rocks (Rutter et al., 2001), and that their weakness is persistent. Thus, tectonic loading of a faulted rock volume, as occurs continuously in numerous geological settings (e.g. tectonic plate boundaries), will always lead to failure along the same, pre-existing fault structures. In the case of earthquakes, sliding along faults is achieved by unstable, periodic slip events instead of by stable, continuous motion. Indeed, (paleo-) seismological observations of small (e.g. Nadeau et al., 1995; Nadeau & Johnson, 1998; Wu et al., 2014) as well as large earthquakes (Schwartz & Coppersmith, 1984; Sieh, 1996; Ohnaka, 2013), show that they occur repeatedly with well-defined recurrence times. In other words, earthquakes are recurring slip instabilities on essentially permanent faults that remain (quasi-)stationary between seismic events.

As first put forward in a classic paper by W.F. Brace and J. D. Byerlee in the sixties, this behaviour is similar to the jerky sliding motion that is frequently observed in laboratory friction experiments, known as “stick-slip” (Brace & Byerlee, 1966; see also e.g. Ohnaka, 1973, 2013; Scholz, 2002; Paterson & Wong, 2005; Twiss & Moores, 2007). Regular stick-slip behaviour can be easily envisioned using a spring-block model system (Fig. 1.1), consisting of a rigid block or slider of mass (m) on a nominally flat surface, driven via a spring of a certain stiffness (k). When the spring is pulled at constant speed, an instability may develop depending on the frictional properties of the slider-surface contact, the mass of the block, the spring stiffness, and the loading rate (v), resulting in intermittent slider acceleration and stationary contact (e.g. Dieterich, 1979a; Ruina, 1983;

Baumberger et al., 1994; see also Twiss & Moores, 2007). In addition to providing a way to explain the periodicity of fault slip instability, the analogy of stick-slip behaviour to natural earthquake faulting is that i) the associated stress drops are small compared to the strength of (most) rocks, as observed in earthquakes, and that ii) stick-slip represents a mechanism that produces events of sudden energy release in a pre-fractured medium (Brace & Byerlee, 1966).

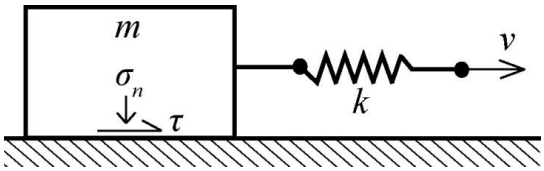

Figure 1.1. Schematic illustration of a spring-block model. m is the mass of the block, k the spring stiffness, and v the loading rate. σ_n is the normal stress and τ the shear stress acting on the block-surface contact. When pulled under the right conditions this will exhibit stick-slip behaviour, which is a mechanical analogue for earthquakes.

Since Brace & Byerlee (1966), much theoretical and experimental work has focused on the processes leading to frictional instability (for recent examples see McLaskey et al., 2012; Kaproth & Marone, 2013), and its applicability to earthquake faulting (see reviews by Marone, 1998a; Scholz, 1998, 2002; Paterson & Wong, 2005; Ohnaka, 2013). Using a spring-slider model system similar to that illustrated in Figure 1.1, Ruina (1983) showed that for regular stick-slip to occur, the slider-surface contact must decrease in strength with increasing displacement rate hence be velocity-weakening. In the opposite case velocity-strengthening occurs, which leads to a state of stable sliding (Ruina, 1983; Rice & Ruina, 1983; Tse & Rice, 1986; see also Scholz, 2002; Twiss & Moores, 2007). Importantly, this velocity dependence of frictional strength is a material property of the sliding medium which constitutes the slider-surface contact. Applying this to natural faults, the sliding medium would be represented by the granular wear material present in the fault core, or "fault gouge", which is the wear product of cumulative slip along the fault (Sibson, 1977; see also Snoke et al., 1998; Scholz, 2002).

In the classical view, the strength of the upper-crust is approximated using a Coulomb-type, brittle failure law representing the upper part, abruptly giving way to ductile deformation below~15 to 20 km depth (Fig. 1.2; e.g. Brace & Kohlstedt, 1980; Kohlstedt et al., 1995). A brittle-to-ductile transition at ~15 to 20 km depth is consistent with geological and seismological observations of the base of the so-called "seismogenic

zone", i.e. the depth interval in the upper-crust in which the bulk of upper-crustal seismogenesis occurs (Sibson, 1982, 1983, 1984; Meissner & Strehlau, 1982; Scholz, 1988; Ito, 1990, 1999; Chiarabba et al., 2005, 2014; Shibazaki et al., 2008; Fagereng & Toy, 2011), suggesting that at greater depths earthquake rupture nucleation is inhibited by intrinsically stable, ductile or viscous flow in shear zones (e.g. Tse & Rice, 1986; Shimamoto, 1986, 1989). Microphysical and empirical modelling studies suggest that, within seismogenic zone, 'multi-mechanism' or 'frictional-viscous' fault slip -involving coincident rate-sensitive (creep) and rate-insensitive (e.g. cataclasis) deformation mechanisms- plays an important role (Chester & Higgs, 1992; Reinen et al., 1992; Chester, 1994, 1995; Bos et al., 2000a, b; Bos & Spiers, 2002a, b; Niemeijer & Spiers, 2005, 2006). This is believed to be especially important close to the brittle-to-ductile transition (Holdsworth et al., 2001; Rutter et al., 2001; Imber et al., 2008; Noda & Shimamoto, 2010, 2012; Shimamoto & Noda, 2014), i.e. the base of the seismogenic zone, where the largest magnitude earthquakes nucleate (Fig. 1.2; Sibson, 1982, 1983, 1984; Scholz, 1988, 2002). However, in general, the processes responsible for aseismic fault sliding above the seismogenic zone, and for seismogenic slip within, remain poorly understood for most rock types, including monomineralic calcite rocks such as limestones.

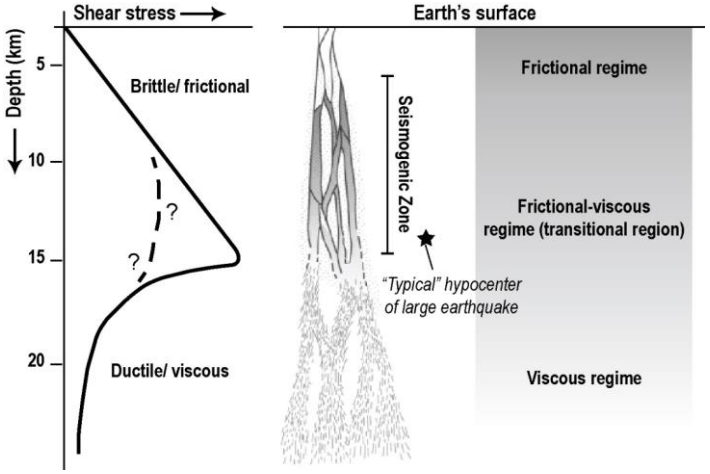

Figure 1.2. Conceptual models for the upper ~20-25 km of Earth's crust. Left: crustal fault strength profile (Brace & Kohlstedt, 1980; Kohlstedt et al., 1995). Right: Fault zone as it transitions from frictional behaviour at shallow depths to frictional-viscous and then viscous behaviour at greater depths (after Holdsworth et al., 2001). The depth range of the seismogenic zone is based on that expected for a quartzofeldspathic crust (e.g. Sibson, 1982; Scholz, 1988; Fagereng & Toy, 2011).

1.4. Rate-and-state friction models

From the above, it is clear that the strength and stability of active fault sliding depend at least in part on the frictional properties of the sliding medium, i.e. upon the resistance to shear displacement along the fault. Static friction is the resistance to movement from a state of rest, whereas dynamic friction refers to the resistance experienced to maintain sliding. In a more general context, fault strength can be described using the shear stress (τ), or the force supported parallel to the sliding surface per unit area of fault surface. In the classical view, from early friction experiments performed by Leonardo Da Vinci (1452-1519), and later by Guillaume Amontons (1663-1705), the shear stress is proportional to the applied normal stress (σ_n), or the force acting per unit area at right angles to the sliding surface (see Scholz, 2002; Paterson & Wong, 2005; Jaeger et al., 2007), implying a constant value of the coefficient of friction, given $\mu = \tau/\sigma_n$. Although the empirical laws of Amontons and Da Vinci are generally obeyed to a first degree, laboratory friction experiments conducted in mainly the 1960's and 70's show that the value of μ tends to decrease towards elevated normal stresses (Paterson & Wong, 2005 and references therein). This non-linearity can be described empirically using a Mohr-Coulomb type expression of the form $\tau = S_0 + \mu\sigma_n$, where S_o is the 'intrinsic cohesion' of the rock surface or gouge-filled fault (e.g. Hoskins et al., 1968; Byerlee, 1978; see also Paterson and Wong, 2005; Jaeger et al., 2007). In the presence of a pore fluid pressure (P_f) acting on the pore walls of the sliding medium, the effective normal stress $\sigma_n^{eff} = \sigma_n - \alpha P_f$ should be taken into account (Hubbert & Rubey, 1959; Byerlee, 1967; Nur & Byerlee, 1971; see also Morrow et al., 1992), so that

$$\tau = S_0 + \mu\left(\sigma_n - \alpha P_f\right). \qquad (1.1)$$

To a first approximation, most faulted rock surfaces and gouge-filled faults obey equation 1.1, using $\alpha \approx 1$, rather well (Byerlee, 1978; see also e.g. Morrow et al., 1992; Scholz, 2002; Paterson & Wong, 2005). Specifically, for slip on pre-existing faults, Byerlee (1978) showed on empirical basis that as a general rule, $\tau \approx 0.85\sigma_n$, with cohesion being negligible for $\sigma_n < 200$ MPa, whereas $\tau \approx 50 + 0.6\sigma_n$ for $200 < \sigma_n < 1700$ MPa. This has come to be known as "Byerlee's Law".

Notwithstanding the above empirical relations, upon closer examination, fault frictional strength appears to be affected by surface roughness conditions (e.g. Byerlee,

1967; Ohnaka, 1975; Barton, 1976), the presence of moisture or pressurized fluids such as water (e.g. Brace, 1972; Morrow et al., 2000; Moore & Lockner, 2004), temperature (e.g. Stesky et al., 1974; Olsson, 1974; Stesky, 1978; Shimamoto, 1986; Blanpied et al., 1991, 1995, 1998), and time-dependent healing and sliding velocity-dependent effects (e.g. Dieterich, 1972, 1978, 1979a; Ohnaka, 1975; Marone, 1998b). In particular, as we have seen in the foregoing sections, velocity-strengthening or -weakening effects may play a crucial role in controlling the stability of frictional sliding (Ruina, 1983; Rice & Ruina, 1983; Tse & Rice, 1986). To capture the experimentally observed and highly complex time dependence of static friction and the velocity dependence of dynamic friction, in an empirical way, Dieterich (1979a) developed the rate-and-state-dependent friction model (RSF), which enabled highly successful reproduction of laboratory rock friction data over a wide range of conditions (e.g. Dieterich, 1981; Ruina, 1983; Tullis & Weeks, 1986; Reinen & Weeks, 1993; Dieterich & Kilgore, 1994; Rathbun & Marone, 2013; for a review see Marone, 1998a). In RSF relations, the coefficient of (dynamic) friction μ for steady-state slip at velocity v is described with respect to sliding at a reference state via the relation (Dieterich, 1979a; Ruina, 1983)

$$\mu = \mu_* + a\ln(v/v_*) + b\ln(v_*\theta/D_c) \qquad (1.2)$$

Here, μ_* is the coefficient of friction for steady-state slip at a reference velocity v_*, θ is a state variable with dimensions of time, a and b are dimensionless empirical parameters, and D_c is the characteristic slip distance. While this relation can be accurately fitted to laboratory friction data, it is hard to extrapolate to other conditions beyond these specific experiments. Indeed, there has been considerable debate on the use and physical interpretation of the state variable θ and the parameters a, b and D_c occurring in the RSF model (see e.g. Marone, 1998a), and different formulations for the "state" evolution $\dot{\theta}$ or 'evolution law' have been proposed (Dieterich, 1981; Ruina, 1983; Linker & Dieterich, 1992; Perrin et al., 1995; for reviews see Marone, 1998a; Paterson & Wong, 2005). The two most widely used evolution laws are the "slowness" law and the "slip" law (Ruina, 1983), which differ in physical interpretation and mathematical definition of the parameters appearing in equation 1.2. In the case of the slowness law, the evolution of the state variable under constant effective normal stress is described by $\dot{\theta} = 1 - (v\theta/D_c)$ (Dieterich, 1981, 1986, 1992). Here, the state variable θ evolves with time, even when the frictional surface is under truly stationary contact (v = 0). For the slip law, again at

constant effective normal stress, the evolution of the state variable is described by the relation $\dot{\theta} = -(v\theta/D_c)\ln(v\theta/D_c)$ (Ruina, 1983). In this case, the state variable changes only during active slip and does not change ($\mathrm{d}\theta/\mathrm{d}t = 0$) during stationary contact. Despite being essentially phenomenological, RSF models have been highly successful in simulations of the seismic cycle, including modelling earthquake rupture nucleation (e.g. Lapusta & Rice, 2003; Ampuero & Rubin, 2008) and propagation (e.g. Noda et al., 2009; Noda & Lapusta, 2013), aftershock decay (Dieterich, 1994; Ziv & Rubin, 2003), and slow slip events (Liu & Rice, 2005, 2007, 2009; Rubin, 2008). They are also being used for modelling problems related to human-induced seismicity (e.g. McClure & Horne, 2011).

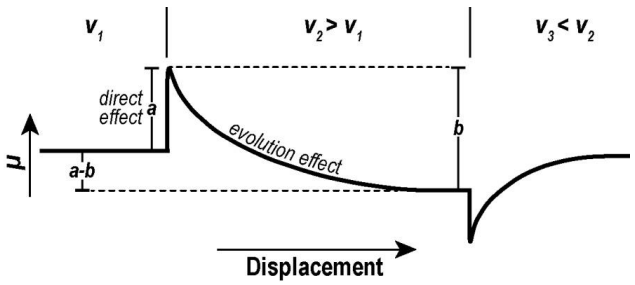

Figure 1.3. Plot of coefficient of friction (μ) against displacement, representing the frictional response to a perturbation in sliding velocity ($v_1 \rightarrow v_2 \rightarrow v_3$). In the case of an e-fold step in sliding velocity ($v2 = e{\cdot}v_1$), the magnitudes of the direct and evolution effects are respectively equal to the RSF parameters 'a' and 'b'. In this example $(a\text{-}b) < 0$, thus implying velocity weakening frictional behaviour.

In the framework of the RSF model for describing frictional strength, the parameters a and b appearing in eq. 1.2 determine whether slip is velocity-strengthening or velocity-weakening. These have magnitudes usually of the order of $a \approx b \approx 0.01$, and respectively describe the magnitudes of the direct and evolution effects (Fig. 1.3). The direct effect is the instantaneous jump in strength that occurs upon perturbation of the sliding velocity at steady-state, while the evolution effect describes transient adjustments of frictional strength that occur over the characteristic slip distance (D_c) required to re-attain steady-state strength. This means that the difference $(a\text{-}b)$ quantifies the net effect of sliding velocity on steady-state frictional strength (Fig. 1.3), implying that $(a\text{-}b) > 0$ for (inherently stable) velocity strengthening slip and $(a\text{-}b) < 0$ for (potentially unstable) velocity-weakening slip. In the case that $(a\text{-}b) = 0$, frictional sliding is velocity neutral or rate independent. Furthermore, regardless of which evolution law, at steady-state $\dot{\theta} = 0$, so that $\theta_{ss} = D_c/v$. From equation 1.2 it then follows that the magnitude of $(a\text{-}b)$ at

steady-state is given by $(a - b) = \mathrm{d}\mu_{ss}/\mathrm{dln}(v)$ (e.g. Marone, 1998a; Scholz, 1998).

1.5. Microphysical models of fault gouge frictional sliding

The time-dependent healing and sliding velocity dependent effects of friction are generally explained in terms of creep of asperities or contact junctions characterizing the slider-surface contact or fault plane (Scholz & Engelder, 1976; Dieterich & Kilgore, 1994; Berthoud et al., 1999). Asperity creep or time dependence can result from the operation of Arrhenius-type (thermally-activated) deformation mechanisms such as intracrystalline plasticity, diffusive mass transfer (including pressure solution), or subcritical cracking (Chester & Higgs, 1992; Chester, 1994). For this reason, physical interpretations of the RSF model as discussed above typically rely on a thermally-activated, Arrhenius-type rheology active at the asperity (contact) scale (Chester & Higgs, 1992; Chester, 1994; Sleep, 1997, 2005; Baumberger et al., 1999; Berthoud et al., 1999; Nakatani, 2001; Rice et al., 2001; Noda & Shimamoto, 2010; He et al., 2013; Shimamoto & Noda, 2014). However, RSF descriptions have remained empirical to date, with little physical basis regarding the internal deformation and healing processes active during gouge frictional slip, and without taking internal geometric or microstructural aspects into account (Bos, 2000; Niemeijer, 2006; Niemeijer & Spiers, 2006, 2007; Den Hartog, 2013; Den Hartog & Spiers, 2014; Chen, 2015). Extrapolation to nature, i.e. to slip rates, length scales, pressure-temperature conditions, or other boundary conditions not attainable in laboratory friction experiments, therefore presents a major source of uncertainty in numerical modelling of natural fault motion (for a recent discussion see Ide, 2014).

An understanding of the chemical and micromechanical interactions that occur during frictional sliding of granular aggregates, such as fault gouge, requires knowledge of the relevant bulk and intergranular deformation processes, plus a model framework. Bos & Spiers (2002a) for the first time formulated a microphysical model for frictional-viscous flow of halite-phyllosillicate mixtures (simulated fault gouge analogue), at low slip rates (0.05 to 10 μm/s), involving a serial process of slip over phyllosillicate foliae and pressure solution of intervening halite clasts. This provided a theoretical framework that could explain the normal stress sensitive, velocity strengthening behaviour seen in their experiments (see Bos, 2000). In order to explain frictional velocity weakening behaviour seen in experiments on halite-phyllosillicate mixtures sheared at 1 to 13 μm/s, Niemeijer & Spiers (2005, 2006) developed this concept further by incorporating effects of dilatancy at high(er) slip rates. In their model, frictional sliding is described as a

granular flow process involving competition between dilatation and intergranular compaction by pressure solution (Niemeijer & Spiers, 2007). Changes in frictional strength and its rate dependence *(a-b)*, with velocity and temperature, are due to changes in their relative contribution to strain-accommodation.

The approach employed by Bos & Spiers (2002a) and Niemeijer & Spiers (2007) allows for gouge frictional behaviour to be expressed as a function of effective normal stress, shear strain rate, temperature, and the relevant microstructural parameters or materials properties. Den Hartog & Spiers (2013, 2014) developed the model further, and showed that it can explain frictional velocity strengthening and –weakening in phyllosillicate-quartz mixtures over a wide range of conditions of pressure, temperature, displacement rate, and effective normal stress (see Den Hartog, 2013). The fundamental principle of the model as developed by Niemeijer & Spiers (2006, 2007) rests on the simultaneous operation of (relatively) time-insensitive dilatant processes (e.g. granular flow) and time-dependent creep (e.g. pressure solution, crystal plasticity), within the sheared granular aggregate, the competition between which controls frictional strength and its velocity dependence. An important topic to address remains whether this conceptual model is generally applicable, i.e. whether it can explain the frictional properties of granular media other than halite- or quartz-phyllosillicate mixtures. Since (simulated) calcite gouge is monomineralic, and since the ease of plasticity in calcite, this material is highly suitable for exploring this question.

1.6. Structure and aims of this thesis

From the foregoing, it is clear that i) calcite dominated lithologies, such as limestone, form a major constituent of tectonically-active terrains such as rifts and orogens, ii) improved modelling of seismogenesis in tectonically-active carbonate terrains is needed, and iii) little is known about the frictional behaviour of carbonate rocks in general. The research conducted here aims to address these points by providing new mechanical and microstructural data on calcite fault gouge, which will be used to test and calibrate mechanism-based models describing fault frictional behaviour. Shearing experiments are reported that make use of (simulated) calcite(-rich) fault gouge, under (near) in-situ conditions relevant to earthquake nucleation in tectonically-active carbonate terrains, and resultant microstructures are analyzed using the latest techniques in electron microscopy.

The specific aims of this thesis are:

1. To determine experimentally the frictional and microstructural properties of (simulated) calcite fault gouge sheared at slip velocities and at pressure-temperature conditions relevant to seismogenesis in the shallow (~≤10 km) crust. The primary focus here is the frictional strength and stability of calcite fault gouges compared with gouges prepared from other common upper-crustal rock types, as well as the microstructural features developed during shear.
2. To determine the deformation mechanisms involved, and how these control shear resistance and stability of fault slip. This aim targets the physical properties of calcite fault gouge expected to be relevant to nucleation of earthquakes.
3. To qualitatively compare the experimental results and sheared gouge microstructures with a micromechanical model for shear of granular media involving dilatant granular flow and creep-controlled compaction, i.e. with the model proposed by Bos & Spiers (2002a), Niemeijer & Spiers (2007), and Den Hartog & Spiers (2014) for the frictional behaviour of phyllosillicate/ halite or phyllosillicate/ quartz mixtures.
4. To investigate the shear strength, slip stability, and microstructure of (simulated) calcite fault gouge throughout the frictional-to-viscous transition, i.e. over a range of temperatures ultimately high enough for shear to be accommodated by viscous or plastic flow.

Addressing these points will help to improve model prognoses on the frequency, location, and magnitude of future earthquakes in tectonically-active limestone terrains, such as the Apennines of Italy or the Corinth Rift Zone of Greece, thus contributing to seismic hazard assessment. Also, it will help generate a much-needed, fundamental understanding of the processes leading to seismogenesis, which may benefit hazard reduction in the context of both natural earthquakes, as well as earthquakes induced by human activities such as natural gas production (e.g. Segall, 1989; Talwani, 1997; Hettema et al., 2000; Schutjens et al., 2004). In the following, each of the above aims will be addressed in Chapters II to VI, followed by a general conclusion and suggestions for future research in Chapter VII.

Chapter II

Frictional properties of sedimentary rocks and natural fault gouge from the Longmenshan Fault Zone, Sichuan, China

After:

Verberne, B. A., He, C., and Spiers, C. J. (2010). Frictional properties of sedimentary rocks and natural fault gouge from the Longmenshan Fault Zone, Sichuan, China. B. Seismol. Soc. Am. **100,** 2767-2790.

Abstract

This Chapter reports friction experiments performed on samples collected from the region hit by the 2008 Wenchuan earthquake in the Longmenshan Fault Zone (LFZ) of Sichuan, southwestern China. The materials tested consisted of simulated gouges prepared from intact clay-rich mudstone and sandstone, a calcite limestone, plus a natural fault gouge from a trenched, surface rupture cutting the mudstone and sandstone. The clay-rich samples, including the natural gouge, were dominated by illite and quartz. In our experiments, we sheared 1-mm-thick gouge layers between saw-cut driver blocks, using a triaxial testing machine at conditions corresponding to ~2 km depth in the LFZ. Temperature was varied from 25 to 150°C and, to investigate the velocity dependence of friction, we stepped the shear displacement rate between 1.22 and 0.122 μm/s. Our results show that the natural gouge was more illite-rich and much weaker than the protolith mudstone and sandstone, and showed a steady-state friction coefficient of ~0.4 compared with ~0.6 for the latter. The limestone gouge displayed values of 0.6 to 0.7. All samples, except the limestone, showed stable, velocity-strengthening slip. The limestone showed velocity-strengthening at 25° to 50°C, but quasi-static oscillations at 100° to 150°C along with velocity-weakening behaviour at 150°C. We apply our results to discuss the role of the sedimentary rocks studied during events such as the Wenchuan earthquake, and argue that the clay-rich sediments of the region may have a damping effect upon ruptures propagating from depth, whereas the limestone may accelerate propagation, producing significant stress drops.

2.1. Introduction

The Longmenshan Fault Zone (LFZ; Fig. 2.1), which runs some 400 km northeastwards through the Wenchuan, Beichuan and Qingchuan counties of Sichuan province, southwestern China, slipped catastrophically during the Great Wenchuan Earthquake (M_w 7.9) of May 12th 2008. Immediately after this event, multiple field surveys were initiated by the Chinese government to investigate the newly developed surface ruptures and associated exposures of the LFZ (Liu-Zeng et al., 2009; Xu et al., 2009). At the same time, a comprehensive research program was initiated, including work on the physical and mechanical properties of the main rock types of the region, with the aim of understanding in detail the rupture phenomena associated with the Wenchuan earthquake.

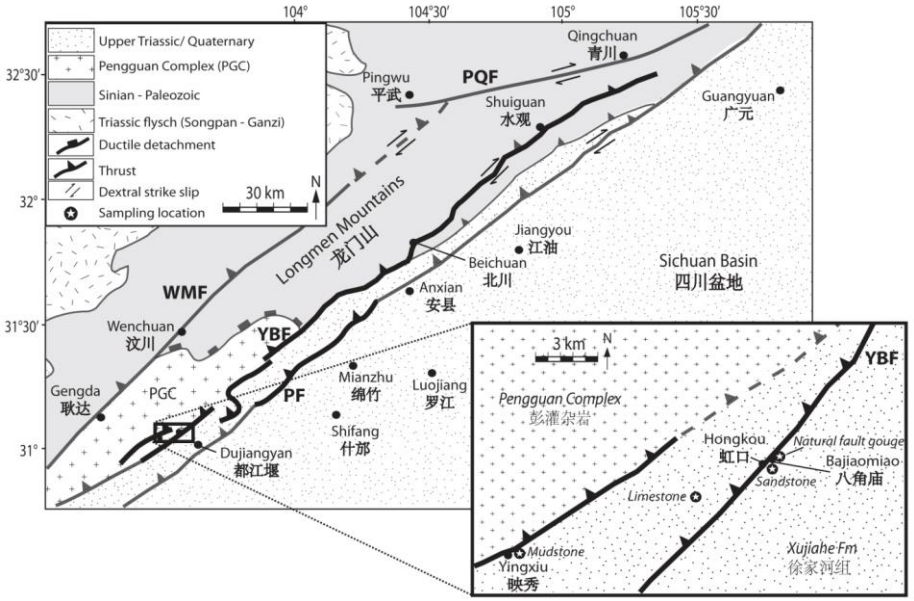

Figure 2.1. The central part of the Longmenshan Fault Zone (LFZ) in Sichuan, southwestern China, roughly 60 km to the northwest of Chengdu. The surface rupture induced by the Wenchuan Earthquake is indicated by the bold portions of the various fault traces (Liu – Zeng et al. (2009); Xu et al. (2009)). The main map was compiled after Xu et al. (2008). YBF = Yingxiu – Beichuan Fault; WMF = Wenchuan – Maoxian Fault; PF = Pengguan Fault; PQF = Pingwu – Qingchuan Fault.

During the course of several field campaigns, samples were collected from the main rock formations cut by the faults making up the LFZ, and from trenched, surface

ruptures. The samples were brought to the China Earthquake Administration (CEA) laboratory in Beijing for detailed investigation of their rock mechanical properties. In this Chapter, we report and discuss the results of rock friction experiments performed on samples prepared from representative sedimentary rocks and from a trenched fault gouge from the Yingxiu – Beichuan portion (YBF) of the LFZ (Fig. 2.1). According to on-going field and seismological research, the central section of the YBF is one of the most heavily ruptured parts of the LFZ. Slip on this section initiated at a depth of 13-16 km (Huang et al., 2008; U.S. Geological Survey Earthquake Hazards Program, 2008; Pei et al., 2010; Wang et al., 2009).

Rock friction studies provide constraints on the frictional strength of fault zone rocks during pre-, co- and post-seismic slip. All of these aspects need to be understood in detail if we are to build numerical models that link stress-field evolution and fault response, with the aim of gaining better insight into the likely location, frequency and magnitude of future seismogenic events (Tullis, 1988; Sykes et al., 1999; Rebetskii, 2002; Scholz, 2002). In particular, near-surface dynamic rupture propagation, triggered by ruptures propagating from depth, can only be constrained if we understand the frictional properties of the lithologies that dominate the shallow subsurface (Boatwright and Cocco, 1996; Tinti et al., 2005; Mizoguchi et al., 2008). For the LFZ, this means that we need to investigate representative sedimentary rocks collected in the field, as well as fresh, natural fault gouge collected from active faults, i.e. surface ruptures.

Using this strategy, we attempt to answer the following questions:

i. What is the effect of seismic rupture and gouge formation on the frictional strength of typical sedimentary rocks from the LFZ region? In other words, how weak are natural fault gouges from the LFZ with respect to their protoliths?F
ii. How weak are the shallow sedimentary rocks of the LFZ, in terms of frictional strength, compared with the crystalline quartzofeldspathic and/ or mafic rocks expected at hypocentral depths?
iii. What is the role of these shallow sediments during seismic slip, compared with underlying basement rock? Do they offer stable resistance to coseismic rupture propagating from below without producing abrupt stress drops, or do they show unstable slip plus a major internal stress drop?

Answering question (i) should help predict the loci of surface ruptures associated with

future earthquakes. Answering questions (ii) and (iii) may help predict future damage risk from a knowledge of the relationship between basement and overlying sediments. Combining our results with the principles of rate and state dependent friction analysis, we discuss the implications of our findings for the seismotectonic setting of the LFZ and the earthquake process.

2.2. Background

Before proceeding to describe our experiments, we first present essential background information on the regional geology of the LFZ and on the sampling strategy used. In addition, an introduction is given to the rate and state dependent friction law used as a theoretical framework to interpret our experimental results.

2.2.1. Regional geology and sampling strategy

The Longmenshan fault zone is an imbricated, oblique thrust-fault system that accommodates eastward crustal extrusion of the Tibetan Plateau over the rigid lithosphere of the Yangtze block (Zhang et al., 2004; Densmore et al., 2007; Xu et al., 2008; Hubbard and Shaw, 2009). Located at the eastern edge of the Longmen Mountains, it marks the interface between the Songpan – Ganzi terrane (a Triassic orogenic belt) to the west and the Paleozoic – Cenozoic sediments of the Sichuan Basin to the east (Fig. 2.1). The fault system itself cuts through NNE-SSW trending, Neoproterozoic basement metamorphics marked by steeply westward dipping detachments (e.g. the Pengguan Complex). Overlapping these, Paleozoic to Triassic sediments of the Sichuan Basin are also found in the fault zone. (Tang et al., 2008; Xu et al., 2008). The sediments in particular are cut by numerous imbricate thrust faults that form a wedge of northeast-trending oblique thrusts dipping steeply to the northwest. These include the presently active Wenchuan – Maoxian Fault (WMF), the Yingxiu – Beichuan Fault (YBF) and the Pengguan Fault (PF) (or Guanxian – Anxian fault). Field mapping and post-earthquake satellite imaging showed that the Wenchuan earthquake ruptured both the YBF and PF, along the middle-segment of the LFZ, producing rupture scarps up to 10 m in height (Liu-Zeng et al., 2009; Xu et al., 2009).

In the present study, we focused on Upper Triassic sedimentary rocks from the Xujiahe Formation, found near the southernmost ruptured part of the YBF in the central LFZ region (Fig. 2.1 inset map). The Xujiahe Fm is widespread in the LFZ and Sichuan basin. It shows strong lateral variations in lithology, but in essence comprises rocks deposited in a fluvio-deltaic setting, including conglomerates, sandstones, siltstones,

lacustrine limestones and mudstones, with some coal interbeds and often high carbonaceous content (Tang et al., 2008; Zhu et al., 2009). To investigate the response of the Xujiahe Fm to seismic rupturing, various end-member lithologies found in the Xujiahe Fm were sampled. Our samples thus consisted of a grey lacustrine limestone (08-WC-34), a black carbonaceous sandstone (08-WC-39) and a black carbonaceous mudstone (08-WC-05), sampled at the locations shown in Fig. 2.1. In addition, a ruptured segment of the YBF cutting sandstone and mudstone of the Xujiahe Fm, was trenched at Bajiaomiao, near Hongkou, to study the structure of the fault and to sample the black fault gouge (WF-09-06-10; Fig. 2.1). From surface ruptures along the fault trace it was inferred that the fault slipped at least 2 m at this location during the Wenchuan earthquake of May 2008. Gouge samples measuring roughly 10 cm x 10 cm x 2.5 cm (~250 mL in volume) were extracted from a prominent planar band exposed in the trench.

2.2.2. Rate and State dependent Friction laws

To date, laboratory rock friction studies have focused mainly on the resistance to and stability of sliding exhibited by bare rock surfaces and simulated, gouge-filled faults. The resistance to sliding, or frictional strength, is generally expressed in terms of the coefficient of friction μ, i.e. the ratio between the shear stress τ and the effective normal stress σ_{eff} acting on the fault plane. The effective normal stress is defined as the stress acting at right angles to the sliding surface (the normal stress σ_n) minus the pore fluid pressure (P_f) acting on the pore walls within the fault rock.

The stability of frictional sliding of rock is thought to be related to the stability of natural fault zones (e.g. Lapusta and Rice, 2003; Paterson and Wong, 2005). An important unstable slip phenomenon that is commonly encountered in rock friction experiments is regular stick-slip behaviour, also thought to be closely related to the periodic nature of earthquakes (Brace and Byerlee, 1966). Insight into stick-slip behaviour was first obtained in slide-hold-slide and velocity stepping experiments performed both on sliding rock surfaces and simulated fault gouges (e.g. Dieterich, 1972, 1979, 1981; Scholz and Engelder, 1976). These experiments led to the formulation of the phenomenological rate and state dependent friction law, or RSF law, which has proved to reproduce laboratory-derived rock friction data well and to describe key features such as regular stick-slip and the transition from stable sliding to unstable slip (e.g. Dieterich, 1979; Ruina, 1983; Rice and Ruina, 1983; Gu et al., 1984).

In RSF constitutive relations, the coefficient of friction is expressed as a function of slip velocity V and a state variable θ, as follows:

$$\mu = \mu_* + a\ln(V/V_*) + b\ln(\theta/\theta_*) \quad (2.1a)$$

or

$$\mu = \mu_* + a\ln(V/V_*) + b\ln(V_*\theta/D_c) \quad (2.1b)$$

where μ_* is the coefficient of friction for steady-state slip at a reference velocity V_* characterized by an internal reference state θ_* (e.g. Linker and Dieterich, 1992; Marone, 1998a). Note that the state variable θ has dimensions of time and can be interpreted as the average age of the population of contacts between two sliding surfaces, or their average life-time when the fault surfaces or gouge are in motion. The parameters a and b are empirical constants that describe the magnitudes of the direct and evolution effects, respectively. The direct effect is the instantaneous jump in friction coefficient that is observed upon perturbation of the sliding velocity at steady-state, i.e. from sliding at velocity V_*, while the evolution effect describes transient adjustments that occur over a characteristic slip distance D_c required to re-attain steady-state friction at the new sliding velocity V (Marone, 1998a).

In practice, two classes of evolution laws have been put forward to describe the transient evolution of θ, namely the slip and slowness laws. These differ in physical interpretation and mathematical definition of the parameters appearing in (2.1). In the case of the slowness law, the evolution of the state variable under constant effective normal stress is described by the differential equation (Dieterich, 1979; 1981)

$$d\theta/dt = 1 - V\theta/D_c \quad (2.2a)$$

Here, the state variable θ evolves with time, even when the frictional surface is under truly stationary contact ($V = 0$). For the slip law, again at constant effective normal stress, the evolution of the state variable is described by the relation (Ruina, 1983; Linker and Dieterich, 1992)

$$d\theta/dt = -(V\theta/D_c)\ln(V\theta/D_c) \quad (2.2b)$$

In this case, it is evident that the state variable changes only during active slip and does not change ($d\theta/dt = 0$) during stationary contact ($V = 0$).

These evolution laws can simulate different aspects of the mechanical data obtained from frictional sliding experiments (Perrin et al., 1995; Marone, 1998a; He et al., 2003; Ampuero and Rubin, 2008), but microphysical models that can fully describe frictional sliding phenomena are yet to be agreed upon (for a discussion see Paterson and Wong, 2005). The slowness law is more commonly used because of observations of time-dependent healing phenomena between sliding surfaces (e.g. Dieterich and Kilgore, 1994; 1996). Nonetheless, from (2.1b) and (2.2) it follows that the coefficient of friction at steady-state, μ_{ss}, for both evolution laws reduces to

$$\mu_{SS} = \mu_* + (a-b)\ln(V/V_*) \qquad (2.3)$$

For both forms of RSF evolution law, the sign and magnitude of the difference between the rate dependence constants *(a-b)*, is a measure of so-called velocity strengthening versus velocity weakening behaviour. This is crucial to the stability of frictional systems (Ruina, 1983), and is determined by interaction between frictional sliding of the sliding surfaces (or shearing of gouge) and their elastic surroundings. A velocity strengthening system exhibits a positive dependence of steady-state frictional strength on displacement rate. In such systems, slip instabilities are quickly damped to a state of stable sliding. By contrast, velocity weakening systems show a negative rate dependence, and slip rate perturbations can lead to a state of regular stick-slip provided that the stiffness of the system falls below a given critical value (Ruina, 1983). Whether a fault displays velocity strengthening or velocity weakening is recognized to be of key importance in determining whether earthquake nucleation is possible and what the response will be to dynamic rupture propagation (Tse and Rice, 1986; Rudnicki, 1988; Dieterich, 1992; Boatwright and Cocco, 1996; Tinti et al., 2005; Ampuero and Rubin, 2008).

The value of *(a-b)* is therefore key. It can be quantified using a differential expression implicit in (2.3), i.e. using the relation

$$(a-b) = \partial\mu_{ss} / \partial\ln(V) \qquad (2.4)$$

Previous studies have investigated how *(a-b)* depends upon temperature, normal stress, chemical environment and the intrinsic properties of the sliding surfaces, such as roughness, gouge mineral constituents and gouge particle size (e.g. Dieterich, 1981; Lockner et al., 1986; Biegel et al., 1989; Linker and Dieterich, 1992; Kilgore et al., 1993; Saffer and Marone, 2003; Blanpied et al., 1995; He et al., 2006, 2007). The absolute values of *a*, *b* and of other constants in the RSF law as expressed in equations 2.1 and 2.2 cannot be directly extracted from experimental data individually, because of the mechanical interaction between the sample and the loading system. To do so, forward and inverse modeling techniques are required (e.g. Tullis and Weeks, 1986; Reinen and Weeks, 1993). Fortunately, however, the rate dependence *(a-b)* can be estimated using a finite difference form of equation 2.4, i.e. from measurements of the steady-state coefficient of friction at high and low velocities.

2.3. Experiments

2.3.1. Approach and choice of conditions

In the present study, we make use of the RSF formulation and analysis described above to investigate the frictional properties of the sedimentary lithologies and fault rocks sampled from the Xujiahe Fm (Fig. 2.1). The experiments aim to address the frictional behaviour of these materials under shallow, upper crustal pressure and temperature conditions.

The present friction tests consist of so-called 'saw-cut' sliding experiments performed in a servo-controlled, triaxial testing machine at the Institute of Geology of the CEA in Beijing. In this type of experiment, samples prepared from crushed rock or natural gouge are sheared between obliquely cut, cylindrical driver blocks under a given confining pressure. The shear and normal stresses acting on the slipping surface are measured, and, after applying appropriate corrections to the data, the frictional behaviour of the sample can be analyzed. Note that the triaxial machine used allows the normal stress acting on the simulated fault plane to be held constant during an individual experiment, through servo-control of the confining pressure. We ran the experiments at a nominal confining pressure and pore pressure corresponding to in-situ values of the lithostatic pressure and pore pressure at a depth of ~2 km in the LFZ. The lithostatic pressure was estimated to be roughly 50 MPa, taking an overburden density of $\rho \approx 2450$ kg m^{-3} (Jiang and Jin, 2005). Assuming high connectivity of fractures in the fault zone, the pore fluid pressure was taken to be hydrostatic, i.e. 20 MPa. To simulate various crustal depths in our

experiments and to assess the effect of temperature on friction, we varied the temperature from 25 to 150°C. Based on a heat flow of 55.3 mW/m^2 for the Longmenshan region (Wang, 1996), we estimated a one-dimensional geothermal gradient of ~18.5°C/ km. Temperatures of 100-150°C thus correspond to depths up to ~5 – 8 km, while 50°C corresponds to the in-situ temperature expected at 2 km depth alongside the applied confining pressure of ~50 MPa and the pore pressure of 20 MPa.

2.3.2. Sample material

The experiments were performed on crushed granular samples prepared from intact limestone, sandstone and mudstone, and on an untreated natural fault gouge. Thin section analysis of the intact sedimentary rocks revealed that the carbonaceous mudstone and sandstone consisted mainly of quartz, feldspar and plant fragments embedded in a clayey, carbon-rich matrix. The mudstone consisted of ~65-70% of very fine grained (<20 μm) matrix material (clay minerals, fossil fragments), plus 30-35% of coarser detritus such as angular grains of quartz and feldspar with a grain size up to ~100 μm. The sandstone was characterized by a larger portion of relatively coarse grains of quartz and feldspar (~40-50%), showing a much wider particle size distribution (up to ~1 mm), again embedded in a clayey, carbon-rich matrix. Both the mudstone and sandstone showed sedimentary layering weakly defined by alternating layers of clay-rich and coarser material typically 50-300 μm in thickness. The limestone consisted of a dense carbonate wackestone containing ~85-90% of fine grained calcareous matrix plus 10-15% of recrystallized microfossils and microfossil fragments. None of the sedimentary rocks sampled showed pre-existing deformation textures. The natural fault gouge consisted of an extremely fine grained, black, soft and sticky clay.

To prepare simulated fault gouge from our intact sedimentary rock samples, the samples were crushed, ground, and then sieved using a 200-mesh sieve. Crushing and sieving were repeated until all the material passed through the sieve, yielding a grain size of ≤75 μm. For the natural gouge we applied a different procedure. In this case, for each friction experiment we took a ~10 mL scoop of material from the ~250 cm^3 parent block of gouge, as extracted from the fault trench. We then removed fragments of coarser material (i.e. contaminant quartz grains) that were introduced when the sample was extracted from the fault, and used the material directly without crushing, grinding or sieving.

Prior to deformation, quantitative X-ray diffraction (XRD) and laser particle size analyses were performed on all of the (simulated) gouges to investigate their mineral compositions and the particle size distributions (Table 2.1). Particle size analysis indicated that the median particle diameter (d_{50}) for all samples was <10 μm (Fig. 2.2). However, the simulated mudstone and sandstone gouges contained a much larger proportion of relatively coarse grained material than the limestone and natural gouge (Table 2.1). This is likely due to the presence of relatively hard quartz and feldspar grains.

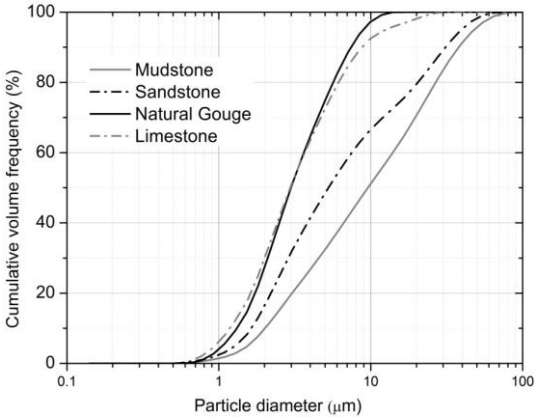

Figure 2.2. Cumulative grain size distributions of the simulated limestone, mudstone and sandstone gouges, and for the natural fault gouge extracted from a fault cutting the sandstone and mudstone. Determined using a laser particle sizer.

XRD analysis of the mineral phases present in the various gouges was performed using standard methods and software, achieving a resolution of 1-2 vol. %. To estimate the abundance of different clay minerals, we followed the Chinese Petroleum and Gas Industrial Standard method (SY/T 5163-1995). This method employs three types of oriented sample mount, namely, ethylene-glycol-saturated samples, air-dried samples, and samples heated to 550°C. Clay minerals having a particle size <2 μm were separated from the bulk sample by suspension in deionized water followed by settling to prepare the oriented samples. Results indicated that the mudstone and sandstone gouges contained ~49-58% quartz and ~23-29% illite, along with dolomite, plagioclase, chlorite and smectite in minor amounts (Table 2.1). The natural fault gouge contained a much higher percentage of illite (~54%) compared to the sandstone (~29%) and mudstone (~23%). Our simulated limestone gouge consisted almost entirely (~96%) of calcite with

Sample	Mineral content (vol. %)									Particle diameter (μm)		
	qtz	*plg*	*K-fsp.*	*calcite*	*dol.*	*illite*	*smect.*	*chl.*	*kaol.*	d_{10}	d_{50}	d_{90}
Simulated mudstone gouge (08-WC-05)	49	6	--	--	16	23	trace	5	--	2.0	9.6	37.9
Simulated sandstone gouge (08-WC-39)	58	10	--	--	2	29	2	--	--	1.6	5.3	31.0
Natural gouge (WF-09-06-10)	31	4	trace	--	--	54	4	7	--	1.3	3.0	7.4
Simulated limestone gouge (08-WC-34)	trace	--	--	96	--	2	--	--	--	1.2	2.9	8.7

Table 2.1. Starting materials, their mineralogical compositions and grain size statistics. Mineralogical compositions are given to the nearest integer percentage, as the XRD method used to determine them has a resolution of ~1-2 vol. %. qtz = quartz; plg = plagioclase; K-fsp = potassium feldspar; dol. = dolomite; smect. = smectite; chl. = chlorite; kaol. = kaolinite. Smectite was identified as a component of mixed-layer illite-smectite. Note that '--' indicates that the corresponding phase is below the detection limit of XRD analysis (<1-2 vol.%); dx refers to the particle diameter corresponding to the x^{th} percentile of the cumulative grain size distribution as determined using laser sizing.

only traces of clay minerals and quartz. Note that, on the basis of the low diagenetic/ metamorphic grade of the samples, we assumed that potentially indistinguishable or mixed illite/ mica peaks in the XRD spectra represent illite.

2.3.3. Sample assembly

The 'saw-cut' sample assembly used in the present experiments consisted of an upper and a lower driver block sandwiching the fault gouge. All experiments used cylinders of Fontainebleau sandstone and Fengzhen gabbro as the upper and lower driver block respectively (Fig. 2.3), with the saw-cut oriented at 35° to the central axis. The Fontainebleau sandstone we used in our experiments was well-indurated, but relatively porous (~22%) and permeable (~10^{-14} m^2), and allowed for a swift and uniform distribution of pore fluid pressure across the sliding surface. The Fengzhen gabbro - from Dashakou quarry, Fengzhen, Inner Mongolia, China (see He et al., 2006, 2007) - is a dense, fully crystalline rock with an exceedingly low porosity and permeability. It therefore acted as a barrier to fluid flow, ensuring spreading of the pore fluid throughout the gouge sample. Driver block dimensions were 20 mm in diameter by 40 mm total length for both driver blocks combined. Before introduction of the gouge layer, we ground the elliptical sliding surfaces flat and roughened them with a #300 grit abrasive, i.e. an abrasive grain size of ~40 μm.

Prior to experimentation all loose gouge samples were mixed into a paste with deionized water, in proportions of roughly 10:1 gouge to water. A purpose built jig allowed easy emplacement of a 1 mm thick gouge paste layer onto the surface of either the sandstone or gabbro driver block. The sample assembly, including the gouge, driver blocks, tungsten-carbide spacers, alumina pistons and steel end-pieces, was then jacketed with heat-shrink Fluorinated Ethylene Propylene (FEP) tubing of ~0.4 mm initial thickness (Fig. 2.3). The jacket was shrunk onto the assembly with a hair drier to produce a stiff, well-supported assembly. Double O-rings were used to seal the FEP tube against both ends of the assembly, i.e. against the steel end-pieces. Finally, a sheet of Teflon was attached with MoS_2-based lubricant to the lower end-piece, minimizing the frictional resistance to horizontal slip between the lower end-piece and the main loading piston.

In experiments at temperatures above 25°C, the FEP shrunk considerably in a direction parallel to the sample axis, to the extent that the jacket slid past the O-rings and lost its sealing capacity. To overcome this problem, we added an extra steel spacer of a

slightly larger diameter to the bottom end of the sample assembly, and we extended the length of the jacket to cover both this spacer and the step in the diameter of the upper piston/sealing-block. In this way, a step in diameter was produced at both ends of the jacket. This provided enhanced shrink-grip, which prevented inward sliding motion of the jacket parallel to the sample axis. This grip was reinforced at the lower spacer using a steel wire tourniquet, sunk in a groove in the spacer (Fig. 2.3).

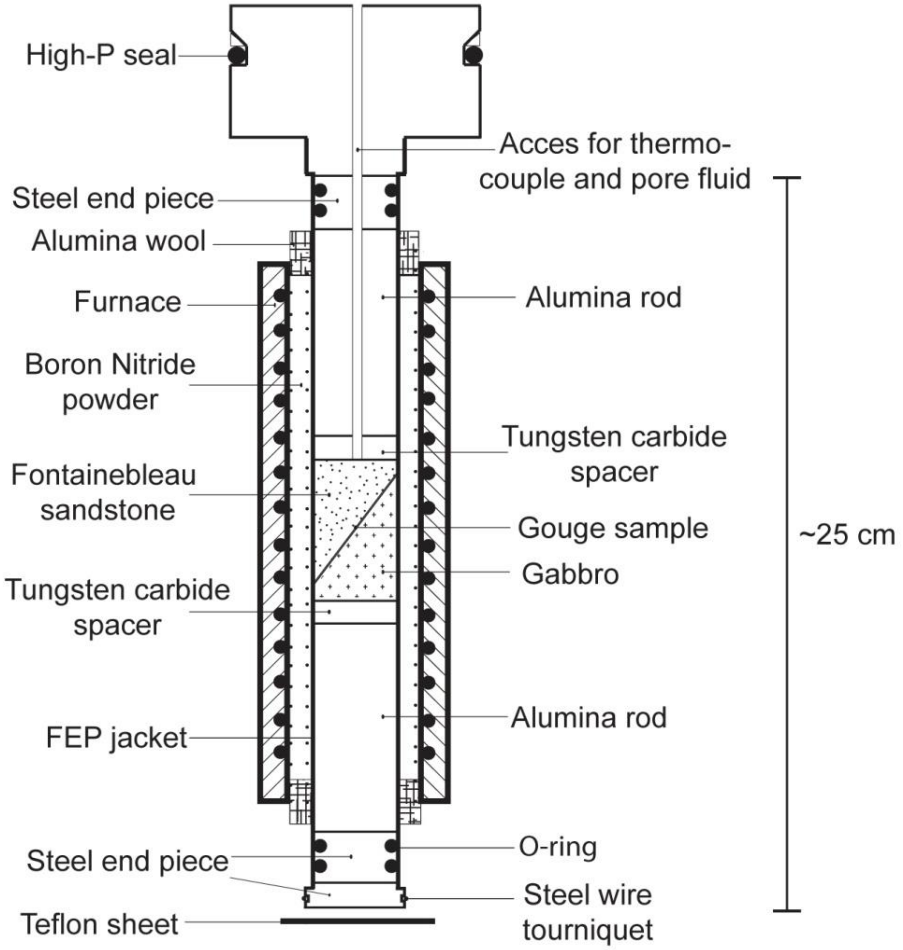

Figure 2.3. Schematic illustration of the sample assembly plus surrounding furnace.

2.3.4. Experimental apparatus

The experimental apparatus consists of a high pressure and high temperature triaxial testing apparatus comprising an Ar-gas medium pressure vessel, a servo-controlled hydraulic ram for axial loading, and a system of pressure boosters. The boosters generate confining pressure which can be controlled to within 0.5 MPa by a servo-controlled intensifier. For more details on the apparatus the reader is referred to He et al. (2006).

Temperature was applied using an independently controllable two-zone internal furnace. This allowed for a symmetric temperature distribution along the sample axis. All temperatures quoted here were measured with a thermocouple located at the top of the sandstone driver block (Fig. 2.3). Previous calibration demonstrated that for the range used in this study the temperature at the top of the driver block differs by at most 1°C from the temperature in the gouge zone. Also, the maximum temperature difference across the gouge zone itself is <1°C. Heat transfer by gas convection was reduced by filling the space between the furnace and the sample assembly with Boron Nitride (BN) powder. To hold the BN in place, both ends of the furnace-sample column were plugged with insulating Al_2O_3 wool (Fig. 2.3). Temperature control was achieved with a Yamatake-Honeywell DCP30 industrial controller, using a constant heating ramp to reach the desired set point temperature. This enabled control to within 2°C of the set value.

All experiments presented here were performed by applying a constant normal stress (σ_n) to the gouge zone. As already indicated, this was achieved through servo-control of the confining pressure system, accounting for changes in applied axial load within the servo-control loop. For slow variations in the axial stress, σ_n-control could be held to within 0.5 MPa of a set value. Deionized water was used to apply pore pressure, which was generated and held to within 0.3 MPa of the desired value by a second servo-controlled intensifier. Axial displacement was measured with a linear variable differential transformer (LVDT) that was attached to the hydraulic loading ram. Velocity steps were applied by switching the (axial) displacement rate between 0.1 and 1 μm/s. The axial load was measured with an external load cell which therefore required correction for seal friction.

2.3.5. Data acquisition and processing

Data was recorded at a sampling rate of 1 Hz using a 16-bit A/D converter connected to a digital interface. After confining pressure and temperature were applied at the

desired values for each run, the seal friction force (F_{in}, F_{out}) was measured by moving the loading piston up and down, prior to making contact with the sample assembly. The correction factor C_f quantifying the seal friction was then calculated using $C_f = ½(F_{in} - F_{out})/P_c$, and entered as a parameter into an algorithm that automatically corrected the axial force data. This provided an accurate way to correct the axial stress for seal friction, yielding an absolute error in the coefficient of friction of about 0.0025. Any rate dependence of the seal friction was not detectable for the range of loading rates we used in this study.

Another correction that must be applied to the raw data arises from the decrease in load supporting surface area that occurs during progressive displacement of the saw-cut sample assembly. We corrected the axial stress for this geometric effect following He et al. (2006). The area-corrected shear stress supported by the sample is then given

$$\tau_{ac} = ½\left(\sigma_{ac} - P_c\right)\cdot\sin(2\varphi) \qquad (2.5)$$

where σ_{ac} is the area-corrected axial stress, P_c is the confining pressure and φ the angle between the sliding surface and the central loading axis.

The shear stress obtained was further corrected for the shear resistance offered by the FEP jacket. To do this we performed sliding tests at both high (100°C) and low (25°C) temperature on a Teflon sheet of known frictional characteristics. In this way, the strength of FEP could be quantified as a function of displacement. The sheet was sandwiched between two steel saw-cuts that were cut to an angle of 30° to the central axis. After correction for decreasing contact area, the known frictional resistance of the Teflon-steel contact was subtracted to obtain the shear resistance vs. slip curve of the jacket. Remarkably, this curve was virtually independent of temperature, and was accurately approximated using a linear relation with a slope of 1.1 MPa/mm (goodness-of-fit R^2 = 0.996). The true shear stress τ supported by the sample was calculated by subtracting this correction from τ_{ac} in eq. 2.5 as a function of slip displacement. Finally, the instantaneous coefficient of friction was calculated from $\mu = \tau/\sigma_{eff}$, where σ_{eff} is the effective normal stress on the sliding surface.

At temperatures exceeding ~100°C, the FEP became slightly permeable to the Ar gas confining medium. At the standard test pressures of 50 MPa confining pressure (P_c) and 20 MPa pore fluid pressure (P_p), this caused a confining pressure leak into the sample of ~0.01 MPa/s at 100°C, which rose to ~0.02 MPa/s at 150°C. To investigate the effect of

this leak, i.e. of the permeation of argon into the sample, on the frictional properties of the gouges, we performed a limited number of control runs using copper tubing of 0.35 mm initial thickness instead of FEP. We found that the effect on the mechanical data was negligible compared with the uncertainties introduced by the relatively strong copper jacket.

2.3.6. Experimental procedure

In performing each experiment, the sample assembly was loaded into the pressure vessel and the vessel end-closure emplaced. Note that sealing of the vessel is achieved via a high pressure O-ring located in the top block of the sample assembly (Fig. 2.3). For experiments above 25°C the vessel was subsequently evacuated to protect the furnace from residual water vapor and air. To account for the pressure increase upon temperature elevation, we initially applied about half of the desired final values of confining pressure and pore fluid pressure. We next heated the sample assembly to the required test temperature at a constant rate of 3°C/min. To trim to the desired confining pressure (~50 MPa) and pore pressure (20 MPa), we then pumped in extra argon and water accordingly, holding these pressures constant to within 0.5 and 0.3 MPa of the respective set values using the corresponding servo-controlled intensifiers. After thermal equilibration and determination of the seal friction, the main loading piston was then advanced to shorten the saw-cut assembly and thus shear the sample. The total duration of the deformation experiments was at most 2 hours.

Normal stress control automatically initiated when a pre-determined threshold for the normal stress was reached. The normal stress acting on the sliding surface is a function of the frictional strength of the sliding material and the minimum compressive stress, i.e. the confining pressure. To calculate the threshold value for σ_n-control that corresponds to a confining pressure of ~50 MPa, we used estimates of the frictional strengths of the materials studied, as obtained from pilot frictional sliding tests. In this way, the servo-control maintained the normal stress constant through adjusting the confining pressure, and each material was tested at a normal stress that, theoretically, corresponds to the normal stress acting on a fault cutting the material at in-situ conditions pertaining to ~2 km depth in the LFZ (Table 2.2).

Tests were performed at temperatures of 25°C, 50°C, 100°C and 150°C. The initial axial displacement rate was 1 μm/s, yielding a shear displacement rate of 1.22 μm/s. Velocity steps were applied by switching this value to a shear displacement rate of 0.122

μm/s when steady-state was achieved, or when the slope of the μ vs. shear displacement curve reached a constant value. Following steps down to 0.122 μm/s, the displacement rate was held constant for roughly 1000 s, beyond which a new steady-state was generally approached and we could again apply a higher displacement rate. Upon stepping up to 1.22 μm/s, steady-state was usually approached within roughly 200 s. The number of velocity steps carried out depended on the total shear displacement achieved, which varied from 1.4 to 3.5 mm. Because the gouge layer thickness was not necessarily constant throughout individual experiments, the bulk shear strain γ achieved in our tests cannot be measured in a straightforward manner. However, as the initial gouge layer thickness was 1 mm, and the final value was 0.7 – 0.9 mm, the maximum shear displacements of 1.3 – 3.5 mm achieved in our experiments imply final bulk shear strains γ of 1.3 to 5.0. The maximum shear displacement, or shear strain achieved, was limited by failure of the FEP jacket which we were unable to control.

2.4. Results

2.4.1. Friction coefficient vs. displacement data

A list of the experiments performed and the key parameter values obtained is given in Table 2.2. Our friction coefficient (μ) versus shear displacement (x) data for all tests are plotted in Figures 2.4 and 2.5.

Most experiments showed rapid near-linear loading in the first 0.25-0.5 mm of displacement, giving way to a sharp "yield" point followed by gradual slip strengthening until near steady-state sliding was achieved at a displacement of typically 1-3 mm. Subsequent stepping of sliding velocity from the initial value of 1.22 μm/s to 0.122 μm/s showed a noisier signal at the latter rates. Nonetheless, clear effects on the friction coefficient were observed.

For the sandstone, mudstone and natural gouges, we found slip strengthening behaviour and stable sliding motion at all conditions tested (Figs. 2.4 and 2.5). Friction coefficients fell in the range of typically 0.5-0.6 for the sandstone and mudstone gouges and in the range of 0.3-0.4 for the natural gouge. Slip strengthening occurred at rates ($d\mu/dx$) of 0.026 to 0.053 mm^{-1} for the sandstone gouge, 0.006 to 0.027 mm^{-1} for the mudstone gouge and 0.018 to 0.045 mm^{-1} for the natural gouge. In most cases, slip strengthening rates decreased with ongoing displacement, with the sample approaching steady-state sliding at 2.0 to 2.5 mm displacement. In a few experiments, notably mud@25°C (Fig. 3.4), initial "yield" was followed by a sudden stress drop with more or

less immediate strength recovery. The origin of these stress drops is unknown. However, as the full μ vs. shear displacement curves obtained in the experiments showing this phenomenon are otherwise closely similar to the remaining curves for the same material, and as strength recovery to the trend shown by the original loading curve is fast, we infer that this stress drop effect reflects an apparatus artefact, such as lateral slip effects at the lower piston/ end-piece interface (Fig. 2.3). In response to velocity stepping, we found velocity strengthening behaviour for the simulated sandstone, mudstone and natural gouges at all displacements and loading rates investigated (Figs. 2.4 and 2.5).

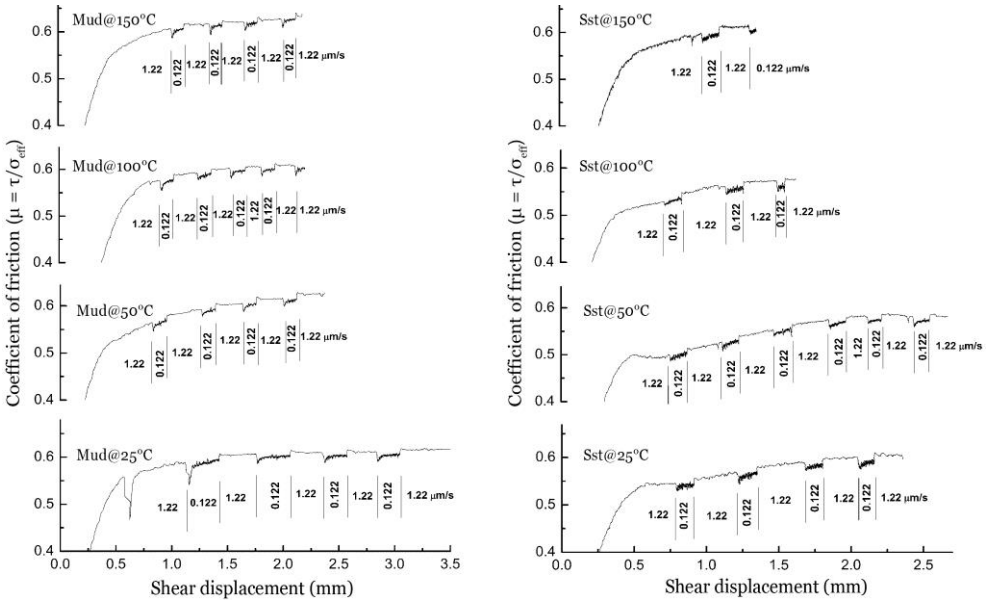

Figure 2.4. Friction coefficient against shear displacement curves for simulated mudstone (left) and sandstone gouges (right) at temperatures ranging from 25 to 150°C. Shear displacement rates are indicated in μm/s beneath the curves. Key parameters listed in Table 2.2.

For the simulated limestone gouge deformed at temperatures of 25 and 50°C (Fig. 2.5), steady-state sliding was achieved more quickly, i.e. at shear displacements of only 0.8 – 1 mm, and was characterized by friction coefficient values of ~0.7. The response to velocity stepping was one of velocity strengthening behaviour for all displacements and loading rates. In contrast, for limestone gouge sheared at 100 and 150°C, a peak frictional strength was achieved at a displacement of 0.75 mm, followed by slip weakening up to a total displacement of ~1.25 mm. At 100°C, more or less steady-state

sliding followed at μ values of ~0.67 at 1.22 μm/s displacement rate. However, steps down to 0.122 μm/s showed on-going slip weakening and clear strength oscillations at total displacements beyond 2.0-2.5 mm. At 150°C, slip weakening beyond the peak strength was followed by marked oscillations in μ at all rates and displacements beyond ~1 mm, with a mean friction coefficient of ~0.62 at 1.22 μm/s.

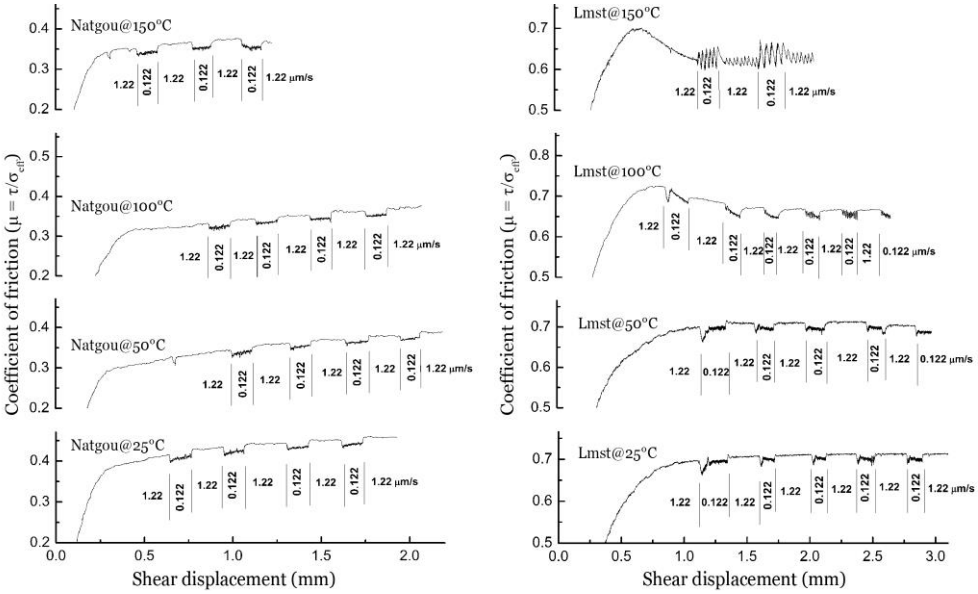

Figure 2.5. Friction coefficient against shear displacement curves for natural fault gouge (left) and simulated limestone gouge (right) at temperatures ranging from 25 to 150°C. Shear displacement rates are indicated beneath the curves. Key parameters listed in Table 2.2.

Our friction coefficient vs. shear displacement data for simulated limestone gouge (Fig. 2.5) thus show a transition from stable sliding to quasi-static oscillation with increasing temperature. This transition is best seen in experiment lmst@100°C, where oscillations occurred in the low displacement rate stages of the run, but only after ~2 mm of shear displacement. In these oscillatory stages, the mean coefficient of friction decreased with increasing displacement, indicating unstable slip weakening behaviour. In experiment lmst@150°C, oscillations occurred at the high and low displacement rates, with the amplitude of oscillation being higher at the lower displacement rate. In this run, the mean coefficient of friction increased with decreasing sliding velocity, indicating unstable, velocity weakening behaviour. At the same time, the mean coefficient of friction increased with displacement in the low velocity stages of the experiment, demonstrating

ongoing slip strengthening with increasing shear displacement. In the higher velocity stages of experiment lmst@150°C, the mean coefficient of friction remained more or less constant.

Starting material	Experiment	T (°C)	σ_N (MPa)	μ_{ss}	$\Delta\mu_{ss}$	(a-b)	Type of motion at max. displ.
Simulated mudstone gouge	Mud@25°C	25	68	0.61	0.0090	0.0039 ± 0.0003	Stable sliding
	Mud@50°C	50	68	0.61	0.0110	0.0050 ± 0.0007	Stable sliding
	Mud@100°C	100	68	0.61	0.0090	0.0039 ± 0.0004	Stable sliding
	Mud@150°C	150	68	0.63	0.0078	0.0034 ± 0.0005	Stable sliding
Simulated sandstone gouge	Sst@25°C	25	68	0.60	0.0112	0.0048 ± 0.0006	Stable sliding
	Sst@50°C	50	68	0.58	0.0094	0.0041 ± 0.0005	Stable sliding
	Sst@100°C	100	68	0.58	0.0115	0.0050 ± 0.0006	Stable sliding
	Sst@150°C	150	68	0.61	0.0117	0.0051 ± 0.0005	Stable sliding
Natural gouge	Natgou@25°C	25	58	0.46	0.0136	0.0059 ± 0.0004	Stable sliding
	Natgou@50°C	50	58	0.38	0.0092	0.0040 ± 0.0005	Stable sliding
	Natgou@100°C	100	58	0.37	0.0102	0.0044 ± 0.0005	Stable sliding
	Natgou@150°C	150	58	0.37	0.0140	0.0061 ± 0.0009	Stable sliding
Simulated limestone gouge	Lmst@25°C	25	73	0.71	0.0118	0.0051 ± 0.0006	Stable sliding
	Lmst@50°C	50	73	0.71	0.0158	0.0069 ± 0.0004	Stable sliding
	Lmst@100°C	100	73	0.67	0.0170	0.0074 ± 0.0009	Stable sliding
	Lmst@150°C	150	73	0.62	-0.019	-0.003 ± 0.002[1)] -0.004 ± 0.001[2)]	Quasi-static oscillations

Table 2.2. List of experiments performed and key parameter values obtained. All experiments were performed at a constant pore fluid pressure of 20 MPa. All involved a velocity stepping procedure between shear displacement rates of 1.22 μm/s and 0.122 μm/s (when steady-state sliding was achieved). T = temperature; σ_N = constant normal stress applied to the gouge layer in each experiment, by means of servo-control of the confining pressure system; μ_{ss} = steady-state friction coefficient measured at a sliding rate of 1.22 μm/s, and at 2 mm shear displacement or else at the displacement where the FEP jacket broke (if less than 2 mm). Note that the value of 'μ_{ss}' for experiment Lmst@150°C is a mean value rather than a steady-state value and was estimated from the mean coefficient of friction μm of oscillations at 1.22 μm/s. $\Delta\mu_{ss}$ = the difference in the value of the friction coefficient at steady-state, or else the final values, in the high and low velocity stages (see text for discussion). Note that '$\Delta\mu_{ss}$' for experiment lmst@150°C is the difference in μm at the high and low velocity stages rather than a difference in steady-state strength. *(a-b)* = measure of the velocity dependence as derived using RSF laws; (+) = vel. strengthening, (-) = vel. weakening. 1) Obtained using eq. (2.6), with $D_c \approx 3$ μm. 2) Obtained using eq.'s (2.A2) and (2.7).

2.4.2. Dependence of friction coefficient on temperature

To elucidate the influence of temperature on gouge strength, the steady-state or else mean friction coefficient values measured at a sliding velocity of 1.22 μm/s (μ_{ss} in Table

2.2) are plotted against temperature in Fig. 2.6. The simulated sandstone and mudstone gouges do not show any significant variation in μ_{ss} as a function of temperature. However, the natural gouge was significantly stronger at 25°C than at higher temperatures, showing a decrease in steady-state friction coefficient from 0.46 at 25°C to ~0.38 at 50°C, and remaining more or less constant at higher temperatures. Our crushed limestone samples show a more steady decrease in strength, notably at temperatures exceeding 50°C. The decrease in coefficient of friction is nearly 0.1, falling from 0.71 at 25-50°C to 0.62 at 150°C, and accompanies the transition from stable sliding to oscillating motion.

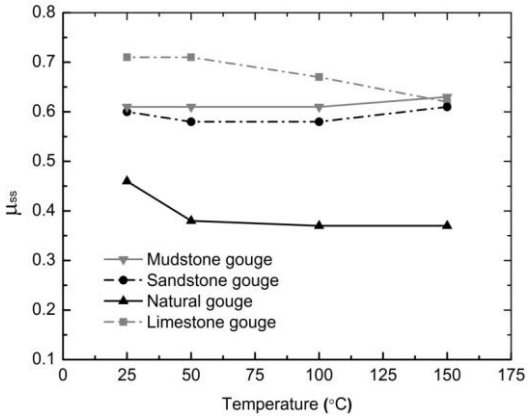

Figure 2.6. Friction coefficient at steady-state (μ_{ss}) plotted against temperature. Note the μ_{ss} plotted for oscillatory slip of limestone at 150°C are mean values rather than steady-state values.

2.4.3. RSF constitutive parameters

To investigate the velocity dependence of friction exhibited by the deformed gouges, we make use of the rate and state (RSF) friction laws introduced earlier. The steady-state velocity dependence *(a-b)* can be quantified using a finite difference form of eq. 2.4, i.e. by calculating the ratio of the difference in steady-state strengths $(\Delta\mu_{ss})$ at high and low loading rates to the difference in natural logarithm of the shear displacement rate *(ΔlnV)*.

The value for ΔlnV is constant for each velocity step in all experiments, as we consistently applied velocity steps differing by one order in magnitude ($\Delta lnV = \ln(10) \approx 2.3$). In the case of experiments exhibiting stable sliding throughout, we determined $\Delta\mu_{ss}$ graphically for each velocity step, and then took the average value for all steps as the $\Delta\mu_{ss}$ – value for the entire experiment. We then calculated the corresponding value of *(a-b)* for the experiment of interest using the finite difference form of eq. 2.4 (Table 2.2).

Averaging of $\Delta\mu_{ss}$ over the measured velocity steps led to a standard deviation that was used as a measure for the error in *(a-b)*. Values of $\Delta\mu_{ss}$ associated with individual velocity steps were obtained by subtracting the near-final strengths displayed in low velocity stages from the interpolated final or steady-state strengths displayed in the neighbouring high velocity stages (Table 2.2). In general, we only made use of the velocity steps for which $\Delta\mu_{ss}$ could be estimated with reasonable accuracy.

In experiment lmst@100°C, the μ vs. shear displacement curve showed slip weakening at a sliding rate of 0.122 μm/s, but not at 1.22 μm/s, and oscillatory behaviour in the low velocity stages at shear displacements ≥2.0 mm. For displacements <2.0 mm, we estimated individual values of $\Delta\mu_{ss}$ by taking the difference between the final strength at 0.122 μm/s and the steady-state strength at 1.22 μm/s. In the case of oscillatory behaviour (shear displacement ≥2.0 mm), we subtracted the estimated mean value of the coefficient of friction μ_m in the low velocity stage from the steady-state friction coefficient in the high velocity stage, yielding an estimate for $\Delta\mu_{ss}$. In the case of experiment lmst@150°C, steady-state is not achieved in either fast or slow velocity intervals, so the finite difference form of eq. 2.4 cannot be applied to calculate *(a-b)*.

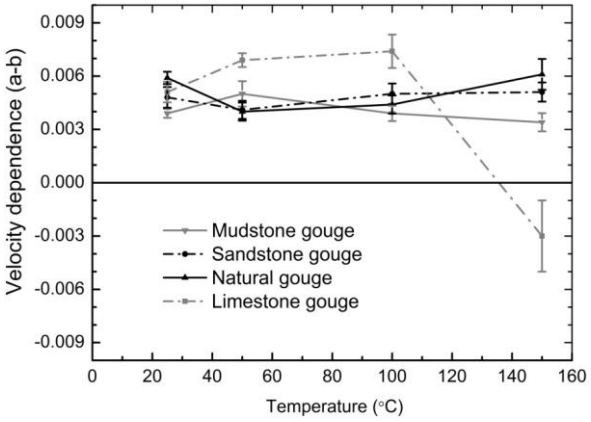

Figure 2.7. Velocity dependence *(a-b)* plotted against temperature. For limestone at 150°C we estimated *(a-b)* by using the condition for unstable sliding for an RSF law with one state variable (Ruina, 1983) and by using a numerical modeling exercise (Appendix 2.A). See text for discussion.

To investigate the effect of temperature on the rate dependence of friction coefficient, we plot *(a-b)* against temperature in Fig. 2.7. For the simulated sandstone, mudstone and natural gouges we found *(a-b)* values ranging from ~0.003 to 0.006 (Table 2.2) without

obvious trends or changes as a function of temperature. By contrast, for the velocity strengthening limestone gouges, at 25, 50 and 100°C, we found that *(a-b)* increases gradually from ~0.005 at 25°C to ~0.007 at 100°C.

Because *(a-b)* could not be estimated for experiment lmst@150°C using the finite difference form of eq. 2.4, we estimated the lower bound of $|a\text{-}b|$ for this sample following the approach of He et al. (2006). These authors used the condition for unstable sliding, as obtained from linear stability analysis performed using the rate and state friction laws with one state variable (Ruina, 1983). This conditions is written

$$k \le k_{cr} = \frac{(b-a)\cdot\sigma_{eff}}{D_c} \qquad (2.6)$$

where k is the equivalent elastic stiffness of the system in the shear direction (≈ 60.3 MPa/mm for experiment lmst@150°C), k_{cr} is the critical stiffness required for unstable motion and σ_{eff} is the effective normal stress acting on the sliding surface (≈ 53 MPa). To apply equation 2.6 appropriately, a reliable estimate of the value for the characteristic slip distance D_c is needed. From the experiments on granite gouge reported by Dieterich (1981), we see that D_c for that material scales with the median particle size d_{50} via a roughly linear relation given by $D_c \approx -27.9 + 0.75\times d_{50}$. Unfortunately, this relation becomes geometrically meaningless when d_{50} decreases to ~37 μm and beyond, because of the zero or negative value implied for D_c. It can therefore not be applied to our limestone gouge for which d_{50} = 2.9 μm. However, from experiments lmst@25°C and lmst@50°C, the transient response after a step change in displacement rate is short-lived. After a switch from 1.22 μm/s to 0.122 μm/s, we see that the evolution effect, evolves mostly along the elastic loading line. Based on this data, i.e. the associated displacement, the D_c value was estimated from the digital data logs to be of the order of ~3 μm. This is closely similar to the median particle size d_{50} (Table 2.1). To account for uncertainties in this rough estimate, and in applying it at temperatures up to 150°C, D_c is assumed here to range from 1-5 μm, which results in a value of $(b\text{-}a)$ at 150°C ranging from 0.001 to 0.005, and thus a value for *(a-b)* ranging from -0.001 to -0.005.

To test further the validity of this estimate of *(a-b)* for the velocity weakening regime in the simulated limestone gouge at 150°C, an estimate independent of the value of D_c is required. To achieve this, we performed numerical simulations of the combined

behaviour of the sample – loading system using the single state variable slowness (eq. 2.1, 2.2a) and slip laws (eq. 2.1, 2.2b) as described in Appendix 2.A. In the framework of these RSF laws, strength oscillations of the type observed in experiment lmst@150°C are analogous to periodic oscillations of a spring-block slider system with a single degree of freedom, at the critical point where $k = k_{cr}$. Through numerical integration of the governing differential equations (Appendix 2.A), we simulated how the amplitude and the mean value of the oscillatory frictional strength vary with loading velocity and b/a values, at fixed effective normal stress using a procedure employed in previous studies (He and Ma, 1997; He et al., 1998). By finding an appropriate analytical formulation describing the relationships obtained, we can arrive at an estimate of *(a-b)* independently of D_c (see Appendix 2.A).

Results obtained using the slowness law showed a well-defined relation between the normalized mean shear stress change upon stepping $(\tau_m - \tau_*)/\left[(b-a)\sigma_{eff}\right]$ and the velocity step ratio $v_o = V_o/V_*$, which holds up to v_o values of 11 (Fig. 2.A3, eq. A2). In contrast, for the slip law, such a single relation can only be established up to $v_o \approx 1.5$ (Fig. 2.A4), while at $v_o = 1.22/0.122 = 10$ quasi-static oscillations give way to triggered unstable slips. On this basis, we used the fit obtained for the slowness law (eq. A2) to calculate a value for $(\tau_m - \tau_*)/\left[(b-a)\sigma_{eff}\right]$ at a velocity step ratio of $v_o = 10$. The value obtained is -4.71 (Fig. 2.A3). Using the expression,

$$(\tau_m - \tau_*) / [(b-a)\sigma_{eff}] \equiv (\mu_m - \mu_*) / (b-a) \qquad (2.7)$$

where the quantity $(\mu_m - \mu_*)$ corresponds to the difference in mean friction coefficient between the high and low displacement rate stages of experiment lmst@150°C, *(a-b)* can be calculated. From the data for experiment lmst@150°C shown in Figure 5, we estimated $\mu_m - \mu_* \approx 0.019$ (Table 2.2). Therefore, from eq. 2.7 we obtain
-4.71 = -0.019/*(b-a)*, and hence an *(a-b)* value of -0.004, which is in good agreement with the estimates obtained above using eq. 2.6.

As indicated above, the estimate of *(a-b)* obtained from equation 2.7 is independent of the value of D_c. However, it should be noted that it is only applicable to systems obeying the slowness law, so that the accuracy also depends on the validity of the evolution law itself. With this value of *(a-b)* in mind and returning to expression 2.6, D_c is inferred to be ~3.5 μm, which is in rough agreement with the value for D_c estimated

directly from the μ vs. shear displacement data. On the basis of these estimates of *(a-b)* for experiment lmst@150°C, i.e. the values obtained from equations 2.6 and 2.7 (Table 2.2), we infer that *(a-b)* for this sample falls in the range -0.003 ± 0.002. This value is plotted for experiment lmst@150°C in the *(a-b)* vs. temperature plot of Figure 2.7.

2.5. Discussion

2.5.1. Frictional strength

We have obtained friction coefficients for simulated mudstone, sandstone and limestone gouges, and for a natural fault gouge, at temperatures of 25, 50, 100 and 150°C, at simulated in-situ conditions corresponding to a depth of ~2 km in the sedimentary rocks of the LFZ (Table 2.2). In general, we found either slip strengthening or steady-state frictional sliding at all conditions and displacements (Figs. 2.4 and 2.5), except for the simulated limestone gouges sheared at $T \geq 100$°C. These showed a peak strength followed by slip weakening and then either stable sliding (at 100°C and 1.22 μm/s) or else oscillatory slip (at 150°C). The steady-state friction coefficients measured at 1.22 μm/s for the simulated mudstone and sandstone gouges were independent of temperature in the range explored and of similar magnitude, with $\mu_{ss} \approx 0.6$ (Fig. 2.6). The natural fault gouge, derived from the same lithological formation as the mudstone and sandstone, was much weaker than simulated gouge prepared from its protoliths, with a μ_{ss} value ranging from 0.46 at 25°C to a constant value of 0.38 at higher temperatures. The simulated limestone gouge was the strongest material tested in this study, with $\mu_{ss} \approx 0.7$ at 25-50°C falling to a mean oscillatory value of ~0.6 at 150°C.

Several trends emerge from our frictional strength data. First, we consider the behaviour of the natural gouge and the gouge prepared from its sandstone and mudstone protoliths. These samples were relatively clay-rich (Table 2.1), with the natural fault gouge in particular containing ~54% illite compared to ~25% in the crushed sandstone and mudstone. Previous experimental results on binary and ternary mixtures of smectite, illite, kaolinite and quartz show a systematic decrease in friction coefficient with increasing clay mineral content (Logan and Rauenzahn, 1987; Brown et al., 2003; Takahashi et al., 2007; Crawford et al., 2008, Tembe et al., 2010). Our data are consistent with these results, as the illitic natural gouge is considerably weaker than the simulated sandstone and mudstone gouges. To illustrate this, the relation between illite content and friction coefficient is plotted in Figure 2.8, which is a compilation of the room temperature (25°C) μ_{ss} data reported in this study plus those obtained by Tembe et

al. (2010) for quartz-illite mixtures at similar displacements (2 mm and 4 mm axial displacement). The initial particle sizes of quartz and illite in the experiments of Tembe et al. (2010) were much larger than in ours, with peak frequencies (modal grain sizes) at ~100 μm and ~20 μm respectively. In their experiments, a larger slip distance was therefore required for cataclastic comminution and to evolve to steady-state. Hence our μ_{ss} data for the sandstone, mudstone and natural gouge agree best when compared with the friction coefficients obtained at 4 mm by Tembe et al. (2010).

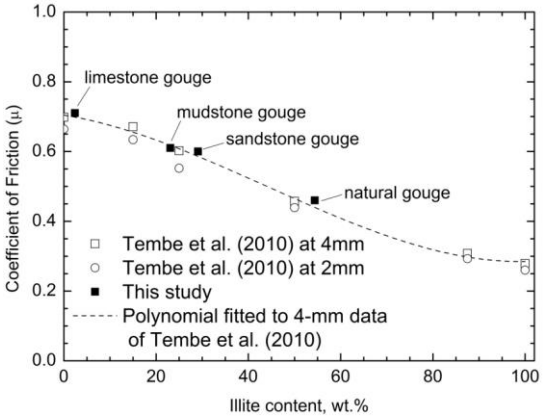

Figure 2.8. Coefficient of friction at room temperature and 1.22 μm/s plotted against illite content (wt %). Compilation of data obtained for the sample materials used in this study (Tables 1, 2), with the data given by Tembe et al. (2010) for axial displacements of 2 and 4 mm (shear displacements of 2.3 and 4.6 mm). Because the density of illite (≈ 2.7 g/cm³) is approximately equivalent to that of quartz (≈ 2.6 g/cm³), our vol. % data can be interpreted in wt. %.

Although the curve of Tembe et al. (2010) drawn in Figure 2.8 is based on their data for quartz-illite mixtures, our limestone data also fall remarkably close to it. This, plus the overall agreement of our remaining data with that of Tembe et al. (2010), suggests that it is the proportion of illite in combination with harder minerals that controls the frictional strength of illite-bearing gouges, regardless of the composition of the hard phases. This implies that the coefficient of friction obtained from our mudstone, sandstone and natural gouge samples is controlled by the volume percentage of quartz and feldspars relative to that of illite. The estimated amount of illite in our natural gouge was almost twice that measured in the simulated mudstone and sandstone gouges, while the quartz and feldspar contents were significantly lower in the natural gouge. This difference in mineralogy between the natural fault gouge and its protolith probably

reflects a natural fault-rock evolution process that leads to conversion of quartz, feldspars and perhaps other phyllosilicates, through cataclastic comminution, fluid-gouge interaction and transport into the fault of chemical components derived from the surroundings (cf. Vrolijk and Van der Pluijm, 1999; Solum et al., 2005; Solum and Van der Pluijm, 2009). Clearly, gouge formation is associated with a major reduction in frictional strength (cf. Wintsch et al., 1995; Tembe et al., 2010).

The sharp drop in the mean friction coefficient from 0.46 to 0.38 observed between 25 and 50°C in the natural gouge samples (Fig. 2.6) could be due to two reasons. First, the increased temperature may have induced chemical or mineralogical changes in the clay minerals that dominate the natural gouge, or changes in their interlayer water content, which reduced frictional strength. Such effects, notably changes in water content, might be possible in gouges containing significant amounts of smectite (cf. Ikari et al., 2007). They seem unlikely, however, in our rather short-duration, pore-fluid-charged experiments on the illite-dominated natural gouge. Alternatively, the initial character of the gouge used in experiment Natgou@25°C may have been different from that used in the higher temperature experiments on this material. In our experiments on the natural gouge, we used samples taken directly from the bulk gouge sample (size ~10x10x2.5 cm) as extracted from the fault trench, i.e. without homogenization. Therefore, the observed differences in frictional strength could reflect heterogeneities in composition or grain size within the fault gouge sampled, or perhaps contamination of the 25°C sample with detritus during sampling. In view of the short, wet nature of our tests, we infer that the apparent temperature effect is probably due to such sample variability or contamination effects.

The laser particle size data obtained for our mudstone, sandstone and natural gouges (Table 2.1) showed that the simulated mudstone gouge had the coarsest median particle size ($d_{50} \approx 10$ μm), the sandstone an intermediate value ($d_{50} \approx 5$ μm), and the natural gouge the finest median particle diameter ($d_{50} \approx 3$ μm). The compositional data as interpreted from X-ray diffraction spectra showed that the sandstone and mudstone have similar mineralogical composition, i.e. a roughly 2:1 quartz to clay ratio, with 2-16% dolomite and 5-10% plagioclase (Table 2.1). However, our experiments showed that the frictional strengths of our simulated sandstone and mudstone gouges are comparable (Fig. 2.4), whereas that of the natural gouge was distinctly lower. Hence, our results indicate that, for a median particle diameter ≤10 μm, the initial grain size distribution does not influence the frictional properties of the clastically derived gouges investigated

in this study. Instead, the mineralogy of the sample is of primary importance. This is also evident from the quite distinct behaviour exhibited by the limestone gouges tested (Figs. 2.4, 2.5 and 2.8).

The crushed limestone gouge, consisting over ~95% of calcite, showed the highest coefficient of friction found in all our experiments, with $\mu_{ss} \approx 0.7$ at 25-50°C falling to a mean value of ~0.6 at 150°C (Fig. 2.6). As the total content of clay minerals is only ~2%, the frictional properties of these samples are clearly controlled by the behaviour of calcite. Our values are lower than the ultimate strength ($\mu \approx 0.74$) reported by Shimamoto and Logan (1981), who performed experiments on calcite gouge with an average grain size of 0.45 mm without pore fluid. At confining pressure of 50 MPa, however, their residual strength after slip weakening showed a value of ~0.7, which is similar to ours despite the difference in initial grain sizes. Our results also fall in the range expected for sliding friction between smooth limestone surfaces, as compiled by Barton (1976). Barton compiled room temperature data for sliding limestone surfaces of varying roughness under dry and wet conditions. By correcting the measured coefficient of friction for dilatation effects related to overcoming the initial surface roughness, which presumably produced at least some fine fault gouge, Barton obtained coefficients of friction (his "basic friction coefficient") in the range 0.65-0.78.

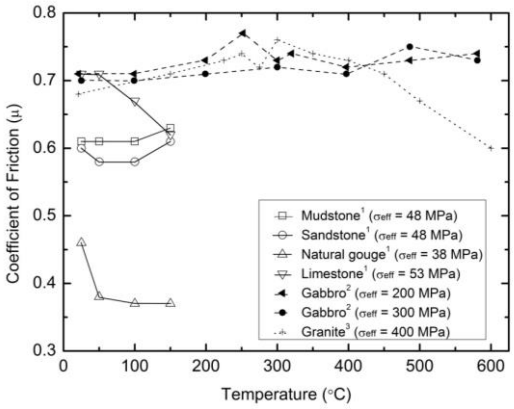

Figure 2.9. Steady-state and/or mean coefficient of friction plotted against temperature for the present samples, alongside data for crushed gabbro and crushed granite. All data originate from triaxial, shear-loading experiments under hydrothermal conditions. [1)]Data obtained in this study for simulated sedimentary gouges and natural, clay-rich gouge (Table 2.2). [2)]Data for simulated gabbro gouge from Dashakou quarry, Fengzhen, China (He et al., 2007). [3)]Data for simulated Westerly granite gouge (Blanpied et al., 1995). Note that σ_{eff} refers to the effective normal stress acting on the sliding surface. Data from the present study and that of He et al. (2007) were generated at a shear displacement rate of 1.22 μm/s. The data of Blanpied et al. (1995) were obtained using shear rates of 1.15 μm/s.

All frictional strength data reported in the present study were obtained from experiments conducted at simulated in-situ conditions corresponding to a depth of ~2 km. To provide a basis for comparing the in-situ frictional strengths of the sedimentary rocks studied with crystalline rocks expected at hypocentral depths along the LFZ, the results reported in this study are plotted in Figure 2.9, together with those of previous studies on granite and gabbro gouges. This plot shows that our simulated mudstone and sandstone gouges, and especially the natural gouge, are much (i.e. 14-50%) weaker than granite and gabbro gouges. Moreover, applying the empirical relationship established by Barton (1976) between the frictional strength of sliding fractures and intact rock strength, it is likely that the intact mudstone and sandstone protoliths of our gouge samples are at least 15% weaker than granite and gabbros. By contrast, the present limestone gouge is similar in frictional strength to granite and gabbro gouges at 25-100°C, with the implication that the intact limestone is also similar in failure strength to intact granite and gabbro. Finally, we note that of the gouge materials represented in Figure 2.9, only the limestone and granite gouges show a significant temperature effect. Hence, the strength of only these materials is likely to be affected by in-situ geotherms. We have already shown that the apparent temperature dependence of our natural gouge strength was probably due to some form of sample variability. Note, however, that illite will transform to stronger phyllosilicates such as mica at temperatures corresponding to epizone metamorphic conditions (~300°C; Abad, 2007).

2.5.2. Velocity dependence

In the present frictional sliding experiments, stepping the slip velocity between 0.122 and 1.22 μm/s showed that our sandstone, mudstone and natural fault gouges exhibited velocity strengthening behaviour at all conditions tested. The velocity dependence, characterized by the mean value of *(a-b)*, varied from +0.0034 to +0.0050 for the simulated mudstone gouge, from +0.0041 to +0.0051 for the simulated sandstone gouge, and from +0.0040 to +0.0061 for the natural fault gouge, and was independent of temperature within the range of temperatures investigated (Table 2.2; Fig. 2.7). For the simulated limestone gouge, we found velocity strengthening behaviour in experiments conducted at 25 and 50°C with mean *(a-b)* values increasing from +0.0051 to +0.0069 respectively. At 100°C, quasi-static oscillations in frictional strength occurred after 2 mm of displacement and the corresponding mean value of *(a-b)* was +0.0074. However, at 150°C, velocity weakening was associated with oscillatory behaviour (periodic slow slips),

and the mean value of *(a-b)* was estimated to be -0.003.

Numerous previous studies of clastic, granitic and gabbroic gouges have shown that steady-state frictional behaviour is attained at bulk mean shear strains comparable to our tests, and can be either velocity strengthening or weakening, depending on the presence of water, on pressure and temperature, and on gouge composition (Scholz and Engelder, 1976; Dieterich and Conrad, 1984; Solberg and Byerlee, 1984; Lockner et al., 1986; Blanpied et al., 1995; He et al., 2006, 2007; Mizoguchi et al., 2008). Several studies also indicate that the run-in displacement or strain required to attain steady mean friction levels is lower in fine grained samples, such as ours, than in the coarser samples used in most experiments (cf. Marone et al., 1990; Wong and Zhao, 1990; Wong et al., 1992). On this basis, we assume that our *(a-b)* or velocity dependence data are more or less unaffected by slip strengthening or weakening, and can be usefully compared with previous *(a-b)* data thought to reflect steady-state. Note that, in general, *(a-b)* values only represent the difference in magnitude of the direct and indirect effects measured with respect to steady-state stable sliding. For experiment lmst@150°C, where we observed periodic slow slips, a representative value for *(a-b)* could only be obtained using the condition for unstable slip (eq. 2.6; Ruina, 1983) or numerical simulations (Appendix 2.A).

Following our conclusion that illite content controls the frictional strength of our mudstone, sandstone and natural gouges, we continue by comparing the velocity dependence seen in these gouges with earlier work on illite-rich samples. Previous studies have investigated the frictional behaviour of illite-rich shale (Saffer and Marone, 2003) and binary illite-quartz mixtures (Tembe et al., 2010) at room temperature, in the presence of humid air and under water-saturated conditions respectively. The illite-rich shale used by Saffer and Marone (2003) contained at least 59% illite and showed velocity strengthening at sliding rates ranging from 0.1 to 200 μm/s and normal stresses ranging from 5 to 150 MPa. The associated values of *(a-b)* were found to range from 0.0015 to 0.0036 for shear displacement rate steps from 2 to 20 μm/s (Saffer and Marone, 2003). The binary quartz-illite mixtures tested by Tembe et al. (2010) showed prominent velocity strengthening for an illite content ranging from 15% to 100%, at shear displacement rates from 0.115 to 1.15 μm/s and an effective normal stress of 40 MPa. Their calculation of *(a-b)* resulted in values of 0.0025 to 0.0052. Compared with these studies, our sandstone, mudstone and natural fault gouges, with illite content ranging from ~23 to ~54%, showed *(a-b)* values ranging from 0.0034 to 0.0061 for shear

displacement rate steps between 0.122 and 1.22 μm/s (Table 2.1). Our results are therefore consistent with those of Saffer and Marone (2003) and Tembe et al. (2010) and again support the notion that the intrinsic properties and proportion of illite control the frictional behaviour of our simulated sandstone, mudstone and natural fault gouges.

We have been unable to find any previous data on *(a-b)* values for limestone or limestone gouge which could be compared with our findings for the simulated limestone gouge. However, the transition we observed in our limestone experiments, from velocity strengthening to weakening with increasing temperature, clearly indicates a change in deformation mechanism controlling slip. We will discuss this in a later section.

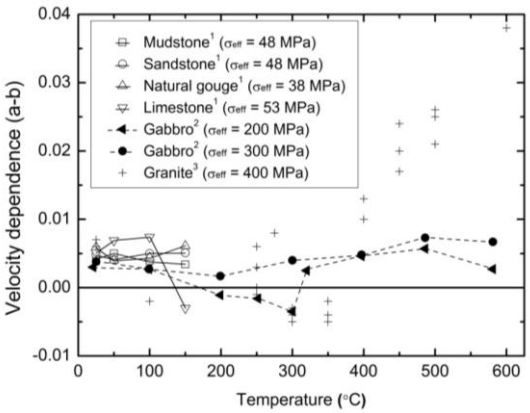

Figure 2.10. Velocity dependence *(a-b)* plotted against temperature for the present samples, alongside data for crushed gabbro and crushed granite. All data originate from triaxial, shear-loading experiments under hydrothermal conditions. [1)]Data obtained in this study for simulated sedimentary gouges and natural, clay-rich gouge (Table 2.2). [2)]Data for simulated gabbro gouge from Dashakou quarry, Fengzhen, China (He et al., 2007). [3)]Data for simulated Westerly granite gouge (Blanpied et al., 1995). Note that σ_{eff} refers to the effective normal stress acting on the sliding surface. Data from the present study and that of He et al. (2007) were generated from shear displacement rate steps between 1.22 and 0.122 μm/s. The data of Blanpied et al. (1995) were obtained using shear rate steps between of 1.15 and 0.115 μm/s.

To understand better the transient, velocity-dependent frictional properties of our samples in relation to those of typical crystalline basement rock types, we compare the mean *(a-b)* values obtained from our experiments with those obtained in previous studies on simulated gabbro and granite gouges (Fig. 2.10; cf. Fig. 2.9). Figure 2.10 shows that most of the gouges considered show velocity strengthening behaviour with *(a-b)* > 0, with the notable exception of gabbro (tested at 200 MPa effective normal stress) and granite (σ_{eff} = 300 MPa) which show velocity weakening in the range of 200 to 350°C.

Granite gouge shows a strong increase in *(a-b)* to high positive values at higher temperatures. The *(a-b)* values exhibited by our mudstone, sandstone and natural gouges, which we sheared under conditions pertaining to the upper ~2 km of continental crust, are all positive and similar to or larger than the values displayed by gabbro, suggesting relatively stable behaviour at in-situ conditions in the uppermost crust, i.e. at 25 – 150°C. By contrast, the negative *(a-b)* value shown by our simulated limestone gouge at 150°C is similar in magnitude to the negative *(a-b)* values shown at ~300°C by gabbro (200 MPa) and granite (300 MPa). This suggests that limestone in the upper crust may be equally prone to unstable, velocity-weakening slip as are gabbros and granites at depths of 10 – 15 km (~300°C depending on the geotherm).

2.5.3. Microphysical mechanisms controlling friction

We have provided evidence that the frictional behaviour of our mudstone, sandstone and natural gouges was controlled by the proportion of illite present, relative to comminuted hard phases such as quartz and feldspar. Numerous studies have addressed the intrinsic properties of clay minerals with respect to frictional sliding of clay-rich gouges (e.g. Wu et al., 1975; Morrow et al., 2000; Moore and Saffer, 2001; Saffer and Marone, 2003; Takahashi et al., 2007). On the basis of these, it is widely accepted that the low strength and bulk weakening effect of clays such as illite are related to easy interparticulate slip, aided by surface water films (e.g. Summers and Byerlee, 1977; Morrow et al., 2000), and to easy internal plastic deformation of the layered, clay-mineral platelets (e.g. Moore et al., 1997). However, the detailed manner in which clays and rigid clasts interact to control frictional strength and its rate dependence, and the role of shear localization and partitioning phenomena, remain poorly understood at a quantitative, mechanistic level, though models moving in this direction have recently appeared in the literature (Bos and Spiers, 2000, 2002; Niemeijer and Spiers, 2006, 2007).

Of much more interest in the present study is the question of what microscale process controls the behaviour of the simulated limestone gouge investigated, notably the transition from velocity strengthening to velocity weakening with increasing temperature. Very few frictional data are available on limestone gouges and, to our knowledge such an effect has not previously been reported. As the observed velocity weakening behaviour can potentially lead to unstable seismogenic slip with significant stress drops, reflecting the relatively high strength of limestone, it is important to gain insight into the

controlling mechanism and the conditions under which it can operate.

The present experiments on the simulated limestone gouge at temperatures of 25-50°C displayed stable slip strengthening, reaching a steady-state friction coefficient of ~0.7 in the initial loading phase, followed by velocity strengthening slip with mean *(a-b)* values of 0.0051 - 0.0069 (Fig. 2.5; Table 2.2). However, the behaviour exhibited in experiments lmst@100°C and lmst@150°C was markedly different. These showed peak frictional strengths of 0.72 and 0.70 respectively, followed by slip weakening towards steady-state friction coefficient values of 0.67 and 0.62 (Fig. 2.5; Table 2.2). At 100°C in particular, the frictional behaviour switched from stable sliding to quasi-static strength oscillations after ~2 mm of shear displacement, but only in the lower velocity steps employed (0.122 vs.1.22 μm/s). At 150°C, slip weakening was followed by quasi-static oscillations at both the high and low displacement rates used (Fig. 2.5). Velocity weakening occurred in this region with *(a-b)* = -0.003 (Figs. 2.5 and 2.7; Table 2.2). This change in sign of *(a-b)* with increasing temperature reflects a reversal in the relative magnitudes of *a* and *b* values. From inspection of the magnitude of the direct versus evolution effects seen in the friction coefficient versus shear displacement curves of Figure 2.5, it seems that *b* increased significantly between 100 and 150°C, while *a* changed little. Since *b* represents the magnitude of the evolution effect in the RSF formulation (eq.'s 2.1a-b, 2.3), this implies that some time- or slip-dependent process or processes must become important at temperatures of 100-150°C.

These observations must reflect a change in the micromechanism controlling slip within the limestone gouge, or at the interface with the saw-cut driver blocks. The temperature dependence, combined with the rate dependence of slip stability seen at 100°C, provide strong evidence that a thermally activated, kinetic (Arrhenius – type) process is involved. The observed peak strength behaviour and displacement-dependence of slip stability at 100–150°C further suggests a displacement-related microstructural evolution effect. Candidate mechanisms for the transition of velocity weakening seen only in our limestone gouge at 100-150°C should therefore be thermally activated, allow or be promoted by microstructural evolution, and be specific to calcite. The mechanism in question could be operative on the grain scale within the gouge, influencing grain contact area and strength (cf. Niemeijer and Spiers, 2007), or on the scale of Dieterich – type asperities within grain contact slip zones (Dieterich, 1979). Possible thermally activated mechanisms at both of these scales include a) crystal plastic deformation (e.g. de Bresser et al., 2002), b) subcritical or stress corrosion cracking (Atkinson, 1984) and c)

pressure solution (e.g. Spiers et al., 2004).

Due to their high temperature sensitivity (i.e. high activation energy), crystal plastic (dislocation) creep mechanisms become significant in laboratory experiments at temperatures above 100°C, under both wet and dry conditions (Rutter, 1972, 1974; De Bresser et al., 2002, 2005; Zhang et al., 2002). Creep deformation by both subcritical crack growth and pressure solution, at the grain scale, has also been reported in experiments on wet calcite powder at temperatures in the range 20 to 150°C (Zhang et al., 2002; Zhang and Spiers, 2005; Liteanu and Spiers, 2009). However, recent work indicates that pressure solution in calcite decreases in rate with increasing temperature because, unlike other minerals, the solubility of calcite decreases with increasing temperature (Liteanu et al., 2009; X. Zhang pers. comm., 2009). This makes pressure solution seem an unlikely cause of velocity weakening in our tests. On the other hand, the model of Niemeijer and Spiers (2007), for velocity weakening of fault gouge due to combined granular flow plus pressure solution, predicts an increased tendency for velocity weakening as pressure solution decreases in rate.

This means that at present we cannot unambiguously indentify the mechanism causing velocity weakening in our experiments on limestone gouge at 100-150°C. Nonetheless, the marked transition from velocity strengthening at 25-50°C to velocity weakening at 100-150°C, coupled with the fact that subcritical cracking in wet calcite is important even at room temperature, suggests that the observed velocity weakening may be related to enhanced crystal plasticity at grain or asperity contacts, or to a coupled granular flow plus pressure solution process of the type proposed by Niemeijer and Spiers (2007). Clearly, future work is needed to resolve this issue.

2.5.4. Implications for the Wenchuan earthquake and LFZ

Finally, we consider the implications of the present results for the behaviour of the faults involved in the Wenchuan earthquake and for the seismotectonic behaviour of the LFZ in general and in the future. Central issues addressed include the likely locus of repeated rupture of the upper crustal sedimentary rocks in response to rupture propagation from the basement below, the dynamics of such rupture phenomena, and the possible influence of the transition from velocity strengthening to velocity weakening behaviour seen in our simulated limestone gouge samples with increasing temperature.

Illite-rich, Triassic to Quaternary, fluvio-deltaic sediments similar to those sampled from the Xujiahe Formation in this study, are widespread in the broader LFZ region (Fig.

2.1). As we have shown, the frictional strength and sliding stability of such materials are mainly controlled by the relative abundances of relatively weak illite versus quartz and/ or feldspar (Fig. 2.8). The natural fault gouge extracted from the trenched portion of the YBF shows much lower frictional strength (μ_{ss} = 0.37 to 0.46) than the simulated mudstone and sandstone gouges ($\mu_{ss} \approx 0.6$) derived from the protoliths. This difference in strength is due to the far higher illite content of the natural fault gouge. As discussed earlier, the increased illite content likely reflects cataclastic comminution of feldspar, quartz, and the other phyllosilicates derived from the protolith, followed by slow reaction with fluids carrying additional components from the surroundings (cf. Vrolijk and Van der Pluijm, 1999; Solum et al., 2005; Solum and Van der Pluijm, 2009). On the basis of this plus the very low friction coefficient observed for the natural gouge compared with the other materials we tested, we expect that in the event of coseismic slip nucleating in the basement at depth, the shallow portions of the LFZ that slipped during the Wenchuan earthquake will (again) be reactivated rather than forming new rupture branches.

Aside from the issue of reactivation, the differences between the mechanical properties of the shallow sedimentary rocks in the LFZ and those of the crystalline basement rocks expected at hypocentral depths corresponding to the Wenchuan earthquake (~13-16 km), have important implications for the dynamics of rupture propagation upward from these depths. Comparison of the frictional strengths of our simulated mudstone and sandstone gouges, and natural fault gouge, with those of granite and gabbro gouges representing mid or lower crustal material (Figure 2.9), showed that the sedimentary rocks were generally much weaker with a coefficient of friction of 0.4 – 0.6 versus 0.7 – 0.8 for the crystalline rocks at temperatures up to 400°C. The crystalline basement rocks of the broader LFZ region are believed to resemble those of the crystalline rocks of the Pengguan Complex (Fig. 2.1; Xu et al., 2008), and presumably show μ-values typical for such materials, i.e. for quartzofeldspathic and gabbroic compositions. With such a large difference in frictional strength between crystalline basement and sediments, the initial fault zone is expected to have propagated upward from the basement, following a route that was refracted into a steeper, or at least different, orientation when approaching the sediments. For our limestone gouge sheared at 25 - 50°C, the frictional strengths are comparable to those of crystalline basement rocks, and hence fault refraction significantly changing the orientation of rupture is less likely (cf. Maillot and Koyi, 2006).

The behaviour of such a fault system will also clearly be influenced by the velocity dependence of frictional behaviour of both crystalline and sedimentary rocks. The clay-rich sediments and natural fault gouge material tested in our experiments are expected to show velocity strengthening behaviour at shallow crustal conditions, i.e. at temperatures up to 100 or 150°C and hence depths up to 5 to 8 km – assuming a one-dimensional geothermal gradient of 18.5°C/ km as implied by the heat flow data reported by Wang (1996). However at temperatures of ~300°C, and hence depths of ~16 km, gabbroic and granite gouges can show pronounced velocity weakening (Fig. 2.10). Hence, in the upper 5 km of the crust, for example, faults in clastic sedimentary rocks are likely to offer stable sliding resistance to coseismic rupture propagating from the velocity-weakening basement, without abrupt stress drops occurring in the sediments. Via numerical simulations using the slip law (Ruina, 1983; eq. 2.2b), Boatwright and Cocco (1996) defined rupture-decelerating (i.e. viscous) patches in the subsurface using the criterion $\sim 0.4 \leq (a-b)/a \leq 1$. Through inspection of our results in Figs. 2.4 and 2.5 and from Table 2.2, we infer that the $(a-b)/a$ ratios for our simulated clay-rich and natural gouges satisfy this criterion. In addition, we note that if the slowness law (eq. 2.2a) is used for numerical modelling of the "viscous area" criterion, the lower bound value of the criterion may drop in value due to the implicit damping properties of the slowness law (see He et al., 2003). The velocity-strengthening properties of the clay-rich fault rocks in the cover may therefore point to possibility of partial "viscous" damping, through stable sliding that dynamically decelerates seismic rupture propagation compared with that occurring in the crystalline basement below (Kanamori, 1981; Boatwright and Cocco, 1996; Tinti et al., 2005).

Finally, the implications of our experimental results on the mechanical behaviour of limestone under in-situ conditions are considered, for the Longmenshan area. A temperature of ~100°C in the LFZ corresponds to a depth of ~5.4 km, whereas 150°C corresponds to ~8.1 km, assuming the geothermal gradient (~18.5°C/km) mentioned above. For simulated limestone gouge, we found a frictional strength similar to gabbro and granite at temperatures below 50°C (Fig. 2.9), along with velocity-strengthening behaviour showing $(a-b)$ values around twice those of our clay-rich samples (Fig. 2.10). These data suggest that at depths up to ~2.5 km or so in the Longmenshan area, velocity strengthening will tend to occur on faults cutting such limestones, again indicating the possibility of stable sliding resistance to ruptures propagating from below, without producing stress drops. On the other hand, at temperatures in the range 100-150°C,

corresponding to depths of ~5 – 8 km in the LFZ, our experiments on simulated limestone gouge suggest that velocity weakening may occur (cf. Fig. 2.5). Hence, if limestone is present at depths of 5 – 8 km in the LFZ, faults within it may show velocity weakening behaviour and, when driven from below by coseismic rupture propagation, may promote (accelerate) unstable propagation. Stress drops associated with such unstable motion could be considerable as the frictional strength of the present limestone gouge samples is relatively high (μ_{ss} ~0.6) when unstable motion is exhibited, i.e. at 100-150°C. On this basis, we infer that the presence of large masses of limestone may enhance seismic hazard in seismic hazard regions.

2.6. Conclusions

This study has addressed the frictional properties of simulated fault gouges prepared from intact sedimentary rocks sampled from the Yingxiu-Beichuan (YBF) portion of the Longmenshan Fault Zone (LFZ) in Sichuan, southwestern China (Fig. 2.1). A natural fault gouge was also investigated. The intact sedimentary rocks consisted of clay-rich sandstone and mudstone, and a relatively pure calcite limestone. The simulated gouges prepared from these materials possessed a median grain size ranging from ~3 to ~10 μm. The natural fault gouge consisted of fine, illite-rich gouge (median grain size ~3 μm), extracted from a trench cut through a surface rupture formed in the YBF in the 2008 Wenchuan earthquake. This material is derived from the sandstone and mudstone protoliths. Frictional sliding experiments were performed on the various gouge samples at confining and pore-pressure conditions corresponding to around 2 km depth in the LFZ, i.e. at ~50 MPa and 20 MPa respectively, and at temperatures ranging from 25 to 150°C. Deionized water was used as a pore fluid. To investigate the velocity dependence of frictional behaviour, we sheared the various materials at displacement rates alternating between 1.22 and 0.122 μm/s, interpreting our results in the framework of rate and state friction (RSF) models. On the basis of our experimental results and discussions we conclude the following:

1. The natural gouge and the simulated sandstone and mudstone gouges exhibited either slip strengthening or steady-state sliding behaviour, with steady-state friction coefficients measured at 1.22 μm/s (μss) varying from ~0.4 for the natural gouge to ~0.6 for the sandstone and mudstone gouges. Allowing for minor compositional variation in the natural gouge, the frictional strengths of all these materials were

independent of temperature within the range investigated. For the simulated limestone gouge sheared at 25-50°C, we found slip strengthening followed by steady-state sliding with a μss value of ~0.7. At 100-150°C, a peak strength (at μ ≈ 0.7) was followed by slip weakening, giving way to stable steady-state slip (100°C, 1.22 μm/s) or else unstable oscillatory slip, with the mean coefficient of friction measured at 1.22 μm/s falling to 0.67 at 100°C and 0.62 at 150°C.

2. The steady-state frictional strength of our samples showed a systematic dependence on illite-content versus relatively hard phases, such as quartz, feldspar and calcite, which agrees well with previous data on frictional strength versus illite-to-quartz ratio (Tembe et al., 2010). The low strength of the natural gouge was therefore attributed to its high illite content, which is characterized by a 2:1 illite-to-quartz ratio, as opposed to 1:2 in the mudstone and sandstone protoliths. The increased illite-content of the natural gouge was inferred to be due to the natural fault-rock evolution process, i.e. due to cataclastic comminution and reaction of quartz, feldspars and other phyllosilicates, probably with fluids carrying reactive components derived from the surrounding rocks.
3. The simulated mudstone and sandstone gouges, and the natural gouge samples, all showed stable velocity-strengthening behaviour with mean values of the RSF parameter (a-b) ranging from +0.003 to +0.005 for the mudstone, from +0.004 to +0.005 for the sandstone and from +0.004 to +0.006 for the natural fault gouge. These values of (a-b) were independent of temperature within the range investigated.
4. In our experiments on simulated limestone gouge stable, velocity-strengthening slip occurred at 25 and 50°C, with estimated (a-b) values of +0.005 and +0.006 respectively. At 100°C, the limestone showed velocity-strengthening slip at a displacement rate of 1.22 μm/s, giving way to quasi-static strength oscillations at 0.122 μm/s at displacements beyond ~2.0 mm. The corresponding mean value of (a-b) was estimated to be +0.0074 ± 0.001, using the difference between the coefficient of friction during stable sliding (at 1.22 μm/s) and the mean coefficient of friction estimated in the oscillatory stage (at 0.122 μm/s). At 150°C, the limestone gouge exhibited unstable velocity weakening slip at both the high and low velocities investigated (1.22 and 0.122 μm/s). Using both the condition for unstable slip (Ruina, 1983) and numerical simulations of a spring-block system (cf. He and Ma, 1997; He et al., 1998), the (a-b) value for the limestone gouge at 150°C was estimated to be -0.003 ± 0.002. The experiments on limestone gouge thus showed a transition from

stable, velocity-strengthening slip at 25-100°C to unstable velocity weakening slip at 100-150°C.

5. In the experiments on simulated limestone gouge, the marked temperature dependence of friction coefficient and of (a-b), combined with the rate dependence of slip stability seen at 100°C, provide strong evidence that a thermally activated deformation mechanism is involved in controlling the frictional behaviour of the limestone gouge. Candidate mechanisms include coupled granular flow plus pressure solution processes within the gouge, or else crystal plasticity at asperity or grain contacts. The peak strength behaviour and displacement-dependence of slip stability, seen in our experiments on simulated limestone gouge at 100–150°C, further suggest a displacement related microstructural evolution effect. However, more work is needed to elucidate the exact mechanisms controlling friction in the limestone gouges.
6. The friction coefficients obtained for the crushed clastic sedimentary rocks and the natural fault gouge are much weaker than gouges prepared from granitic or gabbroic basement rocks expected at hypocentral depths of the LFZ. The initial rupture is accordingly expected to have propagated upward from the basement, being refracted by the weaker sedimentary cover, hence changing its orientation. In the case of our simulated limestone gouge at 25-50°C, the frictional strengths are comparable to those expected for basement fault gouges, so that fault refraction is less likely.
7. The weakness of the natural fault gouge studied, compared with its mudstone and sandstone protoliths, suggests an intrinsic weakness of pre-existing faults cutting clastic sedimentary rocks. This is why the surface ruptures induced by the Wenchuan earthquake formed on older reactivated faults. The same faults are expected to accommodate surface rupturing associated with future earthquakes in the LFZ.
8. The simulated clastic gouges and natural fault gouge studied show stable velocity strengthening behaviour at shallow crustal conditions, i.e. at temperatures up to 150°C and hence depths up to ~8 km in the Longmenshan region. Similarly, velocity strengthening behaviour in the limestone gouge at temperatures up to 50°C corresponds with depths up to ~2.7 km. On this basis, faults cutting the present clastic lithologies up to ~8 km depth and limestone up to ~2.7 km depth in the LFZ are likely to offer stable sliding resistance, damping coseismic rupture propagating from below. In contrast, faulted limestone at 150°C, and hence depths of ~8 km, may exhibit pronounced velocity weakening behaviour, promoting unstable rupture

propagation. The high strength of limestone at this temperature (mean friction coefficient μm ≈ 0.6) implies that associated stress drops are expected to be high, and that the presence of large masses of limestone may enhance seismic hazard in seismic hazard regions.

Appendix 2.A. Simulation of RSF behaviour and scaling relations for quasi-static oscillations at k = kcr

To simulate how the amplitude and the mean value of oscillatory frictional strength scale with loading rate, for comparison with our experiments on limestone gouge at 150°C, we analyzed the behaviour of an equivalent spring-block slider system with a single degree of freedom (Figure 2.A1), using the slowness law of Dieterich (1979; eq. 2.1, 2.2a) and the slip law of Ruina (1983; eq. 2.1, 2.2b). Following He et al. (2003), the equation of motion for such a system can be expressed as,

$$m\frac{d^2\delta}{dt^2} = k(\delta_o - \delta) - \tau \qquad (2.A1)$$

where δ is the slip distance of the block, δ_0 is the load point displacement, τ is the shear stress acting on the system, m is the mass of the block and k is the spring stiffness, i.e. the equivalent elastic stiffness of the system measured in the shear direction (≈ 60.3 MPa/ mm). In addition, $V_0 = \mathrm{d}\delta_0/\mathrm{d}t$ is the load point velocity and $V = \mathrm{d}\delta/\mathrm{d}t$ is the sliding velocity of the block.

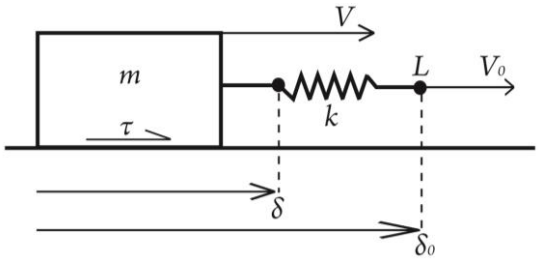

Figure 2.A1. Schematic representation of a spring-block slider model. Symbols: m = mass of slider; k = spring stiffness; τ = shear stress; δ = slip distance of the block; δ_o = load point displacement; V = sliding velocity of the block; V_o = load point velocity; L = load point.

Numerical integration of the full set of differential equations represented by

equations (2.1), (2.2a) or (2.2b) and (2.A1) was performed employing a procedure identical to that of He and Ma (1997) and He et al. (1998). The numerical calculations were performed with the variables represented in dimensionless form, to generalize the limited results. For the same reason, the results described in the coming figures and/or equations are also presented in dimensionless form.

Step changes in loading rate were applied to the system thus described as perturbations from steady-state at a reference sliding velocity V_*. For the slowness law, the velocity step ratios were varied such that $V_0/V_* = 0.1$, 0.2, 0.4, 0.8, 1.25, 2.5, 5 and 10 using b/a ratios of 1.25, 1.5, 2 and 2.25. For the slip law, the same velocity steps were applied but only up to a value approaching the stability boundary at $V_0/V_* = b/(b\text{-}a)$ (Gu et al., 1984), to avoid triggering dynamic slip due to step perturbation. Three hundred oscillations were calculated for each parameter set, yielding peak, trough and peak-trough amplitude values for each run. The last 10 oscillations were picked as representative data points for each parameter set.

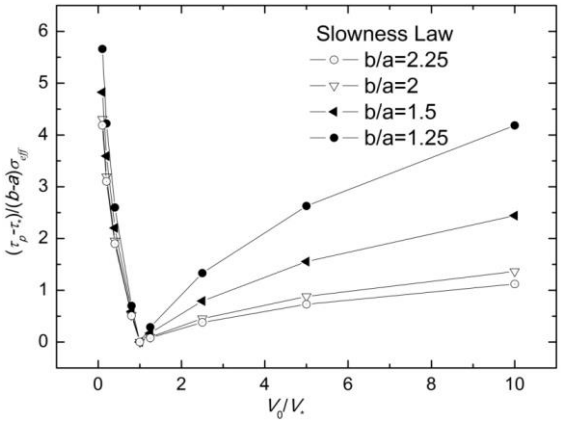

Figure 2.A2. Normalized peak shear stress calculated as a function of velocity step ratio $v = V_0/V_*$ for the slowness law. The shape of the curves demonstrates that no straightforward relation can be fitted to the results.

The peak, trough and peak-trough amplitude values were found to be complexly related to the loading rate, with the result that we were unable to find simple, empirical formulas describing the relationships. For the slowness law (eq. 2.2a), the complex relations obtained are exemplified in Figure 2.A2. Here we plot the normalized peak amplitude τ_p, against the velocity step ratio V_0 for the different parameter values shown. Clearly, a simple expression relating both variables is absent. However, the mean shear

stress τ_m during oscillation, defined as the average of the peak and trough values, was found to scale monotonically with loading rate (Figure 2.A3). By normalizing the mean shear stress change $(\tau_m - \tau^*)$ with respect to the quantity $(b\text{-}a)\sigma_{eff}$, where σ_{eff} is the effective normal stress, this scaling relation could be accurately described for the slowness law using

$$\frac{\tau_m - \tau_*}{(b-a)\sigma_{eff}} = 1.35\ln\left(\frac{5.5}{1+4.5v_0}\right) + 0.02(1-v_0^{1.97}) \qquad (2.A2)$$

where $v_0 = V_0/V^*$ and τ^* is the mean shear stress at the reference velocity. This empirical relation demonstrates that τ_m is systematically related to the displacement rate, effective normal stress and the rate dependence $(a\text{-}b)$, and is valid at least up to $v_0 = 11$ (Fig. 2.A3).

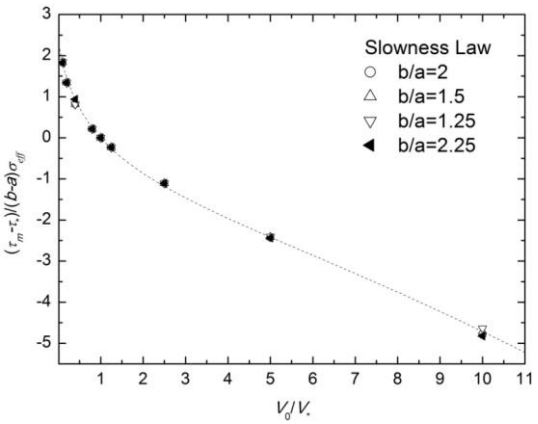

Figure 2.A3. Normalized mean shear stress calculated as a function of velocity step ratio $v = V_0/V^*$ for the slowness law. The generalized relation (eq. A2) holds for loading velocities up to $11V^*$.

For the slip law we found similar behaviour up to a loading rate of $V_0 = 1.5V^*$, beyond which the results diverge strongly (Figure 2.A4). At the lower velocities, where $v_0 \equiv V_0/V^* \leq 1.5$ and both RSF laws led to similar results, the behaviour associated with the slip law can be described by the scaling relation

$$\frac{\tau_m - \tau_*}{(b-a)\sigma_{eff}} = 0.85\ln\left(\frac{8.5}{1+7.5v_0}\right) + 0.02(1-v_0^{6}) \qquad (2.A3)$$

In our experiments, we stepped the sliding velocity between 1.22 and 0.122 μm/s, i.e. up and down by one order of magnitude. Because numerical simulations using the slowness law are applicable up to at least $v_0 \equiv V_0/V_* = 11$, equation 2.A2 is more suitable for describing the quasi-static oscillations found in our experiments than equation 2.A3, which is valid only for $v_0 \leq 1.5$. Equation 2.A2 was therefore used to obtain *(a-b)* in our experiments on limestone gouge at 150°C, as described in the main text. Note, however, that in making this choice an RSF law with one state variable is assumed, with the state variable being determined by the Dieterich-type slowness law.

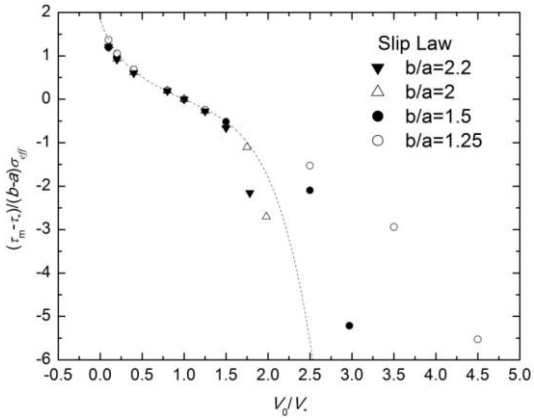

Figure 2.A4. Normalized mean shear stress calculated as a function of velocity step ratio $v = V_0/V_*$ for the slip law. The generalized relation (eq. 2.A3) only holds for loading velocities up to $1.5V_*$.

Acknowledgements

The experimental work reported here was carried out at, and funded by, the State key Laboratory of Earthquake Dynamics, Institute of Geology, China Earthquake Administration (CEA), under grant LED2008A03. It was also partly supported by the CEA under grant 200708014, and by the Ministry of Science and Technology, through the Wenchuan Earthquake Fault Scientific Drilling (WFSD) program and a National Key Basic Research and Development Program under grant 2004CB418405. We would also like to thank the Karel Frederik (KF) Hein fund for providing the funds necessary to support B.A.V. to visit China. Jiaxiang Dang, Xiaosong Yang, Yongsheng Zhou and Honglin He are thanked for their contributions to the fieldwork. Colin Peach and Xiangmin Zhang are thanked for insightful discussions, and Xisheng Lin is thanked for his advice and assistance in analyzing the quantitative mineral compositions of the samples using X-ray diffraction.

Chapter III

Frictional properties and microstructure of calcite-rich fault gouges sheared at sub-seismic sliding velocities

After:
Verberne, B. A., De Bresser, J. H. P., Niemeijer, A. R., Spiers, C. J., De Winter, D. A. M., and Plümper, O. (2013a). Nanocrystalline slip zones in calcite fault gouge show intense crystallographic preferred orientation: Crystal plasticity at sub-seismic slip rates at 18-150°C. *Geology* **41,** 863-866.
Verberne, B. A., Spiers, C. J., Niemeijer, A. R., De Bresser, J. H. P., De Winter, D. A. M., and Plümper, O. (2013b). Frictional properties and microstructure of calcite-rich fault gouges sheared at sub-seismic sliding velocities. *Pure Appl. Geophys.* **171**, 2617-2640.

Abstract

This Chapter reports an experimental and microstructural study of the frictional properties of simulated fault gouges prepared from natural limestone (96% $CaCO_3$) and pure calcite. Our experiments consisted of direct shear tests performed, under dry and wet conditions, at an effective normal stress of 50 MPa, at 18 to 150°C, and sliding velocities of 0.1-10 μm/s. Wet experiments used a pore water pressure of 10 MPa. Wet gouges typically showed a lower steady-state frictional strength (μ = 0.6) than dry gouges (μ = 0.7-0.8), particularly in the case of the pure calcite samples. All runs showed a transition from stable velocity strengthening to (potentially) unstable velocity weakening slip above 80-100 °C. All recovered samples showed patchy, mirror-like surfaces marking boundary shear planes. Optical study of sections cut normal to the shear plane and parallel to the shear direction showed both boundary and inclined shear bands, characterized by extreme grain comminution and a crystallographic preferred orientation. Cross-sections of boundary shears, cut normal to the shear direction using focused ion beam – SEM, from pure calcite gouges sheared at 18 and 150°C, revealed dense arrays of rounded, ~0.3 μm-sized particles in the shear band core. Transmission electron microscopy (TEM) showed that these particles consist of 5 to 20 nm sized calcite nanocrystals. Outside the shear bands, all samples showed evidence for cataclasis and crystal plasticity. Comparing our results with previous models for gouge friction, we suggest that frictional behaviour was controlled by competition between crystal plastic and granular flow processes active in the shear bands, with water facilitating pressure solution, subcritical cracking and intergranular lubrication. Our data have important implications for the depth of the seismogenic zone in tectonically-active limestone terrains. Contrary to recent claims, they also demonstrate that nanocrystalline mirror-like slip surfaces in calcite(-rich) faults are not necessarily indicative of seismic slip rates.

3.1. Introduction

Natural faults are often marked by the presence of a narrow principal slip zone (PSZ) at the core, which is thought to accommodate the bulk of the slip imposed on the fault (Sibson, 1986). The PSZ consists of the fine-grained granular wear material, or fault gouge, that is the product of cumulative slip along the fault (e.g. Chester and Chester, 1998). Understanding the frictional properties of fault gouges and their role in seismic rupture nucleation and propagation, as well as in interseismic strength recovery, is crucial for improving our understanding of the seismic cycle. Laboratory studies focusing on the frictional properties of crustal fault rocks, in particular through experiments simulating the conditions pertaining to natural faults, have a key role to play here (e.g. Blanpied et al., 1995; He et al., 2007; Carpenter et al., 2011; Den Hartog et al., 2012; Ikari et al., 2013; Zhang and He, 2013).

Since Brace and Byerlee (1966) identified unstable frictional slip, i.e. stick-slips, as an analogue for earthquakes, much experimental and theoretical work has focused on the processes leading to frictional instability (see Marone (1998a) or Scholz (1998) for reviews). It was recognized that regular stick-slip may occur when a sliding medium decreases in strength with increasing sliding rate, i.e. when it exhibits velocity weakening behaviour (Dieterich, 1979; Ruina, 1983). For this reason, much laboratory work aimed to characterize the velocity dependence of (fault) rock frictional sliding, and in particular the phenomenology and constitutive modelling of transitions from stable to (potentially) unstable slip (e.g. Blanpied et al., 1995; He et al., 2007) and on the microphysical mechanisms controlling them (e.g. Bos and Spiers, 2002a; Niemeijer and Spiers, 2007; He et al., 2013). In this context, Verberne et al. (2010) (i.e. Chapter II) reported on friction experiments conducted on (simulated) fault gouges from the Longmenshan Fault Zone (LFZ), Sichuan, China, with the aim of characterizing the frictional strength and stability of crushed rocks sampled from surface outcrops cut by a natural, earthquake-prone fault. Our samples consisted of clay-rich, quartz-rich, and calcite-rich gouges, which were sheared at low sliding velocities (0.1- 1 μm/s), under water-saturated conditions at an effective normal stress of ~53 MPa, at temperatures ranging from room temperature (~20°C) to 150°C. In the range of conditions investigated, the clay- and quartz-rich samples invariably exhibited stable velocity strengthening behaviour, while the calcite-rich gouge showed a transition from stable slip at 20-50°C to unstable velocity weakening slip at 100-150°C (see Figs. 3.4, 3.5, 3.7). These results offer potential constraints on the depth to the upper limit of the seismogenic zone in the LFZ, implying

that calcite-rich lithologies may be particularly susceptible to shallow-focus seismicity.

Indeed, recent experimental studies focusing on upper-crustal fault-frictional behaviour show growing evidence for an intrinsic tendency towards frictional instability of calcite-rich fault rocks (Collettini et al., 2011; Ikari et al., 2013; Zhang and He, 2013; Niemeijer and Collettini, 2014). In experiment and nature, calcite(-rich) rocks are well-known to exhibit ductile deformation by mechanisms such as pressure solution and crystal plasticity, at lower pressures and temperatures than generally required for these mechanisms to operate in other upper crustal rocks, such as granite (e.g. Burkhard, 1990, 1993; Spiers et al., 2004). These time-dependent deformation mechanisms offer important fault gouge healing and compaction or re-strengthening mechanisms (Bos et al., 2000a, b; Bos and Spiers, 2002a; Nakatani and Scholz, 2004; Niemeijer and Spiers, 2006) and are known, from microphysical modelling and analogue experiments, to play a key role in causing potentially unstable velocity weakening behaviour in gouge-bearing faults at low slip rates (Nakatani, 2001; Bos and Spiers, 2002b; Niemeijer and Spiers, 2007; Den Hartog and Spiers, 2013; He et al., 2013). Crystal plasticity or pressure solution processes may therefore offer the key to explaining the unusual frictional behaviour of calcite-rich fault rocks compared with other sedimentary rocks.

To further investigate this hypothesis, we conducted dry and wet friction experiments on simulated gouges prepared from natural limestone and pure calcite, at upper crustal effective normal stresses (50 MPa) at temperatures ranging from 18 to 150°C, imposing sliding velocities ranging from 0.1 to 10 μm/s. We provide an in-depth comparison of the frictional behaviour of natural limestone and calcite gouge, tested dry and in the presence of water, at temperatures of 18°C, 50°C, 100°C, and 150°C. Our specific research questions are:

i) What is the effect of water on the frictional strength and slip stability of simulated calcite(-rich) fault gouges?
ii) Are there differences in frictional strength and/ or slip stability related to the rock composition, i.e. between gouges prepared from natural limestone and pure calcite (crushed Iceland Spar), and, if so, why?
iii) On the basis of the microstructural characteristics, can we identify what deformation mechanisms control the frictional strength and slip stability of calcite(-rich) fault gouges, and, if so, can we establish microstructural indicators for unstable frictional slip?

Answering these questions will provide more insight into the microphysical processes controlling frictional sliding of calcite fault gouges, and on the role of limestone faults in the seismic cycle.

3.2. Methodology

3.2.1. Sample materials

We used simulated fault gouges prepared from natural limestone from the Xujiahe (XJ) Formation, Wenchuan, China (see Verberne et al., 2010, or Chapter II), and from crushed single crystals of calcite (Iceland Spar). The XJ Formation is cut by a branch of the Longmenshan Fault Zone that experienced surface rupture during the 2008 Mw 7.9 Wenchuan earthquake (Xu et al., 2009) in Sichuan, China (see Fig. 3.1). X-ray Diffraction (XRD) analysis of the crushed XJ limestone showed that it consists for 95-96% of CaCO3, ~2-3% of illite, and ~1-2% of quartz. XRD analysis of the crushed calcite revealed a mineralogy comprising ~98% calcite, with <2% dolomite (see Table 3.1). Grain size distributions (GSD's) of the crushed and sieved samples, measured using a Malvern laser particle sizer, showed that the simulated XJ limestone gouge used has a wider GSD ($1 < d \leq 100$ μm) compared with that of the crushed calcite ($1 < d \leq 65$ μm), but that the median particle size (d_{50}) for both gouges is similar (~15-20 μm) (Fig. 3.1).

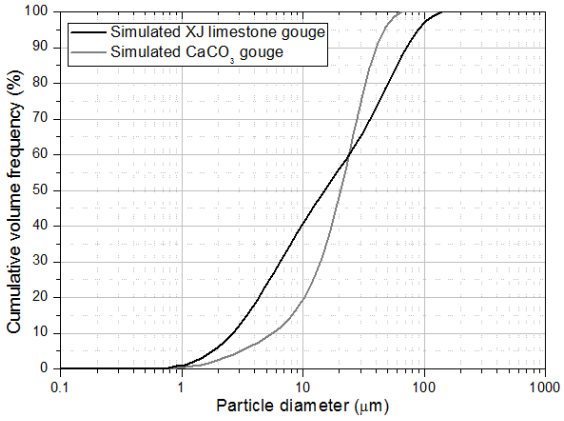

Figure 3.1. Initial grain size distributions of simulated Xujiahe (XJ) limestone and pure $CaCO_3$ gouge (crushed Iceland Spar) used in our experiments. Measured using a Malvern laser particle sizer.

3.2.2. Experimental apparatus

All experiments reported here were performed using the "Shuttle vessel" installed at

the HPT laboratory of Utrecht University, i.e. a conventional triaxial deformation apparatus comprising a self-compensated, constant volume pressure vessel plus an Instron electro-servo-controlled ram for axial loading. The confining medium is silicone-oil. Figure 3.2a shows a schematic cross-section of the pressure vessel.

When performing individual experiments, axial force is transmitted to the sample using a Ti-grade 5 piston, furnished with an internal differential variable reluctance transformer (DVRT), to allow for measurement of piston distortion hence axial force, independently of seal friction (Fig. 3.2a). This internal force gauge has a full-scale of 100 kN, with a resolution of ~33 N. Displacement of the Instron ram was measured externally using a linear variable differential transformer (LVDT) with 100 mm full-scale and 5 μm resolution. Confining pressure was applied using a compressed-air driven diaphragm pump. During testing, pressure was manually regulated with a 20 mL hand pump, which enabled control to within ~0.1 MPa of the desired value. In wet experiments, we used demineralized water to apply pore pressure, which was held constant to within ~0.05 MPa of the desired value (10 MPa typically) using a three-term (P.-I.-D.) electro-servo-mechanical pump. Heating was achieved using a Thermocoax internal furnace, and temperature controlled with a three-term CAL2300 industrial controller that enables control to within 0.1°C of set-point temperature. The sample temperature was measured by a thermocouple penetrating the upper direct shear piston to a position close to the sample layer (Fig. 3.2a, b).

3.2.3. Direct shear testing assembly

We ran our experiments using a so-called “69” piston assembly designed for direct shear testing in a triaxial deformation apparatus (Fig. 3.2b), as used by Logan et al. (1992) and Samuelson and Spiers (2012). This testing geometry has the advantage over the conventional “saw-cut” assembly (e.g. Logan et al., 1979; Blanpied et al., 1995) that the normal stress acting on the sample layer is independent of shear displacement, and is at all times equal to the confining pressure. Moreover, in the set-up used here, sample extrusion at the gouge layer-ends is minimized.

Each test used a set of two direct shear or 69 pistons with individual dimensions of 35 mm in diameter by 70 mm total length, comprising a 35 x 49 mm, grooved piston face (in contact with the sample), a 35 x 9 mm smooth surface, plus a cylindrical 35 x 12 mm end-piece (Fig. 3.2b). In wet experiments, the piston face consisted of a sintered stainless steel, high-porosity frit, which ensured even distribution of the pore-fluid over the

sample layer. The groove pattern was spark-eroded in the porous frit, and comprises a set of 0.1 mm regularly spaced, half-circular grooves of 0.12 mm in diameter, i.e. cutting 0.06 mm into the frit (Fig. 3.2c). For dry experiments, the piston face used supported of a set of regularly spaced (0.1 mm), triangular grooves 0.1 mm wide and 0.05 mm deep (Fig. 3.2d).

In preparing each experiment, all powders were mixed with demineralized water in proportions of roughly 4:1 gouge-to-water, yielding a mouldable paste. A purpose-built jig allowed for easy emplacement of a ~1.1 mm thick gouge paste layer onto the sample-piston interface, forming a plate measuring 35 mm wide by 47 mm long. For dry experiments, the sample was dried in an oven at ~115˚C for at least 4 hours before starting the test. We confirmed complete dehydration of the sample by using a dummy sample-paste, and weighing before and after drying. To avoid contamination from atmospheric water vapour the sample was assembled while the piston plus sample layer were still hot. All experiments used two Indium bars measuring 35 x 1 x 1 mm, placed at each end of the sample layer to avoid volume-loss of the gouge layer upon shearing (Fig. 3.2b). The displacement-accommodating voids characterizing the 69 direct shear assembly were filled with a pack of polytetrafluorethylene (PTFE), Ethylene-Propylene-Diene Monomer (EPDM) rubber, and classic white silicone putty (Fig. 3.2b). This design ensured that the silicone putty flowed outwards upon loading the sample assembly, offering zero resistance to the piston motion and without contaminating the sample. The entire assembly, including sample layer and the displacement-accommodating void-fills, was jacketed first in a thin Fluorinated-Ethylene-Propylene (FEP) sleeve for support, and then in an EPDM rubber sleeve of ~1.4 mm thickness. The FEP sleeve was cut along the parts covering the displacement-accommodating voids. In order to reduce shear resistance between the pistons and the load-transmitting forcing blocks, circular PTFE sheets were placed onto the base of the direct shear pistons (Fig. 3.2b).

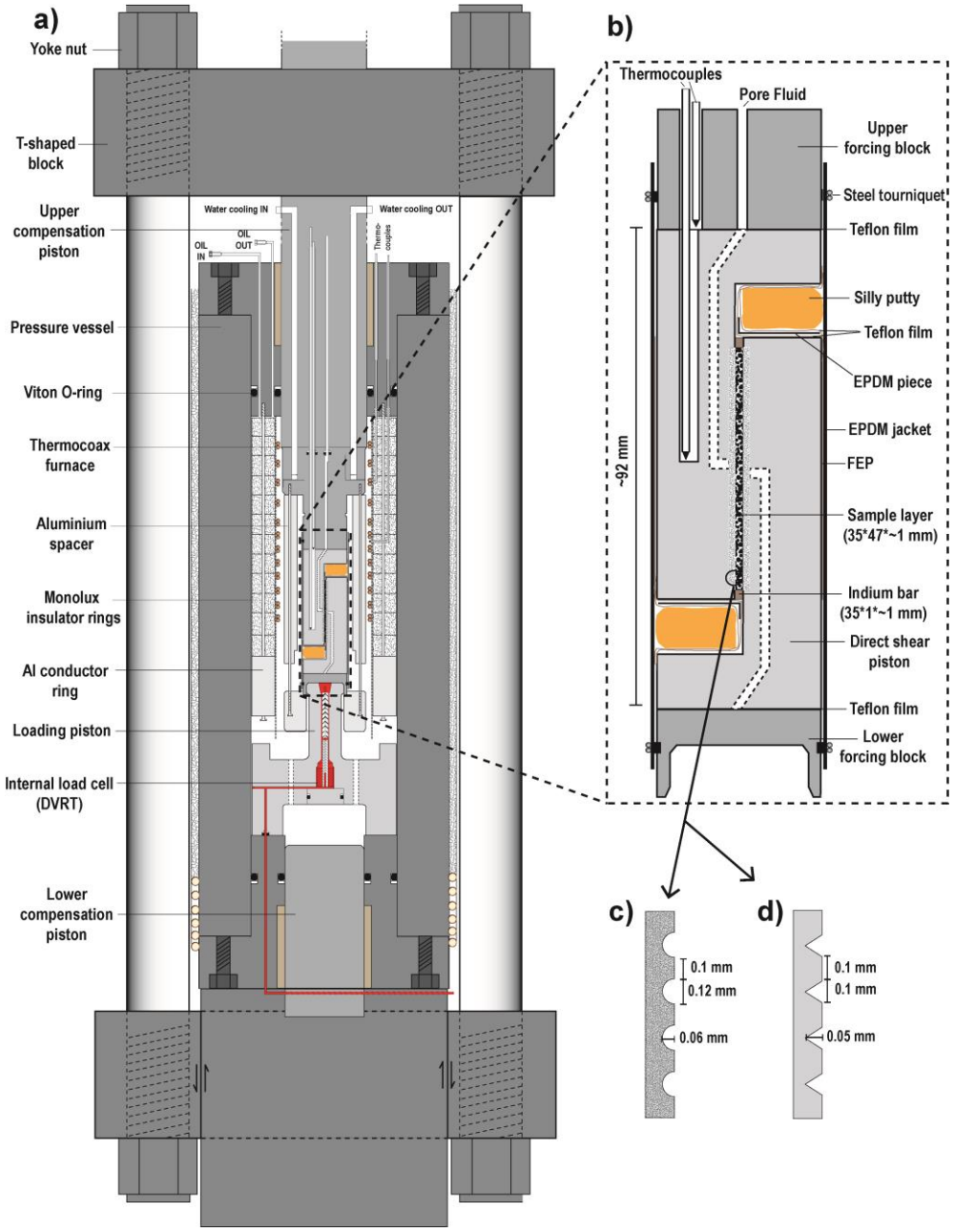

Figure 3.2. Schematic cross-sections of the testing apparatus (a) and direct shear assembly (b). Groove imprint on the sample-piston interface as indicated for wet(c) and dry tests (d).

To examine potential effects of the sample assembly to the measurement of gouge layer frictional properties we performed test runs at room temperature (~18°C), at a normal stress σ_n = 50 MPa, using 35 x 47 x 1 mm sheets of PTFE and Indium. The peak shear strength measured in these tests was ≤3 MPa and ≤4 MPa for the PTFE and Indium sheets respectively (Fig. 3.3). This suggests that the sample assembly has a very low contribution to the total frictional strength measured, i.e. <<4 MPa. In response to velocity steps we invariably found velocity strengthening behaviour, for both PTFE and Indium. To investigate sample-assembly effects to the velocity dependence of friction strength, we performed a test on talc gouge at room temperature and σ_n = 50 MPa for comparison with previously published data. The results showed a peak coefficient of sliding friction (μ) of 0.18, decreasing to a residual value of 0.14-0.16 (Fig. 3.3). In response to velocity steps the talc gouge showed velocity strengthening behaviour, with an average value of the rate sensitivity parameter Γ of 0.0061 ± 0.0005 over the five velocity steps applied. These data are in good agreement with data from triaxial saw-cut experiments on talc gouge reported previously (cf. e.g. Moore and Lockner, 2008). Therefore we are confident that the sample assembly used here has a negligible effect on the frictional properties measured from our sample layers.

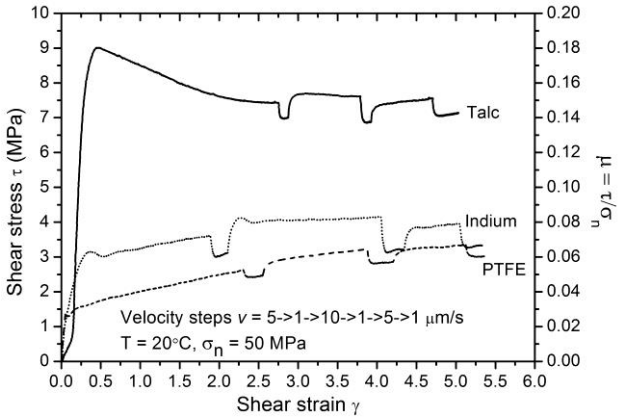

Figure 3.3. Shear stress against shear strain, of data from direct shear on sheets of PTFE and Indium, and on a Talc gouge layer.

3.2.4. Experimental procedure and conditions

We ran our dry experiments using a confining pressure (P_c) of 50 MPa, while the wet experiments were conducted using P_c = 60 MPa, and a pore fluid pressure of 10 MPa.

Because the confining pressure equals the normal stress in the testing assembly used here (Fig. 3.2), this implies that for all experiments we used a nominal effective normal stress of 50 MPa. The sample temperatures used measured ~18, ~50, ~100, and ~150°C. For every individual test, the jacketed sample assembly including gouge layer was loaded into the pressure vessel, which was then sealed with a closure nut and de-aerated before applying a confining pressure of ~20 MPa. For the wet experiments, the pore fluid system was filled with de-mineralized water and subsequently de-aerated followed by pressurization to the testing value of 10 MPa. The pore fluid may not have been fully saturated prior to each test, hence we cannot exclude possible effects of differences in saturation states between or during our wet experiments. However, departures from saturation of the pore fluid over the duration of the experiments are likely to be small due to the extremely fine grain size of our crushed samples (20-40 vol. % <10 μm – Fig. 3.1), their high dislocation stored energy content due to crushing, and the further refinement of grain size and increase in mechanical damage that occurs during deformation. For experiments at elevated temperature, we switched on the internal furnace for heating to the desired test temperature. In the first minute after switching on the internal furnace, the confining pressure increased at a rate of ~1-2 MPa/s, followed by a slow approach (<<1 MPa/s) to a near-constant value. By intermittent bleeding of the vessel during heating, the confining pressure was at all times held below that used during the test. Equilibration of the testing apparatus with respect to pressure and temperature took from around 1 hour at room temperature to 4 hours at 150˚C. In some experiments at elevated temperatures the testing apparatus was left to equilibrate overnight.

Upon starting an experiment, we used a ramp generator connected to a digital interface to apply the desired load-point displacement rate. The initial displacement rate (v) used in each test was 1 μm/s. After achieving sliding at a constant (average) strength, or else slip-weakening along a near-linear trend, the displacement rate was stepped in the sequence 0.1, 10, 1, 0.1, 10, and 1 μm/s, employing 0.2-1.0 mm displacement intervals in each step. In terminating each experiment, the axial loading ram was backed off at a rate of 10 μm/s. Upon complete removal of the axial load, the furnace was switched off in the case of experiments at elevated temperature, and the sample was depressurized to atmospheric conditions at a rate of < ~0.5 MPa/s.

3.2.5. Data processing and analysis

All data were recorded at a sampling rate of 10 Hz using a 16-bit National

Instruments DAQPad-6015 A/D converter. The axial force supported by the sample was calculated from the DVRT internal load signal (Fig. 3.2a), which was calibrated against an Instron (external) load cell with an accuracy of ±0.25% on full scale (100 kN). The measured axial displacement was corrected for elastic machine distortions using calibrations obtained from compression tests on a steel dummy of known elastic properties. Calibrations were generated at or near the pressure and temperature conditions used in this study.

To calculate the shear stress (τ) supported by the sample layer we divided the measured axial force by the load-bearing sample-area. However, in some experiments, the true load-bearing sample area decreased with increasing displacement due to small changes in the detailed deformation geometry. Correction for this effect proved unsuccessful due to subtle differences between each test, although in the experiments reported here it was negligible anyway. Therefore, to avoid over-correction hence artefacts in the strength data, we assumed a constant load-bearing sample area for each experiment, i.e. 35 x 47 = 1645 mm². From the ratio of the shear stress τ over the effective normal stress σ_n^{eff} we determined the apparent coefficient of sliding friction μ, defined

$$\mu = \frac{\tau - S_0}{\sigma_n - \alpha \cdot P_f} \approx \frac{\tau}{\sigma_n^{eff}} \qquad (3.1)$$

To qualify as a friction coefficient, this widely used expression implicitly assumes that i) the cohesion (S_o) of the sliding medium is negligible (e.g. Byerlee, 1978), and ii) that α in equation (3.1) is equal to 1 (e.g. Morrow et al., 1992). To quantify the velocity dependence of strength, for each velocity step, i.e. including both up- and downward steps, we determined the ratio of the change in (steady-state) strength ($\mu_n \rightarrow \mu_{n+1}$) over the change in the logarithm of the sliding velocity ($\ln(v_n) \rightarrow \ln(v_{n+1})$), thus using the rate sensitivity parameter

$$\Gamma = \frac{\mu_{n+1} - \mu_n}{\ln(v_{n+1}) - \ln(v_n)} = \frac{\Delta\mu}{\Delta \ln(v)} \qquad (3.2)$$

In the case of true steady-state frictional sliding before and after the velocity step, as was the case in most of our dry experiments, equation (3.2) yields the equivalent of the

parameter Γ used in rate-and-state-friction modeling (Dieterich, 1979; Ruina, 1983; Marone, 1998a; Scholz, 1998; see Fig. 3.4). However, some of our experiments exhibited unstable stick-slip, and in particular the wet experiments sometimes exhibited (linear) slip hardening or weakening characteristic for a single velocity interval. In the case of stick-slips we used the change in the maximum strengths reached at the corresponding sliding velocities (Fig. 3.4). In the case of linear slip hardening or weakening we corrected using non-progressive linear detrending of the data, i.e. characteristic for a single velocity interval (following Blanpied et al. 1995; Den Hartog et al., 2012) (Fig. 3.4). In this way, each value of Γ characterizes the change in strength associated with a single velocity step while assuming that linear weakening or hardening trends are independent of the rate-sensitivity of frictional strength. A positive value of Γ indicates stable velocity strengthening and a negative value indicates (potentially) unstable velocity weakening (see Scholz, 1998).

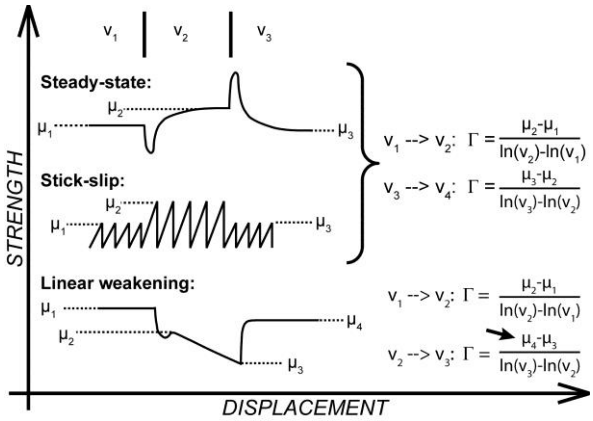

Figure 3.4. Method for determining the rate sensitivity Γ (eq. 3.2) from velocity stepping data in our experiments.

3.2.6. Sample recovery and microstructure analyses

After each experiment, the sample assembly was unloaded from the pressure vessel and dismantled. Fragments of some sheared samples were used for investigation using an incident light microscope, but for most experiments the complete sheared gouge layer was recovered, and subsequently impregnated with Araldite 2020 epoxy resin. The completeness of sample recovery depended strongly on the splitting fabric that developed upon separation of the direct shear pistons. Especially for the wet experiments this often

prevented preservation of the complete microstructure. After hardening for several days, the samples were cut in an orientation normal to the shear plane and parallel to the shear direction. Selected samples were also cut in an orientation normal to the shear plane and normal to the shear direction. The cut sections were used to prepare ultrathin sections (~5-10 μm thickness).

All transmitted and incident light analyses were performed using a Leica DMR polarizing light microscope. Selected samples were analyzed in more detail using a Universal (U-)stage mounted on a Leitz Wetzlar microscope, using a Nova Nanolab 600 focused ion beam – scanning electron microscope (FIB-SEM), and using a Technai 20F transmission electron microscope (TEM). FIB-SEM combines the milling capabilities of the ion beam and the imaging capabilities of the electron beam. Momentum-transfer from Gallium ions to the sample causes local sputtering, enabling sectioning at micron-scales with nano-scale precision, and the excavation of electron transparent foils for further analysis (e.g. Volkert and Minor, 2007). Optical imaging in the SEM is done in secondary electron (SE) mode. Cross sections and FIB-SEM tomography series are imaged in backscatter electron (BSE) mode. TEM foils were prepared in the FIB-SEM following standard protocol (e.g. Mayer et al., 2007), i.e. a selected cross-section was trenched using the ion-beam, extracted with a micromanipulator, and then mounted on a C-mount TEM grid. The section was polished to a thickness ~100 nm, yielding an electron transparent TEM foil. For some foils used in this study, an additional polishing step was performed to locally reduce the thickness of the foil to ~50 nm. The TEM was operated at 200 kV. In high-resolution (HR) mode, we strictly limited beam exposure times to avoid damaging the sample.

To investigate the crystallographic orientation distribution of calcite grains in the shear band, we explored transmission-electron backscattered diffraction (t-EBSD) (Keller & Geiss, 2011; Trimby et al., 2012). 'Standard' EBSD was discounted because of the extremely small grain size and the grain size heterogeneity encountered in our samples. In conducting t-EBSD, we attached the C-mount grid with a ~50 nm thick foil to a pre-tilted holder, obtaining an angle of approximately 20° relative to the horizontal. Forward diffracted electrons were captured using a Nordlys II EBSD detector mounted on the FIB-SEM, at an acceleration voltage of 30 kV. All Kikuchi band diffraction patterns were indexed manually. Despite obtaining some promising diffraction data, just ~15% out of >5000 spot analyses yielded a diffraction pattern strong enough for indexation, which were demonstrably from the larger grain fragments (> ~0.5 μm)

present in the sample. Therefore, it was concluded that our t-EBSD analyses did not allow for a statistically robust data set.

3.3. Mechanical results

3.3.1. Frictional strength data

A list of the experiments performed and the key frictional strength parameters obtained is given in Table 3.1. We plot the apparent coefficient of sliding friction (eq. 3.1) against displacement (x) for all tests in Figure 3.5.

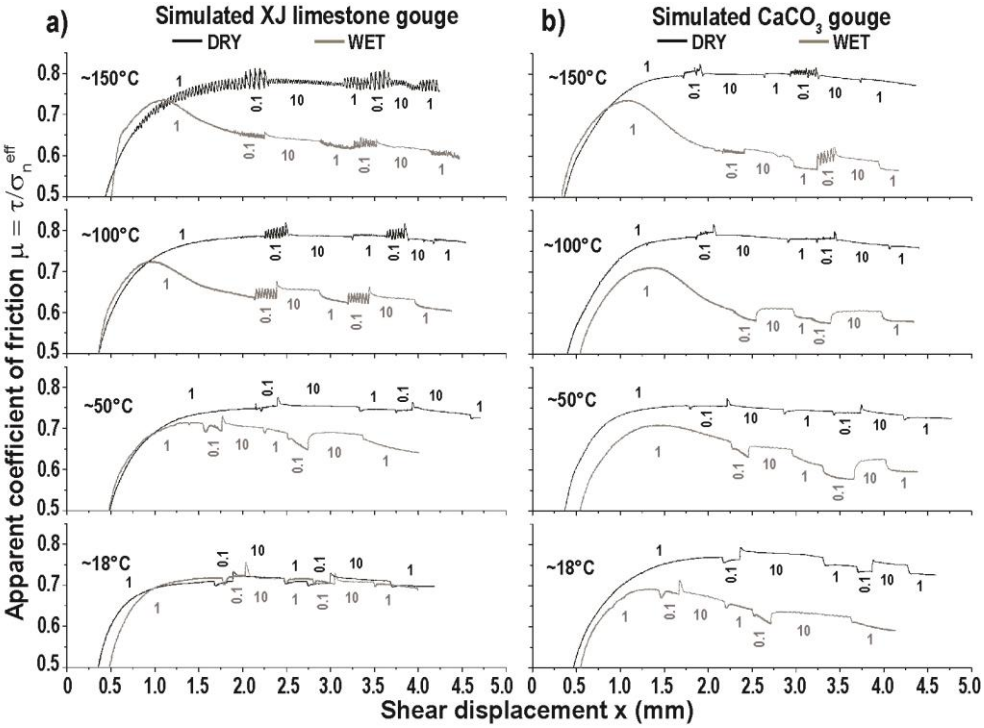

Figure 3.5. Plots of the apparent coefficient of sliding friction against shear displacement (x) for dry (black lines) and wet (grey lines) experiments using a) simulated Xujiahe (XJ) limestone and b) pure $CaCO_3$ gouge, at temperatures of ~18°C, ~50°C, ~100°C, and ~150°C. All experiments used a velocity stepping scheme indicated under the curves (in μm/s). A list of the experiments and key frictional strength parameters obtained is given in Table 3.1.

All experiments showed rapid, near-linear loading in the first $x \approx$ 0.3-0.5 mm of displacement, followed by apparent yield and subsequent hardening towards a peak frictional strength (μ_{pk}) attained at $x \approx$ 1-2 mm. After reaching the peak strength, sliding

continued at a near-constant average strength in the dry experiments, while the wet experiments showed gradual slip weakening (except experiment XJ-RT-wet). Experiment XJ-RT-wet showed a similar frictional strength evolution with displacement as the dry experiments. Our observations on wet simulated XJ limestone gouge are consistent with those reported by Verberne et al. (2010) (or Chapter II), i.e. from saw-cut friction tests on the same material, performed under similar conditions of effective normal stress and temperature (see Fig. 3.5). Although some tests did not reach steady-state at maximum displacements (notably XJ-50-wet and $CaCO_3$-RT-wet), in all experiments a near-steady-state final value of the frictional strength (μ_{fnl}) can be defined for $x \geq 4$ mm (Table 3.1, Fig. 3.5). Comparison of μ_{fnl} between tests will provide insight into the magnitude of displacement weakening with increasing temperature.

In response to velocity stepping, all experiments showed stable sliding at $T \approx 18$-50°C, at all sliding velocities at all displacements (Fig. 3.5; Table 3.1). In experiments performed at $T \geq 100$°C, we observed velocity weakening behaviour for all dry experiments plus for wet experiments using simulated XJ limestone gouge. Wet experiments using simulated pure $CaCO_3$ gouge showed stable velocity strengthening at all sliding velocities for $T \approx 18$-100°C but unstable velocity weakening at $T \approx 150$°C at $v = 0.1$ μm/s. In general, experiments showing velocity weakening first exhibited stick-slip at the lowest sliding velocity ($v = 0.1$ μm/s), at the higher strains imposed (Fig. 3.5; Table 3.1). Experiment XJ-150-dry showed spontaneous stick-slip at $v = 1$ μm/s at $x \approx 0.7$ mm (Fig. 3.5). In this experiment, in the displacement interval $x \approx 0.7$-1.9 mm, the frictional strength drop associated with the 'slip'-phase increased with increasing displacement, before reaching a near-constant maximum or 'peak' strength of $\mu_{pk} \approx 0.79$ at $x \approx 1.9$ mm. Stick-slip was observed at all subsequent sliding velocities imposed, with the frictional strength drop consistently larger at lower sliding velocities. In experiment XJ-150-wet, gradual displacement weakening was followed by spontaneous nucleation of stick-slip at $v = 1$ μm/s at $x \approx 1.7$ mm.

Experiment	T (°C)	d_{fnl}[1] (mm)	Gouge strength			Λ[5]	Type of motion[6]
			μ_{pk}[2]	μ_{fnl}[3]	$\Delta\mu_x$[4]		
Simulated XJ limestone gouge							
XJ-RT-dry	17.8	1.05	0.71	0.70	0.01	-	stable vs
XJ-50-dry	50.4	1.10	0.75	0.73	0.02	-	stable vs
XJ-100-dry	103	0.90	0.79	0.78	0.01	-	unstable vw (0.1); osc. vw (1.0); stable vw (10)
XJ-150-dry	150	1.00	0.79	0.78	0.01	-	unstable vw
XJ-RT-wet	18.3	0.95	0.72	0.70	0.02	0%	stable vs
XJ-50-wet	52.0	1.00	0.71	0.66	0.05	10%	stable vs
XJ-100-wet	102	0.90	0.72	0.61	0.11	22%	unstable vw (0.1); stable vs (1.0, 10)
XJ-150-wet	149	1.05	0.74	0.61	0.13	22%	unstable vw (0.1); osc. vw (1.0); stable vs (10)
Simulated pure $CaCO_3$ gouge							
$CaCO_3$-RT-dry	17.9	1.10	0.77	0.73	0.04	-	stable vs
$CaCO_3$-50-dry	49.9	0.80	0.76	0.72	0.04	-	stable vs
$CaCO_3$-100-dry	101	0.80	0.78	0.76	0.02	-	unstable vw (0.1, 1.0); stable vs (1.0, 10)
$CaCO_3$-150-dry	150	0.95	0.80	0.78	0.02	-	osc/unstable vw (0.1); stable vw (1.0, 10)
$CaCO_3$-RT-wet	18.6	0.80	0.69	0.59	0.10	19%	stable vs
$CaCO_3$-50-wet	50.6	0.80	0.71	0.60	0.11	17%	stable vs
$CaCO_3$-100-wet	99.6	0.75	0.71	0.58	0.13	24%	stable vs
$CaCO_3$-150-wet	149	0.70	0.74	0.57	0.17	27%	unst. vw (0.1); stable vs (1.0); stable vw (10)

Table 3.1. Frictional strength data. The error to the absolute frictional strength μ is ≤0.5%. [1] d_{fnl} = Thickness of the sample layer after shear deformation. [2] μ_{pk} = peak strength (v = 1 μm/s). In the case of stick-slip we picked the failure strength. [3] μ_{fnl} = near-steady-state final strength (x > 4 mm, v = 1 μm/s). In the case of stick-slip we picked the failure strength. [4] $\Delta\mu_x = \mu_{pk} - \mu_{fnl}$. [5] $\Lambda = [\mu_{fnl}(\text{dry}) - \mu_{fnl}(\text{wet})] / \mu_{fnl}(\text{dry})$ x 100%, i.e. the relative decrease of μ_{fnl} in wet experiments compared with dry tests. [6] Slip stability and velocity dependence. vs = velocity strengthening; vw = velocity weakening; osc = oscillations. In parentheses the reference velocity in μm/s.

The peak and near-steady-state values of the apparent coefficient of friction determined at v = 1 μm/s, and the finite difference $\Delta\mu = \mu_{pk} - \mu_{fnl}$, are plotted against temperature in Figure 3.6. For both samples tested, dry and wet, the enveloping surfaces defined by the values of μ_{pk} showed a weakly increasing trend with increasing temperature (Fig. 3.6a). However, for the near-steady-state strengths, we found a (weakly) increasing trend with increasing temperature for the dry experiments, but a decreasing trend with increasing temperature for the wet experiments, especially for tests using simulated XJ limestone gouge (Fig. 3.6b). Thus, for all dry experiments $\Delta\mu$ < 0.05 (Table 3.1), while for the wet experiments $\Delta\mu$ increased with increasing temperature (Fig. 3.6c). The decrease in the near-steady-state strength of the wet gouges relative to that of the dry gouges, i.e. Λ = [μ_{fnl}(dry) - μ_{fnl}(wet)] / μ_{fnl}(dry) x 100%, at corresponding testing temperatures, measured Λ = 0% at 18°C, 10% at 50°C, and 22% at 100°C and 150°C for the simulated XJ limestone gouge, and Λ = 19% at 18°C, 17% at 50°C, 24% at 100°C, and 27% at 150°C for the simulated pure $CaCO_3$ gouge (Table 3.1).

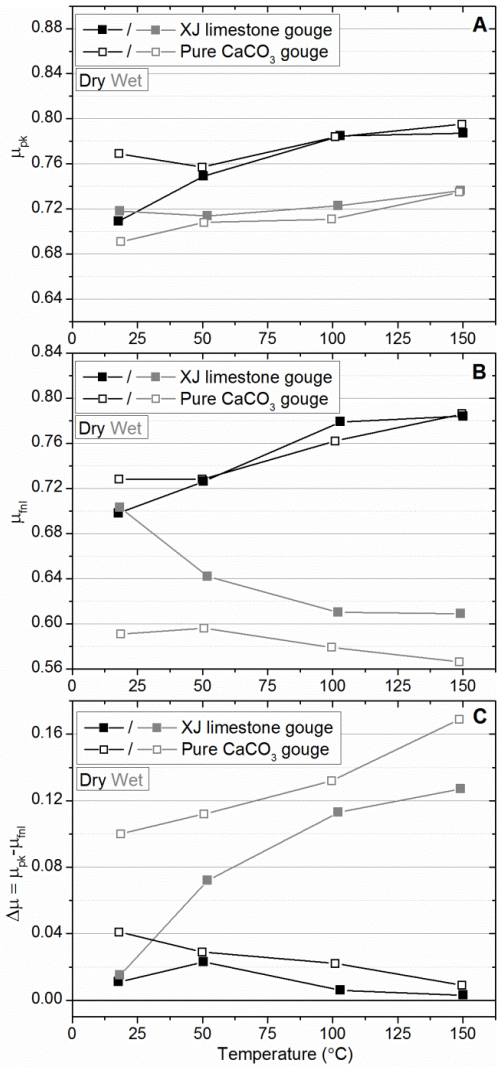

Figure 3.6. Plots of a) the peak (μ_{pk}) and b) the final (μ_{fnl}) frictional strength, for each test picked at v = 1 μm/s, against temperature. Black lines show results from dry experiments, grey lines those from wet experiments. The relative error to the frictional strength μ from experimental uncertainty is estimated to be ≤0.5%.) The finite difference $\Delta\mu = \mu_{pk} - \mu_{fnl}$.

3.3.2. Velocity dependence data

A list of the rate sensitivity parameter values Γ determined for all experiments, at each velocity step applied, is given in Table 3.2. All values of Γ are plotted against temperature in Figure 3.7. The scatter seen between the data points at each temperature, i.e. for each experiment, indicates the spread in the values of Γ with increasing displacement and/or type of the velocity step (up- or down-step) in the experiment (see also Table 3.2). For experiments showing velocity weakening, minima in the values of Γ are associated with strength data exhibiting stick-slip (Tables 3.1, 3.2). For both materials tested and for all velocity steps, the dry experiments showed a near-linear decrease of Γ with increasing temperature (Figs. 3.7a, b). For dry experiments using simulated XJ limestone gouge, linear interpolation of the mean values of Γ, i.e. averaged over the individual velocity steps, showed that a transition from positive to negative Γ occurs at $T \approx 70$°C. Similarly, for dry experiments using simulated pure $CaCO_3$ gouge this transition occurs at $T \approx 80$°C. Compared with the dry experiments, the wet experiments showed much more scatter in the values of Γ at each temperature. Nonetheless, the results showed that Γ first increased with increasing temperature up to $T \approx 50$°C, and then decreased toward $T \approx 150$°C. Negative values of Γ were first observed at $v = 0.1$ μm/s, at $T \approx 100$°C for wet simulated XJ limestone gouge, and at $T \approx 150$°C for wet simulated pure $CaCO_3$ gouge (Figs. 3.7a, b).

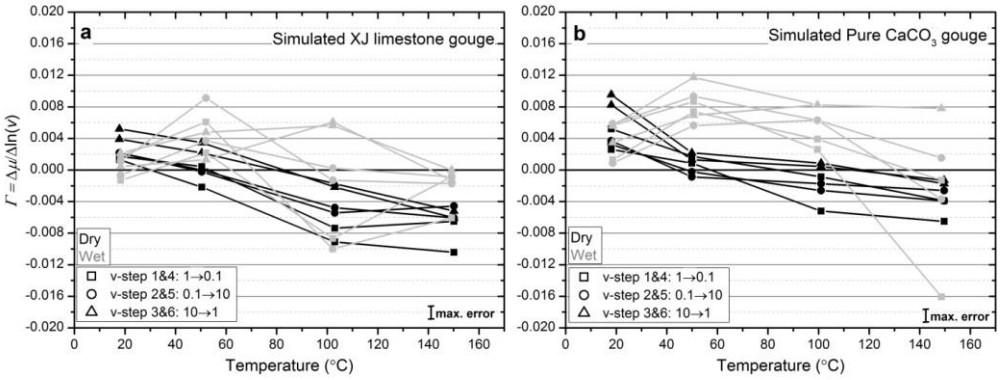

Figure 3.7. Plots of Γ (eq. 3.2) determined for each velocity step, against temperature, from experiments using a) simulated XJ limestone and b) pure $CaCO_3$ gouge. Standard error propagation shows that the error to each value of Γ is ~±0.0017. A list of all Γ values is given in Table 3.2.

	Experiment	T (°C)	Γ (see eq. 3.2)					
			step 1 1→0.1	step 2 0.1→10	step 3 10→1	step 4 1→0.1	step 5 0.1→10	step 6 10→1
Simulated XJ limestone gouge	XJ-RT-dry	17.8	0.0013	0.0022	0.0039	0.0017	0.0022	0.0052
	XJ-50-dry	50.4	-0.0022	0.0000	0.0022	0.0004	-0.0002	0.0035
	XJ-100-dry	103	-0.0091	-0.0048	-0.0017	-0.0074	-0.0054	-0.0022
	XJ-150-dry	150	-0.0104	-0.0061	-0.0052	-0.0065	-0.0046	-0.0061
	XJ-RT-wet	18.3	-0.0013	-0.0007	0.0004	0.0017	0.0011	0.0022
	XJ-50-wet	52.0	0.0022	0.0037	0.0013	0.0061	0.0091	0.0048
	XJ-100-wet	102	-0.0087	0.0002	0.0061	-0.0100	-0.0013	0.0056
	XJ-150-wet	149	-0.0009	-0.0009	-0.0013	-0.0061	-0.0017	0.0000
Simulated pure $CaCO_3$ gouge	$CaCO_3$-RT-dry	17.9	0.0026	0.0037	0.0083	0.0052	0.0033	0.0096
	$CaCO_3$-50-dry	49.9	0.0009	-0.0009	0.0013	0.0017	-0.0002	0.0022
	$CaCO_3$-100-dry	101	-0.0052	-0.0017	0.0004	-0.0009	-0.0026	0.0009
	$CaCO_3$-150-dry	150	-0.0065	-0.0026	-0.0013	-0.0039	-0.0039	-0.0017
	$CaCO_3$-RT-wet	18.6	0.0013	0.0009	0.0035	0.0056	0.0059	0.0056
	$CaCO_3$-50-wet	50.6	0.0074	0.0056	0.0069	0.0087	0.0093	0.0117
	$CaCO_3$-100-wet	99.6	0.0039	0.0063	0.0083	0.0026	0.0063	0.0083
	$CaCO_3$-150-wet	149	-0.0013	0.0015	0.0078	-0.0161	-0.0037	0.0078

Table 3.2. Rate sensitivity parameter Γ determined for each velocity step (1 to 6), with the reference sliding velocities as indicated in μm/s. The error to each value of Γ is ~±0.0017

3.4. Microstructures

3.4.1. Inspection of samples upon retrieval

When separating the 69 piston blocks to expose the sheared gouge within, all samples split along a shear-induced fabric developed near the sample-piston interfaces, as well as obliquely to this fabric. Split surfaces developed parallel to the shear plane displayed shiny, elongate patches, measuring ~0.1-0.5 mm wide and up to 3 mm long, aligned with their long axis parallel to the shear direction (Fig. 3.8a). Incident light microscopy revealed these shiny patches to be striated at the sub-μm scale, but topographically flat at the μm-mm scales (Fig. 3.8b). While the shiny surfaces were mainly exposed on planes that split parallel to the shear plane, they were also observed on obliquely split planes. In the former case, they are located directly beneath the imprint of the piston groove pattern (Figs. 3.8a, c). The total number and dimensions of individual shiny surfaces exposed varied from experiment to experiment. However, this variability strongly depended on the splitting fabric produced upon sample recovery and was therefore not investigated further in this study.

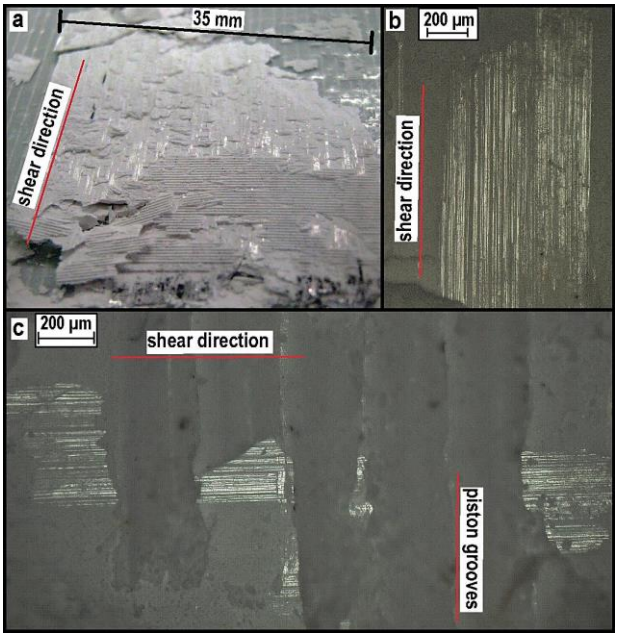

Figure 3.8. a). Patchy shiny surfaces marking the shear plane in sample CaCO3-50-dry. b and c) Incident light micrographs of shiny patches found in sample CaCO3-RT-dry.

3.4.2. Optical analysis of thin sections

From thin sections prepared parallel to the shear direction and normal to the shear plane, transmitted light optical analysis revealed that all sheared gouge microstructures developed horizontal and inclined shear bands, comprising mainly boundary and R_1 shears and, much less common, P-, Y- and R_2-shears (terminology following Logan et al., 1979; see also Appendix 3.A). In all samples, shear bands are seen as sharply-defined zones of strongly reduced grain size cutting the gouge matrix (Figs. 3.9a, b). The maximum grain size in the matrix is similar to the median grain size of the starting material (~15-20 µm – cf. Fig. 3.1). Deformation twins are common in the larger matrix grains. Close to a shear band the grain size abruptly decreases, and the larger grains are often seen truncated, and sometimes bent, in a sense consistent with the imposed shear direction (Figs. 3.9c, d). Fractured grains seen close or within a shear band are often clustered, reflecting the shape of the parent grain. The mean shear band width is ~30-40 µm, but varies from ~10 to ~150 µm. Boundary shears developed in all samples, and are continuous and straight, located immediately adjacent to the grooved surface of at least one of the sample-piston interfaces (Figs. 3.9a, b, and Appendices 3.A and 3.B). The

wider parts of a boundary shear have an internal structure characterized by an anastamosing pattern of shears parallel and at an angle to the shear plane (Fig. 3.9a). Some of these segments are seen to emanate from the piston groove apices at an angle ~10-20° to the shear plane, to connect with the anastamosing structure underneath. Inclined shear bands (R_1-, R_2-, P-shears) consist of bands of comminuted grains cross-cutting the gouge matrix. They are often seen to interfere with each other, and with horizontal shears, to form branching patterns (Figs. 3.A1, 3.A2). The angle between R_1-shears and the shear plane is usually largest (~18-24°) in the centre of the gouge, gradually decreasing to zero nearing the sample-piston interface where they merge with the boundary shear.

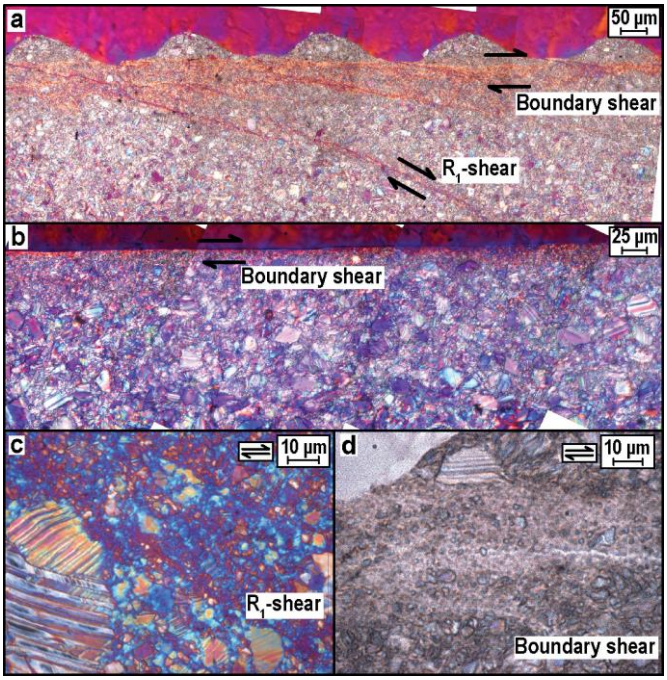

Figure 3.9. Transmitted light micrographs of thin sections prepared from recovered sheared gouges. Micrographs a-c were taken using cross polarized light with the gypsum plate inserted, while d was taken using plane polarized light only. a) Sample $CaCO_3$-RT-dry. b) Sample $CaCO_3$-150-wet. c) Sample XJ-150-dry. d) Sample $CaCO_3$-100-dry. Complete photomosaics of micrographs of sheared simulated $CaCO_3$ gouge, from dry and wet experiments performed at $T \approx 18$°C, 100°C, and 150°C, are shown in Appendices 3.A1 and 3.A2. A list of all experiments is given in Table 3.1.

The only systematic difference between dry and wet sheared gouges was found in the number of (#) of R_1-shears normalized to the length of the recovered gouge sample (l).

For the dry experiments using simulated $CaCO_3$ gouge, the ratio $\#R_1/l$ measured ~0.6 mm^{-1} for all temperatures tested, while for the wet experiments $\#R1/l \approx 0.8$ mm^{-1} at $T \approx$ 18°C and 100°C, but 0.1 mm^{-1} at 150°C (Figs. 3.A1, 3.A2). However, the value of $\#R1/l$ may depend strongly on sample recovery, and on the location in the sheared gouge of the cross-section chosen for thin section preparation.

For all sheared gouge microstructures, for both inclined and boundary shears, we observed that grains in the shear band core cannot be distinguished with an optical light microscope, hence are <1 μm in size. When using crossed nicols these aggregates of grains show near-uniform optical interference, i.e. blue or orange when using the gypsum plate (Figs. 3.9a-c, 3.10a, b and Appendices 3.A and 3.B). Rotation of the microscope stage over 45° causes the interference colour to change near-uniformly, i.e. from blue to orange or vice-versa, over the entire width of the shear band core. This suggests a distinct crystallographic preferred orientation (CPO) of the sub-micron grains present here.

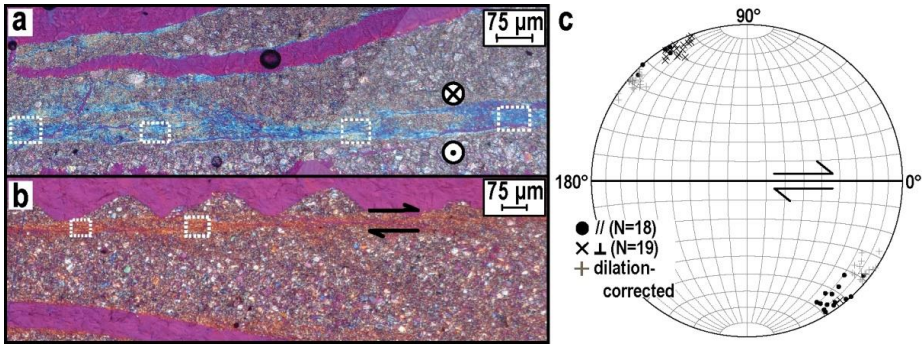

Figure 3.10. Optic axis data from shear band segments collected with U-stage. a). Sample $CaCO_3$-150-dry, normal to the shear plane and normal to the shear direction. b). Sample $CaCO_3$-150-dry, normal to the shear plane and parallel to the shear direction. Dashed boxes in a) and b) show examples of shear band segments used for measuring the average optic axis. c). Average optic axes from a) and b) plotted in a lower hemisphere Schmidt net projection, with the shear plane and shear direction oriented E-W. Also plotted are the optic axis data corrected for post-test sample dilation.

To investigate this in more detail, we used a U-stage to determine the average orientation of the optical indicatrix of well-exposed segments of boundary shears found in sample $CaCO_3$-150-dry. From roughly square-shaped shear band segments with sides measuring ~50-100 μm in length (Figs. 3.10a, b) we determined the angles at which >90-100% of the grains present here went into optical extinction. In this way we measured the average optic axis of shear band segments, hence average calcite c-axes orientations

(calcite is uniaxial optically negative). We performed this analysis on sample $CaCO_3$-150-dry, on thin sections prepared in a direction normal to the shear plane, and normal (Fig. 3.10a) and parallel (Fig. 3.10b) to the shear direction, i.e. from mutually perpendicular sections of boundary shears developed in the same sample. All optic axis data were plotted in a lower hemisphere equal-area (Schmidt) stereographic projection, and then rotated to a common orientation using the shear plane and shear direction as reference (Fig. 3.10c). The results revealed a strong clustering of all optic axes hence c-axes, at 120-130° to the shear direction, i.e. at 30-40° to the shear plane normal.

3.4.3. FIB-SEM and TEM analysis

To determine the internal sub-micron structure of the shear bands, we used FIB-SEM to mill cross-sections of boundary shear bands formed in experiments $CaCO_3$-RT-dry (Fig. 3.11a) and $CaCO_3$-150-dry (Fig. 3.11b). In this way we obtained boundary shear cross-sections in an orientation normal to the shear plane and the shear direction, for both velocity strengthening and velocity weakening samples (see also Appendix 3.B). Regardless of testing conditions, the shear band cross-sections showed a localized structure with grains decreasing in size from ~10-20 μm at the outer margins to <1 μm in the shear band core (Figs. 3.11a, b). Coarser grains (0.3-20 μm in size) at the margins, and those present in the shear band core, having survived grain size reduction, are angular, whereas the finer particles (<300 nm) in the shear band core are rounded, and clustered in dense aggregates. From sample $CaCO_3$-150-dry we also prepared cross-sections of boundary shear bands parallel to the shear direction and normal to the shear plane (Fig. 3.11c). This revealed an alignment of porosity and a Shape Preferred Orientation (SPO) of elongate particles ~0.3-2 μm in length, oriented at 140-150° to the shear direction (Fig. 3.11c). Based on all boundary shear cross-sections investigated, the width of the shear band core, i.e. the zone containing dense, sub-micron-sized particle aggregates, is estimated to range from 1-10 μm.

All samples involved dilation of the shear bands resulting from sample depressurization and handling, e.g. seen as the resin-filled crack splitting the boundary shear band core (Fig. 3.11). To determine the orientations of the observed CPO and SPO in the shear bands with respect to the shear plane during deformation, this must be corrected for. Using the linear intercept method and Figure 3.11c, the strain perpendicular to the shear zone resulting from post-shear dilation was estimated to be ~23%. Taking zero pre-dilation porosity, and using the above value for strain, a

(maximum) estimate of the orientation of the shear band c-axes and SPO yields 130-135° (Fig. 3.11c) and 150-155° respectively.

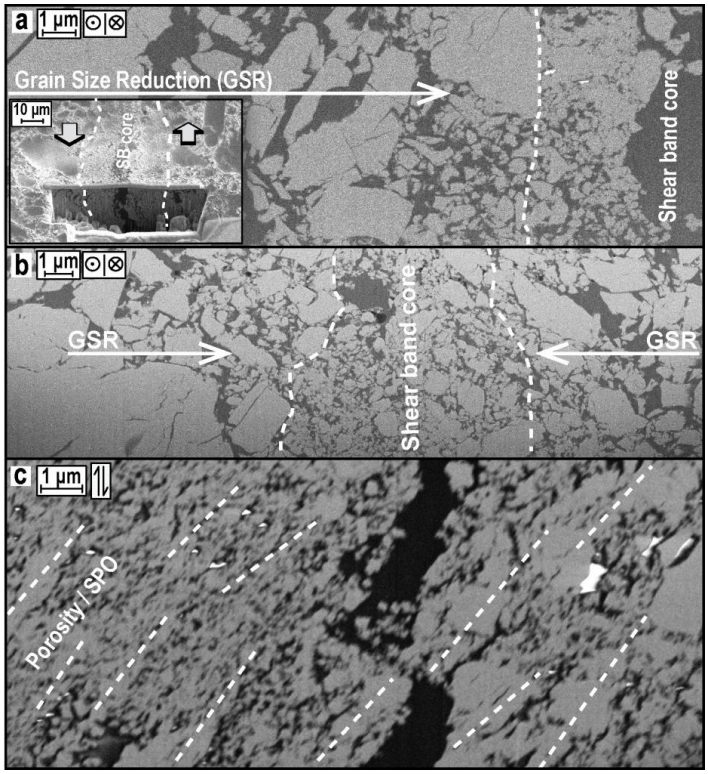

Figure 3.11. BSE micrographs of cross-sections of boundary shear bands prepared using FIB-SEM. Black regions are resin-filled porosity, mainly due to post-test dilation. a) Sample $CaCO_3$-RT-dry, normal to the shear direction. Inset shows the FIB-cut on a smaller scale. b) Sample $CaCO_3$-150-dry, normal to the shear direction. Dashed lines in a) and b) highlight the shear band core. c). Sample $CaCO_3$-150-dry, parallel to the shear direction, showing an alignment of porosity/ a shape preferred orientation (SPO). See also Appendix 3.B for an overview of sample selection and the FIB-SEM procedure.

To further investigate the shear band core nanostructure and crystallography, we used FIB-SEM to prepare electron-transparent foils from boundary shear band cross-sections for study using TEM. The sections were selected on the basis of observations made using the light microscope, i.e. TEM foils were prepared from samples showing a strong preferred optical birefringence (see Appendix 3.B). Bright-field and High Resolution TEM imaging showed that dense particle aggregates seen in the shear band cores of samples $CaCO_3$-RT-dry and $CaCO_3$-150-dry (Fig. 3.11) comprise nanocrystalline

calcite grains ~5-20 nm in size (Figs. 3.12a-c). Selected-area electron diffraction patterns taken from the nanocrystallite aggregates showed ring-shaped diffraction patterns, with distinct arcs developed on the (104) reciprocal plane (hexagonal structural cell; Fig. 3.12d-inset), suggesting a polycrystalline aggregate with a CPO. Using any of the higher-intensity arcs to form a dark-field image, i.e. satisfying the individual Bragg condition, resulted in a preferred illumination of grains in the shear band core (Figs. 3.12d, e). This suggests a preferred alignment of the (104) calcite (r-)planes parallel to the shear plane.

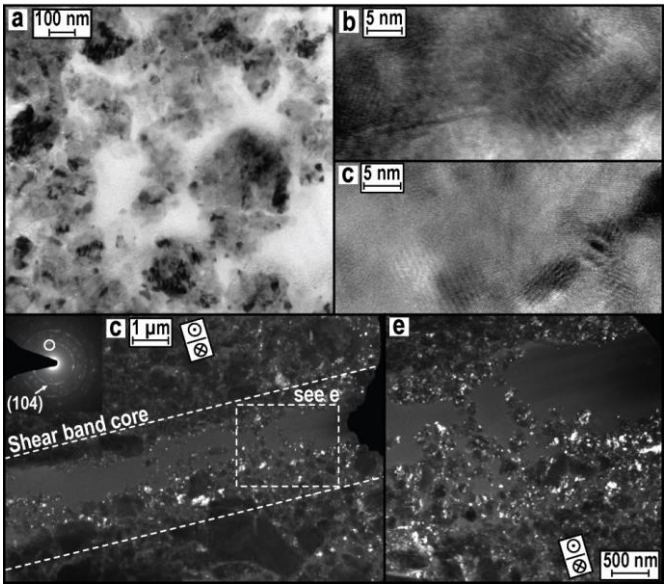

Figure 3.12. TEM images of electron transparent foils prepared using FIB-SEM from boundary shears in an orientation normal to the shear plane and shear direction. a) Bright-field image of sub-micron particle aggregates found in the shear band core of sample $CaCO_3$-150-dry. b and c) HRTEM images from rounded sub-micron particle aggregates in the shear band cores of samples $CaCO_3$-RT-dry (b) and $CaCO_3$-150-dry (c). d) Dark-field image of the shear band core of sample $CaCO_3$-150-dry, generated using a tilt angle corresponding with the (104) plane of calcite. Inset shows a ring-shaped selected area diffraction pattern taken from a nanocrystallite aggregate. e) Magnification of part of d). The apparent preferred illumination of nanograins in this image is enhanced due to better resolution at higher magnification.

3.5. Discussion

The frictional strength and velocity dependence data obtained in this study showed important differences between experiments at different temperatures, but also between dry and wet experiments, and between experiments using simulated XJ limestone gouge and those using simulated pure $CaCO_3$ gouge (Figs. 3.5-3.7). Although the different

testing materials showed contrasts in frictional behaviour, wet and dry, all sheared gouge microstructures showed essentially the same shear-induced features, i.e. localization into boundary and inclined shear bands, characterized by cataclasis and grain size reduction, plus a CPO (Figs. 3.8-3.10, 3.A1, 3.A2). In both velocity strengthening and weakening samples, cross-sections of boundary shear bands images and prepared using FIB-SEM showed a localized internal structure with grains decreasing from 10-20 μm in size in the outer margins to dense nanoparticle aggregates in the shear band core (Fig. 3.11). TEM showed that these aggregates consist of nanocrystallites down to ~5-20 nm in size (Fig. 3.12). In the following, we focus on the mechanisms controlling the frictional strength and velocity dependence in simulated calcite fault gouges, and discuss on the possible origin of the contrasts in the frictional behaviours observed, especially with regard to the role of water. We also discuss the implications of our results in the context of natural faulting in tectonically-active carbonate terrains.

3.5.1. Microphysical mechanisms operating in dry and wet samples

From the extreme grain size reduction seen in all sheared gouge microstructures, and the fractured grains and angular shapes of larger grains surviving in and at the margins of shear bands (Figs. 3.9-3.11), we infer that cataclasis must have played a role in all our experiments. However, the finer grains within the shear band cores are rounded rather than angular, and cataclastic flow alone is not expected to produce the c-axis preferred orientation observed here (Figs. 3.10-3.12). Rather, our observations of the preferred alignment of calcite r-planes in the shear band core parallel to the shear plane (Fig. 3.12) suggests a role of r-glide crystal plasticity in the shear bands. Together with e-twinning, glide on r is the dominant crystal plastic (dislocation) deformation mechanism in calcite at low temperatures (De Bresser and Spiers, 1997). We investigated the role of r-glide and e-twinning in our experiments by postulating that the e- or r-planes lie parallel to the shear plane, and using a stereographic projection to compare the predicted angles to the c-axis with our measured bulk c-axis preferred orientation (Fig. 3.13). From the known crystal structure of calcite (e.g. De Bresser and Spiers, 1993, 1997), the conic section (small circle) that describes the possible orientations of a hypothetically projected calcite c-axes predicts an angle of 116° and 135° between the e- (108) or r- (104) planes and the shear direction, respectively (Fig. 3.13). The dilation-corrected c-axes orientation in the shear bands measured ~130-135° to the shear direction, i.e. consistent with that of a projected c-axis orientation when the r-plane lies parallel to the shear plane (Fig. 3.13).

Together with our dark-field micrographs from TEM (Figs. 3.12d,e), this convincingly shows that the r-glide system is aligned (sub-)parallel to the shear plane and direction, suggesting that r-glide crystal plasticity has played a role in the shear band system. Because we found a CPO in all our samples, that is, because all samples showed essentially the same sheared-induced micro- and nanostructures, we infer that r-glide plasticity played a role in all our experiments, wet and dry, including those sheared at room temperature.

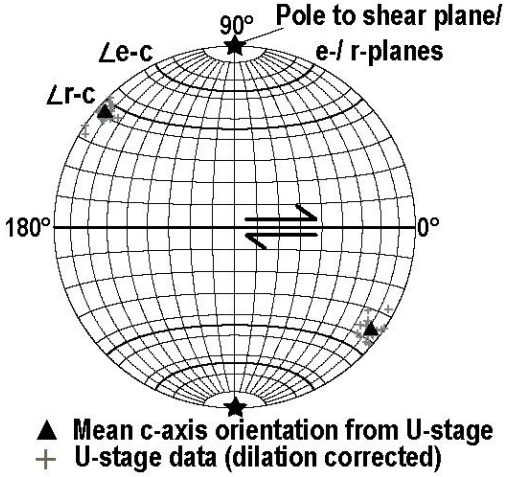

Figure 3.13. Lower hemisphere Schmidt net projection representing the shear plane and shear direction E-W. Assuming the e- or r-plane lies parallel to the shear plane, the conic sections (small circles) plot the possible angles (∠) of (the pole of) the shear plane to the calcite c-axis. Also plotted are the optic axis data (c-axes) from our samples (Fig. 3.9), corrected for post-test dilation assuming zero shear band porosity.

Although r-glide may account for the CPO in the shear band core, and accommodated at least part of the strain here, it does not explain the alignment of nanopores and the SPO defined by angular grains (>0.3-2 μm) as seen in FIB sections cut normal to the shear plane and parallel to the shear direction (Fig. 3.11c). The dilation-corrected angle of ~150-155° observed between the SPO/ nanopore alignment and the shear direction is roughly consistent with an R_1- or T-shear band configuration within the boundary shear (Logan et al., 1979). However, we cannot discriminate whether the nanopore alignment reflects slip on R_1 shears that dilated after sample extraction, or else elongate dilatational cavities formed at grain boundaries lying roughly parallel to the incremental shortening direction, implying some type of grain boundary sliding of the nanoparticles within the

shear bands (cf. Ma, 2004; Shan et al., 2004).

Returning to the origin of the CPO, which would seem inconsistent with the operation of significant grain boundary sliding, we note that the strain rates characterizing the shear bands in our experiments (10^{-2}-10^{1} s^{-1}) are similar to those needed for plasticity-induced formation of cellular equiaxed nanograins in experiments on metals (10^{0}-10^{3} s^{-1}) at room temperature (Umemoto, 2003; Li et al., 2008; Yang et al., 2010). This supports crystal plasticity as the most likely explanation for the formation of both the nanograins and their CPO. However, we cannot exclude the possibility that, after nanograin formation, some kind of orientation-dependent, diffusive sintering or grain growth process is responsible for the CPO seen in the nanocrystalline shear bands. Such a process could lead to a CPO, even during grain boundary sliding dominated flow (Power and Tullis, 1989; Zhang et al., 2010a). In the case of our dry experiments, reasonable measures were taken to avoid contamination by water prior to shear, but in view of the much lower (~20%) surface energy of hydrous versus anhydrous nanocrystalline calcite (Forbes et al., 2011), nanograins in the shear bands may have adsorbed atmospheric water during our experiments. The presence of such a thin water film (≤ 1 nm) can facilitate surface-diffusion processes (Rutter, 1983; Zhang et al., 2010b; Koelemeijer et al., 2012). Clearly, the microphysical processes controlling strain accommodation in the shear band system is as yet incompletely understood, and more research is needed to elucidate the underlying mechanisms of nanograin formation and deformation, and their role in controlling frictional strength and slip stability.

3.5.2. Mechanisms controlling the velocity dependence of strength

Both materials investigated showed a transition from velocity strengthening to velocity weakening slip with increasing temperature, regardless whether or not (pressurized) pore fluid water was present. Because crystal plasticity is strongly thermally-activated, we infer that this process is responsible for the observed decrease of Γ with increasing temperature (Fig. 3.7). Taking an (empirical) exponential creep law used to describe dislocation glide-controlled flow of calcite at 20-500°C at laboratory strain rates, the plastic strain rate ($\dot{\varepsilon}$) depends on absolute temperature (T) at fixed stress (σ) via the relation (Rutter, 1974; Schmid et al., 1980; De Bresser et al., 2002)

$$\dot{\varepsilon}(T) \propto \exp\left(-\frac{Q}{RT}\right) \cdot \exp\left(\frac{\sigma}{\sigma_0}\right) \qquad (3.3)$$

In this relation, Q is the activation energy for flow, R is the gas constant, and σ_o is the flow stress at 0 K. To evaluate the acceleration in glide-controlled creep between our experiments at room temperature and 150°C, we calculated the ratio of the strain rate at a given temperature T relative to that at 18°C (291 K), i.e.

$$\frac{\dot{\varepsilon}(T)}{\dot{\varepsilon}(291)} = \exp\left[\frac{Q}{R}\left(\frac{1}{291} - \frac{1}{T}\right)\right] \qquad (3.4)$$

Equation (3.4) is plotted against temperature in Figure 3.14, using activation energies reported for exponential-type crystal plastic flow in Solnhofen Limestone (197 kJ/mol) and Carrara Marble (260 kJ/mol) at 400-500°C (Rutter, 1974; De Bresser et al., 2002). These graphs demonstrate that at $T \approx 80$°C, i.e. nearing the transition to velocity weakening slip seen in our dry experiments, dislocation plasticity in calcite is $10^6 - 10^8$ times faster than at 18°C, while at 150°C it is 10^{11}-10^{15} times faster.

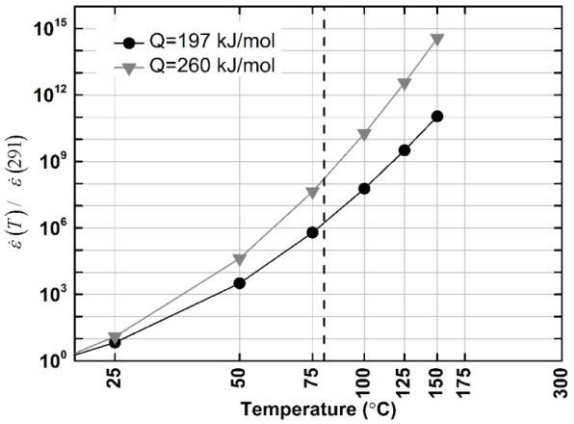

Figure 3.14. Plot of $\dot{\varepsilon}(T)/\dot{\varepsilon}(291)$ against temperature, using activation energies (Q) characteristic for exponential-type crystal plastic flow in Solnhofen limestone (197 kJ/mol) and Carrara Marble (260 kJ/mol) (Rutter, 1974; De Bresser et al., 2002).

However, plasticity alone cannot explain velocity weakening slip or a transition thereto, since pure crystal plastic flow is intrinsically velocity strengthening ($\partial\sigma/\partial\dot{\varepsilon} > 0$ in equation 3.3). Our interpretation is that both cataclastic/granular flow and dislocation glide-controlled crystal plasticity have been operative at all temperatures in our experiments, but that their relative contribution to strain-accommodation in the shear

band system varies with temperature, and, presumably, in the presence of water. Because of the acceleration of crystal plastic creep with increasing temperature (Fig. 3.13), time-dependent decrease in porosity and increase in grain contact area becomes increasingly important towards higher temperatures. At lower sliding velocities, pores then have more time to compact and grain contacts have more time to spread and possibly "bond" by plastic creep, ultimately imparting higher strength at lower sliding velocities, i.e. producing velocity weakening. In this framework, we propose that it is competition between time-dependent (e.g. crystal plasticity) versus relatively time-insensitive (e.g. granular flow) strain accommodation mechanisms that controls the sign of the velocity dependence. When velocities are high enough to maintain some porosity, and temperatures are sufficiently high, then creep processes allowing compaction and contact area increase are possible, and velocity weakening behaviour will be observed. Such a conceptual model is similar to the classical asperity model for friction of Bowden and Tabor (1950) and to that based on competition between compaction creep and dilatational granular flow of gouge as proposed by Niemeijer and Spiers (2007). When temperatures are lower, creep processes will ultimately be too slow to allow significant porosity reduction and contact area increase, and critical-state granular/cataclastic flow will dominate, with friction being controlled by processes operating within grain contacts (cf. Niemeijer and Spiers, 2007), i.e. much finer scale asperity processes. These in turn are likely to involve micro/nano-plasticity (Bhushan, 2005), as opposed to grain-contact-scale plastic creep, and will therefore be velocity strengthening, producing macroscopic velocity strengthening.

3.5.3. The role of water and impurities

All wet experiments using simulated pure $CaCO_3$ gouge showed a well-defined peak strength after apparent yield, i.e. slip hardening and subsequent slip weakening (Fig. 3.5). In contrast, the dry experiments using this material showed a near-constant frictional strength in the post-yield region (Fig. 3.5). For experiments using simulated XJ limestone gouge we observed the same difference in frictional behaviour between the dry and wet tests, except at room temperature. The magnitude of slip weakening, i.e. the value of $\Delta\mu = \mu_{pk} - \mu_{fnl}$, increased with increasing temperature for both materials tested (Fig. 3.6). In addition, the differences between the simulated XJ limestone and pure $CaCO_3$ gouge were only substantial in the presence of (pressurized) pore water, i.e. revealed in the frictional strength evolution with displacement seen at room temperature,

but also in the sign of Γ with increasing temperature (Figs. 3.5 to 3.7). In view of the similarity between the shear-induced microstructures of the simulated XJ limestone and pure $CaCO_3$ gouges, the contrast observed in the frictional behaviour with displacement in the wet experiments are likely to be due to the compositional differences between the sample materials. In the following we discuss which processes are likely to be active in the wet experiments and not in the dry, and qualitatively assess their effect on the frictional behaviours observed.

The frictional strength evolution with displacement seen in most of our wet experiments have the same broad peak as seen in shear experiments on over-consolidated soils (e.g. Yong et al., 2012). Gouge compaction during equilibration of the testing apparatus prior to each test may have produced over-consolidated samples such that the gouge must dilate, hence do work against the normal stress, to reach the critical state porosity that is associated with steady-state frictional sliding (Morrow and Byerlee, 1989). Indeed, compaction of granular calcite is accelerated in the presence of water, mainly due to fluid-enhanced deformation mechanisms such as sub-critical cracking (e.g. Rice, 1978; Atkinson, 1984) and/or pressure solution (e.g. Rutter, 1983; Spiers et al., 2004). Moreover, the total pre-test compaction times in our tests have been longer for experiments performed at higher temperatures, hence this may explain the increase of μ_{pk} seen with increasing temperature (Fig. 3.6), in particular for the wet experiments. However, if the presence of water only promotes consolidation of the gouge prior to shear, than the near-steady-state strengths (at $x > 4$ mm) of the dry experiments are expected to be the same as those of the wet experiments (cf. Morrow and Byerlee, 1989; Yong et al., 2012). Clearly this is not the case for both materials investigated here (Figs. 3.5, 3.6, Table 3.1). Therefore, pre-test over-consolidation of the gouge may have produced the broad shape of the strength-displacement curves in the wet experiments (Fig. 3.5), but other, water-assisted dynamic chemical and/or mechanical weakening effects must have played a role as well.

In the presence of water, the calcite fracture surface energy is 2 to 3 times lower compared with that of a dry calcite fracture surface (Røyne et al., 2011). This means that the energy needed for grain failure is much higher in dry experiments compared with that needed in wet experiments (Rice, 1978; Atkinson, 1984). The microstructural evidence for cataclasis and grain size reduction seen in the gouge microstructures indeed suggests that grain fracturing played an important role in all our experiments, wet and dry. Thus, reduced fracture surface energy may explain the lower strengths of wet

samples compared with dry samples. However, Logan et al. (1992) showed that for (calcite) gouge shear deformation the post-yield region of the curve describing frictional strength with displacement corresponds to initial shear band formation in the sample microstructure (see also Gu and Wong, 1994 and Marone, 1998a). At higher displacements the comminution rate decreases substantially (Marone and Scholz, 1989). Therefore, a decrease in the calcite fracture surface energy may explain the lower peak strengths of the wet gouges compared with the dry, but not the major differences seen between the near-steady-state strengths (μ_{fnl}; Fig. 3.6).

On the other hand, intergranular pressure solution likely became more important in the shear band system at higher displacements, i.e. once it had fully developed, especially in view of the very fine grains present here. Assuming diffusion-controlled pressure solution for calcite (Zhang et al., 2010b), the rate of pressure solution creep $(\dot{\varepsilon}_{ps})$ is proportional to the inverse of the grain size (d) cubed, i.e. $\dot{\varepsilon}_{ps} \propto 1/d^3$. A high intergranular pressure solution creep rate will lead to porosity reduction hence increasing grain contact area (Bos et al., 2000a; Bos and Spiers, 2002a; Niemeijer and Spiers, 2006) as well as cohesion through cementation (e.g. Zhang et al., 2010b; Gratier et al., 2013). Recent experimental work showed that pressure solution creep rates in calcite decrease with increasing temperature, probably because the solubility of calcite decreases with increasing temperature (Liteanu et al., 2012). This is consistent with our data, which show that the near-steady state strength of wet gouges decreases with increasing temperature (Fig. 3.6), i.e. suggesting that porosity reduction and growth of asperity contact-areas due to compaction by pressure solution will be less effective at higher temperatures, resulting in lower frictional strength. Note that this effect would be enhanced if the pore fluid was more under-saturated with calcite at room temperature than at 150°C, as the driving force for compaction by pressure solution would be increased. However, if pressure solution is the only water-assisted mechanism active, the increased gouge cohesion in wet experiments should lead to a higher steady-state frictional strength (μ_{fnl}) than in dry tests, which is the opposite of that seen here (Fig. 3.6, Table 3.1). Thus, albeit likely that pressure solution played a substantial role in the shear bands in the presence of water, some other water-assisted process must have played a role as well, i.e. in addition to subcritical cracking.

A third mechanism that may have been operative is intergranular lubrication due to water-adsorption to (nano-)grains. In view of the very large surface area of grains in the shear bands this may have been very effective in decreasing intergranular friction and/or

adhesion. Water-adsorption is mainly controlled by the grain surface electrokinetic potential, which, in the case of calcite, is complexly dependent on the presence of impurities (Cicerone et al., 1992) and on pressure and temperature (Rodríguez and Araujo, 2006), and is generally non-neutral (Stipp, 1999). In this study we observed that the compositional difference between the simulated XJ limestone and pure $CaCO_3$ gouge is only relevant in the wet experiments (Figs. 3.5 to 3.7, Tables 3.1, 3.2), suggesting that the type or presence of impurities only influences the frictional behaviour of our gouges in the presence of (pressurized) pore water. At the same time, it is well established that the presence of clay or quartz (XJ limestone gouge) compared with Mg impurities ($CaCO_3$ gouge) may have profound effects on the electrokinetic potential of the calcite-water interface (Cicerone et al., 1992; Dunning et al., 1994). Therefore, we suggest that water-adsorption also facilitated an intergranular (grain-boundary) lubrication mechanism in our wet experiments, which effectively lowered the steady-state frictional strength (μ_{fnl}) of wet gouges compared with dry gouges. Moreover, in view of the lower near-steady-state strengths (μ_{fnl}) of the wet gouges compared with dry (Table 3.1, Fig. 3.6), weakening due to intergranular lubrication must substantially outweigh that of strengthening due to compaction (hence porosity decrease and grain contact increase) by pressure solution.

Regarding the effect of (pressurized) pore water on the velocity dependence of strength, the values of Γ from the wet experiments showed more complex trends with increasing temperature than those of the dry experiments (Fig. 3.7). For both materials tested wet, the values of Γ first increased with increasing temperature (i.e. from 18°C to 50°C), followed by a decrease toward higher temperatures. Velocity weakening first occurred at the lowest sliding velocities imposed, at T = 100°C for the simulated XJ limestone gouge but not until T = 150°C for the simulated $CaCO_3$ gouge. In the preceding discussion, we inferred that both pressure solution and intergranular lubrication by grain-surface water-adsorption must have played a role in controlling the steady-state frictional strength of our wet gouges. These micromechanisms likely also affect the velocity dependence of strength. For wet samples, in the case of an upward step in sliding velocity in the velocity weakening regime, dilatation will result in net weakening of the gouge at steady state. However, compared with dry gouges, the net dilation and hence net strength decrease at steady state will be less, because net compaction rates are faster due to pressure solution. Also, in the wet experiments, the effect of changing porosity hence contact area on strength will be less compared with dry samples, due to intergranular

lubrication by water. Therefore, in the velocity weakening regime of our wet gouges, the value of Γ should be less negative compared with dry samples. At the same time, for both dry and wet samples, velocity strengthening can only be explained if grain boundary friction is velocity strengthening, as discussed above (as in the case of phyllosillicates - Ikari et al., 2011; Den Hartog and Spiers, 2013), and if this effect outweighs any velocity weakening tendency due to competition between dilation and compaction. In the limiting case of high velocity and low temperature, compaction creep effects of any kind will be negligible, so that critical state granular flow will occur, in which case the strength and the value of Γ are entirely controlled by grain boundary friction (i.e. nanoscale processes acting within grain contacts). In the wet gouges, in the velocity strengthening regime, intergranular lubrication by water would imply that grain boundary friction will be less velocity strengthening than in dry samples, hence yielding lower values of Γ, compared with dry gouges. We cannot rule out other explanations for the trends in Γ seen in our wet versus dry experiments, but this interpretation is consistent with all of our results, i.e. with the trends in both frictional strength and Γ seen with increasing temperature, for both dry and wet experiments. The detailed microphysical processes controlling frictional sliding in wet calcite gouges, especially in the case of transients in the frictional strength, remains a subject for further research.

3.5.4. Geological implications

Our results have important implications for understanding faulting and seismicity in tectonically-active carbonate terrains, such as those commonly found in rifts and the external zones of orogenic belts. Examples of recent destructive earthquakes in such terrains include the 1995 Aigion event (M_w 6.2) in the Corinth Rift Zone of Greece, and the 2009 L'Aquila (M_w 6.3) and 2012 Emilia-Romagna earthquakes (M_w 6.0-6.1) in the Apennines of Italy. Assuming a typical geotherm of ~20-25°C/km, faults cutting calcite-rich rocks can be expected to show the onset of velocity weakening and hence possible seismogenesis at depths of ~4-8 km. This, coupled with the high frictional strength measured ($\mu \approx 0.7–0.8$), suggests that tectonically-active limestone terrains may be particularly prone to shallow-focus seismicity characterized by large stress drops, compared to e.g. clay-rich upper crustal faults which show much lower strength ($\mu \approx 0.3$) and velocity strengthening behaviour up to 250°C (Den Hartog et al., 2012; see also Verberne et al., 2010, or Chapter II). Indeed, earthquakes that have occurred in the Apennines or the Corinth Rift Zone are commonly associated with shallow focus (≤10 km)

hypocentral depths of the main shock and aftershock sequences (Bernard et al., 2006; Mirabella et al., 2008; Valoroso et al., 2013).

In addition, we note that the shiny surfaces seen in our experiments are similar to the smooth, strongly reflecting slip surfaces recently reported from high-velocity friction experiments on carbonate rocks and gouges (Tisato et al., 2012; Smith et al., 2013; Fondriest et al., 2013), and from natural samples taken from the slip zone of faults cutting limestones (so called 'fault mirrors' - Siman-Tov et al., 2013). Our micro- and nanostructural analyses are consistent with these authors' conclusions that these surfaces comprise nano-coatings marking a principal slip zone. However, we emphasize that our results demonstrate that these nano-coated surfaces are not necessarily diagnostic for co-seismic slip, and that natural calcite gouge microstructures showing such features must be interpreted with caution.

3.6. Conclusions

We have obtained data on frictional strength and velocity dependence parameters for simulated fault gouges prepared from natural Xujiahe (XJ) limestone (96% $CaCO_3$) and pure $CaCO_3$ single crystals. Dry and wet, direct-shear, friction experiments were conducted on both materials at an effective normal stress of 50 MPa, at temperatures in the range 18° to 150°C, at sliding velocities of 0.1 to 10 μm/s. Final shear displacements of 4-5 mm were imposed in each experiment. The mechanical observations were coupled with microstructural analysis, at the mm- to the nm-scales, using optical and electron microscopy methods. Our main conclusions are summarized below:

1. The gouges studied exhibited peak frictional strengths of $\mu_{pk} \approx 0.7$-0.8. Dry samples, and wet XJ limestone samples sheared at room temperature, subsequently showed minor slip weakening, reaching steady-state frictional strengths (μ_{fnl}), measured at the end of each experiment at v = 1 μm/s, that differed from the peak strength by < 0.05. In contrast, most wet experiments showed a marked post-peak displacement-weakening, resulting in a steady-state frictional strength (μ_{fnl}), measured at maximum displacement, of around 0.6. This strength drop was generally more pronounced in the pure calcite samples (17-27% compared to dry samples) than in those derived from XJ limestone (0-22%). At the same time, the different composition of the samples had no significant effect on frictional strength in the dry state.

2. The velocity dependence of strength of our samples, quantified using the rate sensitivity parameter Γ, decreased nearly linearly with increasing temperature for the dry gouges, with a transition to negative values (i.e. velocity weakening slip) occurring at around 70-80°C. For the wet samples, Γ-values showed a similar overall trend but with more scatter, and with velocity weakening first occurring at ~100°C for the simulated XJ limestone and at ~150°C for the simulated pure $CaCO_3$ gouge. This implies that the presence of (pressurized) pore water is not crucial for promoting or inhibiting velocity weakening in calcite(-rich) gouges with increasing temperature. In other words, the presence of water has relatively little effect on velocity dependence, but influences friction coefficient significantly.
3. All recovered gouge samples revealed a microstructure characterized by boundary and inclined shear bands (cf. Logan et al., 1979). These shears showed extreme internal grain size reduction to ~5-20 nm and the development of a crystallographic preferred orientation (CPO). The latter involved alignment of the $(104)[\bar{2}01]$ or r-slip system of the calcite nanocrystallites (sub-) parallel to the shear direction. On this basis, we suggest that crystal plasticity involving r-glide played a key role in shear band development, alongside cataclasis (i.e. cataclastic/granular flow). We found no microstructural indicators specific to samples showing (stable) velocity strengthening versus (potentially unstable) velocity weakening slip, or specific to dry versus wet samples.
4. In the wet experiments, the slip weakening observed relative to dry samples suggests that water-assisted chemical and mechanical processes must have played a role, in addition to cataclastic/granular flow and crystal plasticity. These processes likely involved pressure solution, fluid-assisted sub-critical cracking, and intergranular lubrication due to water adsorption on grain surfaces.
5. All recovered sheared gouge samples showed patchy, mirror-like surfaces exposed in the boundary shear planes, with (sub-) micron-scale striations aligned parallel to the shear direction. These mirror-like surfaces correspond to the nanocrystalline shear bands seen in cross-section. Contrary to recent claims, these observations demonstrate that nanocrystalline, mirror-like slip surfaces in

calcite(-rich) faults are not exclusively diagnostic for seismic slip.

Appendix 3.A. Photomosaics of sheared gouge samples

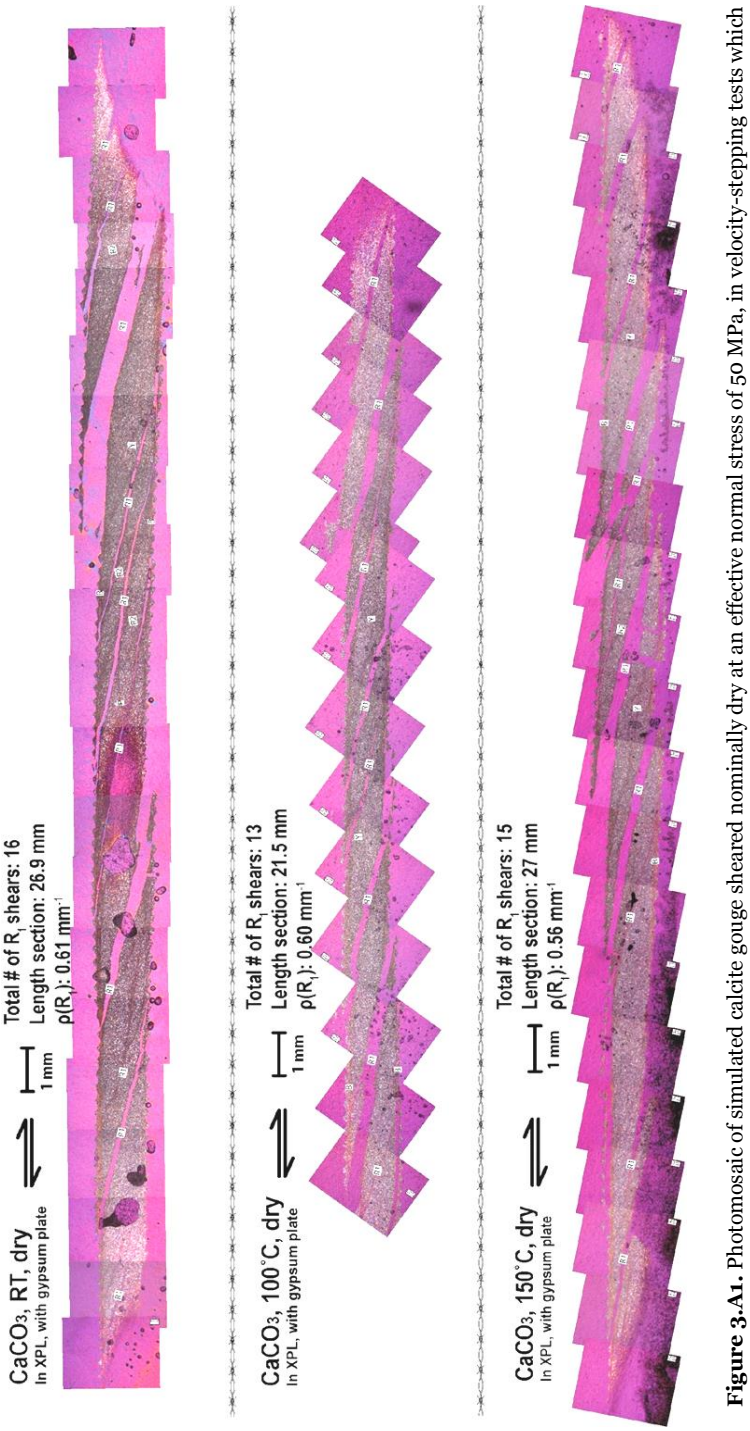

Figure 3.A1. Photomosaic of simulated calcite gouge sheared nominally dry at an effective normal stress of 50 MPa, in velocity-stepping tests which employed sliding rates of 0.1, 1 and 10 µm/s.

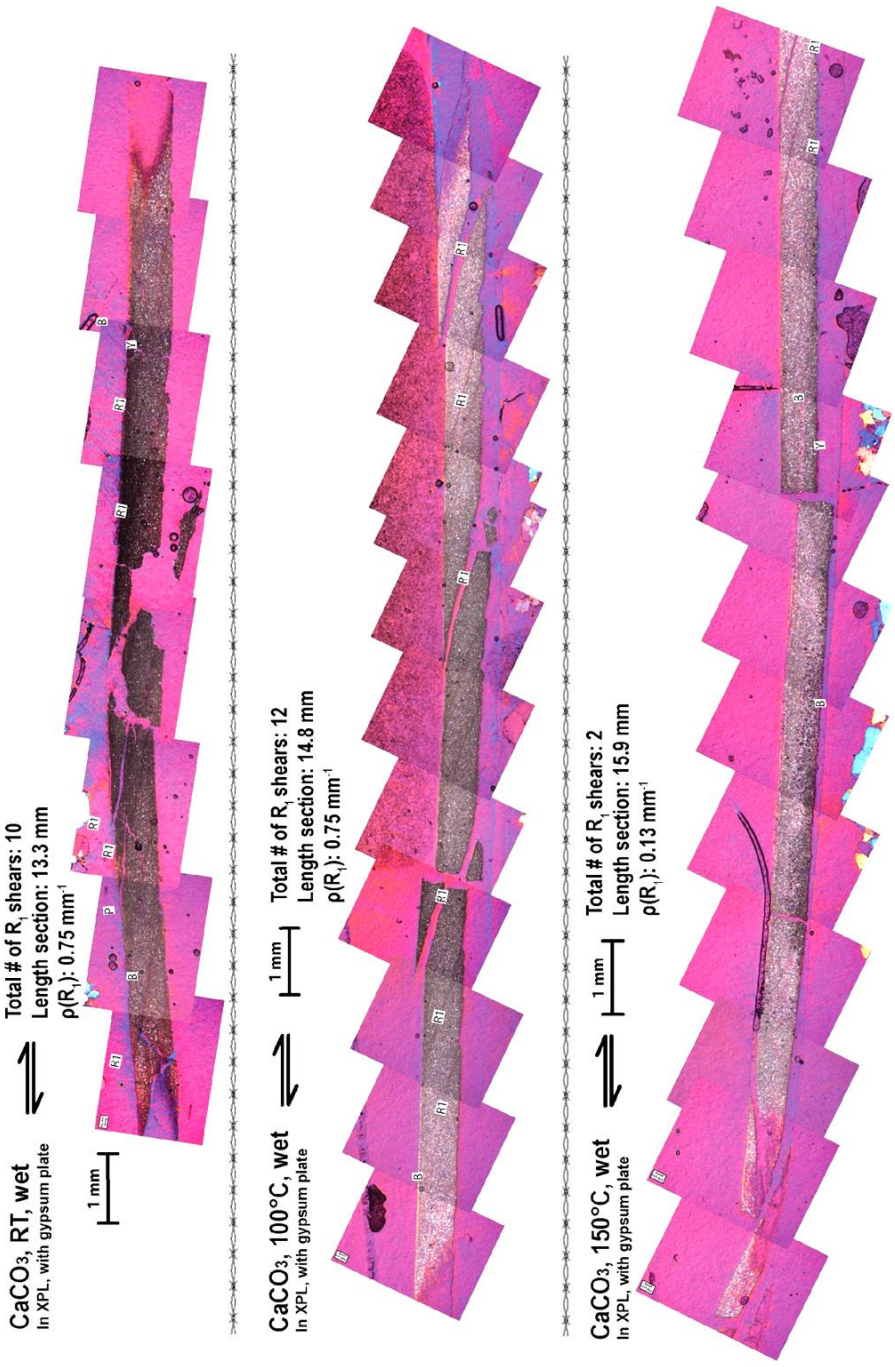

Figure 3.A2. Photomosaic of simulated calcite gouge sheared at an effective normal stress of 50 MPa, using a pore fluid pressure of 10 MPa, in velocity-stepping tests which employed sliding rates of 0.1, 1 and 10 µm/s.

Appendix 3.B. Correlative light- and electron microscopy

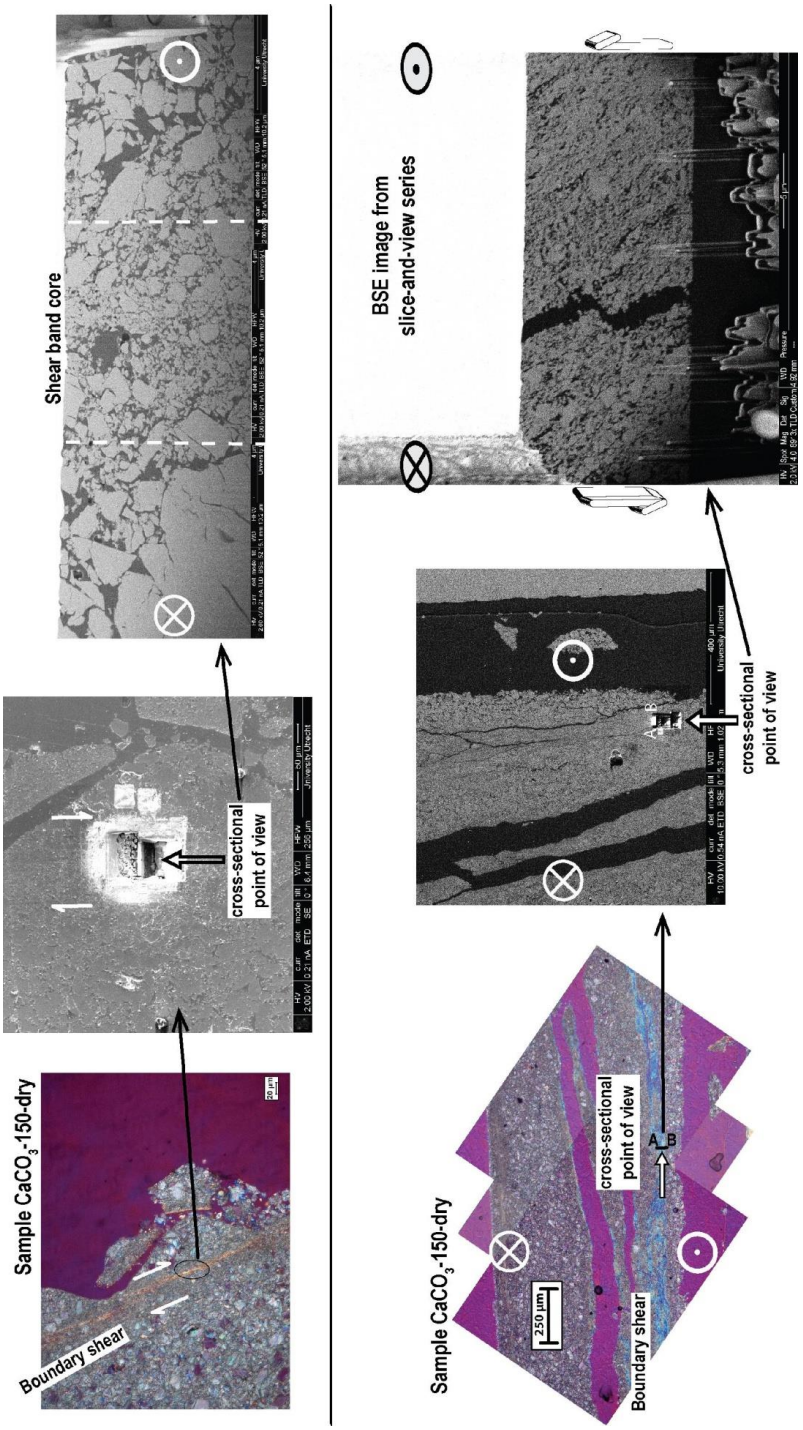

FIgure 3.B. Light and electron micrographs summarizing the correlative approach employed in obtaining cross-sections of boundary shear bands, including TEM foils.

Acknowledgements

This work has benefited from discussions with Martyn Drury, Jianye Chen, and Colin Peach. I further thank Changrong He for providing Xujiahe Limestone sample blocks, Peter van Krieken for carrying out the laser particle and XRD analyses, and Gert Kastelein and Eimert de Graaf for technical support. Hans Meeldijk is acknowledged for carrying out the TEM sessions, and Otto Stiekema for making the thin sections. Vu Hoang Trung is thanked for helping with Adobe Illustrator technical issues, and Zhao Yue for assistance with thin section analyses.

Chapter IV

Nanogranular principal slip zones in simulated calcite fault gouge sheared at 1 μm/s

After:

Verberne, B. A., Plümper, O., De Winter, D. A. M., and Spiers, C. J. (2014). Superplastic nanofibrous slip zones control seismogenic fault friction. *Science* **346,** 1342-1344.

Verberne, B. A., Plümper, O., De Winter, D. A. M., King, H. E., Thieulot, C., and Spiers, C. J. Nanocrystalline principal slip zones in simulated calcite fault gouge sheared at 1 μm/s. *Submitted to J. Geophys. Res.*

Abstract

Displacement on active fault zones is frequently localized on narrow (mm to cm wide) principal slip zones (PSZs) composed of nanogranular fault rock. However, the internal mechanisms controlling dynamic fault friction and rupture remain unknown. Here, we investigate the micro-/ nanostructure of PSZs developed in simulated calcite fault gouge, which was sheared at constant sliding velocity of 1 μm/s and at temperatures of 18° and 140°C using an effective normal stress of 50 MPa. Upon splitting after an experiment, the PSZ displays patches of highly-reflective (shiny), striated slip-surfaces. Sectioning of the PSZ using focused ion beam - scanning electron microscopy (FIB-SEM) showed that it consists of a porous ($\phi \approx$ 20-30%), 10 to 50 μm thick, sheet-like volume, composed of mainly of rounded, ~100 nm-sized particles or nanospherules that show widespread sintering. The shiny surfaces are seen to consist of locally dense, planar films composed of aligned, nanospherule chains or fibres ~100 nm in thickness, embedded at different topographic levels within the PSZ. TEM analysis showed the nanofibres to consist of ~5 to 20 nm crystallites, at the sub-nanospherule scale, with their (104) rhomb planes aligned preferentially parallel to the shear plane. Our results point to a slip mechanism within the PSZ involving nanogranular flow and diffusive mass transfer, resembling classical Ashby-Verrall superplasticity, but with incomplete accommodation by diffusion plus sintering of nanospherules to form nanofibres. We demonstrate that this mechanism can produce seismogenic slip under both lab and crustal conditions.

4.1. Introduction

Field and drilling studies of active fault zones frequently demonstrate the presence of a narrow (<0.1 m) principal slip zone (PSZ), located in the core of the fault (e.g. Power & Tullis, 1989; Chester & Chester, 1998; Ma et al., 2006; Li et al., 2013; Kuo et al., 2014). These features are composed of the ultra-fine grained wear material or fault gouge, and are believed to accommodate the bulk of fault slip (e.g. Sibson, 1986, 2003). Microstructural analyses of simulated fault rocks, sheared in laboratory experiments over a wide range of slip velocities (10^{-6}-10^{0} m/s), reveal the same pattern of strain localization into narrow shear bands composed of ultrafine (nano-sized) grains (e.g. Yund et al., 1990; Han et al., 2007a, b, 2010; Ree et al., 2014). Understanding the physical properties of the fine-grained fault gouge that constitute such PSZs is accordingly of major importance for understanding the mechanisms controlling fault strength and stability.

Chapter III reported experiments on simulated calcite-rich fault gouge sheared to displacements (x) of 4 to 5 mm, under upper-crustal conditions of effective normal stress (σ_n^{eff} = 50 to 53 MPa) and temperature (T = 20 to 150°C), employing low sliding velocities (v) ranging from 0.1 to 10 µm/s. Their mechanical data showed a transition from velocity strengthening slip at 20-80°C to velocity weakening above 80-100°C (Verberne et al., 2010, 2013a, b; see also Chen et al., 2015). This is important, because the velocity dependence of fault gouge strength is a material property that, through elastic coupling with the surroundings, determines whether a fault exhibits stable or unstable slip (e.g. Scholz, 1998). When the steady-state frictional sliding strength of a fault increases in strength with increasing displacement rate, it is said to exhibit velocity strengthening behaviour. This leads to stable sliding (Rice & Ruina, 1983). By contrast, if a fault is velocity weakening, this can lead to nucleation of periodic instabilities producing stick-slip behaviour characterized by regular stress drops (Ruina, 1983; Rice & Ruina, 1983). Stick-slip in rock friction experiments is widely viewed as a laboratory analogue for earthquakes (Brace & Byerlee, 1966). For this reason, much experimental and theoretical work has focused on the material properties triggering it, i.e. those controlling the velocity dependence of fault strength (for a review see Marone, 1998a).

Despite the above-mentioned transition from velocity strengthening to - weakening slip seen in the experiments by Verberne et al. on simulated calcite gouges, no change in microstructural characteristics seem to accompany the transition (Verberne et al., 2013a, b, or Chapter III). Across the full range of temperatures investigated (20° to 150°C), fault

slip consistently localizes in narrow (10 to 100 μm wide), nanocrystalline shear bands, or PSZs, showing a strong crystallographic preferred orientation (CPO). When split along the shear plane, these zones become partially exposed to display multiple, elongate patches of striated, highly-reflective slip surfaces, typically several mm in length, aligned parallel to the shear direction (Verberne et al., 2013b, 2014). Similar, though more continuous nanogranular "mirror-like" slip surfaces have recently been observed in natural fault zones in limestones (Fondriest et al., 2013; Siman-Tov et al., 2013), as well as in high-velocity friction (HVF) experiments on carbonates run at v = 0.1 to 3 m/s, σ_n^{eff} = 3 to 26 MPa, and x = 0.25 to 8 m (Han et al., 2007b, 2010; Tisato et al., 2012; Boneh et al., 2013; Chen et al., 2013c; Fondriest et al., 2013; Smith et al., 2013). On the basis of such HVF experiments, it has been widely proposed that natural exposures of continuous mirror-slip surfaces may provide useful indicators of past seismic slip (Fondriest et al., 2013; Smith et al., 2013).

Regardless of the continuity of these highly-reflective slip surfaces, their nanogranular nature suggests that nm-scale processes are central to controlling fault friction in carbonates - in both the low-velocity, rupture-nucleation regime, as well as during high-velocity, dynamic fault rupture. In the latter regime, i.e. at coseismic slip rates of the order of ~1 m/s, nanograins have been proposed to facilitate "powder lubrication", causing strong dynamic fault weakening (Han et al., 2010, 2011; Di Toro et al., 2011). However, during slow, pre-seismic and interseismic slip their role remains poorly understood. From experiments on metals and ceramics, nanophase materials are well-known to exhibit unusual deformation phenomena compared with their coarser-grained counterparts (for reviews see Tjong & Chen, 2004; Meyers et al., 2006). For example, due to the short transport distances and high grain boundary surface area, diffusive mass transport is generally fast in nanocrystalline materials (Würschumm et al., 2003), and they frequently exhibit superplastic behaviour at relatively low temperatures and/ or high strain rates (e.g. Nieh et al., 1997; Lu et al., 2000). On this basis, nanogranular carbonate fault rocks can be anticipated to show unusual physical properties compared with coarser-grained fault rocks developed in carbonates. Moreover, as (shiny) nanogranular fault surfaces are emerging to be widespread in tectonically-active terrains, dominated not only by carbonates (Smith et al., 2011; Fondriest et al., 2013; Siman-Tov et al., 2013; Bullock et al., 2014; Collettini et al., 2014) but also by silicate-rich rocks (Power & Tullis, 1989; Chester et al., 2005; Ma et al., 2006; Kirkpatrick et al., 2013; Evans et al., 2014), the unusual properties of nanocrystalline

materials may have important implications for our understanding of crustal faulting in general.

The present Chapter focuses on PSZs developed in simulated calcite fault gouges sheared in a nominally dry state, at v = 1 μm/s and at temperatures favouring both velocity strengthening (18°C) and velocity weakening (140°C) behaviour. We pay special attention to the shiny striated slip patches that are exposed within the PSZ surface upon sample disassembly. Our aim is to elucidate the physical processes that control the frictional strength and slip stability of calcite-rich fault gouges sheared at low velocities, in particular the transition to velocity weakening slip seen with increasing temperature. Specifically, we address the following questions:

i. What are the micro-/ nanostructural characteristics of the PSZ and the internal shiny, striated slip surfaces? Can we distinguish between micro-/ nanostructures formed under velocity strengthening versus velocity weakening conditions?
ii. What are the microphysical processes active within the PSZ and associated shiny surfaces, and how do these control frictional strength and slip stability?
iii. Are the shiny surfaces developed at 1 μm/s distinguishable from similar highly-reflective (mirror-like) slip surfaces reported to form at coseismic slip rates, i.e. can highly-reflective slip surfaces be used as field indicators of past seismic slip?

4.2. Materials & Methods

4.2.1. Samples and direct-shear assembly

We performed 11 experiments on simulated calcite fault gouge in total. Nine were performed using crushed $CaCO_3$ single crystals (high purity Iceland Spar, the same as used in Chapter III), one was conducted using crushed Xujiahe (XJ) limestone (>96% $CaCO_3$, see Verberne et al. (2010), or Chapter II), and one using Merck extra pure (precipitated) $CaCO_3$ powder (Table 4.1). The crushed Iceland Spar and XJ limestone were sieved to a grain size fraction <28 μm. Grain size distributions, determined using a laser particle sizer, revealed that each sample powder had a median grain size below 20 μm (Fig. 4.1).

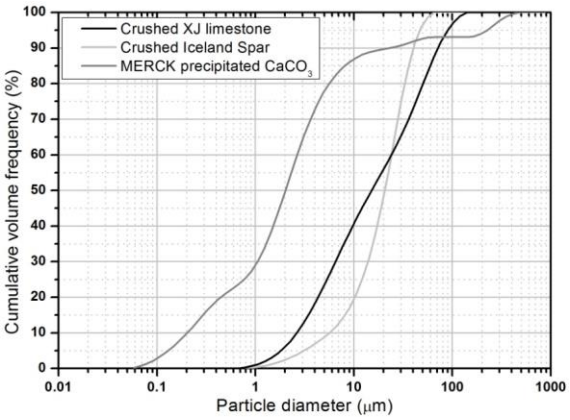

Figure 4.1. Grain size distributions for the samples used in the present study, determined using a Malvern laser particle sizer.

All experiments were conducted using a direct shear sample assembly installed in a conventional, silicone-oil medium, triaxial deformation apparatus. The triaxial machine has been described in detail in Chapter III. The direct shear or '69' sample assembly used consists of two L-shaped, half-cylindrical pistons, sandwiching a layer of simulated gouge with dimensions of 35x49x~1 mm (Fig. 4.2). The sample layer is gripped by grooves machined in the faces of the direct shear pistons. In preparing each experiment, the sample powder was mixed with demineralized water in proportions of roughly 4:1 gouge-to-water, to obtain a mouldable paste. A ~1.1 mm thick layer of gouge paste was then plastered onto the grooved face of one direct shear piston, and the sample plus supporting piston was dried in an oven for at least 4 hours at ~115°C. The second piston was added to the assembly while the sample layer was still hot, and the whole pre-jacketed, over the length of the sample, using a thin, heat-shrink (FEP) sleeve for support.

The displacement-accommodating chambers within the direct shear assembly were filled with a soft polymer pack of negligible strength (Fig. 4.2, Table 4.1). The entire assembly was then outer-jacketed in an EPDM rubber sleeve of ~1.4 mm thickness, sealed against the pistons using wire tourniquets. Initial experiments employed a polymer pack consisting of a polytetrafluorethylene (PTFE) foil liner, an Ethylene-Propylene-Diene Monomer (EPDM rubber) sealing sheet, and a filler of standard white silicone putty, as used by Samuelson & Spiers (2012) and Verberne et al. (2013a, b) (or Chapter III). To determine whether any components of the silicone putty may have contaminated the samples in any way, we also conducted experiments using i) a pack of

PTFE foil plus EcoFlex rubber, and ii) EcoFlex rubber only (Table 4.1). In four experiments using crushed Iceland Spar (Table 4.1), we inserted two soft Indium bars (cuboids), measuring 35x1x1 mm, into the assembly at each end of the sample layer before emplacing the second piston. This was done to fully seal the sample from the silicone putty or EcoFlex filler. While the different packings used could potentially have affected our mechanical data slightly, no systematic effects were observed on the strength, microstructure or chemical characteristics of the samples.

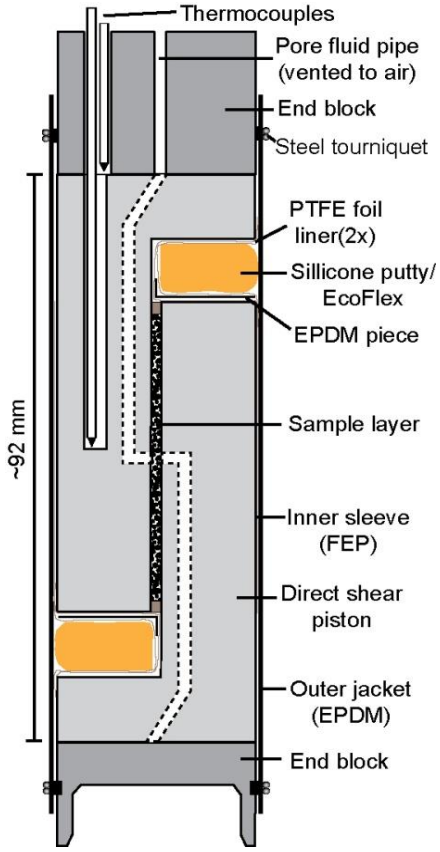

Figure 4.2. Semi-schematic diagram showing the direct-shear testing assembly used in the present experiments. Shear of the simulated fault gouge sample is achieved by compressing the assembly in the axial direction, in a conventional triaxial testing machine. See also Verberne et al. (2013a, b) (or Chapter III).

Experiment	T (°C)	Sample material	Direct shear assembly[1)]	Shiny surfaces found?[2)]	Fibres found?[3)]	Black phase found?[3)]
SEMA	18	Iceland Spar	Silly putty, PTFE	YES	YES	NO
SEMB	18	Iceland Spar	In, Silly putty, PTFE	YES	YES	YES
SEMC	140	Iceland Spar	In, Silly putty, PTFE	YES	YES	NO
SEMD	18	Iceland Spar	In, Silly putty, PTFE	YES	YES	YES
SEME	18	Iceland Spar	In, EcoFlex, PTFE	YES	YES	NO
SEMF	18	Iceland Spar	EcoFlex, PTFE	YES	YES	NO
SEMG	18	Iceland Spar	EcoFlex, PTFE	YES	YES	NO
SEMH	18	MERCK $CaCO_3$	EcoFlex, PTFE	YES	YES	NO
SEMI	18	Iceland Spar	EcoFlex	YES	YES	NO
SEMK	140	XJ limestone	EcoFlex, PTFE	YES	YES	YES
SEML	140	Iceland Spar	EcoFlex, PTFE	YES	YES	YES

Table 4.1. List of experiments and key microstructural observations. [1)]See Fig. 4.2 for a sketch of the testing assembly, and Verberne et al. (2013a, b) (or Chapter III) for further details on the methodology. [2)]From visual inspection of the sheared samples after an experiment. [3)]From inspection using FIB-SEM.

4.2.2. Mechanical testing procedure & sample recovery

All tests were conducted using a confining pressure, hence normal stress (σ_n) in the direct shear assembly used here, of 50 MPa. In all cases, the dry sample was vented to the laboratory atmosphere via the pore fluid system of the triaxial machine (refer Fig. 4.2, plus Verberne et al., 2013b, or Chapter III). For experiments performed at room temperature, we left the apparatus to equilibrate for ~1 hour at the desired testing conditions before starting the experiment. For experiments performed at 140°C, equilibration took around 4 to 5 hours. Each sample was then sheared through ~4 to 6 mm of displacement, at a constant displacement rate of 1 μm/s. In terminating each experiment, the loading ram was arrested and subsequently backed-off at a rate of 10 μm/s. In runs at elevated temperatures, we then switched off the furnace and increased the water cooling rate of the triaxial machine to rapidly cool the sample. After depressurization to atmospheric conditions, the sample assembly was removed from the testing machine and dismantled.

Each sample was recovered from the piston face some 20 to 30 minutes after retracting the loading ram. Upon sample extraction, we first stripped the assembly of its jacket and other polymer components, and then separated the direct shear pistons to expose the sheared gouge within. From each sample, we collected platy, rectangular

fragments measuring ~5 to 10 mm by ~5 to 20 mm, usually displaying mirror-slip patches. Prior to microstructural study, all sample fragments were stored in an opaque container to avoid exposure to light.

4.2.3. Data processing

The shear strength of our samples was quantified using the apparent coefficient of friction μ, determined by dividing the shear stress supported by the sample by the effective normal stress acting on the sample layer. The shear stress was calculated by dividing the measured axial force by the load-bearing sample-area. In most runs, the load-bearing sample area decreases with increasing displacement, due to the imposed shear deformation geometry, producing an apparent, near-linear displacement-weakening effect (see also Verberne et al., 2013b, or Chapter III). However, correction for this proved unreliable due to differences in the detailed deformation geometry of the samples from run to run. Hence, to avoid over-correction, we assumed a constant load-bearing sample area for each experiment. All displacement data were corrected for elastic distortion of the deformation apparatus.

4.2.4. Microscopy methods

We used a Leica DMR microscope for imaging recovered sample fragments using reflected light. For study using scanning electron microscopy (SEM), the recovered fragments were placed on SEM specimen stubs topped with a carbon-sticker. Silver dag was used to secure the sample to the sticker, thus ensuring good conduction and minimizing sample charging. Samples were subsequently sputter-coated with a 5 nm thick layer of Pt. SEM imaging was done using an FEI Nova Nanolab 600 focused ion beam (FIB) – SEM, operated in either backscatter electron (BSE) or secondary electron (SE) mode. We used an acceleration voltage of 2 kV and a beam current of 0.21 nA, unless indicated otherwise. Samples from all experiments reported here (Table 4.1) were investigated in the SEM. However, most high-resolution imaging was done from samples recovered from experiment SEMB (deformed at 18°C). In the case of FIB sectioning, we milled selected samples in an orientation normal to the shear plane and parallel to the shear direction, both for SEM study and to prepare electron-transparent foils for study using transmission electron microscopy (TEM). The TEM used was a Tecnai20 FEG TEM instrument, operated at 200 kV. In high resolution mode, we strictly limited beam exposure-times to avoid damaging the sample. Multiple qualitative chemical analyses were carried out on various samples using electron dispersive X-ray (EDX) detectors

installed in both the FIB-SEM and TEM. The surface structure of selected shiny patches was investigated using an atomic force microscope (AFM). These focused on samples sheared at room temperature in a velocity-stepping, direct shear test reported in Chapter III, using v = 0.1, 1 and 10 μm/s, under otherwise the same conditions as used in the present experiments. The AFM scans were conducted in air, using a Nanoscope III multimode AFM with a Si_3N_4 tip (Bruker, tip model NP-S20 with 0.12 and 0.58 N/m spring constants), scanning at a frequency of 3 Hz. Each image consisted of 256 scan lines. The images were collected and analysed using NanoScope software, Version 5.31r1.

4.3. Results

4.3.1. Mechanical data

All experiments showed rapid, near-linear loading in the first 0.3 to 0.5 mm of displacement (x), followed by apparent yield and subsequent hardening towards a broad peak frictional strength (μ_{pk}) of 0.7-0.8, attained at $x \approx 1$ to 2.5 mm (Fig. 4.3). Beyond μ_{pk}, most samples showed a transition to near-linear weakening with increasing displacement, with μ falling to values of 0.6-0.75 at displacements of 5-6 mm. Experiments SEML and SEMK, conducted at T = 140°C, showed the onset of low-amplitude stick-slip at $x \approx 0.7$ mm (Fig. 4.3). In experiment SEML, this stopped at $x \approx 1.3$ mm, i.e. just after reaching μ_{pk}, whereas in experiment SEMK stick-slip continued throughout the entire duration of the experiment.

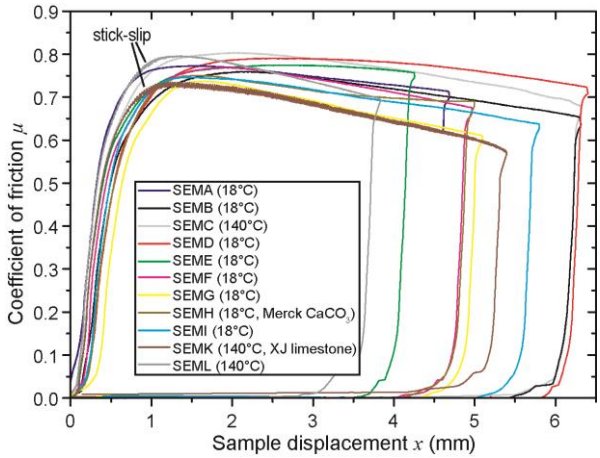

Figure 4.3. Apparent coefficient of friction (μ = shear stress τ / effective normal stress σ_n^{eff}) versus sample displacement for all experiments reported. All samples were prepared from crushed Iceland Spar, except where otherwise indicated. See Table 4.1 for a list of corresponding experiments and their conditions.

4.3.2. Sample-scale and optical observations

Upon separation of the direct shear blocks after each experiment, the sample split along a shear-induced fabric consisting of a marked, boundary-parallel shear band, developed near the sample-piston interface, and less-pronounced, inclined shear bands. In each sheared sample, this boundary-parallel band represents the PSZ (cf. Verberne et al., 2013a, b, or Chapter III).

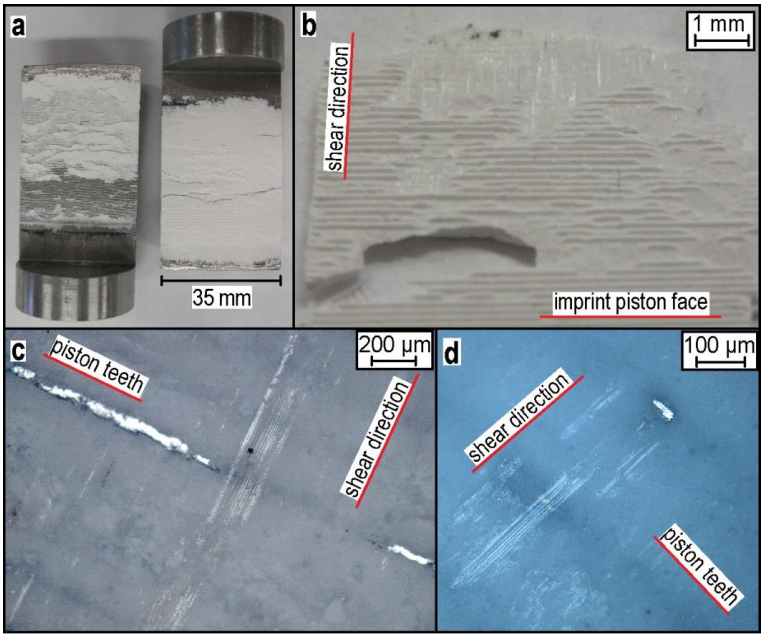

Figure 4.4. Samples as recovered from our constant velocity (1 µm/s) direct shear experiments. a) Separated direct shear pistons showing typical splitting of sheared gouge sample (experiment SEME, 18°C). b) A fragment recovered from the sheared gouge layer represented in (a), showing exposures of the PSZ where grooved portions of the sample surface have been plucked away in sample disassembly. c) and d) Reflected light micrographs of shiny surface patches located within the boundary-parallel shear plane or PSZ on fragments plucked out from a sample surface such as shown in (b). Note that the imprint of the grooves and intervening teeth in the piston surfaces can be seen beneath the striated shiny patches. The photos in c and d are respectively taken from samples recovered from experiments SEMB (18°C) and SEML (140°C). See Table 4.1 for a list of all experiments and key observations.

In all cases, most of the sheared gouge adhered to one piston face upon separation of the 69 shear blocks (Fig. 4.4a). However, at least a part of the load-bearing sample-surface got stuck to the opposite piston face, such that the boundary-parallel band or PSZ split internally. We were unable to control the extent or location of internal PSZ splitting. For samples sheared at high temperatures, the grooved imprint of the removed piston

face on the free sample-surface usually remained intact, limiting exposure of the PSZ developed just beneath (Figs. 4.4a, b). However, in samples sheared at both 18°C and at 140°C, the PSZ split internally revealing highly-reflective, striated patches, measuring 0.1 to 0.5 mm wide by up to 3 mm long, aligned with their long axis parallel to the shear direction (Figs. 4.4b-d, Table 4.1). The exposed surface morphology of the PSZ in some samples suggests the presence of a continuous shiny coating connecting the striated patches (Fig. 4.4b). However, in most cases the PSZ splitting fabric is too irregular to conclude this firmly. Moreover, investigation using reflected light microscopy demonstrates that the base of the exposed PSZs has μm- to mm-scale topography, whereas the shiny patches are topographically flat (see also Verberne et al., 2013b, or Chapter III).

Striated shiny patches are also present on inclined shear band surfaces, but most are found on the boundary-parallel surface developed near the sample-piston interface. In our subsequent analysis, we focus on these exposures, i.e. on shiny surfaces developed in the prominently split boundary shear or PSZ formed adjacent to the piston-sample interface.

4.3.3. (FIB-)SEM analysis

4.3.3.1. General structure of the PSZ

SEM investigation showed that for both velocity-strengthening (18°C) and velocity-weakening (140°C) samples the PSZ consists of a porous, sheet-like volume of ultra-fine grained material. The striated, shiny surface patches are visible at different topographic levels embedded within this volume (Fig. 4.5a). In all samples studied, we observed swathes of porous aggregates of rounded, ~100 to 200 nm sized particles, or nanospherules, located above, below and surrounding these exposed shiny patches (Fig. 4.5b). In addition, we used FIB-SEM to section a sample recovered from experiment SEMC (Table 4.1). This sample showed the full piston (i.e. groove) imprint over its entire surface, implying that the PSZ was recovered from the piston face fully intact (Fig. 4.5c). In a section milled normal to the shear plane and parallel to the shear direction, the PSZ was found to be 10 to 50 μm thick, and composed of 0.3 to 5 μm sized angular clasts embedded in a porous matrix consisting of ~100 to 200 nm sized rounded particles, corresponding to the above-mentioned nanospherules. Necks indicative of sintering were commonly observed to have grown between these rounded matrix particles (Fig. 4.5c, inset). From visible void area, the porosity ϕ was estimated to be ~20 to 30%.

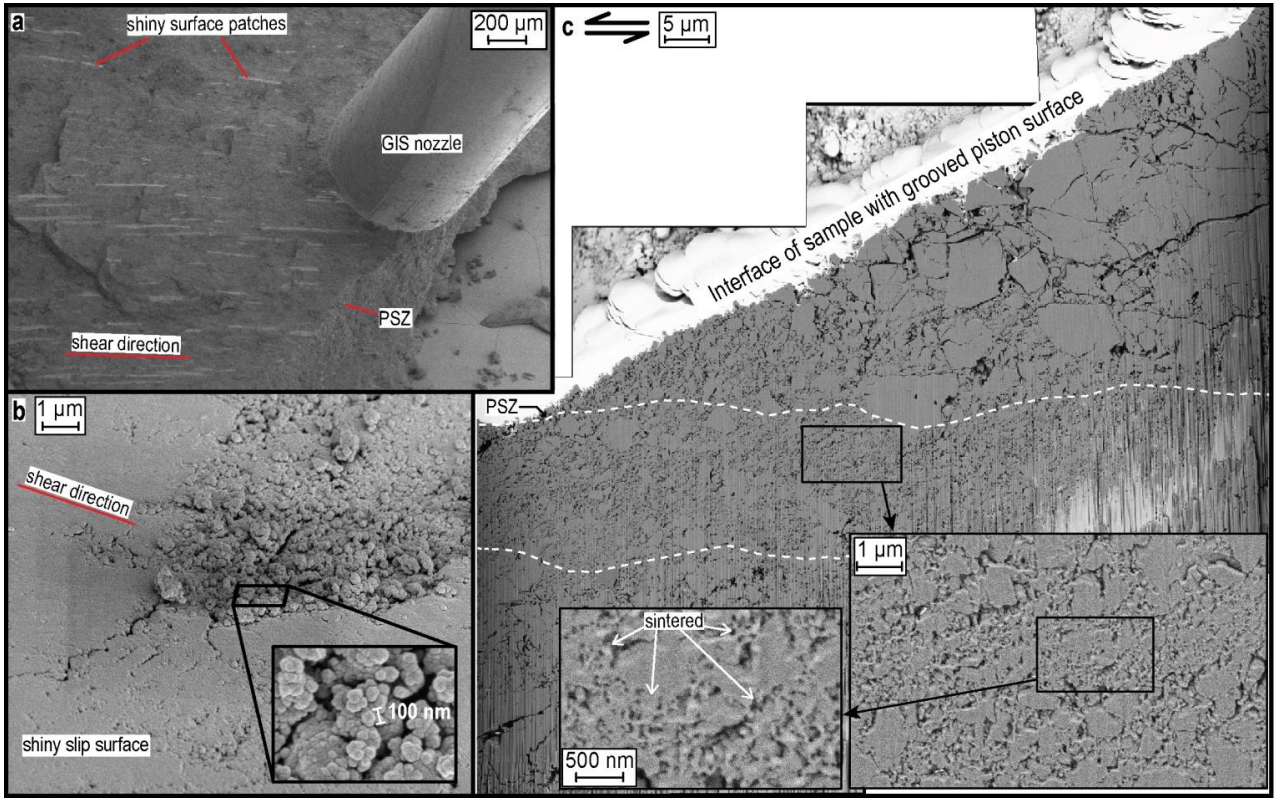

Figure 4.5. Principal slip zones (PSZs) in SEM. a) Secondary electron (SE) micrograph taken with the stage tilted at 52° (experiment SEMB, 18°C). Notice the shiny surface patches at different topographic levels embedded in the PSZ. The needle of the gas injection system (GIS) is used when preparing samples for milling using FIB. b) SE micrograph, showing ~100 nm sized nanospherules lying on a shiny surface patch (experiment SEMB, 18°C). c) Mosaic of backscattered electron (BSE) micrographs showing a cross-section of part of a PSZ, milled normal to the shear plane and parallel to the shear direction using FIB (experiment SEMC, 140°C). Note the evidence for sintering and/ or neck growth of nanoparticles shown in the insets. The vertical striped pattern is an artefact from ion-polishing in the FIB (known as 'curtaining'). This does not affect the inherent sample microstructure or our interpretations.

4.3.3.2. Internal structure of the shiny patches

We focus now on the detailed internal structure of the shiny surface patches, as exposed on split PSZ surfaces (see Figs. 4.4b-d, 4.5a). SEM investigation showed that, in both velocity strengthening (18°C) and velocity weakening (140°C) samples, the shiny patches consist of dense, ultra-fine grained coatings composed of ~100 nm wide fibres aligned (sub-)parallel to the shear direction (Figs. 4.6a-d). Within these fibrous nanocoatings, individual ~100 nm spherules are sometimes visible, especially at the tips of fibres protruding from the surface (Fig. 4.6c). In shiny patches formed in velocity strengthening samples, micro-cracks cutting the nanocoatings show marked extension and plastic bending of the fibres (Figs. 4.6c, d). In view of the high confining stress used in our tests (50 MPa), such crack opening and associated fibre deformation could only have occurred upon sample depressurization or disassembly at room conditions. Multiple fibre stacks are also present (Fig. 4.6e). Near the edge of a shiny patch formed in sample SEMB, i.e. where the fibrous nanocoating transitions into the bulk nanogranular PSZ, aligned successions of sintered nanospherule chains define a weak fabric that merges with the fibres within the shiny patch (Figs. 4.6e-h). The lower end of the same shiny patch of sample SEMB accidentally broke upon loading the sample in the SEM chamber. Along the edge of the fresh fracture, individual fibres within the clearly visible film or nanocoating have bent through 90° with respect to the shear direction, again implying that ductile bending of the fibres occurred at room conditions (Figs. 4.7a, b). Electron dispersive X-ray (EDX) analysis using detectors installed in the FIB-SEM confirmed that the nanofibres are composed of Ca, C and O (Fig. 4.8), consistent with calcite ($CaCO_3$).

►**Figure 4.6.** SE micrographs of shiny surface patches in SEM. a) and b) Shiny surfaces from velocity strengthening sample SEMB deformed at 18°C (a), and velocity weakening sample SEMC sheared at 140°C (b). c) and d) Fibrous nanocoating cut by a post-test crack (experiment SEMB, 18°C). The micrograph shown in (d) was taken from the location indicated in (a), that in (c) was taken from a different shiny patch developed in the same experiment. Inset in (c) shows a protruding fibre with a spherule at its tip. e) and f) Nanofibres at the edge of a shiny surface (experiment SEMB, 18°C). The micrograph shown in (e) was taken with the sample stage tilted at 30°. The micrograph shown in (f) displays the same area as in (e) but in top view (location see (a)) with the sample stage rotated through 180°C. Note the topography in the lower part of this image, where porous nanospherule aggregates are present, compared with the shiny surface (upper part) which is relatively flat. f) and h) Enlarged portions of (g), highlighting chain-like arrays of sintered nanospherules.

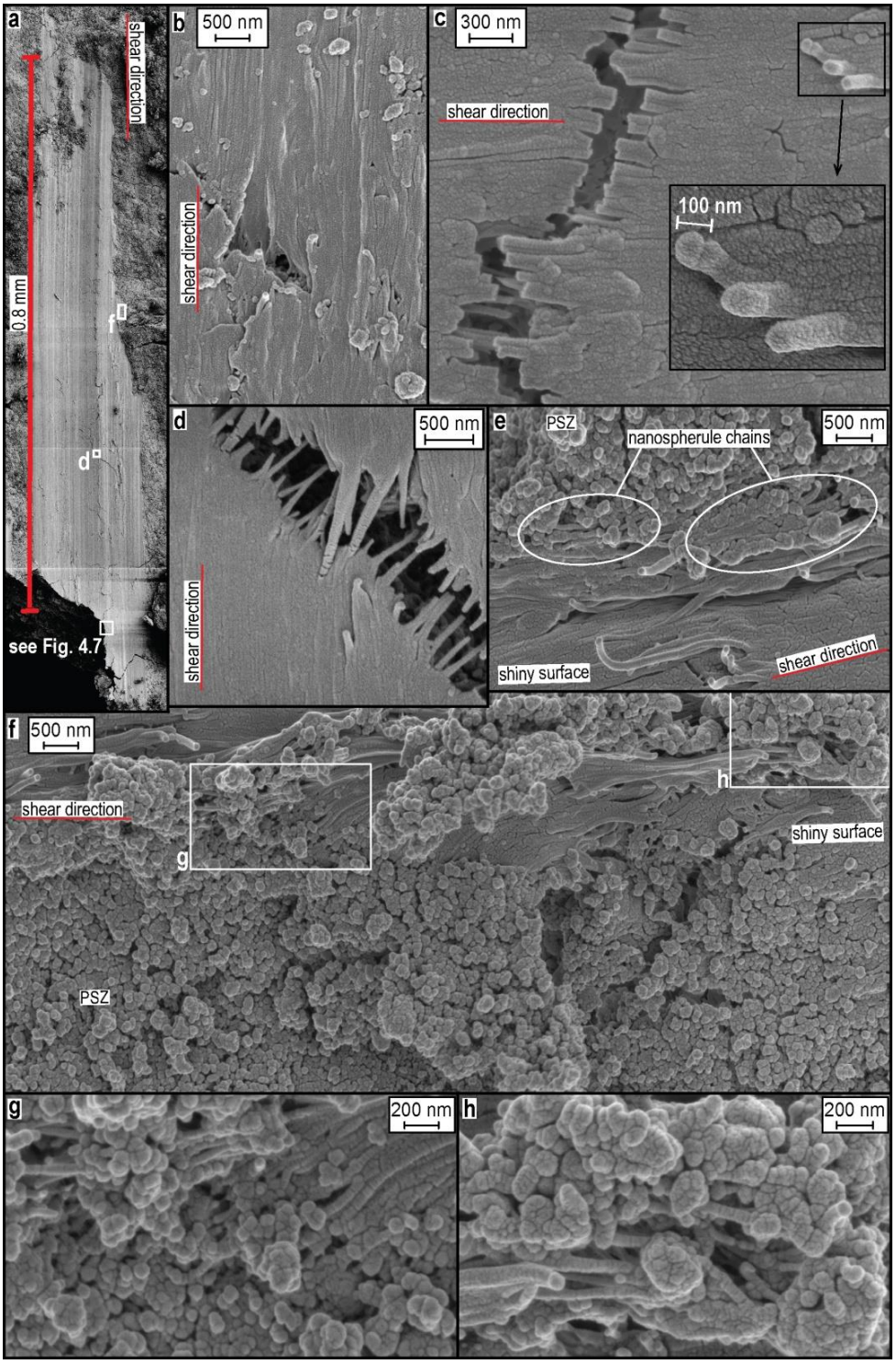
a
shear direction
0.8 mm
f
d
see Fig. 4.7
b
500 nm
shear direction
c
300 nm
shear direction
100 nm
d
500 nm
shear direction
e
PSZ
nanospherule chains
500 nm
shiny surface
shear direction
f
500 nm
shear direction
g
h
shiny surface
PSZ
g
200 nm
h
200 nm

►**Figure 4.7.** SEM images of the lower part of the shiny surface shown in Fig. 4.6a (experiment SEMB, 18°C), which broke off just prior to loading the sample into the SEM sample chamber. a) SE micrograph. Along the fracture margin, the nanofibres are bent through up to 90° with respect to the shear direction. b) BSE micrograph of a tilted and rotated view of the fracture seen in (a).

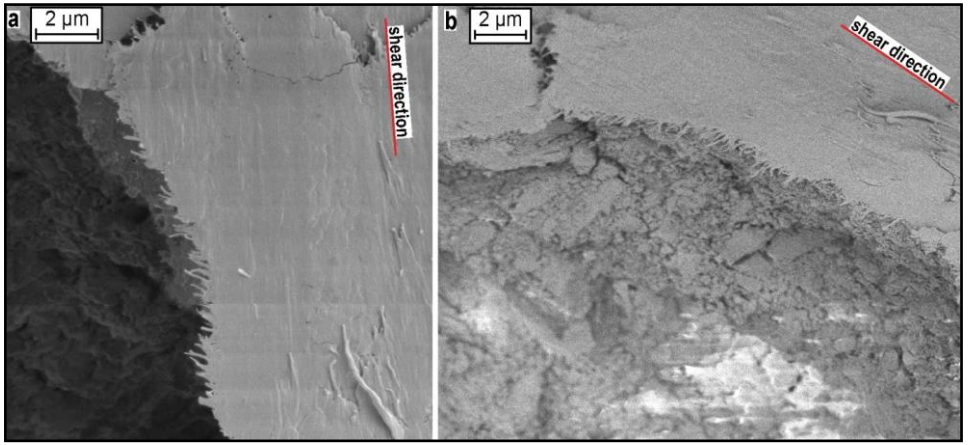

▼**Figure 4.8.** Representative data from EDX spot analyses performed in the FIB-SEM (on a shiny surface recovered from experiment SEMB, 18°C). a) SE micrograph showing nanofibres on a shiny surface cut by a post-experiment crack. The white stars indicate the locations of the spots targeted to obtain EDX spectra. b) EDX spectra from the spots shown in (a). Note that EDX can only be used as a qualitative indicator for the elements present. In all cases where nanofibres have been analyzed we found peaks consistent with Ca, C and O. The high Pt/Pd count originates from the 4 to 6 nm thick, conductive coating applied prior to loading the sample into the SEM sample chamber.

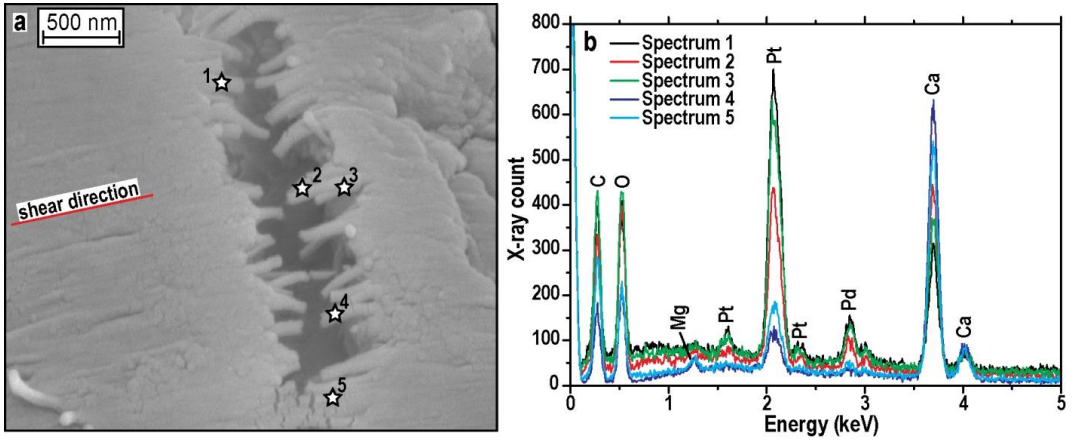

To examine the nature of the fibrous nanocoatings that form the shiny patches seen in our samples, and indeed to successfully locate a shiny patch within a vertical cross-section of a PSZ, we FIB-sectioned the shiny patch shown in Figure 4.9a. We chose this patch because it shows stretched nanofibres bridging a micro-crack, and is partly overlain by a porous nanogranular spherule aggregate representing the enclosing PSZ (Figs. 4.9a, b). The FIB cross-section that we milled revealed that the fibrous nanocoating corresponds to a dense 0.1 to 1 μm thick zone or film (veneer) with little visible internal structure (Fig. 4.9c). This apparently dense zone is over- and underlain by material composed of micron-sized angular grains and rounded matrix particles or nanospherules, consistent with the SEM microstructure that characterizes the broader PSZ (cf. Fig. 4.5c). The dense zone cannot be traced everywhere beneath the portion that is covered by the porous nanogranular aggregate seen in top view in Figure 4.9a (see Figs. 4.9c, d). Where it is visible, it is underlain by a thin zone containing disconnected pores of ~100 nm in diameter. Still further away from the shiny fibrous zone, pore size and connectivity increase, as does the grain size, such that the microstructure grades into that of the bulk of the PSZ (Figs. 4.9c, e).

4.3.3.3. Compositional anomalies

The PSZ and main body of some samples investigated using SEM showed the presence of an amorphous black substance, locally occupying pores ~0.1 to 5 μm in diameter (Figs. 4.9c, d). EDX analysis showed this to be a carbon-rich phase (Ca and O peaks were absent, cf. Fig. 4.8). Its presence showed no correlation with the mechanical behaviour of the samples, nor with any specific microstructural features. Similarly, no correlation was found with the sample material used or with the components of the various filler packs used in the direct-shear testing assembly (refer Fig. 4.1 and Table 4.1).

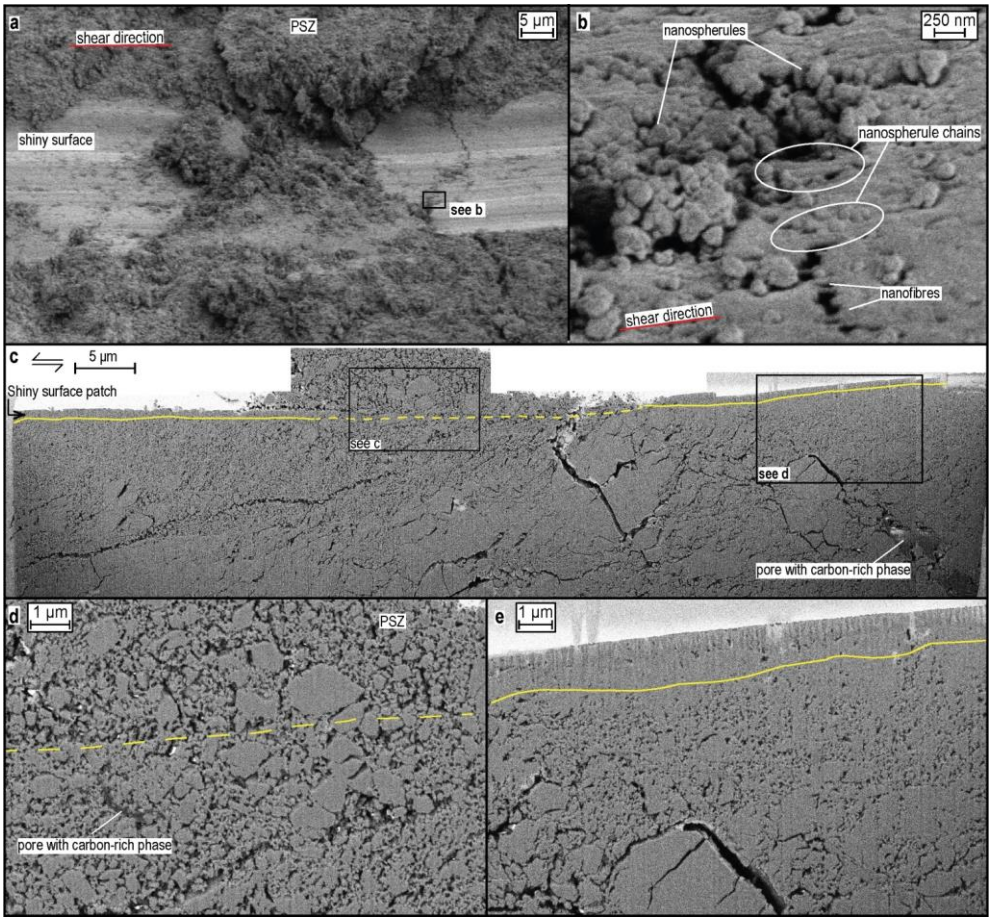

Figure 4.9. a) and b) SE micrographs a shiny surface patch, demonstrating the presence of nanospherules and nanofibres (experiment SEMB, 18°C). c) Mosaic of BSE micrographs of a cross-section of the fibrous nanocoating shown in (a) and (b), prepared in an orientation normal to the shear plane and parallel to the shear direction using FIB-SEM. The yellow line highlights the lower boundary of the dense zone that constitutes the fibrous nanocoating. The dashed interval was interpolated from of the orientation of the dense zones left and right of the part overlain by the porous nanogranular aggregate (or PSZ). d) and e) Magnified portions of (c).

4.3.4. TEM analysis: Internal structure of single fibres

To resolve the internal structure of the fibres forming the mirror-like patches seen in our samples, we used FIB-SEM to prepare an electron-transparent foil, isolating a single nanofibre in a section milled normal to the shear plane and parallel to the shear direction (following the method of Holzapfel et al., 2009, see Figs. 4.10a, b). In bright-field imaging mode, the sectioned nanofibre is seen as a ~100 to 300 nm wide strip, showing internal spherule-like domains of contrast, overlying 1 to 5 µm single calcite fragments (Figs. 4.10c, d). Selected-area electron diffraction (SAED), using a 300 nm aperture, yielded a sharply spotted calcite diffraction pattern for the larger angular fragments (Fig. 4.10e), and a ring-shaped pattern with arcs of greater intensity for the nanocrystalline fibre (Fig. 4.10f). The arcs of greater intensity demonstrate a preferred orientation of the nanocrystallites present within the fibre-volume sampled using SAED. Comparison of the mean ring diameter with the known lattice spacings of calcite (Graf, 1961) showed the second diffracted ring to correspond with the calcite (104)-plane (see also Verberne et al., 2013a, b, or Chapter III).

High resolution TEM applied to the nanocrystalline fibre revealed that, at the sub-spherule scale, the fibre is composed of 5 to 20 nm sized crystallites characterized by mutual misorientations of 5 to 20° (Fig. 4.10g). The spacing between the lattice planes observed using HRTEM measures ~3 Å, which corresponds to the lattice spacing of the (104) planes in calcite (Graf, 1961). These (104) or calcite r-planes (hexagonal structural cell) are clearly oriented sub-parallel to the shear direction (Figs. 4.10d, g). Finally, EDX analysis performed in TEM verified that the nanofibre is composed of Ca, C and O, in proportions corresponding to calcite.

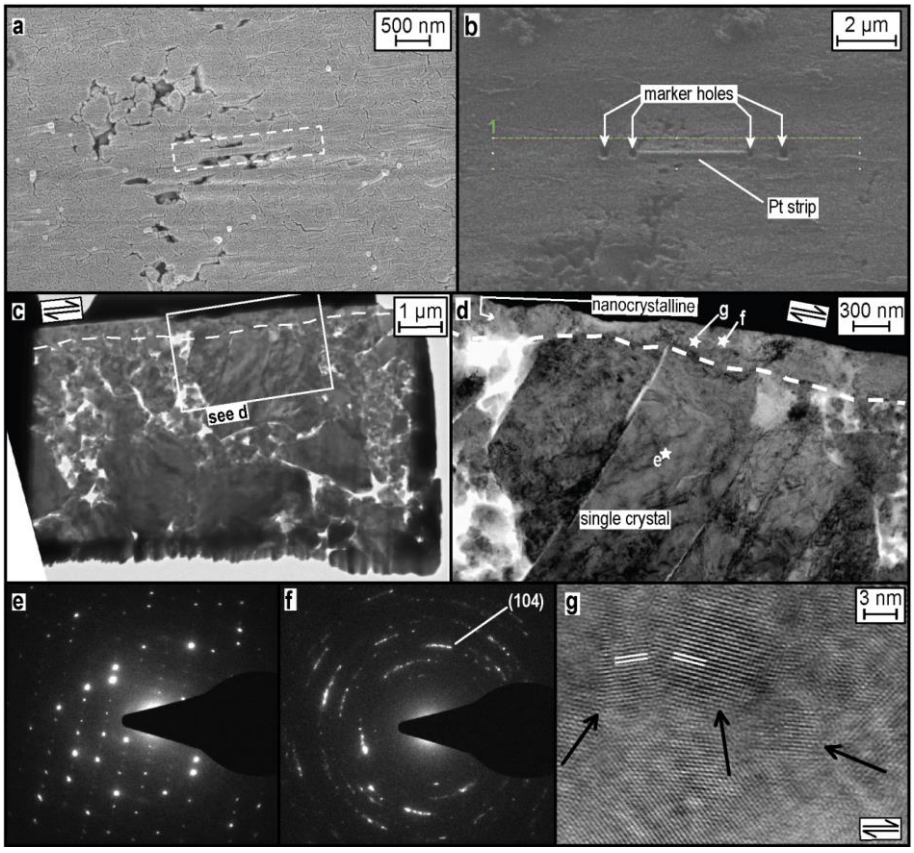

Figure 4.10. TEM analysis on a single nanofibre (experiment SEMD, 18°C). a) and b) SEM (SE) micrographs summarizing the procedure (cf. Holzapfel et al., 2009) for recovery of a single nanofibre for TEM study. To prevent the fibre from being damaged by the ion beam, we first deposited a 0.5 µm thick Pt strip onto the nanofibre before milling holes that mark the location of the fibre (indicated by the white arrows in (b). The entire area was then covered with a 2 µm thick Pt strip (area highlighted by the green dashed box in (b)). c) and d) Bright-field TEM micrographs of an electron transparent foil prepared following the method summarized in (a) and (b). The foil contains a nanofibre at the very top of the section (indicated by the dashed line). Note the spherular zones of contrast located within the fibre in (d). e) and f) SAED patterns (approx. locations see d), taken in the TEM using a 300 nm aperture, from a large angular grain (e) and from within the nanofibre (f). g) HRTEM image taken from within the nanofibre (approx. location see d). Individual lattice fringe domains measure ~5 to 20 nm, and are characterized by mutual misorientations of 5 to 20°. The thick white lines indicate the orientation of the (104) or r-plane.

4.3.5. AFM and surface roughness analyses

AFM data recorded from a 20x20 μm²-sized area of a shiny, striated patch of sample deformed at ~18°C revealed a regularly grooved and ridged topography running parallel to the shear direction, and characterized by a peak-trough height of ±200 nm measured in a section cut normal to the shear direction (Figs. 4.11a, b). A much finer scale topography, with a maximum amplitude ±40 nm, is present in sections oriented parallel to the shear direction (Figs. 4.11a, c). Root mean square (RMS) analysis performed on 256x256 data points from the grooved patch shown in Figure 4.11a showed an RMS roughness of <7.4 nm over a length scale of 550 nm (Fig. 4.11d). This satisfies the Rayleigh roughness criterion for visible light, which states that if the mean roughness amplitude is below ~100 nm at lateral scales corresponding with a wavelength of 550 nm, a surface observed at angles <70° will reflect light specularly, and thus appear shiny or mirror-like (Beckmann & Spizzichino, 1963; see also Siman-Tov et al., 2013). We further quantified the scale dependence of the striated geometry using power spectral density (PSD) analysis (following Chen et al., 2013c). Mean PSD values were obtained by averaging the PSD of each of the 256 AFM profiles, taken both normal and parallel to the shear direction, and plotted against length scale in log-log space (Fig. 4.11e). For all data, the slope β is nominally constant for length scales ranging from $2 \cdot 10^{-7}$ m to $2 \cdot 10^{-6}$ m, i.e. with β measuring 2.3 for the slip-normal profiles and 2.0 for the slip-parallel measurements. Noise in the AFM data, plus the finite length (20 μm) of the shiny patch analyzed, prevent reliable RMS and PSD values being obtained at length scales $<10^{-7}$ and $>10^{-6}$ m.

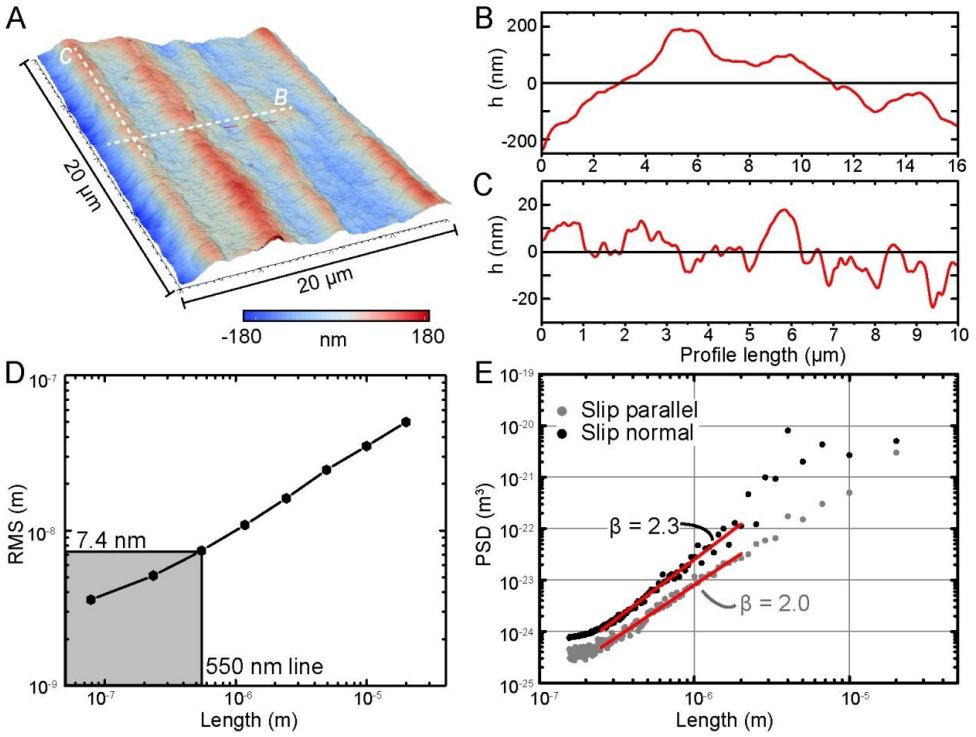

Figure 4.11. Selected AFM data from a 20x20 µm sized area of a shiny surface recovered from a velocity stepping experiment performed at ~18°C (as reported in Chapter III). a) 3D representation of the striated patch, compiled from 256x256 AFM measurements. b) and c) examples of line profiles taken normal (b) and parallel (c) to the striation direction. The zero height datum is chosen at an arbitrary reference level. d) Root mean square (RMS) roughness plotted against length scale. e) Power spectral density (PSD) plotted against length scale (constructed following Chen et al., 2013c).

4.4. Discussion

Our investigation has shown that the PSZs formed in simulated calcite fault gouge, sheared nominally dry at v = 1 µm/s, T = 18 or 140°C, and σ_n^{eff} = 50 MPa, consist of thin, nanogranular sheets containing locally dense planar zones seen as striated shiny surface patches when exposed by splitting (Figs. 4.4 to 4.6). The dense planar zones are embedded in a matrix of nanospherular grains around ~100 nm in diameter. FIB-SEM sectioning showed that the PSZ is generally 10 to 50 µm thick and characterized by a porosity of ~20 to 30%, whereas the dense zones or shiny surface patches are 0.1 to 1 µm thick, with little visible internal structure. Correlative TEM analysis demonstrated that the shiny patches and corresponding thin dense zones consist of aligned nanofibres composed of sintered chains of nanospherules that seemingly contain 5 to 20 nm sized

crystallites characterized by a CPO, i.e. by an alignment of (104) in the shear plane (Figs. 4.6 to 4.10). Remarkably, these fibrous nanocoatings are ductile at room conditions. Surface roughness analysis applied to shiny surface patches revealed a striated nanoscale topography with grooves running parallel to the shear direction and nanofibre orientation (Fig. 4.11).

Mechanically, all samples showed similar near-steady-state frictional strength values, characterized by μ-values of 0.6 to 0.8. These values are fully consistent with those reported by Verberne et al. (2013a, b) (Chapter III) for the same materials, and by Verberne et al. (2010) (Chapter II), Tesei et al. (2014) and Carpenter et al. (2014) for simulated gouges prepared from limestone, sheared under the same or similar testing conditions. Our microstructural observations are also consistent with, though much more extensive than, those of Verberne et al. (2013a, b) (i.e. Chapter III), who reported on the development of nanocrystalline slip zones or PSZs with a c-axis preferred orientation in the same gouge material, sheared under the same testing conditions as used here. In the following, we discuss the microphysical mechanisms that may have controlled the frictional behaviour seen in our experiments, using an existing mechanistic model for shear of granular media under conditions where both dilatation and diffusive mass transfer operate. We continue by discussing the nanoscale mechanisms that may account for the formation of the observed nanocrystallites, the sintered nanospherules, the aligned nanofibres, and the CPO observed in the PSZ, and we compare the microstructures developed in our (low velocity) experiments with those reported to form in calcite sheared at coseismic slip velocities. Finally, we summarize the geological implications of our work.

4.4.1. Microphysical mechanisms controlling friction

We start by making a detailed comparison of the present results with our previous work on microstructure of simulated calcite gouge deformed in direct shear. First, it is clear that the boundary-parallel and inclined shear bands seen in our samples (Fig. 4.4) correspond with the boundary-parallel and inclined, nanocrystalline slip zones reported by Verberne et al. (2013a, b) (i.e. in Chapter III). In contrast to the approach employed here, however, Verberne et al. (2013a, b) used optical thin sections from recovered samples, prepared in an orientation normal to the shear plane and parallel to the shear direction. In this way, the full PSZ was shown to be laterally continuous, measuring ~10 to 150 μm wide, which is consistent with the FIB-SEM analyses of the general structure

of the PSZ reported here (Fig. 4.5). Verberne et al. (2013a, b) also reported the presence, in shear band cores, of dense aggregates of rounded particles composed internally of ~5 to 20 nm-sized crystallites, which is the same as that observed here from FIB-SEM and TEM study of a sectioned nanofibrous coating (Figs. 4.6, 4.9, 4.10). Taking all observations together leaves little doubt that the PSZ developed in all experiments represents a continuous, sheet-like, nanogranular zone with a relatively high porosity (ϕ ≈ 20-30%, see also Chapter III). However, it is more difficult to establish whether, or to what extent, the internal shiny surfaces (i.e. the dense planar bands) developed within the PSZ are laterally continuous in our samples. The fact that shiny surfaces are found at different topographic levels throughout the PSZ, suggests they probably form isolated patches rather than a single, through-going, ~1 μm thick film or veneer. This means that in our samples, the entire, 10 to 100 μm thick PSZ, plus internal nanofibrous films, played a role in accommodating the imposed displacement.

Although we recognize that a (more) continuous, specular film may form at shear strains beyond those applied in our experiments (cf. Han et al., 2007b; Fondriest et al., 2013; Smith et al., 2013), the above means that in order to understand the mechanisms that control frictional strength and stability in our short displacement, low-velocity experiments, we must consider the mechanisms that operated within the bulk PSZ and within the internal shiny surfaces. To this end, using the FIB-SEM and TEM microstructures as a starting point, we constructed the following simple conceptual model (Figs. 4.12a-c). The porous, dominantly spherular grain structure observed within the body of the nanogranular PSZ (Figs. 4.5, 4.9) suggests that dilatant granular flow involving spherule-rolling and neighbour-swapping (Fig. 4.12a) must have occurred in our experiments, while the fibrous films (Figs. 4.6, 4.7) point to sliding of layers of sintered, linear chains of nanospherules, i.e. of nanofibres, over one another (Fig. 4.12b). At the same time, the ubiquitous evidence for neck-growth (sintering) between nanospherules and within fibres (Figs. 4.5 to 4.9), implies that diffusive mass transport was rapid on the nanospherule scale (Figs. 4.12b, c).

A microphysical model for shear of fault gouge involving combined granular flow and diffusive mass transport was recently proposed by Niemeijer & Spiers (2007), and developed further by Den Hartog & Spiers (2013, 2014) and Chen (2015). In this model, shear strength is controlled by competition between dilatational granular flow and diffusion-controlled compaction (Appendix 4.A). The model is, in essence, similar to the Ashby-Verrall model for superplasticity due to diffusion-accommodated grain boundary

sliding (GBS) (Ashby & Verrall, 1973) (Fig. 4.12d), but differs in that it allows for frictional GBS and for intergranular cavitation, i.e. for porosity generation by dilatation when diffusive mass transport is too slow to accommodate GBS fully (e.g. Kassner & Hayes, 2003; Fusseis et al., 2009). The Niemeijer-Spiers mechanism predicts that when stress-driven diffusive mass transfer is negligible, steady state frictional strength is controlled by velocity neutral or velocity strengthening, critical state granular flow (Den Hartog & Spiers, 2014). However, when diffusive mass transfer becomes fast enough (e.g. with increasing temperature or decreasing strain rates), a transition is predicted to occur, to a balance between dilatant granular flow and compaction creep by diffusion. Niemeijer and Spiers (2007) show that such a balance leads to an increase in steady-state porosity with increasing shear rate, causing a decrease in steady-state frictional strength and hence velocity weakening behaviour (see also Appendix 4.A). For an Arrhenius-type creep process such as diffusion, this is consistent with a thermally-activated transition from velocity strengthening to velocity weakening, of the type observed in our experiments on simulated calcite-rich gouges conducted in the range 18-150°C (Verberne et al., 2010, 2013a, b, or Chapters II and III).

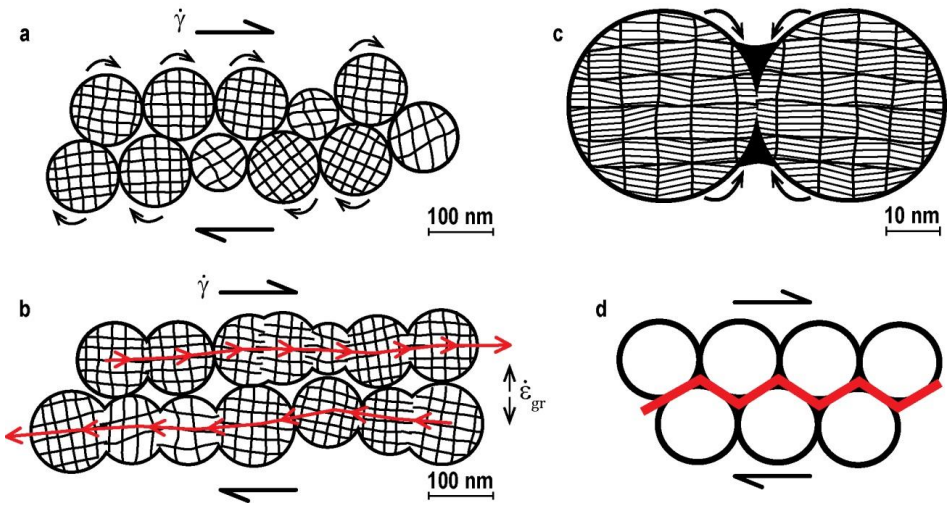

Figure 4.12. Two-dimensional representation of the mechanisms of nanogranular flow and nanofibre formation envisaged within PSZs seen in the present experiments. a) Nanospherule rolling and grain-neighbour swapping with incomplete accommodation by diffusive mass transport hence cavitation/ dilatation. b) Local sintering attachment (neck growth) at preferred high energy interfaces oriented normal to the calcite (104) rhomb plane, leading to c) formation of cooperatively sliding nanofibres (linear arrays or chains of sintered nanospherules). Note the cavitation (porosity) development in (a) to (c), compared with d), a zero-porosity, grain boundary sliding mechanism that is fully diffusion-accommodated, i.e. the mechanism of superplasticity described by Ashby & Verrall (1973).

However, to produce velocity weakening shear involving a balance between dilatation and diffusion-controlled compaction, or to produce a transition thereto, the Niemeijer-Spiers model (Niemeijer & Spiers, 2007) requires that diffusion-controlled deformation rates are of similar order to the imposed shear strain rate ($\dot{\gamma}$). This is explained in detail in Appendix 4.A. Specifically, the compaction strain rate $(\dot{\varepsilon}_{cp})$ of porous nanogouge due to diffusion must be equal to the dilatation strain rate $(\dot{\varepsilon}_{gr} \approx \tan(\Psi) \cdot \dot{\gamma})$ due to pure granular flow, where ψ is the dilatancy angle for granular flow (Niemeijer & Spiers, 2007). To test if this is the case for our samples, we estimate the dilatation rate from the shear rate imposed on the PSZ by assuming a dilatation angle of ~35° for granular flow, i.e. using $\dot{\varepsilon}_{gr} \approx 0.7\dot{\gamma}$, and we compare $\dot{\varepsilon}_{gr}$ with compaction rates $\dot{\varepsilon}_{cp}$ predicted by equations describing compaction of wet calcite by diffusive mass transport (Spiers et al., 2004; Zhang et al., 2010b) – see Appendix 4.B for details. We chose wet calcite because calcite nanoparticles strongly adsorb thin aqueous films from atmospheric water vapour (e.g. Bohr et al., 2010; Forbes et al., 2011), to which our samples were all exposed before and during testing (via the pore fluid system). Moreover, thermogravimetric analysis that we performed on nanocrystalline calcite powder with an average particle size ~80 nm revealed a water content of 2-3 wt% after exposure to lab air (Fig. 4.13). In the case of the

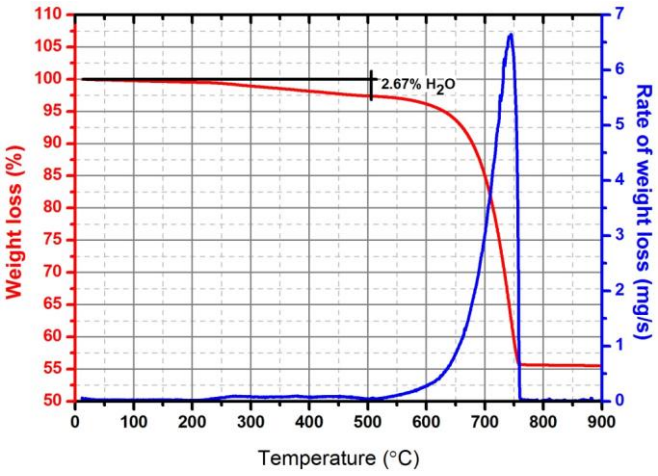

Figure 4.13. Thermogravimetric analysis of pure nanogranular calcite (average particle size ~80 nm) purchased from MK Nano, Canada. The steady decrease in mass starting from around 100°C and continuing to around 500°C, as opposed to a sharp peak, suggests that adsorbed H_2O is progressively removed from the calcite surface (see also Forbes et al., 2011). Full decomposition into CaO and CO_2 occurs at 600-750°C.

nanogranular PSZs formed in our experiments, a simple calculation of the surface area present per unit mass of nanogranular PSZ implies the presence of an adsorbed water film of ~1 to 2 nm coating each ~100 nm particle, which is similar to that considered necessary for water-assisted mass transfer to operate (Spiers et al., 2004; Koelemeijer et al., 2012; Gratier et al., 2013). Taking the width of the active slipping zone in the present experiments, conducted at 18 to 140°C, to be 1 to 50 μm, then $\dot{\gamma}$ or $\dot{\gamma}_{gr}$ in the PSZ was of the order of $[10^{-2} - 10^{-1}]\ s^{-1}$, so that $\dot{\varepsilon}_{gr} \approx [10^{-2} - 10^{0}]\ s^{-1}$ (Appendix 4.B). Using the above-mentioned data on compaction creep of wet calcite by diffusive mass transport (Zhang et al., 2010b), and assuming a nanospherule size of 100 nm, compaction creep of the PSZ is predicted to occur at a rate $\dot{\varepsilon}_{cp} \approx [10^{-2} - 10^{0}]\ s^{-1} \approx \dot{\varepsilon}_{gr}$.

In an order-of-magnitude-sense, this confirms that the compaction creep and dilatation strain rates in our experiments were competitive, and hence that the Niemeijer-Spiers model may be applied to our experiments. According to the model, the transition from velocity strengthening to velocity weakening seen in our experiments above 80° to 100°C is expected to result from the higher relative contribution of creep to the accommodation of imposed strain at these temperatures. This implies that, for the Niemeijer-Spiers model to be (qualitatively) consistent with this transition, the creep strain rate above 80°-100°C should be higher than that at 18° to 80°C, despite a decrease in solubility of calcite in water in this range which will tend to offset the positive effect of temperature on diffusion coefficient in determining net diffusion rates (Liteanu et al., 2012). To investigate this, we calculated the ratio $\dot{\varepsilon}_{cp}(T)/\ \dot{\varepsilon}_{cp}(18°C)$ for $18° \leq T \leq 150°C$, using well-established literature values and/ or expressions for the parameters appearing in the constitutive equation describing$\dot{\varepsilon}_{cp}(T)$, specifically for the solubility and diffusion coefficient of calcium carbonate in water and/or in thin water films (Appendix 4.B). This showed that, for values of the (apparent) activation energy Q_d in excess of ~25 kJ/ mol, the creep strain rate above 80°C is consistently higher than that below this temperature, i.e. $\dot{\varepsilon}_{cp}(80° < T \leq 150°C) > \dot{\varepsilon}_{cp}(18° \leq T \leq 80°C)$ (Fig. 4.A.1). A value for Q_d in excess of ~25 kJ/mol is in reasonable agreement with available data on the (empirical) apparent activation energy for diffusion through a thin aqueous film adsorbed to grain boundaries (Spiers et al., 1990; Nakashima, 1995), with Zhang et al. (2010), and with the diffusion-controlled dissolution reaction of calcite (Sjöberg & Rickard, 1984 - see Appendix 4.B). Therefore, the Niemeijer-Spiers model is capable of explaining the velocity weakening behaviour seen in our experiments at temperatures above 80° to 100°C, and suggests

that this behaviour is caused by enhanced compaction rates due to faster diffusive transport at these temperatures.

To estimate compaction creep rates due to solid state (i.e. fully dry) grain boundary diffusion, for comparison with the above approach, we applied eq. 4.B.1 taking *C* as 1 and *DS* as the product of the grain boundary self-diffusion coefficient and the effective grain boundary thickness in the solid state – as appropriate for self diffusion (cf. Ashby & Verrall, 1973). We used data on *DS* determined at temperatures in the range 650° to 850°C by Farver & Yund (1996), recognizing that extrapolation to temperatures of 18°-140°C relevant to our experiments is useful only in a crude order of magnitude sense. Even for a grain size of 10 nm, as observed at the sub-nanospherule scale within the fibres (Fig. 4.10g), this yields $\dot{\varepsilon}_{cp} \approx [10^{-25} - 10^{-13}]\, s^{-1}$, which is a minimum of eleven orders of magnitude slower than the dilatation rate from granular flow expected in our experiments (Appendix 4.B). Solid state diffusion, therefore, most definitely cannot explain the low temperature behaviour seen in our experiments. However, following the same approach putting again d = 10 nm, but for temperatures of 500° to 700°C, yields $\dot{\varepsilon}_{cp} \approx [10^{-1} - 10^{2}]\, s^{-1}$. Such high temperatures and fine grain sizes are frequently encountered in high-velocity friction experiments on calcite (see Han et al., 2007a, b, 2010). For a PSZ 100 µm wide, the value of $\dot{\varepsilon}_{cp} \approx [10^{-1} - 10^{2}]\, s^{-1}$ is close to the imposed dilatation rates $\dot{\varepsilon}_{gr} \approx [10^{2} - 10^{3}]\, s^{-1}$. (eq. AI.2) in experiments at sliding velocities of 0.1 to 1 m/s. This suggests that the Niemeijer-Spiers mechanism may also apply to ultra-fine grained fault slip surfaces in calcite undergoing frictional heating at co-seismic slip rates, through the action of high temperature creep involving solid state grain boundary diffusion.

However, the micromechanical framework developed by Niemeijer-Spiers (Niemeijer & Spiers, 2007), and its subsequent modifications by Den Hartog & Spiers (2013, 2014) and Chen (2015), are of course idealized. The model assumptions are reasonable at low slip rates, but undoubtedly break down when different, dynamic fault rupture processes such as melting, decarbonation, or flash heating come into play (for a summary see Di Toro et al., 2011). Extrapolation of the Niemeijer-Spiers mechanism to co-seismic slip rates therefore requires more elaborate modelling incorporating such effects. Experiments spanning velocities across the full range of sliding velocities from 1 nm/s to 1 m/s are also needed - these developments have yet to happen, and are beyond the scope of the present study.

4.4.2. Formation of the PSZ nanostructures and CPO

On the basis of the above, the Niemeijer-Spiers model seems able to account for the thermally-activated transition to velocity weakening shear seen in simulated calcite gouges sheared at 18-150°C (see also Appendix 4.B). It is also consistent with the porosity and neck growth structures observed in the PSZ. However, the Niemeijer-Spiers mechanism cannot account for the formation of the observed nanocrystallites, nanospherules, aligned nanofibres or CPO. These micro-/ nanostructures point to the operation of additional deformation processes besides granular flow and diffusive mass transfer.

We reiterate here that all observations from the micro/ nanostructure analyses reported in the present study are consistent with those reported by Verberne et al. (2013a, b) (or Chapter III). To explain the formation of ~5-20 nm crystallites observed here at the sub-spherule scale, these authors pointed out that the shear strain rates characterizing the PSZ are similar to those associated with nanocrystallization of steels due to rapid, high strain plastic deformation (10^0-10^3 s^{-1}) (e.g. Umemoto, 2003). Indeed, the internal polycrystalline substructure of the nanospherules and -fibres that we infer from our present observations (Fig. 4.10), bears a striking similarity to microstructures found in shocked ductile metals (Tao et al., 2002; Yang et al., 2010). As in metals, the high ductility of calcite (e.g. Kennedy & White, 2001; De Bresser et al., 2002) may therefore allow the observed ~5-20 nm substructure (Fig. 4.10g) to form by progressive development of nano-cell walls from dense dislocation networks and tangles generated by low temperature crystal-plasticity (e.g. r(104) slip or e(108) twinning – De Bresser & Spiers, 1997). Following from this, we speculate that plastic deformation and/ or fracturing and abrasion occurring at parent grain surfaces led to the detachment of ~100 nm sized nanocrystalline clusters or fragments from these micron-sized parent grains (cf. Tao et al., 2002; Umemoto, 2003; Yang et al., 2010; Siman-Tov et al., 2013). The nanograins produced in turn rounded to form the rolling, grain-neighbour-swapping nanospherules comprising the porous nanogranular PSZ. To further unravel the formation mechanism of nanocrystallites and nanospherules in calcite gouge is a challenging task which requires more elaborate experiments and micro-/ nanostructural analyses, and we reserve this for future work.

Aside from the origin of the nanospherules, all samples investigated showed evidence for neck growth (sintering) between them, in both the PSZ (Fig. 4.5c, inset) and internal shiny surface zones (Figs. 4.6, 4.9). In particular, near the edge of fibrous shiny surfaces,

where the fibres grade into the bulk nanogranular PSZ, nanospherules clearly form bonded linear arrays, aligned sub-parallel to the shear-direction (Fig. 4.6e-h). This strongly suggests that the fibres that constitute the shiny surfaces formed by progressive, linear, nanospherule chaining involving intergranular neck growth (Fig. 4.12b, c). However, this does not explain the CPO seen in the nanofibre substructure. In view of the general consistency between the CPO data of Verberne et al. (2013a, b) and the CPO seen in the nanofibres here (Fig. 4.10f), we follow Verberne et al. (2013a, b) by inferring that the CPO in the nanofibres represents alignment of the (104)[$\bar{2}$01] plane and direction (sub-) parallel to the shear plane and shear direction respectively. However, Verberne et al. (2013a, b) attributed this CPO to crystal plasticity involving r-glide, i.e. to slip on the (104)[$\bar{2}$01] system in calcite causing an alignment of this system in the shear plane. Along with e-twinning, the r-slip system is the dominant glide system in calcite at low temperatures (De Bresser & Spiers, 1997). Although crystal plasticity dominated by r-glide may have played a role in generating the nanospherules and internal crystallites (cf. Tao et al., 2002), as discussed above it is not self-evident from our results how this process could produce a CPO in the context of the nanogranular flow and nanofibre formation mechanisms proposed here (Fig. 4.12). Clearly, other processes must have (also) played a role.

One potential mechanism for CPO formation during granular flow with active diffusive transport is that of nanoparticle coalescence or aggregation by oriented interface attachment (OA). This is widely reported as a mechanism by which nanocrystallites can rapidly coalesce to form single crystals in numerous nanomaterials (Penn & Banfield, 1998, 1999; see also reviews by Niederberger & Cölfen, 2006; Zhang et al., 2010a), including in calcite (Gehrke et al., 2005). In an OA event, the thermodynamic driving force for coalescence originates from crystallographic orientation-dependent, interatomic Coulombic interactions arising from both the surface atoms and of atoms within the interior of the approaching nanoparticles (Zhang & Banfield, 2012, 2014). This is expected to lead to reduction of total surface energy (Penn & Banfield, 1998; Nieberger & Cölfen, 2006), which, in the case of calcite, would lead to alignment of the lowest energy (104) plane (De Leeuw & Parker, 1997). Following the OA mechanism, we now suggest that in all our shear experiments on simulated calcite gouge (including those reported by Verberne et al., 2013a, b), the strong anisotropy in the surface energy of calcite produced preferred sintering (neck growth) at high-energy crystallographic interfaces between neighbouring spherules undergoing rotational grain neighbour-

swapping during nanogranular flow, leading to dynamic chaining and alignment of the lowest energy (104) plane and [$\bar{2}$01] direction parallel to the shear plane (Figs. 4.12b, c), and thus to the observed fibrous structure and CPO.

4.4.3. Comparison with microstructures formed in HVF experiments

Recent microstructural studies of dolomite and limestone samples sheared at high sliding velocities (v > 0.05 m/s) suggest the following characteristics of shiny, striated slip surfaces and surface patches:

a) They form only at high mechanical work input rates or power densities (PD, given $\dot{W} = \sigma_n^{eff} \cdot \mu \cdot v$ Ws^{-1}) (Boneh et al., 2013; Fondriest et al., 2013)
b) They are associated with dynamic recrystallization caused by heating at coseismic slip rates (Smith et al., 2013)
c) They are at least in part responsible for the strong dynamic weakening often seen in samples sheared at coseismic slip rates (Chen et al., 2013c).

However, the shiny patches formed in our low velocity experiments, i.e. at a shearing velocity of only 1 µm/s, show very similar striated form and nanoscale topography (Fig. 4.10a-c) to those formed in HVF experiments (cf. Tisato et al., 2012; Boneh et al., 2013; Chen et al., 2013c; Fondriest et al., 2013). This suggests at least some degree of shared origin, regardless of areal extent or of shearing velocity.

In rotary shear experiments on cylindrical cores of dolomite and limestone performed at v = 0.002-0.96 m/s and σ_n^{eff} = 0.25-6.9 MPa, Boneh et al. (2013) showed that shiny striated slip-surface patches started to develop only at PD values $\dot{W}$ in excess of 30 kW/m^2. The cumulative area covered by these patches increased with increasing PD, ultimately producing a continuous, highly-reflective principal slip surface, similar in appearance to that reported by Han et al. (2007b) or Smith et al. (2013), for example. In experiments on simulated gouge prepared from dolostone, performed at v = 0.001-1.13 m/s and σ_n^{eff} = 13-26 MPa, Fondriest et al. (2013) showed that shiny surfaces developed only at PD values > 40 kW/m^2, covering an area of the sample that progressively increases with increasing displacement. By contrast, the shiny patches developed in simulated calcite gouge reported here formed at power densities of $\dot{W} = \sigma_n^{eff} \cdot \mu \cdot v$ = 50 MPa x (0.7±0.1) x 10^{-6} m/s = 35±5 W/m^2, i.e. 2 to 5 orders of magnitude lower than considered necessary for them to form in HVF experiments. This demonstrates that such shiny striates surfaces do not exclusively form at the high power densities (>30-40 kW/m^2) associated with HVF experiments and with coseismic slip rates.

This implies that reflective PSZs cannot be used as field indicators of past coseismic slip in carbonates rocks (Siman-Tov et al., 2013; Fondriest et al., 2013), without additional geological or microstructural evidence. In the HVF experiments on simulated calcite gouge performed by Smith et al. (2013), at v > 0.1 μm/s at σ_n^{eff} = 2-26 MPa, the development of highly-reflective PSZs was shown to be associated with the presence of dynamically recrystallized grains adjacent to the slipping zone, while the PSZ itself was composed of statically recrystallized grains. This was explained as due to the attainment of high temperatures (650-900°C) reflecting heat dissipated in the PSZ during localized frictional slip at coseismic rates (Smith et al., 2013). In our experiments, we observed no evidence for conventional dynamic recrystallization or for static recrystallization, either in or adjacent to the PSZ, nor is this likely to have occurred considering the low slip rates, temperatures, and PD values applying to our tests. This suggests that the presence of a statically recrystallized PSZ, with adjacent dynamically recrystallized grains, may indeed offer a useful indicator of past high-velocity slip in limestones (Smith et al., 2013; Ree et al., 2014). At the same time, we argue that microstructures from high displacement, low-velocity shear experiments performed at high temperatures (T = 200-600°C), i.e. where crystal plastic flow and dynamic recrystallization become important at low strain rates (cf. e.g. Heard, 1960; De Bresser et al., 2002; Barnhoorn et al., 2004), must also be critically examined before this can be concluded with certainty (B. A. Verberne et al., manuscript in preparation - see Chapters V and VI).

Lastly, we consider whether the strong dynamic weakening frequently observed in HVF experiments on carbonates (see e.g. Han et al., 2007a, b; 2010, 2011; Di Toro et al., 2011) can be explained by slip-parallel, nanoscale smoothening, as proposed by Chen et al. (2013c). In this context, we note that the mechanical data from our experiments do not show strong dynamic weakening (Fig. 4.2, see also Chapters II and III), though the surface roughness characteristics of the shiny patches formed here are very similar to those formed at coseismic slip rates (Tisato et al., 2012; Chen et al., 2013c; Fondriest et al., 2013). The slope or β-value of 2.3 determined from power spectral density (PSD) analysis normal to the striation/ shear direction, in the AFM analysis of a shiny surface produced in our experiments, is consistent with the value of 2.4±0.1 reported for HVF surfaces by Chen et al. (2013c). Parallel to the striation/ shear direction, these authors found β = 1.4±0.4, which is slightly lower than the value of 2.0 reported here. In both cases, a strong anisotropy in roughness and hence sliding resistance is implied. Of course, the total displacement achieved in our experiments was small (4-5 mm) compared with

that attained in HVF tests (typically >>0.1 m – e.g. Di Toro et al., 2010), and the specular surfaces less continuous. This may explain why strong dynamic weakening effects were not observed in our tests. On the other hand, significant shiny surface area did form at the low displacements achieved in our experiments, implying that the presence of shiny patches within the PSZ does not lead to weakening of the type observed in HVF tests, and that the smoothening process envisioned by Chen et al. (2013c) is not effective at v = 1 μm/s, σ_n^{eff} = 50 MPa, T = 18 to 140°C and displacements < 5 mm.

4.4.4. Origin of carbon-rich phases

Recently, Oohashi et al. (2014) demonstrated the formation of carbonaceous films in HVF experiments involving rotary shear of solid Carrara Marble cylinders, rock on rock. These films formed as a product of the thermal decomposition of calcite. It is therefore important to consider the origin of the amorphous carbon deposits found in our samples (Fig. 4.8e). In the experiments conducted by Oohashi et al. (2014), at v = 1.3 m/s and σ_n^{eff} = 2-3 MPa, the frictional heating temperature reached 580° to 700°C over displacements of 50 to 100 m. Amorphous carbon formed only under strongly reducing conditions, i.e. in the presence of free H_2 gas. In our experiments, the imposed sliding velocity was only 1 μm/s over displacements of just 4 to 5 mm, the power density was only 30 to 40 W/m^2, no temperature increases were measured at the sample, and the sample porosity was at all times drained to air via the pore fluid piping system. On this basis, thermal decomposition of calcite and associated carbon precipitation seem highly unlikely in our samples. Moreover, the presence of the carbon-rich phase appeared to be random in our samples, showing no correlation with any trends in mechanical data, any specific microstructure, or with the origin of the calcite used (Table 4.1). On this basis, we infer that the carbon-rich deposits seen in some of our experiments must be derived from the EPDM jackets used in our sample assembly, as these are the only common factor in the experiments that showed these deposits.

4.4.5. Superplasticity in geological materials vs. the present samples

Homogenous deformation to very large strains without loss of continuity, i.e. "superplastic" deformation (Gilotti & Hull, 1990), is well-known to occur in nanocrystalline metals and ceramics (for reviews see Nieh et al., 1997; Tjong & Chen, 2004; Meyers et al., 2006), even at room temperature and/ or pressure and at relatively high strain rates (10^{-4} to 10^{-2} s^{-1}) (Lu et al., 2000; Liu et al., 2007). However, such deformation phenomena have only recently been demonstrated in geological materials.

Examples include the work by Hiraga et al. (2010), who reported very large tensile strains (up to 515%) sustained without failure in creep tests on synthetic, dense, olivine aggregates (grain size ~1-2 μm) performed in air, at temperatures of 1350° to 1450°C, at strain rates of 10^{-3} to 10^{-4} s^{-1}. More recently still, compression tests on Ge-olivine, conducted at pressures of 2 to 5 GPa and at 700° to 1300°C (Schubnel et al., 2013), showed that superplastic deformation must have been responsible for shear within a 100 nm thick slip zone composed of nanocrystalline spinel (grain size ~20 to 40 nm), which developed upon sample rupture.

The principal mechanism believed to be responsible for superplastic behaviour is grain boundary sliding (GBS) accommodated by diffusion or dislocation motion (Raj & Ashby, 1971; Ashby & Verrall, 1973; see also e.g. Hirth & Kohlstedt, 1995a, b; Hansen et al., 2011). In our work on calcite gouge, we have presented evidence that the Niemeijer-Spiers mechanism of incomplete diffusion-accommodated GBS resembling Ashby-Verrall-type superplasticity (Ashby & Verrall, 1973), i.e. involving nanogranular flow and/ or nanofibre sliding plus diffusive mass transfer (Figs. 4.12a-c), can produce velocity weakening hence seismogenic fault slip on nanogranular PSZs. These processes are possible in our experiments because diffusive mass transfer is dramatically accelerated by i) the nanogranular nature of the slip zone rock that forms (see e.g. Würschumm et al., 2003; Tjong & Chen, 2004), and ii) water-enhanced grain boundary diffusion. We also envisage a similar mechanism to operate at coseismic slip rates, where the high temperatures generated will promote solid-state diffusion, as discussed in Section 4.1.

The evidence found in our experiments for deformation of PSZ material by a mechanism of low temperature nanogranular/ nanofibre sliding with partial accommodation by diffusion, resembling superplasticity, is supported by several microstructural observations that we have not yet discussed. Recall, for example, our observation that the nanofibres developed within the PSZ in our samples become stretched and bent upon sample recovery (Figs. 4.6c-f, 4.7, 4.8a, 4.9b). This was particularly evident in velocity strengthening samples deformed at ~18°C and provides strong evidence for plastic deformation of the nanofibres at room temperature, and. We emphasize here that EDX analyses, applied in both FIB-SEM (Fig. 4.8) and TEM, as well as SAED and HRTEM analyses (Fig. 4.10f, g), confirmed that the fibres consist of nanocrystalline calcite. The nanofibres affected often show extreme extension without localized thinning prior to fracture (Figs. 4.6c, d, 4.8a). This suggests a low stress

sensitivity of the ductile strain rate consistent with superplasticity (see Nieh et al., 1997; Tjong & Chen, 2004). In the velocity weakening samples (Fig. 4.6b), deformed at ~140°C, no evidence for plastic fibre deformation of this type was found. However, the number and area of shiny surfaces exposed was limited compared with the velocity strengthening samples. We suggest that upon termination of experiments at 140°C, ongoing static compaction of the sample microstructure at this temperature may have significantly affected the PSZ and internal shiny surfaces, especially compared with experiments performed at 18°C.

4.4.6. Geological implications

As discussed by Verberne et al. (2010, 2013a, b) (or Chapters II and III), the velocity weakening behaviour observed in our experiments on simulated calcite gouge at temperatures above 80° to 100°C may well explain the location of the upper seismogenic limit at shallow depths (~2-4 km) in tectonically-active limestone terrains, such as those characterizing the Mediterranean region (Bernard et al., 2006; Valoroso et al., 2013; Chiarabba et al., 2014). However, given the abundant recent observations of nanogranular fault surfaces developed in fault rocks of all types, in differing tectonically-active terrains (Chester et al., 2005; Ma et al., 2006; Kirkpatrick et al., 2013; Evans et al., 2014), we speculate that the role of the Niemeijer-Spiers mechanism of frictional GBS with partial accommodation by diffusion, and of superplastic fault slip, may be much more generally widespread than only in faults cutting carbonates (Smith et al., 2011; Siman-Tov et al., 2013; Collettini et al., 2014).

Finally, we emphasize once more that the development of highly-reflective, mirror-like slip surfaces in our low-velocity, small displacement experiments on simulated calcite fault gouge demonstrates that these features are not exclusively indicative of past slip at seismic slip rates. Therefore, their presence in natural fault zones cannot be used as an exclusively diagnostic field indicator of paleoseismicity without additional information.

4.5. Conclusions

We have reported a micro-/ nanostructural investigation of shear bands or PSZs developed in simulated calcite fault gouge, sheared nominally dry at 18 and 140°C, at a frictional sliding velocity (v) of 1 μm/s, and using an effective normal stress (σ_n^{eff}) of 50 MPa. At the lower temperature used, velocity strengthening slip occurs, whereas the higher temperature is characterized by velocity weakening (Verberne et al., 2010, 2013a,

b, or Chapters II and III*)*. After each experiment, PSZs developed in the sheared gouge split internally along the shear plane, displaying elongate, 0.1 to 3 mm long, shiny striated slip surface patches. We characterized samples recovered from velocity strengthening and velocity weakening samples using reflected light and electron microscopy (FIB-SEM, TEM). We also used atomic force microscopy to analyze the surface roughness of the shiny patches. Our main conclusions are as follows:

1. The PSZ consists of a porous (ϕ = 20-30%), sheet-like volume composed of 0.3 to 5 μm angular clasts embedded in a matrix of ~100 nm sized calcite nanospherules. Shiny, striated, slip surfaces are discontinuously distributed throughout the PSZ. These consist of dense, planar patches composed of sheets of aligned, ~100 nm-wide nanospherule chains or fibres, embedded at different topographic levels within the PSZ. Individual nanofibres and their constituent nanospherules contain a substructure of internal crystallites of ~5 to 20 nm in size, characterized by an alignment of the calcite (104) plane parallel to the shear plane, imparting a CPO to the PSZ. Velocity strengthening (18°C) and velocity weakening (140°C) samples showed essentially the same SEM microstructures.
2. The porous structure observed in the bulk PSZ points to neighbour-swapping granular flow of the nanospherule matrix. At the same time, widespread neck growth (sintering) structures formed between ~100 nm nanospherules suggest that diffusive mass transport played an important role. Moreover, within individual shiny surface patches, ductile bending and stretching of nanofibres along post-experiment micro-cracks suggest that the fibrous nanocoatings can deform by superplastic deformation at room conditions. A mechanism of superplastic nanogranular flow with partial accommodation by diffusive mass transport, originally proposed by Niemeijer & Spiers (2007), is put forward to explain the observed PSZ microstructure and frictional behaviour, including the transition from stable velocity strengthening to (potentially) unstable velocity weakening slip above ~80°C seen in simulated calcite gouge. The nanofibrous structure of shiny patches is attributed to crystallographically controlled neck growth between nanospherules.
3. Though less continuous, the shiny slip surfaces formed in our experiments (v = 1 μm/s) have a closely similar nanoscale striated form and topography to those reported to develop in experiments on carbonate rocks run at coseismic slip rates (v > 0.1 m/s). Natural exposures of highly-reflective fault surfaces, or 'fault mirrors', must

therefore be interpreted with caution as they are not uniquely diagnostic of past seismic slip. To confirm paleoseismic slip, additional microstructural or other geological evidence pointing uniquely to frictional heating are needed.

Appendix 4.A. The Niemeijer-Spiers model

The Niemeijer-Spiers model for shear deformation of granular materials (i.e. granular flow) is based on competition between a) athermal, rate-insensitive dilatant processes such as intergranular frictional sliding and b) thermally-activated, rate-sensitive, creep processes that allow deformation by both shear and compaction (Niemeijer & Spiers, 2007; see also Den Hartog & Spiers, 2013, 2014; Chen, 2015). In this model, diffusion is assumed to occur through a thin grain boundary fluid film, but the same principles apply for solid state grain boundary diffusion. A plot showing the type of behaviour qualitatively predicted by the model, in terms of shear strength versus shear strain rate at constant temperature, is illustrated in Fig. 4.A.1. This is drawn following Den Hartog & Spiers (2013), who assumed that grain boundary friction at the nanoscale is a weakly velocity strengthening interaction consistent with a thermally activated, shear-stress-assisted, atomic-scale jump process (cf. Rice et al., 2001).

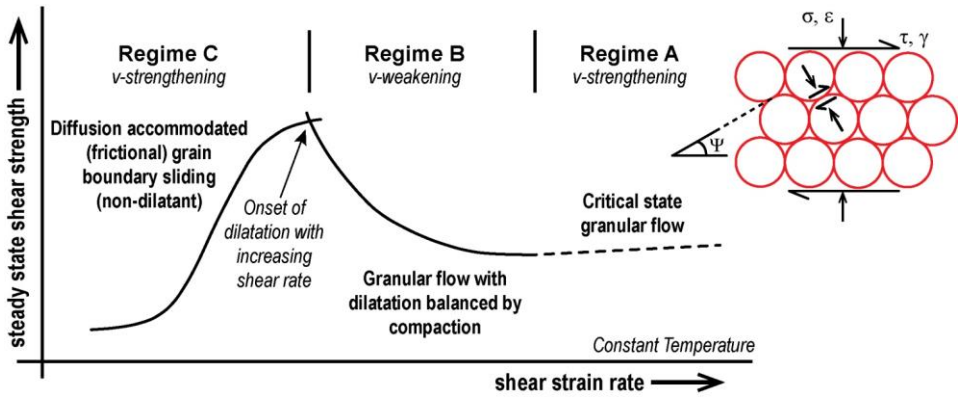

Figure 4.A.1. Qualitative model curve illustrating the dependence of steady state shear strength (or friction coefficient) on shear strain rate (or slip velocity), as predicted by the Niemeijer-Spiers model for shear deformation of granular aggregates (Niemeijer & Spiers, 2007), with the refinements introduced by Den Hartog & Spiers (2013, 2014). Increasing temperature translates this curve rightwards (Niemeijer & Spiers, 2007; Den Hartog & Spiers, 2013). The diagram on the top right illustrates the microstructure assumed in the model, including the dilatation angle. For a detailed formulation of the model see Bos & Spiers (2002a), Niemeijer & Spiers (2007), Den Hartog & Spiers (2013, 2014) and Chen (2015).

At high shear rates or low temperatures (Regime A, Fig. 4.A.1), the model predicts that frictional granular flow will dominate over slow diffusive processes, producing critical-state flow, which will be velocity strengthening due to the assumed nanoscale frictional interaction (Fig. 4.A.1) (Den Hartog & Spiers, 2013; Verberne et al., 2013b). Towards lower shear rates or higher temperatures, i.e. in Regime B (Fig. 4.A.1), compaction creep by diffusive mass transfer is fast enough to compete with dilatation (i.e. porosity generation) due to granular flow. In this regime, this competition leads to steady state flow behaviour which is characterized by a fixed steady state porosity at any given shear rate, corresponding to the condition that the compaction strain rate $\dot{\varepsilon}_{cp}$ due to diffusive mass transfer is equal and opposite to the granular dilation rate $\dot{\varepsilon}_{gr}$. This steady state porosity increases with increasing shear rate, as dilatation due to granular flow becomes more competitive, causing a decrease in steady state frictional strength hence velocity weakening (Fig. 4.A.1). Under these velocity weakening conditions, the shear strength at steady state (τ_{ss}) is described by (Niemeijer & Spiers, 2007)

$$\tau_{ss} = \frac{\mu_{gb} + \tan(\Psi)}{1 - \mu_{gb}\tan(\Psi)} \cdot \sigma_n^{eff} \qquad (4.A.1)$$

where μ_{gb} is the (velocity strengthening) grain boundary friction coefficient, Ψ is the intergranular slip surface inclination or dilatation angle at steady state, and σ_n^{eff} is the effective normal stress acting on the sheared granular material (Fig. 4.A.1). The standard relation for dilatation in granular mechanics (e.g. Gudehus, 2011) now allows tan(Ψ) to be expressed as

$$\dot{\varepsilon}_{gr} = \tan\Psi \cdot \dot{\gamma}_{gr} \approx \tan\Psi \cdot \dot{\gamma} \qquad (4.A.2)$$

at high shear rates where granular flow (strain rate $\dot{\gamma}_{gr}$) is the main strain accommodating slip mechanism. Since at steady state the compaction strain rate $\dot{\varepsilon}_{cp}$ is equal and opposite to the granular dilation rate, Ψ is in turn related to the imposed shear rate and to the rate of compaction creep via

$$\dot{\varepsilon}_{cp} \approx \left|\tan\Psi \cdot \dot{\gamma}\right| \qquad (4.A.3)$$

At the same time, Ψ can be approximated using an empirical function of the form

$$\tan\Psi = H(q-2\phi)^n \qquad (4.A.4)$$

where q = 2 ϕ_c ≈ 0.8-1, ϕ_c is the critical state porosity from granular media mechanics, ϕ is the current porosity, and H and n are constants (Niemeijer & Spiers, 2007).

At still lower shear rates (Regime C in Fig. 4.A.1), or higher temperatures, compaction and shear by diffusive mass transfer is easy hence fast enough to prevent dilatation (i.e. to fully accommodate intergranular sliding), marking a transition from dilatant frictional slip to pervasive, non-dilatant, velocity strengthening ductile flow analogous to Ashby-Verrall creep but with frictional grain boundary sliding (Bos & Spiers, 2002a).

Appendix 4.B. Calculation of dilatation and compaction rates

The dilatation strain rate due to pure granular flow of a shearing fault gouge was calculated using eq. 4.A.2. Following Niemeijer & Spiers (2007), the dilatation angle was approximated using eq. 4.A.4, taking H ≈ 1.15 and n = 1 respectively (Table 4.B.1). To estimate the compaction creep rate $\dot{\varepsilon}_{cp}$, we used an empirically calibrated theoretical law for compaction creep of granular calcite by stress-driven diffusive mass transfer through a thin, intergranular fluid film (Spiers et al., 2004). Assuming diffusion control (Zhang et al., 2010b), the equation used is given

$$\dot{\varepsilon}_{cp} = A_d \frac{\sigma_e \Omega D C S}{RTd^3} f(\varphi) \qquad (4.B.1)$$

where

$\dot{\varepsilon}_{cp}$ = 1-dimensional compaction creep strain rate [s^{-1}]

A_d = Geometrical constant

σ_e = Applied effective axial stress [Pa]

Ω = Molecular volume of the solid [m^3 mol^{-1}]

R = Gas constant = 8.3145 J mol^{-1} K^{-1}

T = Temperature [K]

D = Diffusion coefficient of the solid in the adsorbed intergranular water film [m^2 s^{-1}]

C = Solubility of the solute in the adsorbed grain boundary film [m^3 m^{-3}]

S = Grain boundary fluid film thickness [m]

d = Grain size [m]

$f(\phi)$ = $2\phi/(1\text{-}2\phi)^2$ = Function of porosity that accounts for geometric changes in grain contact area, pore wall area and transport path length during compaction (Spiers et al., 2004; Pluymakers & Spiers, 2014).

All values used for the parameters appearing in equations 4.A.2, 4.A.4, and 4.B.1 are listed in Table 4.B.1. Note that the values of D and S (eq. 4.B.1) were obtained, in terms of the product DS, from compaction experiments on granular calcite with controlled grain sizes in the range 12 to 82 μm, flooded with a saturated solution phase (Zhang et al., 2010b). These parameters roughly describe the diffusive properties of stressed grain boundaries containing a thin fluid film (Spiers et al., 2004). To a first approximation, the value of DS in nanogranular calcite containing only several percent of adsorbed water should be of the same order of magnitude as in the cited experiments, as in both cases the thickness of the grain boundary fluid lies in the same nm-range (Zhang et al., 2010b).

Term	Formula/ value	Source
H	$(\sqrt{(3)}+1/\sqrt{(3)})/2$	Niemeijer & Spiers (2007)
q	1	
ϕ	0.2	Figs. 4.5c, 4.9e
n	1	Niemeijer & Spiers (2007)
A_d	$576/3\pi \approx 61$ (for uniaxial compaction)	Pluymakers & Spiers (2014)
σ_e	$50 \cdot 10^6$ Pa	
d	$1 \cdot 10^{-7}$ m	
T	291 to 423 K	
S	1 to $2 \cdot 10^{-9}$ m	Fig. 4.13
Ω	$3.69 \cdot 10^{-5}$ m^3 mol^{-1}	Zhang et al. (2010)
D	$D = D_0 \exp\left[-Q_d / RT\right]$ $D = 1 \cdot 10^{-10}$ m^2 s^{-1} at T = 298 K $Q_d = 1.5 \cdot 10^4$ to $3.7 \cdot 10^4$ J mol^{-1}	Sjöberg & Rickard, 1984; Nakashima (1995); Spiers et al. (1990);
C	$C \approx \sqrt{K_s}$ $Log(K_s) = -171.9605 - 0.077993T + 2839.319/T + 71.595Log(T)$	Plummer & Busenberg (1982)
$f(\phi)$	$f(\phi) \approx 2\phi/(1\text{-}2\phi)^2 \approx 1.1$	Spiers et al. (2004) Pluymakers & Spiers (2014)

Table 4.B.1: List of values/ expressions used for the terms appearing in equations 4.A.2, 4.A.4, and 4.B.1.

Furthermore, the value of DCS is sensitive to temperature through both the solubility

C and the diffusion coefficient *D*. Within the range from 18° to 150°C, the solubility of calcite decreases monotonically with increasing temperature (Plummer & Busenberg, 1982), while the temperature sensitivity of *D* depends on the value of the apparent activation energy (Q_d) via an Arrhenius relation (see Table 4.B.1). Although to our knowledge the value of Q_d for dissolution of calcite involving diffusive transport through an aqueous thin film adsorbed to nanograin boundaries - as applicable to our experiments – is still unknown, a sound estimate can be made using existing data on transport-controlled dissolution processes. Lasaga (1984, 1998) suggests that the activation energy for diffusion of ions in bulk water is in general ~21 kJ/mol, however, as diffusion through a more rigid, aqueous thin film is much slower (Alcantar et al., 2003) this implies a higher value of Q_d. Spiers et al. (1990) found a value of $Q_d \approx 25$ kJ/mol for water-assisted grain boundary diffusion from compaction experiments on wet granular NaCl powder, consistent with the 'general' range for Q_d of 15-30 kJ/mol as suggested by Nakashima (1995). Meanwhile, for the diffusion-controlled dissolution reaction of calcite in aqueous KCl solutions, Sjöberg & Rickard (1984) found an empirical apparent activation energy of ~37 kJ/mol. Using these values for Q_d to evaluate the acceleration in pressure solution creep between our experiments at 18° and 150°C, we calculated the ratio of the strain rate at a given temperature *T* relative to that at 18°C (291 K), i.e. $\dot{\varepsilon}_{cp}(T)/\dot{\varepsilon}_{cp}(18°C)$ (Figure 4.BI). The results show that for $Q_d \geq$ ~25 kJ/mol, $\dot{\varepsilon}_{cp}$ at 80° < $T \leq$ 150°C is at all times higher than for 18° ≤ $T \leq$ 80°C.

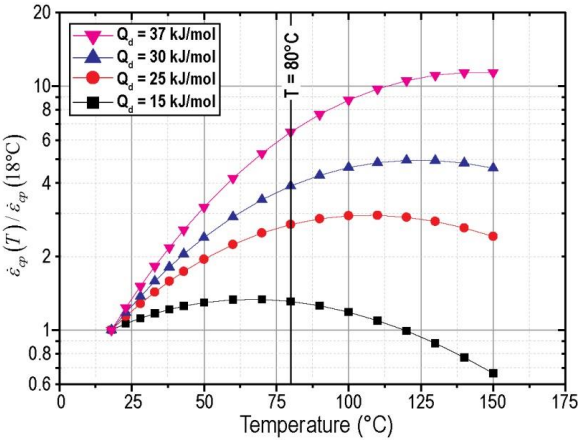

Figure 4.B.1. Plot of $\dot{\varepsilon}_{cp}(T)/\dot{\varepsilon}_{cp}(18°C)$ against temperature, using activation energies (Q_d) ranging from 15 to 37 kJ/mol, characteristic for water-assisted (grain boundary) diffusion of calcite (Sjöberg & Rickard, 1984; Spiers et al., 1990; Nakashima, 1995).

Acknowledgements

André Niemeijer, Hans de Bresser, and Virginia Toy are acknowledged for insightful discussions. Peter van Krieken is thanked for conducting the particle size and thermogravimetric analysis, and Gert Kastelein and Eimert de Graaff are for technical support. Vu Hoang Trung is thanked for additional support. All microscope analyses were carried out at Utrecht University, with the exception of the AFM measurements, which were carried out by Helen King at the University of Münster, Germany.

Chapter V

Frictional-viscous transition in simulated calcite fault gouge sheared at 20-600°C and implications for seismogenesis in limestones

After:
Verberne, B. A., De Bresser, J. H. P., Niemeijer, A. R., and Spiers, C. J. Frictional-to-viscous transition in simulated calcite fault gouge sheared at 20-600°C: Implications for seismogenesis in limestones. *Submitted to J. Geophys. Res.*

Abstract

This Chapter reports ring shear experiments on simulated calcite fault gouges (median grain size ~20 μm) performed at fixed temperatures (T) within the range of 20° to 600°C. The experiments were performed wet, using pore fluid pressures (P_f) in the range 10 ≤ P_f ≤ 100 MPa. One series of experiments employed a constant effective normal stress (σ_n^{eff}) of 50 MPa, while in a second series σ_n^{eff} was stepped in the range 30 to 100 MPa. In all experiments, sliding velocity (v) was stepped in the range 0.03 to 100 μm/s. The results showed velocity strengthening frictional behaviour at 20°C but velocity weakening at 100° to 550°C. The latter was frequently accompanied by stick-slip, especially at the lower sliding velocities and higher temperatures. At 600°C, velocity strengthening occurred. Microstructural observations suggest increasing importance of ductile deformation processes with increasing temperature, reflected by a localized shear band structure at 20°C giving way to a pervasive shear-plane-parallel grain shape fabric at 600°C. While samples sheared at 400-550°C exhibited essentially brittle/ frictional mechanical behaviour including stick-slip, the corresponding microstructures resemble that of a ductile mylonite. From a comparison of our results with flow equations for dense calcite polycrystals, we show that dislocation and/ or diffusion creep processes likely played a role in our experiments conducted at T ≥ 400°C. We argue that the operation of creep processes during granular flow causes velocity weakening hence potentially unstable slip in calcite fault rocks, even at temperatures as high as 550°C. Our results imply that the seismogenic zone in overpressurized carbonates may extend to 13-24 km depth, potentially explaining recent earthquakes recorded in suspected deep carbonates.

5.1. Introduction

The seismogenic zone in the upper-crust is characterized by pressure and temperature conditions under which fault zones exhibit abrupt, periodic failure, producing earthquakes, as opposed to stable sliding or "fault creep". For quartzo-feldspathic crust, this zone typically lies in the depth range from ~2-4 km down to ~10-12 km (Fig. 5.1a) (e.g. Sibson, 1982, 1983; Scholz, 1988; Rutter et al., 2001; Fagereng & Toy, 2011), varying between different tectonic settings, depending especially on local geotherm (e.g. Ito, 1990, 1999). At depths shallower than the upper boundary of the seismogenic zone, aseismic fault slip is believed to reflect stable frictional sliding within poorly consolidated, granular or phyllosilicate-rich, fault rock (Marone & Scholz, 1988; Marone et al., 1990; Moore & Saffer, 2001; Scholz, 2002; Ikari et al., 2009). Below the lower boundary of the seismogenic zone, earthquake nucleation is thought to be inhibited by the dominance of plastic or viscous deformation mechanisms (e.g. Sibson, 1982, 1983; Tse & Rice, 1986; Shimamoto, 1986, 1989; Scholz, 1988). However, the deformation mechanisms that control fault motion and the nucleation of unstable slip within the seismogenic zone, which includes the frictional-to-viscous transition, remains poorly understood.

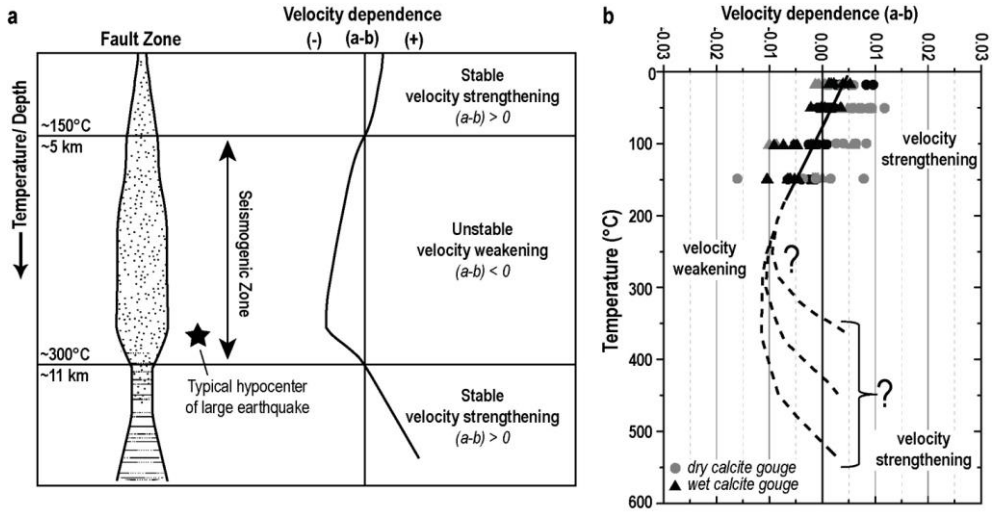

Figure 5.1. a). Conceptual fault zone model, after Sibson (1982, 1983) and Scholz (1988). Seismological evidence suggest that the strongest earthquakes nucleate near the base of the seismogenic zone (e.g. Sibson, 1982, 1983). b). Velocity dependence of the frictional strength of simulated calcite gouges vs. temperature. Data points correspond to measured *(a-b)* values obtained in Chapter III, for dry (black symbols) and wet (grey symbols) samples. Dashed lines illustrate the hypothetical extrapolations to higher temperatures that are under investigation in the present study.

Using a spring-slider model to represent a fault and the surrounding elastic rock, Ruina (1983) showed that for a fault to produce a periodic instability, or seismogenesis (Brace & Byerlee, 1966), it must exhibit velocity weakening frictional properties. If fault strength increases with increasing displacement rate, the fault is said to be velocity strengthening, and will exhibit stable sliding without seismogenesis (Ruina, 1983; Rice & Ruina, 1983). If fault strength decreases with increasing displacement rate, the fault is velocity weakening, and can exhibit unstable, accelerating or seismic slip. These concepts are captured by the empirical rate-and-state-friction (RSF) models proposed by Dieterich (1979), Ruina (1983), and Perrin et al. (1995), which have been highly successful in reproducing experimental fault slip behaviour (e.g. Tullis & Weeks, 1986; Ikari et al., 2009), and in simulating the seismic cycle and aftershock behaviour of active faults in nature (e.g. Dieterich, 1994; Kato & Tullis, 2003; for a review see Marone, 1998a). To describe the velocity dependence of fault frictional strength, RSF descriptions use the dimensionless parameter "*(a-b)*". This measures the change in steady-state frictional sliding strength of a fault following a stepwise increase in sliding velocity by a factor *e*. For $(a-b) < 0$, a fault is velocity weakening, for $(a-b) = 0$ it is velocity neutral, whereas for $(a-b) > 0$ it is velocity strengthening. Thus, under conditions pertaining to the seismogenic zone, faults are generally believed to exhibit velocity weakening frictional behaviour, characterized by negative values of *(a-b)* (Fig. 5.1a).

The velocity dependence of fault frictional strength is controlled by the microphysical processes that accommodate shear deformation within the fault sliding medium, which, in a mature fault, at depths where brittle frictional behaviour dominates, consists of accumulated granular wear material or fault gouge (Sibson, 1977). Laboratory fault slip experiments performed using simulated gouges prepared from halite (Shimamoto, 1986; Kawamoto & Shimamoto, 1997, 1998), granite (e.g. Lockner et al., 1986; Blanpied et al., 1995), gabbro (He et al., 2007), and phyllosilicate-rich rocks (e.g. Moore et al., 1997; Den Hartog et al., 2012, 2013; Lu & He, 2014), have consistently revealed three regimes of velocity dependent strength with increasing temperature. In all of these materials, velocity strengthening occurs at high and low temperatures and velocity weakening at intermediate temperatures. For calcite gouges, however, data on such transitions with temperature are limited, despite the fact that calcite-rich rock formations (e.g. limestones) are widespread in earthquake-prone, tectonically-active terranes, such as the Apennines (Italy – e.g. Chiarabba et al., 2014) or the Corinth Rift Zone (Greece – Bernard et al., 2006). Important here is the fact that calcite(-rich) rocks are relatively ductile at upper-

crustal pressures and temperatures compared to silicate rocks, such as granite (e.g. Kennedy & White, 2001; De Bresser et al., 2002). Both microphysical and empirically-based modelling studies have shown that fault gouge ductility is crucial in controlling the velocity dependence of gouge-filled faults (e.g. Chester & Higgs, 1992; Nakatani, 2001; Niemeijer & Spiers, 2006, 2007; Noda & Shimamoto, 2010, 2012; Den Hartog & Spiers, 2013, 2014; Shimamoto & Noda, 2014; Chen, 2015). Therefore, the question arises as to the pressure, temperature, and strain rate conditions at which calcite-rich fault rocks exhibit velocity strengthening vs. velocity weakening, and whether these conditions are substantially different compared with other crustal rock types. Elucidating this should help not only in delineating the depth-temperature range of the seismogenic zone in tectonically-active limestone terranes, but also in providing new insights into the processes controlling frictional sliding of gouge-bearing faults in general.

Recent experiments conducted using simulated calcite(-rich) fault gouges sheared at upper-crustal effective normal stress (σ_n^{eff}) and temperature (T) conditions have demonstrated a transition from stable velocity strengthening at 20°-50°C to velocity weakening slip at temperatures above ~80 to 100°C (Verberne et al., 2010, 2013a, b, i.e. Chapters II and III; see also Chen et al., 2015). This transition appears to correspond to the upper limit of the seismogenic zone in tectonically-active limestone terrains, located at ~2 to 4 km depth in the Apennines and the Corinth Rift Zone, for example (Bernard et al., 2006; Valoroso et al., 2013). However, laboratory constraints on the velocity dependence of strength at the pressure and temperature conditions corresponding to the lower seismogenic limit are still lacking.

Here, we report experiments on the frictional properties of simulated calcite fault gouges sheared under water-saturated conditions known to span the brittle-plastic transition in conventional deformation experiments on marbles (Heard, 1960; Rutter, 1974; Schmid et al., 1987; Barnhoorn et al., 2004), i.e. at temperatures of 20° to 600°C, pore fluid pressures (P_f) of 10 to 100 MPa, effective normal stresses (σ_n^{eff}) of 30 to 100 MPa, and sliding velocities (v) of 0.01 to 100 μm/s (equivalent to bulk shear strain rates of 10^{-5} to 10^{-1} s^{-1}). In view of the relative ease of plasticity in calcite (e.g. De Bresser & Spiers, 1993, 1997; Kennedy & White, 2001; De Bresser et al., 2002), the higher temperatures addressed ($T \approx$ 500-600°C) can be expected to be sufficient for shear deformation to be controlled, or at least substantially influenced, by ductile creep mechanisms. We explore whether this will result in velocity strengthening behaviour at these high temperatures, such that we can delineate a stability transition corresponding

to the lower limit of the seismogenic zone in limestone terrains (Fig. 5.1b).

5.2. Background

Before proceeding to describe our experiments, we first provide a brief introduction to a microphysical model recently proposed for shear deformation of granular aggregates, which we will later use for qualitative comparison with our experimental data. The model was first developed to describe the shear behaviour of granular halite-phyllosilicate mixtures (Bos et al., 2000a, b; Bos & Spiers, 2001, 2002a, b; Niemeijer & Spiers, 2005, 2006, 2007), providing a microphysical basis for understanding the frictional behaviour of fault gouges and for the phenomenological RSF equations used in fault mechanics modelling (see also Den Hartog & Spiers, 2013, 2014; Chen, 2015). The model is based on competition between a) athermal, rate-insensitive, granular flow by dilatant intergranular frictional sliding and b) thermally-activated, rate-sensitive creep processes that allow deformation by both shear and compaction. It is therefore directly relevant to understanding fault sliding behaviour throughout the frictional-viscous transition, as targeted in our experiments and believed to occur in the seismogenic zone of the upper crust (Fig. 5.1).

Here we apply the Niemeijer-Spiers version of the model, but for a single phase granular material in which intergranular sliding is controlled by grain boundary friction – rather than the frictional properties of a thin film of phyllosilicates in grain boundaries, as addressed in the original model (Niemeijer & Spiers, 2007). A plot of steady-state shear strength (τ_{ss}) versus shear strain rate ($\dot{\gamma}$) at constant temperature (T), as qualitatively predicted by the modified model is drawn in Figure 5.2a, following Den Hartog & Spiers (2013). Fault rock microstructures representative for the different shear regimes predicted by the model (A, B and C in Fig. 5.2a), are drawn in Figure 5.2b. As the present shear tests were performed over a wide range of temperatures (20° to 600°C), we also sketched model predictions for the evolution of τ_{ss} (Fig. 5.2c), and its sensitivity to strain rate ($d\tau_{ss}/d\dot{\gamma}$) (Fig. 5.2d), with increasing temperature, qualitatively applying the relations derived by Niemeijer & Spiers (2007) (see also Den Hartog & Spiers, 2013).

At low shear rates, or sufficiently high temperatures, i.e. corresponding to Regime C in Figure 5.2, the modified Niemeijer-Spiers model predicts that shear strain is achieved by intergranular (grain boundary) sliding accommodated by diffusion or dislocation creep processes. This results in viscous flow, if grain boundary sliding (GBS) is non-frictional (cf. Ashby & Verrall, 1973), vs. frictional-viscous flow if GBS is controlled by a

grain boundary friction coefficient (μ_{gb}). With increasing sliding rate, the strain-rate-strengthening nature of the accommodating creep processes predicts bulk velocity strengthening in this regime (Bos & Spiers, 2002a; Niemeijer & Spiers, 2005, 2006). Bulk velocity strengthening is also predicted in this regime if deformation is dominated by dislocation or diffusion creep with little or no grain boundary sliding by virtue of the linear or power law dependence of strain rate on stress for these mechanisms.

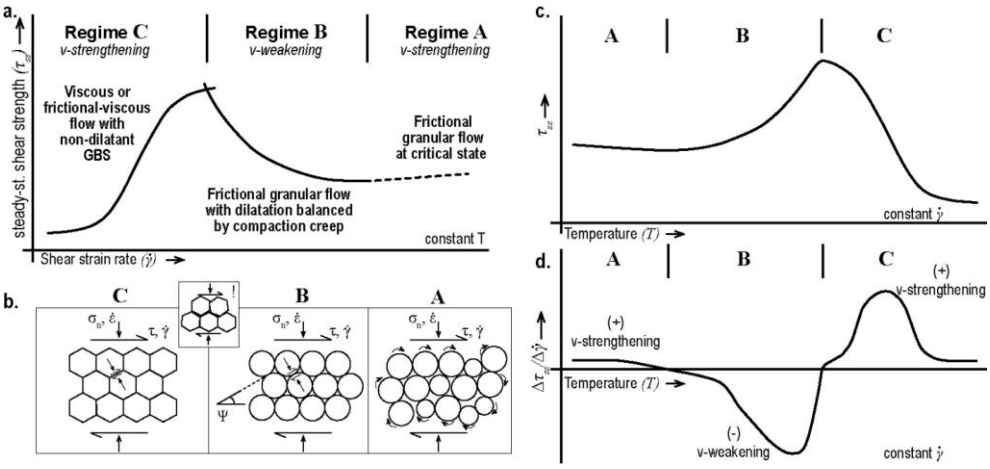

Figure 5.2. a) Schematic model curve illustrating the dependence of steady-state shear strength on shear strain rate, as predicted by the Niemeijer-Spiers model for shear deformation of granular aggregates (Niemeijer & Spiers, 2007; Den Hartog & Spiers, 2013, 2014). Increasing temperature translates this curve rightwards (Niemeijer & Spiers, 2007; Den Hartog & Spiers 2013). b) Schematic model microstructures characterizing each shear Regime in (a). The inset between C and B illustrates the onset of dilatation (i.e. porosity generation or cavitation) associated with the transition from Regime C to B. Ψ = dilatation angle, σ_n = normal stress, τ = shear stress, $\dot{\gamma}$ = shear strain rate. c) The evolution of steady-state shear strength and (d) its shear strain rate dependence $(d\tau_{ss}/d\dot{\gamma})$ with temperature, as qualitatively predicted by the model. Note that the quantity $(d\tau_{ss}/d\dot{\gamma})$ is directly related to the velocity dependence parameter *(a-b)* in classical rate-and-state-friction models. For a detailed formulation see Bos & Spiers (2002a), Niemeijer & Spiers (2007), and Den Hartog & Spiers (2013, 2014).

Towards higher shear rates, or lower temperatures (Regime B in Fig. 5.2), diffusion or dislocation creep processes become too slow to fully accommodate GBS under the imposed shear strain rate, leading to intergranular dilatation and porosity generation (referred to as "cavitations" in the GBS literature, e.g. Chokshi et al., 1993), i.e. to granular flow (Figs. 5.2a, b). Compaction creep by diffusion or plastic flow mechanisms then becomes possible alongside shear deformation. Competition between time-dependent compaction creep and dilatation associated with granular flow can now lead

to steady-state frictional flow, characterized by a fixed steady-state porosity at any given shear rate, effective normal stress and temperature, corresponding to the condition that the compaction strain rate $\dot{\varepsilon}_{cp}$ is equal and opposite to the granular dilatation rate $\dot{\varepsilon}_{gr}$ (Niemeijer & Spiers, 2007). This steady-state porosity increases with increasing shear rate, as the dilatation rate due to granular flow increases, causing a decrease in grain to grain contact area, in steady-state dilatation angle and hence frictional strength, causing velocity weakening. Under these velocity weakening conditions, the shear strength at steady-state is described by (Niemeijer & Spiers, 2007)

$$\tau_{ss} = \frac{\mu_{gb} + \tan(\Psi)}{1 - \mu_{gb}\tan(\Psi)} \cdot \sigma_n^{eff} \approx \frac{\mu_{gb} + \dfrac{L\dot{\varepsilon}_{cp}}{v}}{1 - \mu_{gb}\dfrac{L\dot{\varepsilon}_{cp}}{v}} \cdot \sigma_n^{eff} \qquad (5.1)$$

where Ψ is the mean intergranular slip surface inclination or dilation angle (assuming distributed grain neighbour-swapping granular flow – Fig. 5.2b), and L is the thickness of the slipping zone. Equation (5.1) demonstrates that a perturbation of steady-state frictional sliding due to an increase of the shear strain rate ($\dot{\gamma} = v/L$) will lead to a decrease in steady-state shear strength, hence to velocity weakening slip.

At sufficiently high shear rates, or still lower temperatures (Regime A in Fig. 5.2), the model predicts that frictional granular flow will dominate, as compaction by diffusion or dislocation creep will ultimately become too slow to counteract dilatation, producing steady, critical-state flow (Figs. 5.2a, b) of the type familiar in the mechanics of soils and other granular media (e.g. Schofield & Wroth, 1968; Gudehus, 2011). Under these conditions, bulk shear strength will be controlled by processes operating within grain contacts, i.e. by nanoscale asperity processes (Bhushan, 2005). Assuming that these processes are thermally-activated, shear-stress-assisted, atomic-scale jump process (cf. Rice et al., 2001), then grain boundary friction will be weakly velocity strengthening, producing bulk velocity strengthening frictional behaviour (Den Hartog & Spiers, 2013; see also Verberne et al., 2013b, or Chapter III). Similar arguments presumably imply that μ_{gb} will exhibit weakly velocity strengthening properties at all temperatures and sliding velocities.

5.3. Materials and Methods

5.3.1. Sample material

We used simulated gouges prepared from crushed Iceland Spar single crystals, of the same origin as those used by Verberne et al. (2013a, b, 2014) (i.e. Chapters III and IV). X-ray diffraction (XRD) analysis showed that the simulated gouge material obtained consists of ~98% calcite with minor dolomite (≤2%). The grain size (d) distribution of the unsheared starting material falls in the range $1 \leq d \leq 70$ μm, with a median of ~20 μm (Verberne et al., 2013b). For each individual experiment performed, we used ~0.6 g of room-dry simulated gouge.

5.3.2. Experimental apparatus

All experiments were performed using the hydrothermal ring shear apparatus described by Niemeijer et al. (2008) and by Den Hartog et al. (2012, 2013). This consists of a pressure vessel plus internal ring shear assembly located in an Instron loading frame with servo-controlled ram for applying normal load (Fig. 5.3a). Rotary shear is independently applied via a servo-controlled motor and gearbox system programmed via a digital interface.

In this machine, the annular sample is located in the centre of the pressure vessel, sandwiched between two, grooved René -41, "superalloy" pistons – the upper and lower internal pistons shown in Figures 5.3b and c. The lower internal piston is fixed to the vessel via a clamped, lower forcing block (Fig. 5.3b). The upper internal piston is fixed to a pressure-compensated, external piston, which is held stationary via a torque bar that abuts against the 100 kN Instron load cell (Fig. 5.3a). Axial load is transmitted from the Instron ram to the sample and Instron frame via the lower forcing block (Figs. 5.3a, b), and measured using the 100 kN Instron load cell. This allows for normal stress-control to within 0.02 MPa of a desired value. Displacement of the Instron ram is measured in the Instron drive unit using a Linear Variable Differential Transformer (LVDT) of 100 mm full-scale and 5 μm resolution (see also Den Hartog et al., 2012). When the motor for applying rotation is switched on, the vessel plus lower internal piston rotate with respect to the upper piston assembly and stationary torque bar, i.e. around the central axis of the machine (Fig. 5.3b). This imposes a shear displacement on the ring-shaped sample (Figs. 5.3c, d), resulting in a shear stress that is measured as a moment via the torque bar, using two load cells of 1.2 kN full-scale (or ~60 MPa) each, located at either end of the torque bar (Fig. 5.3a). Shear displacement imposed on the sample is measured externally

with an accuracy of 1 μm, using a potentiometer attached to the forcing block. Pore fluid pressure is applied and adjusted as needed to within 0.1 MPa using a 5 mL hand pump. Each experiment reported here was performed wet, using demineralized water as the pore fluid. In the case of experiments at elevated temperatures, heating is achieved using a Thermocoax internal furnace (Fig. 5.3b) and temperature controlled using a three-term Eurotherm industrial controller, enabling control to within 0.1°C of any set-point value up to 700°C. Sample temperatures quoted here were measured by a thermocouple close (~5 mm) to the sample layer (Fig. 5.3c), and are mean values taken over the duration of each test.

To minimize sample extrusion upon axial loading and shearing, we confined our samples using an inner (diameter Ø = 22 mm) and an outer confining ring (Ø = 28 mm) composed of René-41 superalloy (Fig. 5.3c). To reduce wall friction between the sample and the confining rings, we lubricated the rings using Molykote D-321R anti-friction coating, applied using an aerosol spray. Den Hartog et al. (2012) showed that the lubricated confining rings have negligible effect on the measured torque. Note that active piston faces were roughened with ~0.2 mm deep, cross cut grooves to ensure good grip between the piston and the sample layer.

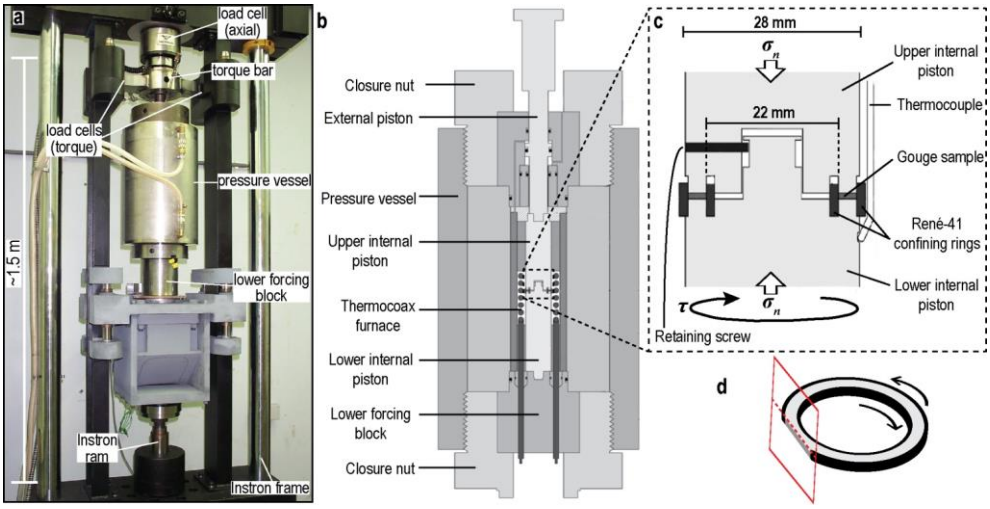

Figure 5.3. a) Photograph of the ring shear apparatus used in this study (after Niemeijer et al., 2008). The motor plus gearbox system constituting the rotational drive are installed behind the pressure vessel. b to d) Schematic representations of (b) the pressure vessel, (c) the sample assembly (both after Den Hartog et al., 2013), and (d) a sample sectioned normal to the shear plane and sub-parallel to the shear direction for microstructural study.

5.3.3. Experimental procedure and conditions

In preparing each experiment, the sample plus upper and lower piston assembly was loaded into the water-filled vessel (ref. Figs. 5.3a, b). The vessel was then sealed using the closure nut and mounted into the Instron frame, followed by emplacement of the torque bar and subsequent application of the desired normal load. In room temperature experiments, the vessel was then pressurized to the test value of pore fluid pressure. In experiments at elevated temperature we simply switched on the internal furnace for heating to the desired testing temperature. This rapidly pressurized the pore fluid within the vessel. By bleeding the vessel intermittently using the hand pump, the pore pressure was as far as possible maintained below that used during the test, adjusting to the desired final value when the system stabilized. To initiate each experiment, we switched on the rotation drive system, and programmed the shear displacement rate to the desired value. In each test, the initial displacement rate used was 1 μm/s.

We ran two series of experiments: i) Constant σ_n^{eff} tests. These consisted of velocity stepping shear tests performed at a constant effective normal stress of σ_n^{eff} = 50 MPa, and ii) σ_n^{eff}-stepping tests. These comprised velocity stepping shear tests performed at sequentially increased σ_n^{eff} values, specifically at fixed values of 30, 50, 80, and 100 MPa. In the case of experiments at elevated temperature, each run was performed using a fixed furnace setpoint temperature of 100°, 200°, 400°, 500°, 550°, or 600°C - see Table 5.1 for a list of all experiments reported and the corresponding conditions. We did not perform experiments at 300°C, because preliminary inspection of data obtained from experiments at 400°C showed that it was similar to that of data from an experiment at 200°C. Instead, we chose to continue increasing temperature. Since the upper piston is pressure-compensated (Fig. 5.3b), the effective normal stress equals the applied normal stress (σ_n) acting on the sample layer (i.e. minus a contribution from seal friction), and steps in the σ_n^{eff} value were achieved by increasing the axial load on the sample. In constant σ_n^{eff} tests performed at $T \leq$ 200°C, we used a pore fluid pressure (P_f) of 10 MPa, i.e. the same as that used in Chapter III. In subsequent runs at elevated temperature we used higher values of P_f, specifically 30 MPa at 400°C, 50 MPa at 500°C, and 60 MPa at 550° and 600°C (Table 5.1). In the σ_n^{eff}-stepping test at room temperature ($CaCO_3$-NS-20), the P_f value was chosen such to maintain a constant ratio of pore fluid pressure over normal stress, i.e. $\lambda = P_f/\sigma_n$. In runs performed at 200°, 400°, and 500°C we used λ = 0.6, except at σ_n^{eff} = 30 MPa, which used P_f = 25 MPa. For the run performed at ~600°C

($CaCO_3$-NS-600) we used a constant P_f value of 40 MPa (Table 5.1). In general, for experiments at $T \geq 200$°C, P_f values were chosen to be sufficiently high such to enable a stable fluid pressure during the run.

In the experiments conducted at a single constant σ_n^{eff} value, we stepped the sliding velocity v in 3- or 3⅓-fold, up- and downward directed velocity steps, from 0.1 to 100 μm/s (Table 5.1, Fig. 5.4a). In experiment $CaCO_3$-500-LV, performed at σ_n^{eff} = 50 MPa, we additionally used velocities of ~0.03 or ~0.05 μm/s (Table 5.1). Note that sliding velocity values are specified here in terms of the ratio of measured displacement to the corresponding time interval (e.g. on the right axis in Figs. 5.4a, b). In the σ_n^{eff}-stepping tests, we applied two cycles of velocity stepping, employing velocities of 1, 10, and 100 μm/s at each normal stress interval employed (Table 5.1, Fig. 5.4b). Upon applying each step in effective normal stress, we first stopped the rotation drive, then increased the axial load to the desired value, and finally re-started shearing of the sample. In total this took around 1 minute. The total shear displacement (x_{fnl}) imposed in the constant σ_n^{eff} tests was 19 to 23 mm, except for experiment $CaCO_3$-500-LV, which reached x_{fnl} = 31.3 mm. That imposed in the σ_n^{eff}-stepping tests ranged from 24 to 26 mm (Table 5.1).

In terminating each experiment, we first switched off the rotational drive system and then the furnace (where T > Room T). After cooling, the vessel was depressurized to atmospheric pressure, the normal load was removed, and the sample assembly was removed from the pressure vessel. This whole procedure took around 30 minutes. From the difference in length of the sample- internal piston assembly (Fig. 5.3b), measured using a calliper before and after a test, we determined the thickness of the gouge layer after each experiment (l_{fnl}) (Table 5.1). Assuming that the thickness of the sample layer is constant and equal to l_{fnl} during each test, the final bulk imposed shear strain (γ_{fnl}) measured ~56 for experiment $CaCO_3$-500-LV, versus 25 to 46 for all other constant σ_n^{eff} tests. Similarly, the final shear strain achieved in the σ_n^{eff}-stepping tests fell in the range 43 to 57 (Table 5.1).

5.3.4. Data acquisition and processing

Voltage signals corresponding to shear displacement, torque, temperature, axial displacement and load, pore fluid pressure, and rotational drive velocity ($\dot{x}$) were logged using a 16 bit A/D converter at a frequency (f) of $10\dot{x}/x_r$, where x_r = 1 μm. For experiments in which $\dot{x}$ < 0.1 μm/s, f was set to be 1 Hz, whereas for those in which $\dot{x}$ =

100 μm/s, we used f = 300 Hz. Because elastic twist of the apparatus during shear loading of our samples was small (<1%) compared with the total imposed shear displacement, we ignored machine distortion in processing sample shear displacement. The effective normal stress was calculated by dividing the applied axial load by the area A of the ring-shaped sample, given as $A = \pi(r_0^2 - r_i^2) = 75\pi$ mm² (Fig. 5.3c), and subtracting the contribution of friction of the water-cooled O-ring seals against the upper external piston. From calibrations using an internal axial load cell, the seal friction was determined to be equivalent to ~1.9 MPa normal stress under (nominally) dry conditions. Similar calibrations performed using a pore fluid pressure of 100 MPa showed that this is ~2.8 MPa, however, we ignored this, and used a value of 1.9 MPa to correct the normal stress for each test under all conditions. Assuming a linear scaling of seal friction with increasing P_f, this implies that the effective normal stress may have been maximally 0.75% lower than the value used here, which we consider negligible. Note that the σ_n^{eff} values listed in Table 5.1 are the targeted values for each experiment, not corrected for seal friction, but that we used the corrected value in processing our data. The externally measured torque was corrected for dynamic seal friction using displacement-dependent and pore-pressure-dependent calibrations following Den Hartog et al. (2012). The shear stress (τ) supported by the sample was determined assuming it to be uniform over the width of the annular sample (3 mm). Standard error analysis showed that error propagation in the measured shear stress is ≤0.1%.

Experiment[1]	σ_n^{eff} (MPa)[2]	P_f (MPa)	T (°C)[3]	T_{mn} (°C)[4]	Sliding velocity (v) sequence (μm/s)	x_{fnl}[5] (mm)	l_{fnl}[6] (mm)	γ_{fnl}[7]
$CaCO_3$-20	50	10	n/a	22.2±0.7	1|0.1|10|1|0.1|10|1|30|100|30|10|3|1|0.3|0.1|0.3|1|3|10|30|100|30|10|3|1|0.1	20.9	0.5	46
$CaCO_3$-100	50	10	100	98.8±1.1	1|0.1|10|1|0.1|10|1|30|100|30|10|3|1|0.3|0.1|0.3|1|3|10|30|100|30|10|3|1|0.1	21.4	0.7	31
$CaCO_3$-200	50	10	200	199±0.9	1|0.1|10|1|0.1|10|1|30|100|30|10|3|1|0.3|0.1|0.3|1|3|10|30|100|30|10|3|1	19.1	0.8	25
$CaCO_3$-400	50	30	400	399±0.9	1|0.1|10|1|0.1|10|1|30|100|30|10|3|1|0.3|0.1|0.3|1|3|10|30|100|30|10|3|1	23.0	0.9	25
$CaCO_3$-500	50	50	500	494±2.3	1|0.1|10|1|0.1|100|10|0.1|10|1|30|100|30|10|3|1|0.3|0.1|0.3|1|3|10|30|100|30|10|3|1|0.3|0.1	22.0	0.8	28
$CaCO_3$-500-LV	50	50	500	501±1.3	1|0.1|10|1|0.1|0.03|0.05|1|3|10|30|100|30|10|3|1|0.3|0.1|0.03|0.05|0.1|0.3|1|3|10|30|100|30|10|3|1|0.1	31.3	0.6	56
$CaCO_3$-550	50	60	550	537±2.3	1|0.1|10|1|0.1|10|1|30|100|30|10|3|1|0.3|0.1|0.3|1|3|10|30|100|30|10|3|1	20.0	0.7	29
$CaCO_3$-600	50	60	600	592±1.9	1|0.1|10|1|0.1|10|1|30|100|30|10|3|1|0.3|0.1|0.3|1|3|10|30|100|30|10|3|1|0.1	23.2	0.6	39
$CaCO_3$-NS-20	30|50|80|100	25|30|48|60	n/a	17.9±0.4	1|10|100|10|1|10|100|10|1	23.8	0.7	34
$CaCO_3$-NS-200	30|50|80|100	25|30|48|60	200	199±1.0	1|10|100|10|1|10|100|10|1	24.5	0.6	43
$CaCO_3$-NS-400	30|50|80|100	25|30|48|60	400	398±4.8	1|10|100|10|1|10|100|10|1	28.7	0.6	49
$CaCO_3$-NS-500	30|50|80|100	25|30|48|60	500	500±9.9	1|10|100|10|1|10|100|10|1	25.2	0.6	45
$CaCO_3$-NS-600	30|50|80|100	40	600	614±5.6	1|10|100|10|1|10|100|10|1	26.0	0.5	57

Table 5.1. List of experiments and conditions. [1]Constant-σ_n^{eff} and σ_n^{eff}-stepping tests. The σ_n^{eff}-stepping tests used the sliding velocity sequence indicated at each value of σ_n^{eff} employed. The σ_n^{eff} value was adjusted by accordingly changing the normal or axial load acting on the sample. [2]Effective normal stress values (not corrected for seal friction, which was taken to be ~1.9 MPa for each experiment under all conditions). [3]Furnace setpoint temperature, "n/a" implies that the furnace was switched off during the test. [4]Mean temperature measured over the duration of a test, with its standard deviation. [5]Total shear displacement [6]Thickness of the sample measured after the experiment [7]Maximum finite bulk strain (= x_{fnl} / l_{fnl}).

All sample strength data obtained are presented as shear stress-displacement plots, unless otherwise indicated. Since run $CaCO_3$-500-LV employed a unique displacement-velocity history (see Table 5.1), we discounted this experiment in our comparisons of the mechanical data. For all other experiments, to provide an objective comparison of strength data between tests performed at different temperatures, we subdivided the shear stress-displacement data into three consecutive stages (Figs. 5.4a, b), characterized by values of shear stress termed τ_I, τ_{II}, and τ_{III}, and corresponding apparent friction coefficients defined $\mu_k = \tau_k/\sigma_n^{eff}$, picked at equivalent displacements, at v = 1 μm/s. In the tests performed at constant σ_n^{eff} (with the exception of experiment $CaCO_3$-500-LV), Stage I runs up to a displacement of $x \approx 6$ mm, Stage II up to $x \approx 18$ mm, whereas Stage III represents the final part of the experiment, i.e. further displacements up to $x = x_{fnl}$ (Fig. 5.4a). Values of τ_I were picked at displacements (x) of 1 to 2 mm, values of τ_{II} at x ≈ 11 to 12 mm (i.e. after a downward step in sliding velocity from 3 to 1 μm/s), and values of τ_{III} at $x \approx 19$ to 23 mm. In the σ_n^{eff}-stepping experiments, we defined Stages I, II and III as consecutive stages of ~1, ~2, and ~1 mm displacement within each interval of constant σ_n^{eff} (Fig. 5.4b). In these runs, values of τ_I were picked at total displacements of ~1 to 2 mm after (re-)starting shear, values of τ_{II} after ~3 to 4 mm (i.e. following a downward step in sliding velocity from 10 to 1 μm/s – see Fig. 5.4b, Table 5.1), and values of τ_{III} after ~6 to 7 mm total displacement after (re-)starting shear. For all tests, in the case of stick-slip, τ_I, τ_{II}, and τ_{III} values were determined by taking the average value of the peak strength, τ_{fail}.

We quantified the velocity dependence of shear strength using

$$\Gamma = \frac{\tau_{i+1} - \tau_i}{\sigma_n^{eff}\left(\ln(v_{i+1}) - \ln(v_i)\right)} = \frac{\Delta\tau}{\sigma_n^{eff}\,\Delta\ln(v)} \qquad (5.2)$$

where the subscript i refers to sliding before a step in displacement rate. The absolute error in Γ is determined by the error in $\Delta\tau$ and in σ_n^{eff}, and is estimated to be ~0.003 for all velocity steps in all experiments. In the case of true steady-state sliding before and after a velocity step, we determined $\Gamma = (a\text{-}b)$, i.e. the rate parameter used in RSF modelling (e.g. Marone, 1998a), using an iterative least-squares fitting procedure (described by e.g. Reinen and Weeks, 1993). This involved inversion of a Dieterich-type RSF equation (Dieterich, 1979), coupled with an equation describing the elastic

interaction between the sample and the loading frame (see Ikari et al, 2009). In applying this routine, we locally detrended the data, obtained in each velocity interval, for linear displacement hardening or –weakening trends (following e.g. Lockner et al., 1986; Blanpied et al., 1995). However, in many experiments we observed stick-slip events, for which a value of *(a-b)* cannot easily be obtained. In this case, we determined Γ by using a value for $\Delta\tau$ in equation 5.2 determined from the average value of τ_{fail} during stick-slip before and after a step in sliding velocity (see also Verberne et al., 2013b, or Chapter III). This value for $\Delta\tau$ is not to be confused with the stress drop $\Delta\tau_{drop}$ associated with the "slip"-phase, which represents the average difference between τ_{fail} and the minimum strength reached immediately after the subsequent slip event, for a single value of v. In the case of stick-slip events occurring over multiple displacement intervals imposed at the same sliding velocity, we averaged $\Delta\tau_{drop}$ to obtain a representative value associated with that velocity.

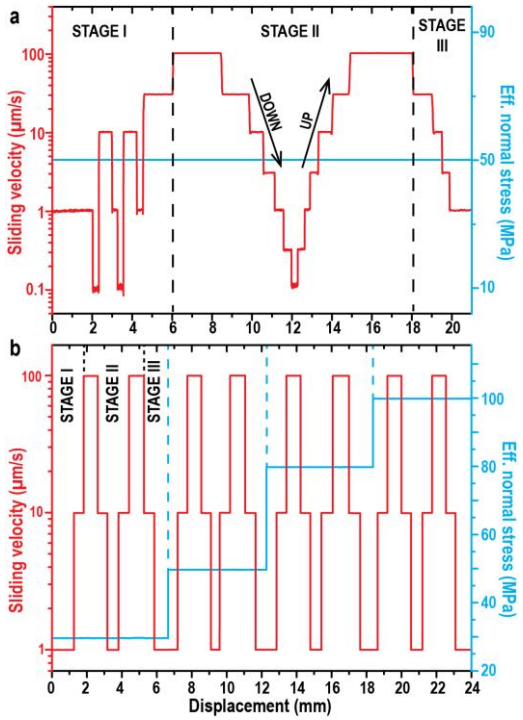

Figure 5.4. Sliding velocity and effective normal stress vs. displacement "history" employed in the present experiments. a) Constant-σ_n^{eff} experiments (σ_n^{eff} = 50 MPa). b) the σ_n^{eff}-stepping experiments. Note that in both types of experiment conducted we defined three consecutive stages of velocity stepping (indicated I, II and III) for each effective normal stress value employed.

5.3.5. Sample recovery and microstructural analysis

Sample fragments were retrieved after testing for microstructural investigation of the sheared gouge. In some cases, especially for the samples sheared at relatively low temperatures (≤200°C), this was not always successful, because upon removal of the confining rings the sheared gouge layer fell apart into fragments that are too small for recovery and subsequent sectioning. Recovered samples were first impregnated using Araldite 2020 epoxy resin and allowed to cure for several days. The samples were then sectioned with a diamond watering saw in a plane cut normal to the shear plane of the sample and tangential to a centrally inscribed circle with radius ~12.5 mm, as shown in Figure 5.3d. In this way, the central portion of the section is oriented parallel to the imposed shear direction, whereas near the outer ends of the section the shear direction plunges at $\cos^{-1}(12.5/14) \approx 27°$ into the section (Fig. 5.3d). All cut sections were used to prepare polished sections of ~5 to 30 μm thickness. Transmitted light analysis was conducted using a Leica DMR polarizing light microscope. Selected thin sections were imaged further using an FEI Nova Nanolab 600 scanning electron microscope (SEM), operated in backscatter electron mode and using an acceleration voltage of 10 kV, except where otherwise indicated.

5.4. Mechanical data

5.4.1. Experiments at constant effective normal stress

5.4.1.1. Strength-displacement curves

The shear strength (τ) versus displacement (x) data obtained in the tests performed at constant σ_n^{eff} are shown in Figure 5.5, except for experiment $CaCO_3$-500-LV, which we consider separately. A list of τ_I, τ_{II}, and τ_{III} values is given in Table 5.2.

All of the experiments showed rapid, near-linear loading in the first 0.4 to 0.6 mm of displacement, followed by apparent yield and subsequent hardening towards a maximum strength (= τ_I) reached at $x \approx$ 1-2 mm (Figs. 5.5a-d). Experiments $CaCO_3$-20 and $CaCO_3$-600 subsequently showed stable sliding behaviour at all displacements and in all velocity intervals (Figs. 5.5a, d). However, all experiments performed at temperatures in the range 100° to 550°C exhibited periodic stick-slip; only at the lowest imposed sliding velocities ($v \leq 1$ μm/s) at 100°C (Figs. 5.5a-c), but at all displacement rates in experiments conducted at 550°C (Fig. 5.5c).

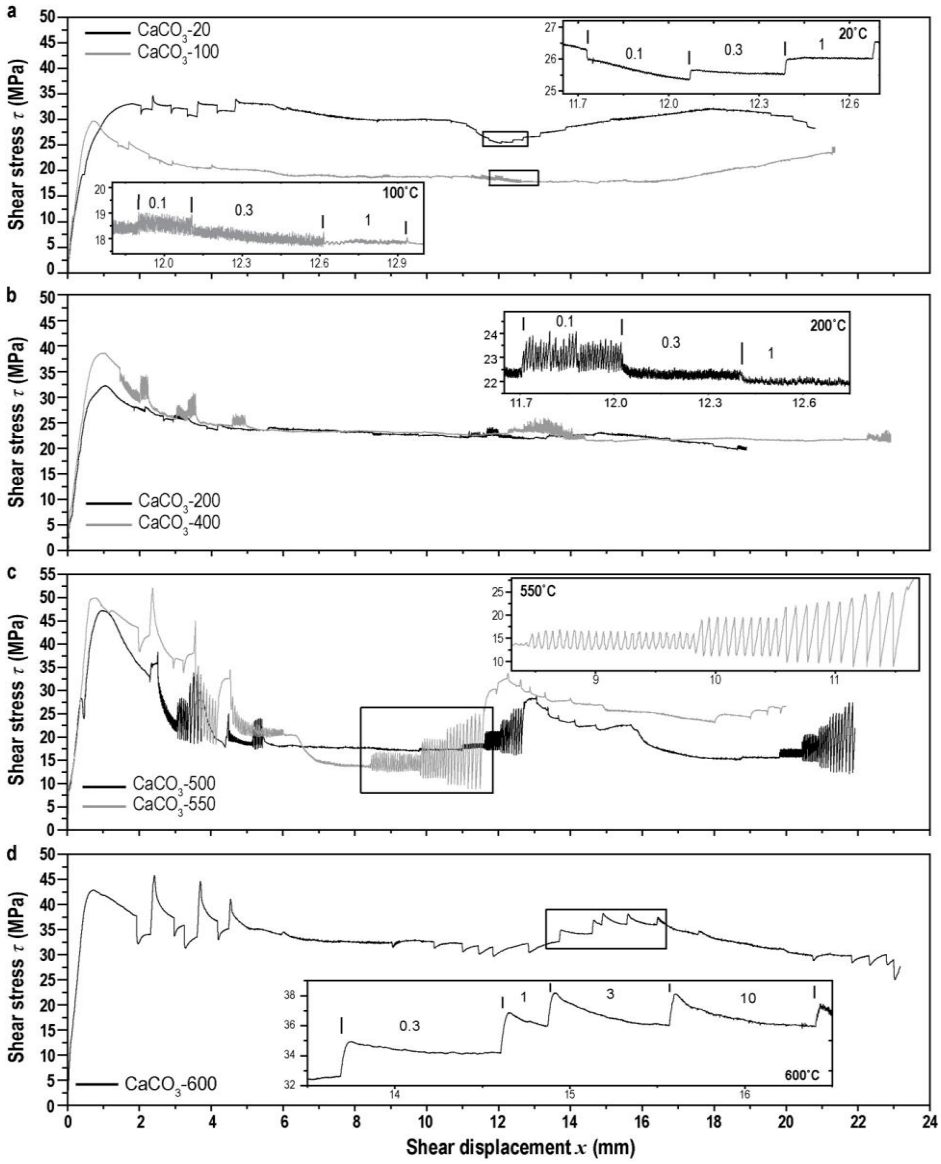

Figure 5.5. Plots of shear stress (τ) against displacement for experiments performed at constant σ_n^{eff} = 50 MPa. a) $T \approx 20°$, 100°, and 200°C. b) $T \approx 400°$, 500°, and 550°C. c) $T \approx 600$°C. Insets highlight examples of the shear strength response to velocity steps. A list of all experiments is given in Table 5.1, and a list shear strength parameters from Stages I, II and III (see Fig. 4a), i.e. of τ_I , τ_{II} , and $\tau_{III,}$ is given in Table 5.2.

Experiment	T_{mn} (°C)	σ_n^{eff} (MPa)	STAGE I [1]		STAGE II [1]		STAGE III [1]	
			τ_I (MPa)[2]	μ_I[2]	τ_{II} (MPa)[3]	μ_{II}[3]	τ_{III} (MPa)[4]	μ_{III}[4]
$CaCO_3$-20	22.2±0.7	50	33.1	0.66	28.0	0.56	28.3	0.57
$CaCO_3$-100	98.8±1.1	50	29.7	0.59	18.6	0.37	23.5	0.47
$CaCO_3$-200	199±0.9	50	32.2	0.64	22.2	0.44	20.2	0.40
$CaCO_3$-400	399±0.9	50	38.6	0.77	24.1	0.48	22.7	0.45
$CaCO_3$-500	494±2.3	50	47.2	0.94	23.4	0.47	22.3	0.45
$CaCO_3$-550	537±2.3	50	49.9	1.00	24.8	0.50	26.6	0.53
$CaCO_3$-600	592±1.9	50	42.8	0.86	31.5	0.63	28.9	0.58
$CaCO_3$-NS-20	17.9±0.4	30	22.3	0.74	21.5	0.72	21.5	0.72
		50	36.1	0.72	37.3	0.75	37.0	0.74
		80	55.5	0.69	57.0	0.71	56.5	0.71
		100	66.7	0.67	68.3	0.68	65.7	0.66
$CaCO_3$-NS-200	199±1.0	30	20.2	0.67	16.0	0.53	16.0	0.53
		50	27.3	0.55	27.8	0.56	27.7	0.55
		80	43.9	0.55	44.7	0.56	44.3	0.55
		100	52.0	0.52	53.7	0.54	53.7	0.54
$CaCO_3$-NS-400	398±4.8	30	24.9	0.83	16.7	0.56	15.3	0.51
		50	30.6	0.61	28.6	0.57	27.9	0.56
		80	48.4	0.60	43.1	0.54	41.5	0.52
		100	52.2	0.52	47.9	0.48	48.6	0.49
$CaCO_3$-NS-500	500±9.9	30	26.0	0.87	16.5	0.55	17.4	0.58
		50	36.1	0.72	29.8	0.60	29.7	0.59
		80	54.7	0.68	49.2	0.62	48.8	0.61
		100	66.0	0.66	59.9	0.60	60.5	0.60
$CaCO_3$-NS-600	614±5.6	30	26.2	0.87	18.6	0.62	17.6	0.59
		50	38.0	0.76	30.5	0.61	30.5	0.61
		80	55.1	0.69	48.2	0.60	48.2	0.60
		100	62.8	0.63	58.8	0.59	58.5	0.58

Table 5.2. List of shear strength values. [1]For a definition of the Stages in the tests using constant σ_n^{eff} and the σ_n^{eff}-stepping tests see Figs. 5.4a, b. [2]In the constant σ_n^{eff} tests determined at displacements of $x \approx 1$ to 2 mm; In the σ_n^{eff}-stepping tests 1 to 2 mm after (re-)shear. [3]In the constant σ_n^{eff} tests determined at $x \approx 11$ to 12 mm; In the σ_n^{eff}-stepping tests 3 to 4 mm after (re-)shear. [4]In the constant σ_n^{eff} tests determined at $x \approx 19$ to 23 mm; In the σ_n^{eff}-stepping tests 6 to 7 mm after (re-)shear.

In most experiments, the value of τ_I given in Table 5.2 represents the maximum strength reached in all velocity steps, though some tests showed a sharp peak coinciding with step changes in sliding velocity. For displacements up to $x \approx 6$ mm, i.e. corresponding to Stage I of the experiments, all experiments showed displacement-weakening (Figs. 5.5a-d), except for run $CaCO_3$-20 which showed near-steady-state sliding at stresses of 30 to 33 MPa (Fig. 5.5a). The maximum strength τ_I (and μ_I) measured at a displacement of 1-2 mm increased from around 30 MPa at 20-200°C to 40-50 MPa at 500-600°C. At $x > 6$ mm, i.e. in Stages II and III, the shear strength value reached in each velocity interval mainly depended on temperature and on the imposed sliding rate. The experiments performed at 500° to 600°C also showed an effect of the direction of velocity stepping (downward vs upward) (Figs. 5.5c, d). In this temperature range, $CaCO_3$-500 and $CaCO_3$-550 showed marked displacement weakening at the highest velocities employed (i.e. at $v = 100$ μm/s and at $x = 6.3$ mm and 15.9 mm respectively - Fig. 5.5c), whereby the onset of this weakening occurred spontaneously during near steady-state sliding. In experiment $CaCO_3$-600, at $v < 10$ μm/s, much longer transient responses to stepping were observed, compared with experiments performed at lower temperatures, such that steady-state sliding was not always achieved in individual velocity intervals (Fig. 5.5d).

5.4.1.2. Effect of temperature on strength

To more explicitly illustrate the effect of temperature on shear strength in Stages I, II and III of the experiments conducted at constant σ_n^{eff}, we plot the strength values τ_I, τ_{II}, and τ_{III} against temperature in Figure 5.6. This demonstrates that τ_I decreased from 33 MPa at 20°C to 30 MPa at 100°C, but then increased steadily to 50 MPa at 550°C before decreasing to 43 MPa at 600°C. At the same time, the shear strength values τ_{II} and τ_{III} showed an initial decrease from 28 MPa at 20°C to ~19-24 MPa at 100-200°C, which remained near-constant before increasing to ~25-30 MPa at 550-600°C (Fig. 5.6).

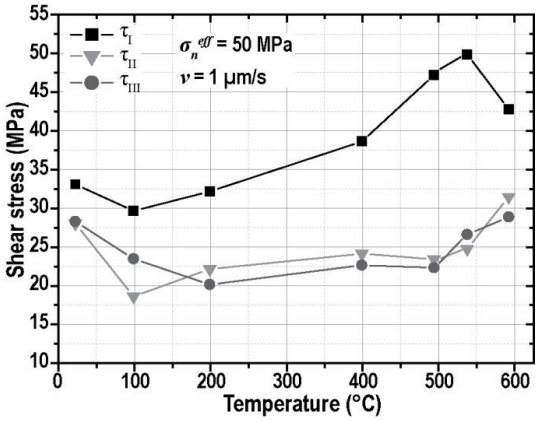

Figure 5.6. Values of τ_I , τ_{II} , and τ_{III} from experiments performed at constant σ_n^{eff} = 50 MPa, plotted against temperature. See Table 5.2 for a list of shear strength values.

5.4.1.3. Behaviour at low displacement rates

The shear strength vs. displacement data obtained for velocity stepping experiment $CaCO_3$-500-LV are presented in Figure 5.7, with the displacement rate data (velocity steps) added. The intervals in which especially low displacement rates to $v \approx 0.03$ and $v \approx 0.05$ µm/s were imposed are shown in detail in Figures 5.7b and c. In this experiment, a maximum shear strength of 43 MPa was reached at $x \approx 2$ mm, followed by gradual displacement weakening until $x \approx 4$ mm. For $x > 4.5$ mm, τ decreases strongly with increasing v (i.e. marked velocity-weakening occurs), and stick-slip events are widespread (Figs. 5.7a-d).

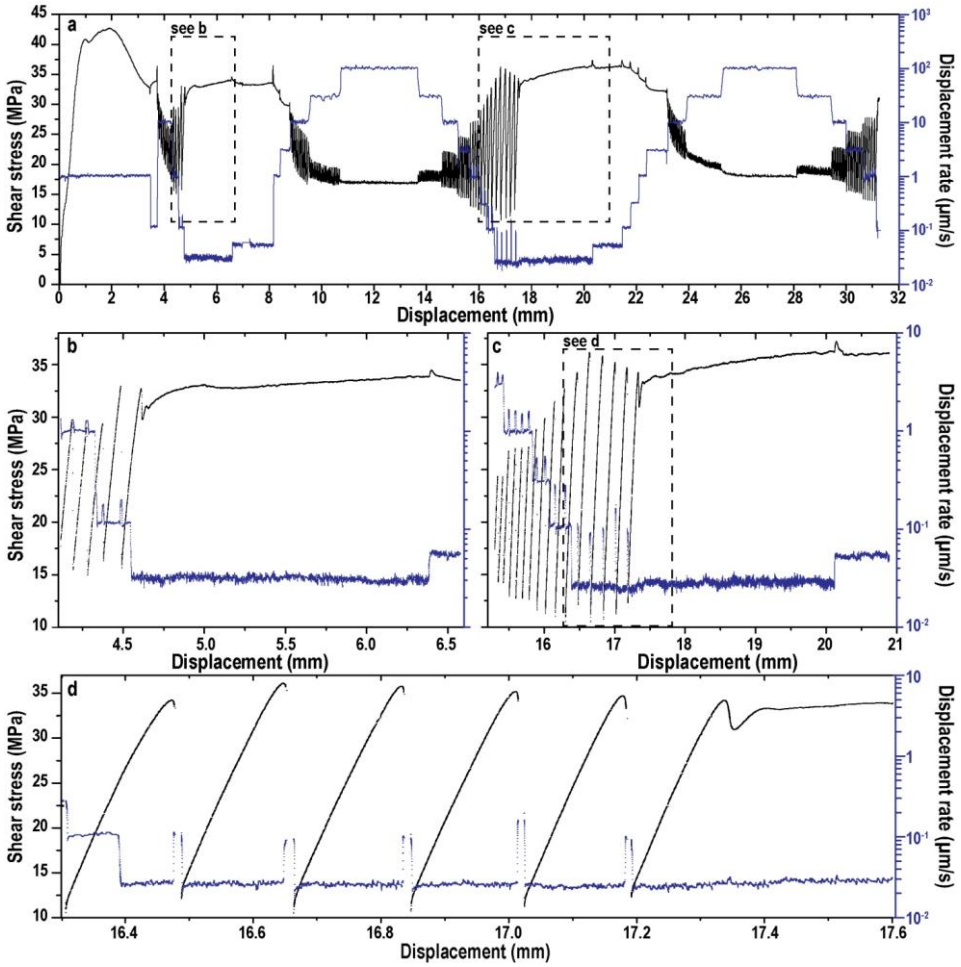

Figure 5.7. a). Plot of shear stress (τ) against displacement for experiment $CaCO_3$-500-LV (performed at 500°C , σ_n^{eff} = 50 MPa, see Table 5.1), with the displacement rate data (velocity steps) added on the right axis. b) Displacement interval x = [4.1, 6.6] mm showing downward steps in sliding velocity from 1 to 0.3 to 0.03 μm/s. c) Displacement interval x = [15.2, 21.0] mm showing downward steps in sliding velocity from 3 to 1 to 0.3 to 0.1 to 0.03 to 0.05 μm/s. d) Highlight of c), showing stick-slips at v = 0.03 μm/s, transitioning to stable sliding at x = 17.4 mm.

5.4.1.4. Amplitude of stick-slip events

As described above, stick-slip behaviour became increasingly marked at temperatures in the range 100° to 550°C, especially at the lower sliding velocities. This is reflected in the amplitude of stick-slip, i.e. in the magnitude of the associated stress drops $\Delta\tau_{drop}$. The largest stress drops seen in our tests were measured in experiment $CaCO_3$-500-LV (Fig. 5.7), which showed $\Delta\tau_{drop} \approx 25$ MPa. For each experiment that showed stick-slip, we plotted the magnitude of the average stress drop $\Delta\tau_{drop}$ against temperature and sliding rate in log-linear and log-log space respectively (Figs. 5.8a, b). These plots demonstrate that $\Delta\tau_{drop}$ increases strongly with increasing temperature in the range 100° to 550°C (Fig. 5.8a), whereas it falls to zero at 600°C where stick-slip ceases. In addition, $\Delta\tau_{drop}$ clearly decreases with increasing sliding velocity (Fig. 5.8b), especially at $v > 1$ µm/s.

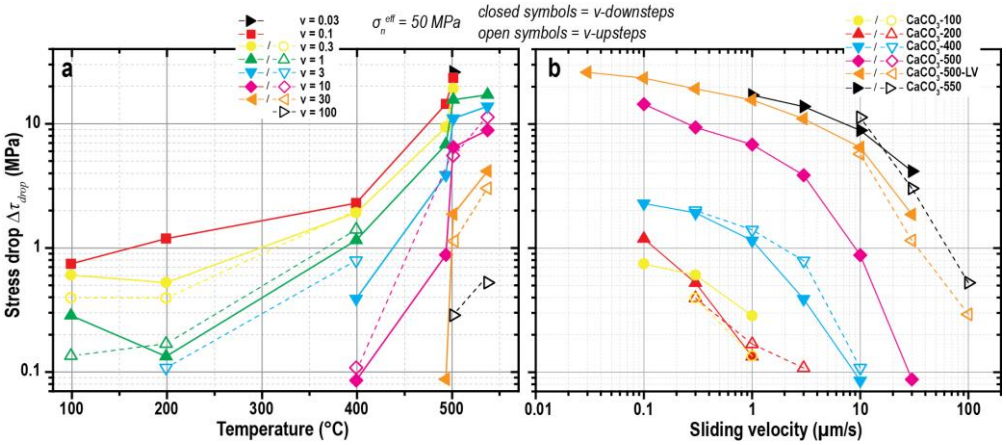

Figure 5.8. Plot of the stress drop (on a log-scale), for those experiments performed at constant σ_n^{eff} = 50 MPa which showed stick-slip, against (a) temperature (on a linear scale) and (b) sliding velocity (on a log-scale).

5.4.2. Effective normal stress stepping experiments

The shear stress vs. displacement curves obtained for all σ_n^{eff}-stepping experiments are presented in Figure 5.9. In each interval of constant σ_n^{eff}, the shear strength (τ) values (τ_I, τ_{II}, and τ_{III}) and apparent friction coefficient (μ) show a similar evolution with displacement, and with temperature and sliding velocity, as seen in the experiments performed at constant σ_n^{eff} (Fig. 5.9 cf. Fig. 5.5, see also Table 5.2). As in the constant σ_n^{eff} tests, in the σ_n^{eff}-stepping tests we frequently observed stick-slip in experiments performed at mid-range temperatures, specifically at 200° to 500°C in this case. Plots of τ_I, τ_{II}, and τ_{III} against effective normal stress are shown in Figure 5.10a, and of τ_{ss} or else τ_{fail} measured at each sliding velocity used in the second cycle of velocity steps applied in each interval of constant σ_n^{eff}, in Figure 5.10b. Note that for the latter, this resulted in two values of τ for each v = 1 and 10 μm/s, and 1 value for v = 100 μm/s (cf. Fig. 5.4b, covering Stage II & III of each σ_n^{eff} interval). Within the range of normal stresses investigated, and for each temperature and sliding velocity studied, all τ vs. σ_n^{eff} data are well described using a straight line. Linear regression analysis, using $\tau_k = S_0 + \mu_0 \sigma_n^{eff}$, yielded the S_o and μ_o given in Table 5.3. The values of μ_o show a similar trend with temperature as μ-values determined from all other experiments (Table 5.3 cf. Table 5.2). Taking into account the standard error, we found no systematic dependence of S_o on temperature or sliding rate.

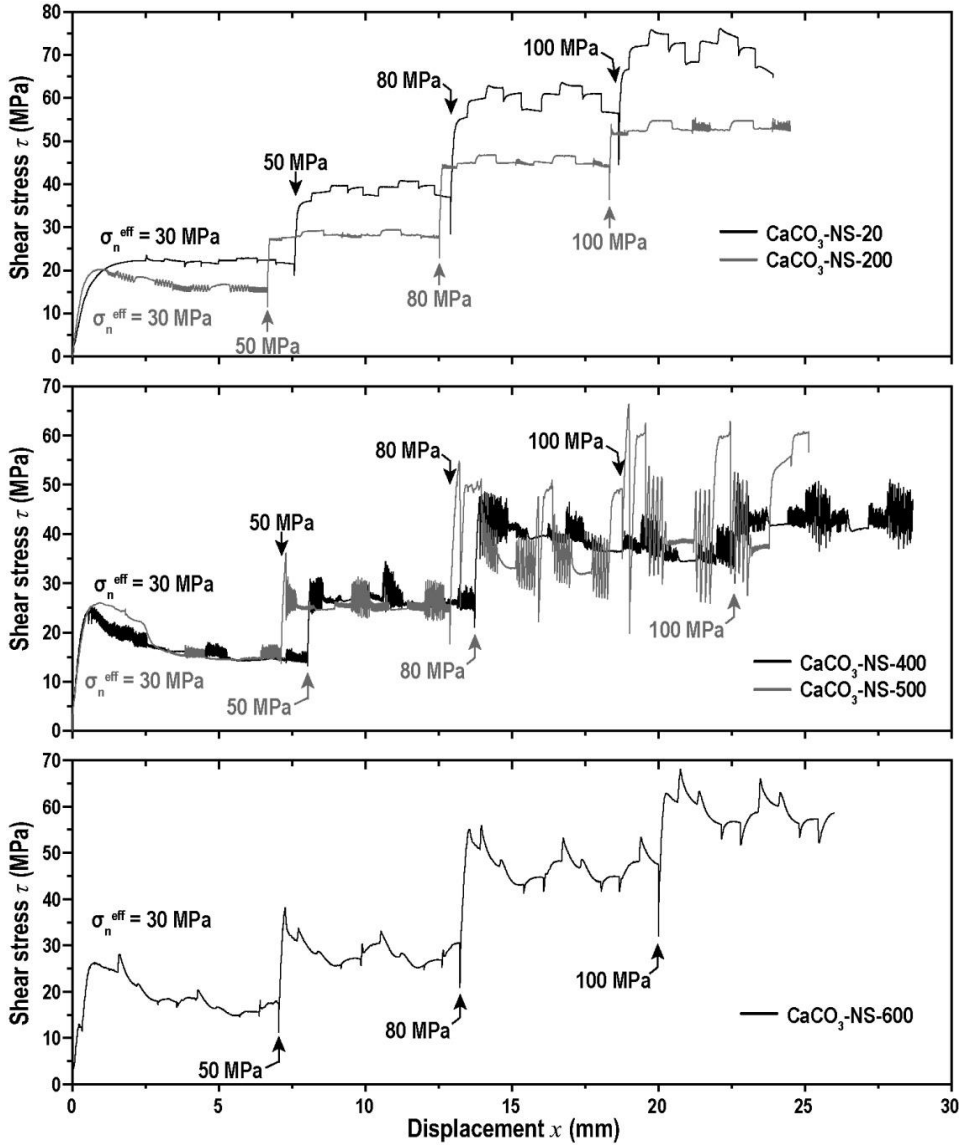

Figure 5.9. Plots of shear stress (τ) against displacement for the σ_n^{eff}-stepping experiments. a) $T \approx 20°$ and 200°C. b) $T \approx 400°$, 500°, and 550°C. c) $T \approx 600°$C. Steps in σ_n^{eff} as indicated. A list of all experiments is given in Table 5.1, and a list of τ_I , τ_{II} , and τ_{III} values is given in Table 5.2.

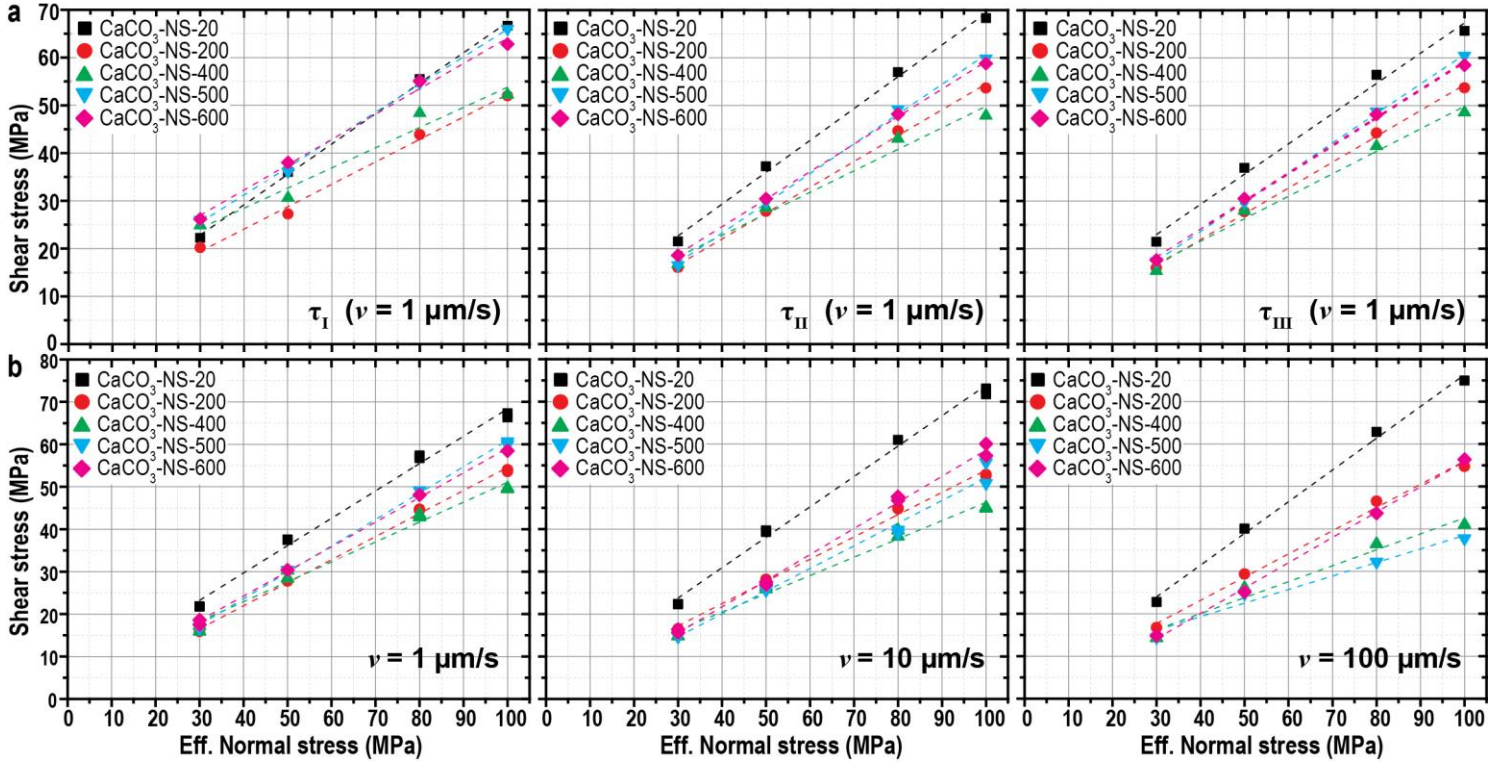

Figure 5.10. Plots of shear stress (τ) against effective normal stress (σ_n^{eff}) for the temperatures indicated in the sample codes and the sliding velocities shown. a) Values of τ_I, τ_{II}, and τ_{III} (for a list of values see Table 5.2). b) Values of τ_{ss} (or else τ_{fail}) measured, at each sliding velocity, in the second cycle of velocity steps, applied within each σ_n^{eff} step (cf. Figs. 5.4b, 5.9). For a list of linear regression parameters, see Table 5.3.

Experiment	T_{mn} (°C)	$\tau_k = S_o + \mu_o \cdot \sigma_n^{eff}$																	
		τ_I			τ_{II}			τ_{III}			v = 1 µm/s			v = 10 µm/s			v = 100 µm/s		
		S_o	μ_o	R^2	S_o	μ_o	R^2	S_o	μ_o	R^2	S_o	μ_o	R^2	S_o	μ_o	R^2	S_o	μ_o	R^2
$CaCO_3$-NS-20	17.9 ±0.4	3.73 ±1.25	0.64± 0.02	0.998	2.64 ±2.05	0.67± 0.03	0.994	3.90± 2.92	0.63± 0.04	0.987	2.29 ±1.58	0.72± 0.02	0.993	3.89 ±1.62	0.64± 0.02	0.991	1.55 ±2.41	0.75± 0.03	0.994
$CaCO_3$-NS-200	199 ±1.0	5.30 ±1.87	0.47± 0.03	0.990	0.36 ±1.37	0.54± 0.02	0.996	0.22± 1.09	0.54 ±0.01	0.998	1.49 ±1.10	0.52± 0.02	0.994	0.19 ±0.73	0.54 ±0.01	0.997	1.27 ±2.11	0.55± 0.03	0.991
$CaCO_3$-NS-400	398 ±4.8	11.6 ±3.72	0.42 ±0.05	0.954	4.75 ±3.30	0.45 ±0.05	0.968	2.68± 2.60	0.47± 0.04	0.982	3.24 ±1.48	0.43± 0.02	0.983	4.16 ±1.80	0.47± 0.03	0.980	5.02 ±3.40	0.38 ±0.05	0.952
$CaCO_3$-NS-500	500 ±9.9	8.09 ±1.04	0.58 ±0.01	0.998	-1.67 ±1.34	0.62± 0.02	0.997	-1.13 ±0.45	0.62 ±0.01	1.000	-1.32 ±1.63	0.53± 0.02	0.984	-1.25 ±0.66	0.62± 0.02	0.998	6.53 ±2.67	0.32± 0.04	0.959
$CaCO_3$-NS-600	614 ±5.6	11.0 ±2.04	0.53± 0.03	0.991	1.52 ±0.65	0.58 ±0.01	0.999	0.68± 1.18	0.58± 0.02	0.998	-2.89 ±1.08	0.62± 0.02	0.995	1.02± 0.60	0.58 ±0.01	0.999	-3.81 ±1.17	0.60± 0.02	0.998

Table 5.3. List of regression parameters obtained from fits on shear stress – effective normal stress curves (see Fig. 5.10).

5.4.3. Velocity dependence of strength (Γ)

We determined the velocity dependence of strength (Γ) using equation 5.2, for all velocity steps performed in Stage II of all experiments (with the exception of $CaCO_3$-500-LV). We determined Γ values from Stage II only because i) strong displacement-weakening associated with low displacements in experiments performed at 100° ≤ T ≤ 600°C has come to an end (see e.g. Fig. 5.5), and ii) Stage II provides a full cycle of downward and upward velocity steps from 100 to 0.1 or else 1 μm/s (see Figs. 4a, b). A list of Γ values is given in Table 5.4. These data were used to plot Γ against temperature, post-step sliding velocity (v_2), and effective normal stress (see Figs. 5.11a-c).

The results show a transition from velocity strengthening ($\Gamma \approx$ 0.00 to 0.02) at 18°C to velocity weakening ($\Gamma \approx$ -0.01) at 100°C (Fig. 5.11a, Table 5.4). At 200°C (experiment $CaCO_3$-200), upward steps in sliding velocity produced velocity strengthening ($\Gamma > 0$) at $v_2 \geq 30$ μm/s versus velocity weakening ($\Gamma < 0$) at $v_2 < 30$ μm/s. Similarly, downward steps in sliding velocity yielded velocity strengthening ($\Gamma > 0$) at $v \geq 3$ μm/s versus velocity weakening ($\Gamma < 0$) at $v < 3$ μm/s (Fig. 5.11b, Table 5.4). In the experiments performed at T = 400-550°C, all steps were characterized by velocity weakening behaviour, with Γ decreasing to a sharp minimum at $T \approx$ 500-550°C (Figs. 5.11a, b and Table 5.4). Note that this temperature range of 400° to 550°C is that where stick-slip behaviour was most marked, particularly at the lower sliding velocities used (Figs. 5.5, 5.8, 5.9). At 600°C (experiment $CaCO_3$-600), near-velocity-neutral behaviour dominated. In detail, minor velocity strengthening occurred in upward steps with v_2 = 0.3 μm/s, versus minor velocity weakening at $v_2 \geq 3$ μm/s. In downward steps, we found velocity strengthening for v_2 = 3 and v_2 = 10 μm/s, versus velocity weakening for v_2 = 30 μm/s. By comparison with the effect of temperature, Γ was found to be more or less independent of velocity (i.e. v_2) and of σ_n^{eff}, except at 500°C where Γ decreased with increasing σ_n^{eff} (Fig. 5.11c, Table 5.4).

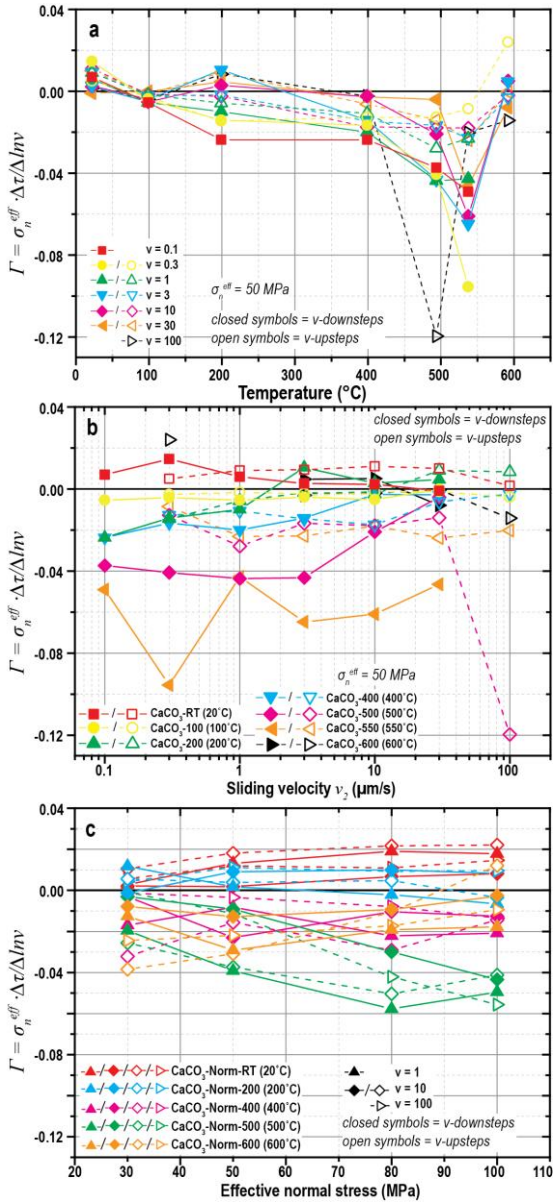

Figure 5.11. Plots of the velocity dependence of strength Γ, determined from Stage II of all experiments (with the exception of $CaCO_3$-500-LV), against a) temperature (T), b) post-step sliding velocity (v_2), and c) effective normal stress (σ_n^{eff}). Γ values were obtained using eq. 5.2, and are listed in Table 5.4. Data from experiment $CaCO_3$-500-LV were excluded because this test employed a unique displacement-velocity history (see Table 5.1).

Experiment[1]	T_{mn} (°C)	σ_n^{eff} (MPa)	*v*-down steps[2]						*v*-up steps[2]					
			100→30	30→10	10→3	3→1	1→0.3	0.3→0.1	0.1→0.3	0.3→1	1→3	3→10	10→30	30→100
$CaCO_3$-RT	22.2±0.7	50	-0.001	0.002	0.003	0.006	0.015	0.007	0.005	0.009	0.009	0.011	0.010	0.002
$CaCO_3$-100	98.8±1.1	50	0.000	-0.005	-0.004	-0.005	-0.004	-0.005	-0.003	-0.002	-0.002	-0.001	-0.001	-0.004
$CaCO_3$-200	199±0.9	50	0.005	0.003	0.010	-0.010	-0.014	-0.024	-0.015	-0.006	-0.002	-0.002	0.009	0.008
$CaCO_3$-400	399±0.9	50	-0.003	-0.003	-0.014	-0.020	-0.017	-0.024	-0.013	-0.011	-0.015	-0.017	-0.006	-0.002
$CaCO_3$-500	494±2.3	50	-0.004	-0.021	-0.043	-0.044	-0.041	-0.037	-0.013	-0.028	-0.017	-0.018	-0.014	-0.120
$CaCO_3$-550	537±2.3	50	-0.047	-0.061	-0.065	-0.043	-0.096	-0.049	-0.009	-0.023	-0.023	-0.018	-0.024	-0.020
$CaCO_3$-600	592±1.9	50	-0.008	0.005	0.005	n/a[3]	n/a[3]	n/a[3]	0.024	n/a[3]	-0.003	-0.002	0.000	-0.014
			100→10			10→1			1→10			10→100		
$CaCO_3$-NS-RT	17.9±0.4	30	0.002			0.003			0.011			0.006		
		50	0.002			0.013			0.018			0.012		
		80	0.007			0.019			0.022			0.011		
		100	0.008			0.018			0.022			0.015		
$CaCO_3$-NS-200	199±1.0	30	n/a[3]			n/a[3]			n/a[3]			n/a[3]		
		50	0.009			0.002			0.004			0.011		
		80	0.010			-0.002			0.005			0.009		
		100	0.008			-0.007			-0.003			0.010		
$CaCO_3$-NS-400	398±4.8	30	-0.003			-0.017			-0.032			-0.001		
		50	-0.023			-0.008			-0.016			-0.003		
		80	-0.010			-0.022			-0.029			-0.008		
		100	-0.013			-0.021			-0.014			-0.013		
$CaCO_3$-NS-500	500±9.9	30	-0.003			-0.020			-0.026			-0.001		
		50	-0.009			-0.039			-0.037			-0.011		
		80	-0.030			-0.058			-0.050			-0.042		
		100	-0.043			-0.050			-0.041			-0.056		
$CaCO_3$-NS-600	614±5.6	30	-0.008			-0.013			-0.038			-0.024		
		50	-0.013			-0.029			-0.031			-0.022		
		80	-0.009			-0.019			-0.011			-0.017		
		100	-0.003			-0.018			0.012			-0.009		

Table 5.4. List of rate sensitivity parameter values ($\Gamma = \Delta\tau / (\sigma_n^{eff} \cdot \Delta ln v)$. [1]Data from experiment $CaCO_3$-500-LV were excluded because this test employed a unique displacement-velocity history (see Table 5.1). [2]Velocity steps applied in Stage II (see Fig. 5.4). Grey shading indicates that the data showed stick-slip after the step. Sliding velocity in μm/s. [3]Sliding did not reach a constant (average) τ_{ss} or τ_{fail}, preventing determination of Γ.

5.5. Microstructural observations

Investigation of the sheared gouge microstructures showed major differences between samples sheared at relatively low (20° to 200°C) versus relatively high (400° to 600°C) temperatures, whereas only minor differences were found between samples recovered from the constant effective normal stress versus the effective normal stress stepping experiments. Therefore, in the following we focus on samples from experiments conducted at different temperatures.

5.5.1. Microstructures developed at 20° to 200°C

Upon separation of the internal ring shear pistons and removal of the outer confining ring, all samples recovered from experiments performed at 20° to 200°C split along a shear-induced fabric developed parallel and/ or inclined to the sample-piston interface. Unfortunately, the samples frequently fell apart into numerous small fragments which we were unable to recover for sectioning. We only retained a cohesive arc-shaped fragment from the gouge layer from experiment $CaCO_3$-NS-20, which yielded a section of high quality (Fig. 12a).

Optical analysis and SEM investigation of the microstructure from experiment $CaCO_3$-NS-20 showed the presence of horizontal boundary and inclined shear bands (Y- and R_1 shears, respectively, using the terminology of *Logan et al., 1979)* characterized by a strongly reduced grain size cutting a relatively coarse-grained matrix (Fig. 12a, b). Matrix grains are mainly angular, the largest ones present being of the order of the median grain size of the starting material (10 to 30 μm). We did not find indicators of severe ductile deformation in the matrix, such as elongated grains or porphyroclasts. Grains within the shear bands fall below the resolution limit of light microscopy, indicating that they are below 1 μm in size (Fig. 12a). SEM imaging of a boundary shear band confirmed the presence of angular grains ~300 nm in size, plus more rounded grains that are even smaller (Figs. 12b to d). Although boundary shears are present at both the upper and lower margins of the sample, the upper margin shear band is generally wider and more continuous. The width of the (upper margin) boundary shear ranges from ~250 μm in the center of the section to ~10 μm at the ends. When using crossed nicols in the light microscope, the submicron-sized grain aggregates in the shear bands show strong, uniform, birefringence colours (Fig. 12a), and uniform extinction, suggestive of a strong crystallographic preferred orientation (CPO) (cf. *Verberne et al., 2013a, b).*

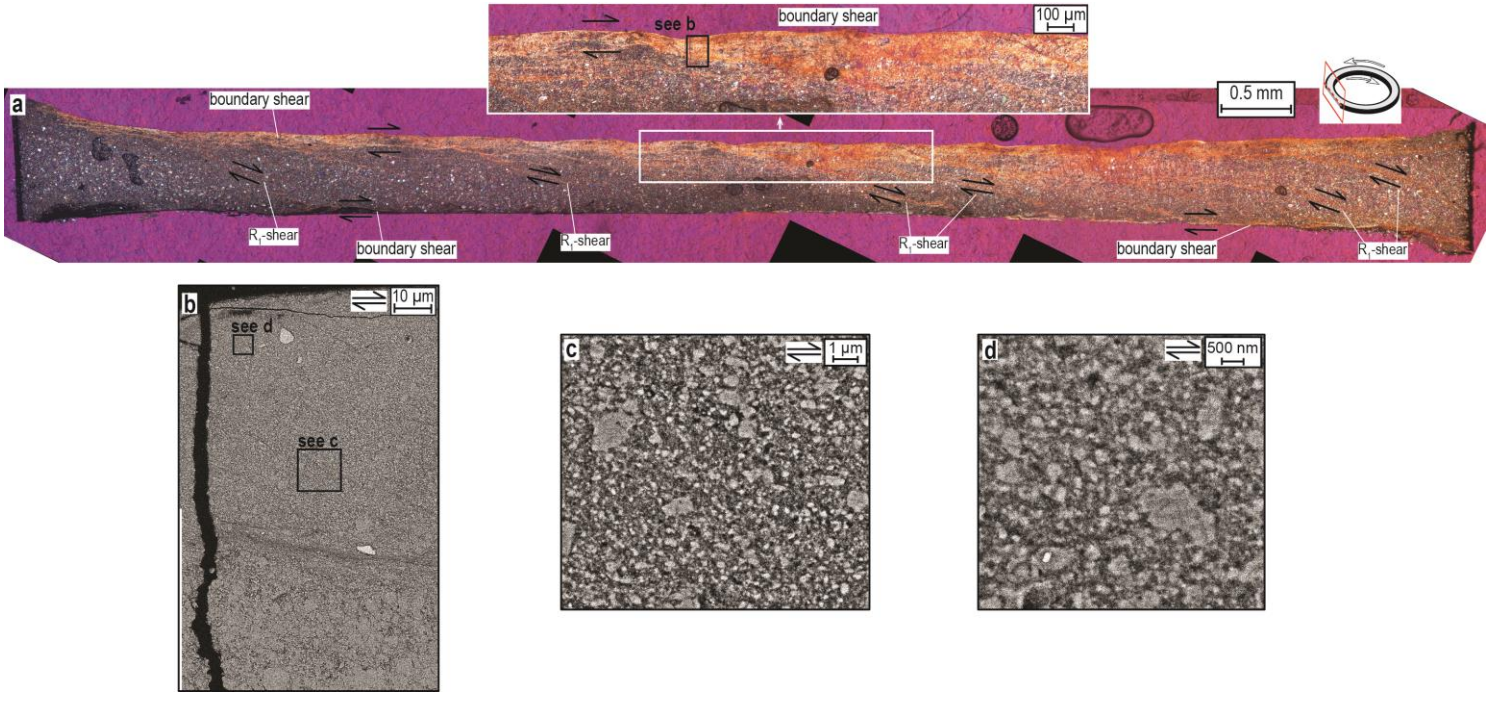

Figure 5.12. Micrographs from a thin section prepared from simulated calcite gouge sheared at ~18°C (experiment $CaCO_3$-NS-20). a) Photomosaic of cross-polarized light micrographs taken with the gypsum plate inserted. Due to incomplete sample recovery, the sample is thicker at the ends (outer perimeter) than in the center. b-d) BSE micrographs taken from the upper, ultra-fine grained (nanoscale) boundary shear band (see inset in (a)).

In a section prepared from a sample fragment recovered from experiment $CaCO_3$-200, performed at 200°C, we confirmed the presence of optically uniformly birefringent boundary and inclined shear bands, similar to those seen in the sample from experiment $CaCO_3$-NS-20. Also, the splitting of the samples along multiple boundary and inclined fractures after an experiment strongly suggests the presence of shear bands in the gouge microstructure.

5.5.2. Microstructures developed at 400° to 550°C

Samples recovered from experiments performed at 400° to 550°C showed a 20 to 100 μm wide boundary-parallel shear band of strongly reduced grain size developed at one of the sample-piston interfaces only (Figs. 5.13a, b). Little evidence was found for R_1 shears. In the matrix, the grain size is of the order of the median grain size of the starting material (10 to 30 μm), whereas within the boundary shear band grains are just visible with a light microscope. Matrix grains remote from the shear band are angular, equidimensional, and chaotically packed (Figs. 5.13a, b). However, in a zone ~50 to 100 μm wide adjacent to the boundary shear, within the bulk gouge, the matrix grains, still typically 10 to 30 μm in size, are elongated to form a pronounced foliation at around +30° to the shear direction (Fig. 5.13c). Immediately adjacent to the shear band this foliation sweeps into parallelism with a boundary shear, constituting a fabric consistent with that expected for ductile deformation close to the boundary shear or piston face (Figs. 5.13a-c). In sample $CaCO_3$-550, elongated grains immediately adjacent to the shear band have dimensions of ~110 μm long by ~3 μm wide, i.e. have an aspect ratio as high as 36:1 (Fig. 5.13c). In contrast to samples sheared at 20° to 200°C, the shear bands developed at 400° to 550°C showed no optical CPO (Fig. 5.13 cf. Fig. 5.12b). Instead, SEM imaging of the boundary shear revealed the presence of marked linear arrays of equigranular, polygonal grains, measuring 0.5 to 2 μm in diameter, characterized by 120° grain boundary triple junctions and cavitated grain boundaries (Figs. 5.13d, e). These arrays are aligned parallel to the shear plane in the shear band core (Fig. 5.13c), but appear to sweep into parallelism with the optical foliation towards the margins (cf. Figs. 5.13d, e, c).

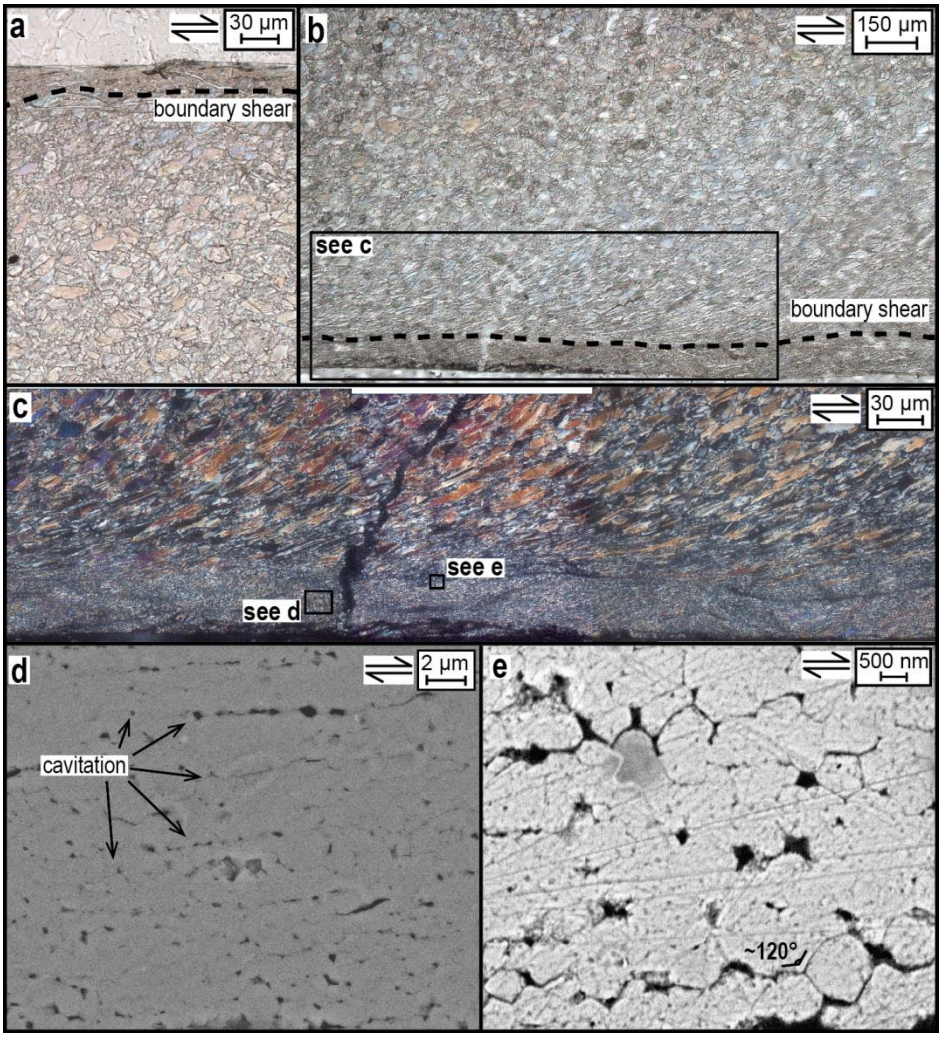

Figure 5.13. Micrographs obtained from thin sections prepared from central parts of samples sheared at $T \approx 400°$ to 550°C. a) Plane polarized light (PPL) micrograph, experiment $CaCO_3$-400. b) PPL micrograph, experiment $CaCO_3$-550. c) Photomosaic enlargement of the portion of the shear band and adjacent zone indicated in (b). Micrograph taken in cross-polarized light. d) and e) Backscatter electron (BSE) micrographs taken from the parts of the boundary shear band shown in c (sample $CaCO_3$-550). Note the apparent continuity in orientation of fabric from the centre of the shear band out into the margin of the band and beyond (of d, e and c).

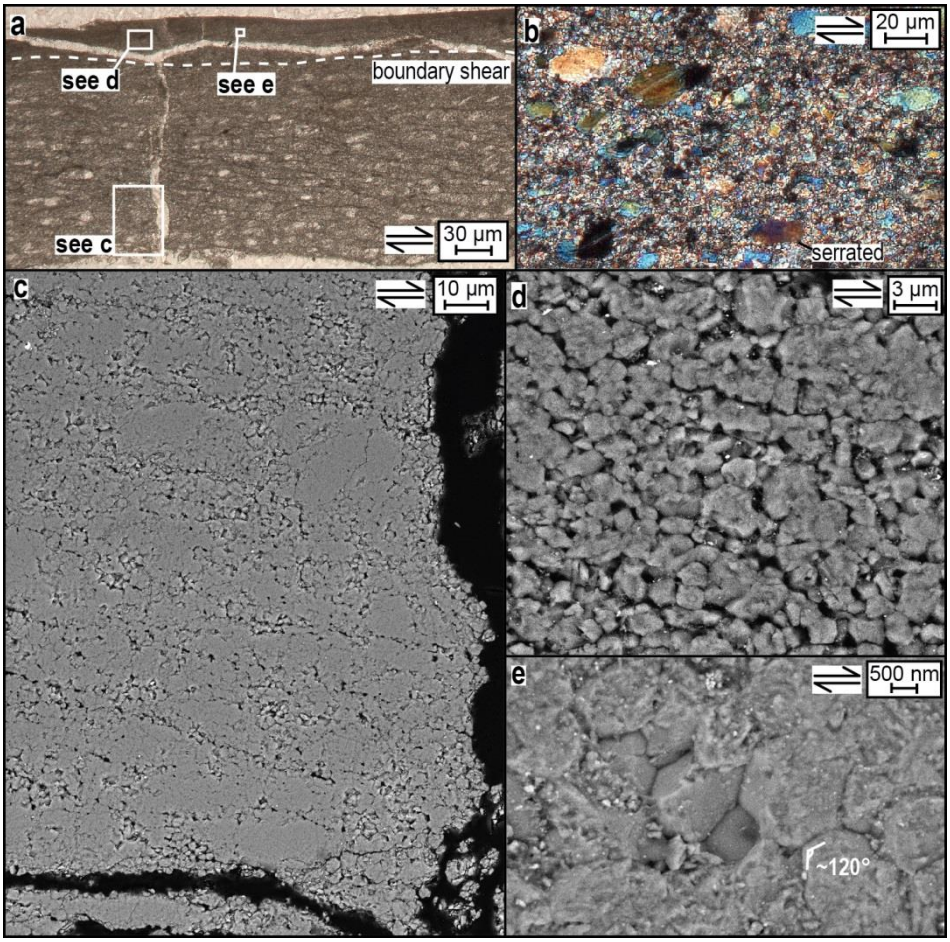

Figure 5.14. Microstructure of sample $CaCO_3$-NS-600 (sheared at ~600°C). a) PPL image showing a fabric defined by fine aligned cracks and elongate porphyroclasts oriented with their long axes (sub) parallel to the shear direction. Note the clast-free, boundary shear band present at the top of the section. b) Optical image (crossed polarizers) showing undulose extinction and serrated boundaries of porphyroclasts plus enveloping fine matrix grains. c) Mosaic of BSE micrographs, highlighting part of the bulk gouge shown in a. d) BSE micrograph highlighting part of the boundary shear shown in a. e) BSE micrograph from the boundary shear showing ~120° triple junctions developed between polygonal, sub-micrometre sized grains.

5.5.3. Microstructures developed at 600°C

Material sheared at ~600°C showed a single fine-grained shear band developed at the margin of a relatively uniform, foliated, porphyroclastic bulk gouge (Fig. 5.14a). The fabric of the bulk is characterized by elongate porphyroclasts aligned sub-parallel to the shear direction, and embedded in a matrix of much finer (~1 to 2 μm) grains. The porphyroclasts are ~10 to 30 μm long by ~5 to 20 μm wide, have serrated boundaries and commonly show undulose extinction (Fig. 5.14b). Numerous fine cracks are visible at the sample scale, aligned sub-parallel to the foliation. The boundary shear band, which is typically ~50 to 100 μm wide, is devoid of the coarse porphyroclasts seen in the body of the sample, and instead only consists of finer grains just visible with a light microscope. As in the samples sheared at 400° to 550°C, no optical CPO was detectable in the shear band, using crossed nicols in a polarizing light microscope. SEM imaging of the matrix in the bulk of the sample showed that the cracks seen optically are dilated zones aligned mainly at an angle of -10 to -15° to the shear direction (i.e. in an R_1 orientation). These follow the zones of fine-grained matrix that anastamose around and envelope the elongate porphyroclasts (Fig. 5.14c). The finer grains in the matrix are equidimensional and equigranular, being 0.5 to 2 μm in diameter. The grains present in the boundary shear band are also 0.5 to-2 μm in size, they are polygonal, with 120° grain boundary triple junctions, and form linear, cavitated arrays aligned parallel to the fine cracks seen at -10 to -15° to the shear direction (Figs. 5.14d, e).

5.6. Discussion

The shear strength and velocity dependence data obtained in this study showed striking trends with changing temperature, sliding velocity, and effective normal stress (Figs. 5.5 to 5.11). Also, the recovered gouge microstructures showed major changes (Figs. 5.12 to 5.14), indicating increasingly ductile deformation in experiments performed at higher temperatures, i.e. towards 600°C. The shear strength data obtained from experiments conducted at a constant effective normal stress of 50 MPa initially showed a decrease as the temperature increased from 20° to 100-200°C, and then increased reaching a maximum at 550-600°C (Fig. 5.6). Treating these data in terms of an apparent friction coefficient ($\mu = \tau/\sigma_n^{eff}$) yielded μ-values of ~0.7 at low displacements (Stage I, τ_I), at room temperature, decreasing to ~0.6 at 100-200°C (Table 5.2). These values are similar to the friction coefficient obtained in previous studies on simulated calcite gouge conducted at 20° to 140°C, at low (≤53 MPa) effective normal stresses using

relatively low displacement rates (1 to 300 μm/s) (Verberne et al., 2010, 2013b; Tesei et al., 2014; Carpenter et al., 2014; Chen et al., 2015).

In the following, we first attempt to place constraints on the deformation mechanisms that operated in our experiments, by comparing our results on the simulated calcite gouges with results obtained in previous experiments on dense calcite polycrystals. We then focus on the microphysical processes controlling frictional strength and slip stability in our tests, by making a qualitative comparison between the observed effects of temperature/ sliding rate on (the velocity dependence of) shear strength, and predictions made by the Niemeijer-Spiers model introduced in Section 5.2. Finally, we discuss the implications of our results in the context of natural fault zones in tectonically-active carbonate terrains.

5.6.1. Deformation mechanisms

5.6.1.1. Mechanisms operating at 20° to 200°C

The shear bands characterized by strong grain size reduction and uniform optical birefringence (CPO) seen in samples sheared in our ring shear set-up at 20° to 200°C (Fig. 5.12) represent the same nanogranular shear band features as those reported by Verberne et al. (2013a, b) (i.e. in Chapter III). These authors demonstrated the development of 10 to 100 μm wide, nanocrystalline, boundary shear bands, with a CPO, in direct shear experiments on simulated calcite gouges performed at σ_n^{eff} = 50 MPa, T = 20° to 150°C, and v = 0.1 to 10 μm/s. An important difference is that our present samples were sheared to displacements of 20 to 25 mm, compared with only 5 to 6 mm in the direct-shear experiments of Verberne et al. (2013a, b). Assuming that virtually all of the imposed displacement is accommodated by a single boundary shear band that has an effective width of ~100 μm, this implies a shear strain (γ) of 200 to 250 in the present ring shear tests compared with ≤50 in the direct shear tests. Given this difference in total accommodated γ, the similarity in microstructure is striking, implying that for calcite gouge sheared to 5-6 mm at temperatures of 20° to 200°C, a steady-state microstructure has already been attained, so that the observed mechanical behaviour and microstructure can be considered to be that of a mature calcite gouge. Following Verberne et al. (2013a, b, 2014) (see Chapters III and IV), nano-scale processes active in the shear bands must have accommodated the bulk of the imposed shear strain, as opposed to the bulk gouge or matrix, which appears relatively undeformed compared with grains in the shear bands. Specifically, we suggest that nanogranular flow, in combination with intergranular

diffusive mass transfer and/ or crystal plasticity played a role in the shear bands. Oriented attachment of coherent nanoparticle interfaces may have been responsible for development of the shear band CPO (Verberne et al., 2014, or Chapter IV).

5.6.1.2. Mechanisms operating at 400° to 600°C

Compared with samples sheared in the temperature range of 20° to 200°C, those sheared at 400° to 600°C showed a less intensely localized shear band microstructure. The boundary shears were coarser grained (0.5-2 μm vs. <<1 μm), lacked the strong optical CPO seen at 20-200°C, and graded into a broader foliated zone (Figs. 5.13, 14 cf. Fig. 5.12). Gouges sheared at 400° to 550°C displayed strongly elongated grains 20 to 30 μm in size (Fig. 5.13), suggestive of intracrystalline plastic deformation (e.g. cf. Schmidt et al., 1987; Barnhoorn et al., 2004; De Raadt et al., 2014). At 600°C, the sheared sample displayed aligned elongated porphyroclasts embedded in a fine-grained matrix of equigranular polygonal grains, throughout the bulk gouge samples. These features, along with serrated boundaries and undulose extinction seen in porphyroclasts (Fig. 5.14), suggest intracrystalline plasticity plus dynamic recrystallization (e.g. Urai et al., 1986; Valcke et al., 2014). This means that in addition to localized deformation occurring within the shear band, involving developments of linear, cavitated arrays of polygonal grains (Figs. 5.13d, e, 5.14d, e), plastic deformation and dynamic recrystallization processes must have played a role in the bulk gouge or matrix of the samples sheared over the range of 400° to 600°C.

An extensive data set exists on the rheology of dense calcite polycrystals in the temperature range of 300° to 1000°C (e.g. Rutter 1974; Schmid et al., 1980, 1987; Walker et al., 1990; De Bresser, 2002; De Bresser et al., 2002; Renner et al., 2002; Herwegh et al., 2003), resulting in relatively well-constrained deformation mechanism maps (DMM's) for calcite (see e.g. De Bresser et al., 2001; Herwegh et al., 2005; Rogowitz et al., 2014). Despite the important differences in experimental and sample character between our tests and those reported in the above-mentioned studies (water saturated gouge vs. relatively dry dense polycrystals), a comparison of the predicted rheology of dense calcite polycrystals with the experimental conditions imposed in our experiments may help to elucidate the processes that played a role in our experiments at $T \approx$ 400-600°C. Therefore, we constructed DMM's for calcite for T = 400, 500 and 600°C, using the creep equations reported by Herwegh et al. (2003) for the grain size sensitive (GSS) field, by Walker et al. (1990) for the GSS + grain size insensitive (GSI) field, and using the

experimental data of De Bresser (2002) fitted to an exponential-type flow equation (e.g. Rutter, 1974; Schmid et al., 1980) to represent the GSI field (Fig. 5.15) (see Appendix 5.A; for a summary of GSI and GSS mechanisms see Herwegh et al., 2005). These flow laws were determined for axial compression. In order to compare our shear stress (τ) – shear strain rate ($\dot{\gamma}$) values with these flow laws, we converted τ and ($\dot{\gamma}$) in equivalent flow stress (σ) and strain rate ($\dot{\varepsilon}$) for compression tests using the relations $\sigma = \tau\sqrt{3}$ and $\dot{\varepsilon} = \dot{\gamma}/\sqrt{3}$ (Schmid et al., 1987). Using $\tau \approx$ 20-50 MPa as a broad range representing the shear stresses τ_I, τ_{II}, and τ_{III} measured in our experiments at 400° to 600°C (Table 5.2), this resulted in an equivalent flow stress of ~35 to 90 MPa for our samples in the DMM (Fig. 5.15). The shear strain rate imposed in our experiments is estimated to be ~10^{-4} to 10^{0} s^{-1}, based on the range of imposed sliding velocities (0.1-100 μm/s) and the width of the slipping zone in samples sheared at 400-600°C (Figs. 5.13, 5.14). Lacking more precise constraints on the active slip zone width at a particular velocity interval, the latter is taken to range from 50 to 700 μm, representing the width of the boundary shear to the entire sample layer. Thus, the equivalent compressive strain rate ($\dot{\varepsilon}$) for our experiments is 10^{-4} to 10^{1} s^{-1}, which we plotted as lines of constant strain rate in Figure 5.15. We also plotted $\dot{\varepsilon} = 10^{-6}$ and $\dot{\varepsilon} = 10^{-5}$ s^{-1}, which more closely approximates the strain rates used in the experiments on which the flow equations of dense calcite are based (Walker et al., 1990; Herwegh et al., 2003; De Bresser, 2002).

The stress and strain rate conditions applying to the calcite gouges as deformed in the present study are in reasonable agreement with the conditions needed for ductile flow of calcite polycrystals in compression, in particular for T = 500° and 600°C (Fig. 5.15). Using the maximum grain size of the starting gouge powder (range $1 < d < 70$ μm) as a starting point, for T = 400°C GSI creep is expected to occur only at the lowest strain rates (<10^{-4} s^{-1}) and the highest equivalent flow stresses (σ > 90 MPa), whereas for T = 500-600°C for shear strain rates of 10^{-4} to 10^{-2} s^{-1}, grains >7 μm in size plot well in the field where both GSI and GSS mechanisms are active (Figs. 5.15b, c). Although our optical inspection of the corresponding sectioned samples did not show evidence for a CPO such as in samples sheared at low temperatures (Figs. 5.13, 5.14 cf. Fig. 5.12), this is consistent with the strongly elongated, 20 to 30 μm sized grains seen in these samples. For grain sizes of ~1 μm, for T = 500-600°C and strain rates relevant to our experiments (10^{-4} to 10^{-2} s^{-1}), GSS mechanisms such as diffusion creep and grain boundary sliding (GBS) may become more important (Figs. 5.15b,c). Notable microstructural criteria indicative for GBS are (Fliervoet et al., 1997): i) the alignment of cavitated grain boundaries (White &

White, 1981; Kassner & Hayes, 2003) and ii) a grain aggregate consisting of fine (<10 μm) equant grains lacking a strong CPO (Rutter et al., 1994; Bestmann & Prior, 2003). These are both consistent with the structures seen in the boundary parallel shears of samples deformed at 400° to 600°C (Figs. 5.13, 5.14), and with the polygonal (~1 μm) matrix grains seen in samples deformed at 600°C (Fig. 5.14). Thus, microstructural evidence as well as comparison with a DMM of calcite suggests that ductile deformation mechanisms via GSI and GSS creep processes have played an important role in our experiments conducted in the temperature range from 400° to 600°C.

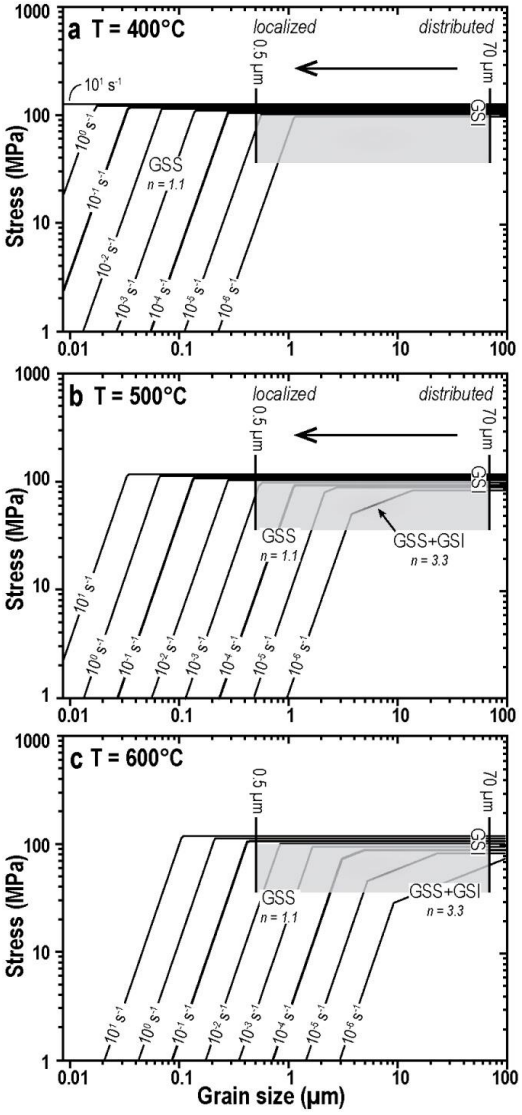

Figure 5.15. Deformation mechanism maps for calcite, drawn for constant temperatures (T) of a) 400°C, b) 500°C, and c) 600°C, using the creep equations fitted by Herwegh et al. (2003) (grain size sensitive (GSS), n = 1.1) and Walker et al. (1990) (grain size insensitive + GSS, n = 3.3) on data from triaxial compression experiments on synthetic calcite aggregates, and using a (GSI) exponential-type creep equation fitted to data from triaxial compression experiments on Carrara marble from De Bresser (2002). See Appendix 5.A for details on their construction. Strain rate contours are shown for $\dot{\varepsilon}$ = 10^{-6}-10^{1} s^{-1}. The shaded area plots the estimated conditions relevant for our experiments.

However, ductile creep mechanisms require higher flow stresses at higher shear strain rates (Fig. 5.15), implying that they are intrinsically velocity strengthening processes. This is inconsistent with the strong velocity weakening behaviour seen in all our experiments performed at 100° to 600°C (Table 5.4, Figs. 5.11), and with the stick-slip behaviour that is frequently seen to be associated with this (Fig. 5.9). Also, GSS and GSI creep processes are (relatively) insensitive to normal stress, so that in the case of pure creep-accommodated shear flow, our σ_n^{eff} -stepping experiments should have demonstrated insensitivity to effective normal stress instead of a linear correlation between τ and σ_n^{eff} (Table 5.3, Figs. 5.9, 5.10). Of course, one of the crucial differences between our experiments and the above-mentioned compression experiments on dense calcite polycrystals is that in those experiments the samples used have a much lower (starting) porosity (<1%) than in our samples (~15 to 30%). Fault gouge porosity, and its evolution during shear, plays a major role in controlling the strength and slip stability of granular media (e.g. Marone et al., 1990; Bos & Spiers, 2002b; Niemeijer & Spiers, 2006, 2007; Samuelson et al., 2009). Moreover, our samples were water-saturated, compared with the nominally dry samples deformed by Walker et al. (1990), De Bresser (2002) and Herwegh et al. (2003), whose results formed the basis of the DMM's used to compare our experiments with (Fig. 5.15, Appendix 5.A). Although water is unlikely to affect GSI processes in calcite in a significant way (Rutter, 1974), its presence can substantially enhance diffusive mass transfer processes, in particular in the range from 20° to 150°C (e.g. Spiers et al., 2004; Zhang & Spiers, 2010). In our experiments performed at temperatures ≥ 400°C, the pore fluid water was supercritical, and had a relatively low density since the pore pressure used was only 60 MPa or lower (Table 5.1). From the present study the importance of fluid-assisted diffusive mass transfer is impossible to evaluate. Nonetheless, we anticipate that these processes will be slow in the presence of low density, supercritical water at temperatures of 400° to 600°C (cf. Rutter, 1983).

Further, we note that the 10 to 30 μm sized elongated grains and/ or porphyroclasts seen adjacent to the fine-grained boundary shear in samples deformed at 400° to 600°C suggests that the width of the actively slipping zone has varied during the experiment, or that there was a gradient in $\dot{\gamma}$ from the boundary shear into the body of the gouge. In view of the complex history of sliding velocities used in our tests (v = 0.03-100 μm/s), we cannot use the recovered sheared gouge microstructures to tie the active slip zone width to a corresponding interval of slip rate. Notwithstanding this, the DMM's of calcite (Fig. 5.15) demonstrate that for temperatures of 400° to 600°C, the lower the shear strain rate

then the more likely it becomes that larger, 10 to 30 μm sized grains in our samples deform by GSI processes such as dislocation creep. This implies that the lower the imposed sliding velocity, the more likely it is that larger matrix grains deform by intracrystalline slip, thus effectively distributing the imposed shear strain over a wider slipping zone, leading to a further decrease of the shear strain rate. This implies that for samples sheared in the range of 400° to 600°C, the lower the imposed sliding rate the wider the actively slipping zone.

5.6.2. Microphysical processes controlling steady-state strength and slip stability

The modified Niemeijer-Spiers model predicts that, with increasing temperature, shear will transition from a i) regime of frictional velocity strengthening granular flow at critical state, to ii) a regime of frictional velocity weakening characterized by balanced dilatant granular flow and compaction creep, and finally to iii) a regime of velocity strengthening, frictional-viscous flow (respectively Regimes A, B, and C in Fig. 5.2; Bos & Spiers, 2002a; Niemeijer & Spiers, 2007; Den Hartog & Spiers, 2013, 2014; Chen, 2015). The transition at low temperature, i.e. from A to B in Figure 5.2, is expected to be accompanied by a gradual decrease in steady-state shear strength (τ_{ss}), followed by a progressive increase of τ_{ss} with increasing temperature within Regime B, i.e. within the frictional velocity weakening regime (see Fig. 5.2c). Towards even higher temperatures, the transition to the frictional-viscous regime (from B to C in Figure 5.2) is expected to be accompanied by an overall decrease of τ_{ss} with increasing temperature (see Fig. 5.2c, Bos & Spiers, 2002a). Similarly, for the rate dependence of shear strength, or $\partial \tau_{ss} / \partial \dot{\gamma}$, with increasing temperature the model (qualitatively) predicts a gradual decrease from positive values in Regime A to negative values in Regime B, where it reaches a minimum, followed by a sharp switch to positive values associated with Regime C (Fig. 5.2d).

Interestingly, the Niemeijer-Spiers model predictions of steady-state shear strength, and its rate sensitivity, with increasing temperature, are broadly consistent with trends in shear strength values (τ_I, τ_{II}, and τ_{III}), and in the velocity dependence of strength (Γ), with increasing temperature as measured in our experiments (Figs. 5.6, 5.11a cf. Figs. 5.2b, c). We note, however, that the minimum in Γ-values around 500-550°C (Fig. 5.11a) corresponds to experiments which showed stick-slip characterized by relatively large stress drops, especially at the lower sliding velocities employed (Figs. 5.5c, 5.8). The slope of the Niemeijer-Spiers model curve of steady-state shear strength against shear strain rate of a sheared gouge (Fig. 5.2a) returns the rate sensitivity of the steady-state

shear strength only, corresponding with the so-called "*(a-b)*" values used in RSF modelling. This implies that we cannot one-on-one compare the present Γ-values, or trends thereof with temperature, with those predicted by the model. However, since stress drop that is associated with stick-slip increases with increasing value of $|a-b|$ (Gu & Wong, 1991), it is reasonable to suppose that the minimum in Γ-values seen in our data corresponds with a minimum in the values of *(a-b)*. Also, the Niemeijer-Spiers model predicts that, within the frictional velocity weakening regime, the magnitude of stress drops will increase exponentially with decreasing sliding velocity (Fig. 5.2a), and with increasing temperature (Fig. 5.2b), as observed in our experiments (Figs. 5.8a, b). Meanwhile, in experiments conducted at 600°C we found velocity-strengthening behaviour (Fig. 5.11a) as well as microstructural indicators for more distributed, ductile flow (Fig. 5.14), consistent with a transition to a sliding regime characterized by velocity strengthening, (frictional-)viscous flow (cf. Figs. 5.2).

From the above it is clear that the results of our experiments are qualitatively consistent with the Niemeijer-Spiers model (see Section 5.2). Since this model describes the dependence of steady-state shear strength on shear strain rate ($\dot{\gamma} = v/L$, see eq. 5.1), the width of the actively slipping zone (L) may play a crucial role in controlling mechanical strength and stability in experiments performed at imposed values of displacement rate. Assuming different values for L, the role of L in equation 5.1 may help to explain the contrasting slip stability seen after downward and upward steps in sliding velocity (e.g. Fig. 5.5). For downward steps in sliding velocity, the sample will first compact, as opposed to dilate for upward steps (e.g. Segall & Rice, 1995; Samuelson et al., 2009), in both cases followed by evolution to a new steady-state (i.e. provided that, under velocity weakening conditions, the system stiffness is sufficient to prevent nucleation of periodic stick-slip - Ruina, 1983; Rice & Ruina, 1983). Due to initial compaction after a downward velocity step, shear may become distributed over a thicker slipping zone, i.e. higher L, compared with after an upward velocity step. Because for equal sliding velocity the higher L the lower $\dot{\gamma}$, this implies that the 'effective' shear strain rate after a downward velocity step is lower than that after an upward velocity step. Following the Niemeijer-Spiers model (see Section 5.2), a lower $\dot{\gamma}$ will produce a higher $\partial\tau/\partial\dot{\gamma}$ (Fig. 5.2a), hence higher $|a-b|$. This may explain why some of our samples exhibited unstable sliding after downward steps in sliding rate, but stable sliding at the same sliding velocity after upward steps (see e.g. in Stage II of experiments performed at 500° to 600°C in Figs. 5.5b, 5.7a-d). In a similar rationale, dynamic widening or delocalization of the

active slip zone can be envisioned to occur at sufficiently low slip rates, which may explain the spontaneous transition from unstable to stable sliding seen at v = 0.03 μm/s in experiment $CaCO_3$-500-LV (Figs. 5.7c, d). More research is needed to investigate this, especially through experiments and coupled microstructure analysis of samples sheared at constant slip rate, which is yet to be undertaken, and beyond the scope of the present study.

5.6.3. Geological implications

Our experiments demonstrate that wet calcite fault gouge exhibits unstable frictional slip when it is sheared at temperatures of 100° to 550°C, at sliding velocities 0.1 to 100 μm/s and at effective normal stresses of 30 to 100 MPa. We note that the low temperature (20° to 200°C) data and microstructures reported here are consistent with those reported by Verberne et al. (2010, 2013a, b), from saw-cut and direct-shear experiments using the same starting material (see Chapters II and III). This implies that our results are independent of the experimental assembly used, and relatively insensitive to the bulk imposed shear strain, which was much higher in our experiments (20 to 30 compared with 4 to 6 in saw-cut or direct shear tests). Therefore, the transition from velocity strengthening to velocity weakening slip for calcite gouge at ~100°C seen in the present experiments is the same as that reported by Verberne et al. (2010, 2013a, b, 2014) (i.e. Chapters II to IV), which, as argued by these authors, may represent the upper boundary of the seismogenic zone at ~2 to 4 km depth in limestone terrains (Fig. 5.1b). We recall here that the mechanism put forward by Verberne et al. (2014) (i.e. in Chapter IV) is one of nanogranular flow with intergranular diffusive mass transfer, leading to oriented attachment of coherent nanoparticle interfaces responsible for the observed CPO.

As for the lower boundary of the seismogenic zone, taking a geothermal gradient of 25° to 30°/km, representative for e.g. the (southern) Apennines (Doglioni et al., 1996), temperatures of 400° to 600°C correspond with depths of ~13 to 24 km. At these depths, a rock column that is completely composed of calcite-rich rocks (density ~2.7 g/cm^3) produces a maximum lithostatic pressure of ~350 to 650 MPa, while the hydrostatic pore water pressure is ~130 to 240 MPa. Such values correspond to a maximum in-situ effective stress of ~220 to 410 MPa at 13 to 24 km depth, which could be reduced to ~150 to 340 MPa for say 25% clastic content, or 5 to 20% porosity. Clearly, these simple estimates suggest that our experiments were not performed at the in-situ hydrothermal

pressure-temperature conditions that are present near the base of the seismogenic zone. However, it is well established that fluids at depth can exhibit overpressures that lower the effective normal stress acting on a fault (e.g. Sibson, 2000, 2014; Hilgers et al., 2006; Suppe, 2014), as a result of CO_2 influx from greater depths (Collettini & Barchi, 2002), for example, or due to poor connectivity accompanied by compaction (cf. Terakawa et al., 2010; Kukla et al., 2011). This means that in carbonate terrains subject to such conditions, the transition from velocity weakening to velocity strengthening at displacement rates of 0.1 to 1 μm/s seen in our experiments at ~550°-600°C, and the associated deformation mechanisms, could still represent the behaviour and processes operating at the lower limit of the seismogenic zone. Moreover, when extrapolated to much lower, tectonic shear loading rates (~10^{-9} m/s – Marone, 1998b), this transition from velocity strengthening to velocity weakening behaviour could occur at lower temperatures (see Niemeijer & Spiers, 2007; Den Hartog & Spiers, 2013, 2014; cf. Fig. 5.7), hence shallower depths. Significantly, seismicity is common at depths of ~18 km in the Southern Apennines, where carbonate rocks are inferred to be present (Boncio et al., 2007). Similarly, Nissen et al. (2014) recently reported concentrated seismicity at depths of ~15 km in the Zagros Mountains (Iran), believed to be specifically associated with the presence of carbonate rocks (Nissen et al., 2014).

Finally, we note that the microstructures recovered from our experiments have important implications for microstructural studies of natural calcite tectonites. Despite the occurrence of stick-slip events with huge stress drops in experiments performed at 400° to 600°C, the microstructures showed evidence for widespread crystal plastic deformation of 20 to 30 μm sized grains, as well as dynamic recrystallization, as well as pointing to the involvement of diffusion creep and/ or grain boundary sliding. Obviously cataclastic microstructures were absent. In other words, while our samples exhibited essentially brittle/ frictional mechanical behaviour (stick-slip, linear dependence of τ on σ_n^{eff}), the dominant microstructure resembles that of a mylonite (elongated grains, aligned elongate porphyroclasts, recrystallization). This implies that microstructures from natural exposures of shear zones cutting calcite rocks, which are apparently formed by plastic flow, may potentially represent seismogenic faults (cf. e.g. Heitzmann, 1987; Kennedy & White, 2001; Rogowitz et al., 2014). In any case, it will be difficult to eliminate this possibility in studying natural calcite tectonites. A possible indicator for former seismogenic slip may be sought in narrow, ultra-fine grained shear bands of the type seen in our experiments at 400°-550°C. However, the fine grain sizes present in

such shear bands when active might well be obliterated via densification creep, annealing and grain growth upon cessation of slip and subsequent exhumation to the surface, leaving just the mylonitic microstructure behind. We accordingly suggest substantial caution in the interpretation of apparently ductile microstructures seen in natural carbonate shear zones.

5.7. Conclusions

Ring shear experiments have been conducted on ~1 mm thick layers of simulated calcite fault gouge (median grain size ~20 μm), at temperatures of 20° to 600°C, stepping the imposed displacement rate at velocities (v) ranging from 0.03 to 100 μm/s. The experiments were performed under water-saturated conditions, using pore fluid pressures (P_f) in the range $10 \leq P_f \leq 100$ MPa. One series of tests employed a constant effective normal stress (σ_n^{eff}) of 50 MPa, and a second series consisted of combined velocity-stepping and effective normal stress-stepping tests, performed using $1 \leq v \leq 100$ μm/s and $30 \leq \sigma_n^{eff} \leq 100$ MPa. Displacements (x) achieved in each test ranged from 19 to 26 mm. Our aim was to explore the strength, stability, and microstructure of sheared simulated calcite gouge as it transitions from a regime dominated by (velocity strengthening or –weakening) frictional slip to one dominated by (velocity strengthening) viscous flow, i.e. over the frictional-to-viscous transition, and to assess the relevant microphysical processes, as well as the implications for the seismogenic zone in limestone terrains. Our conclusions are as follows:

1. At a constant effective normal stress of 50 MPa, the peak strength at low displacements, or τ_I, picked at $x \approx 1$ to 2 mm, measured ~30 to 33 MPa ($\mu \approx 0.6$-0.7) at 20° to 200°C, ~39 to 50 MPa ($\mu \approx 0.8$-1) at 400° to 550°C, and ~43 MPa ($\mu \approx 0.9$) at 600°C. Shear strength values picked at $x \approx$ 11-12 mm and 19-23 mm, or respectively τ_{II} and τ_{III}, both measured ~28 MPa ($\mu \approx 0.6$) at 20°C, 19 to 26 MPa ($\mu \approx$ 0.4-0.5) at 100° to 550°C, and 29 to 32 MPa ($\mu \approx 0.6$) at 600°C. Velocity-stepping showed a transition from velocity strengthening behaviour (rate sensitivity parameter $\Gamma > 0$) at 20°C to velocity weakening ($\Gamma < 0$) at 100°-200°C for all values of post-step sliding velocity $v_2 < 30$ μm/s. At 400° to 550°C, all velocity steps showed velocity weakening behaviour, with Γ decreasing to a sharp minimum at 500 to 550°C. In these experiments violent stick slip frequently occurred, especially at lower displacement rates and higher temperatures. At 600°C near-velocity-neutral to

velocity-strengthening behaviour dominated.

2. Combined velocity-stepping and effective normal stress-stepping tests consistently showed a linear increase of shear stress upon increasing effective normal stress, for all sliding velocities employed. This suggests that in these experiments, shear strain was achieved by frictional sliding. Linear regression showed that the corresponding apparent friction coefficients measured $\mu_o \approx$ 0.6-0.7 at 20°C, 0.4-0.5 at 200° to 400°C, and 0.6 at 500° to 600°C. The apparent cohesion (S_o) measured < 12 MPa, and, taking into account the standard error, we found no systematic dependence of S_o on temperature or sliding rate.
3. Recovered sheared gouge microstructures showed striking differences between samples sheared at relatively low (20° to 200°C) versus relatively high (400° to 600°C) temperatures. At 20° to 200°C, microstructures showed the presence of ultra-fine (nano-) grained slip zones with strong uniform birefringence and optical extinction, suggestive of a CPO, cutting a cataclastically refined matrix of 1 to 30 μm sized, mainly angular grains. At 400° to 600°C, the microstructures showed evidence for localized slip in a boundary shear involving dilatant granular flow, as well as for more distributed deformation, involving grain size sensitive (GSS) and/ or grain size insensitive (GSI) creep mechanisms. A comparison of the present experimental conditions with flow laws derived from axi-symmetric compression tests on dense calcite polycrystals, shows that GSS and GSI processes indeed likely played a role in our tests conducted at 400° to 600°C, specifically at strain rates of 10^{-4} to 10^{-2} s-1.
4. Trends in shear strength and in the velocity dependence of strength, with increasing temperature as measured in our experiments, as well as the recovered sheared gouge microstructures, are consistent with qualitative predictions of the modified Niemeijer-Spiers model. This model predicts that with increasing temperature, at constant shear strain rate, shear will transition from a regime of velocity strengthening, frictional granular flow at critical state, to one of velocity weakening friction characterized by balanced dilatant granular flow and compaction creep, and finally to one of velocity strengthening, non-dilatant, (frictional-)viscous flow. As applied to our experiments, these transitions respectively occurred at ~20° to 100°C and at 550° to 600°C.
5. Our results demonstrate that velocity weakening, seismogenic slip may occur in calcite fault rocks even at temperatures as high as 550°C, at least on overpressurized crustal faults (σ_n^{eff} = 50 MPa) at slip rates of 0.1 to 100 μm/s. The results imply that

the base of the seismogenic zone in overpressurized limestones occurs at depths of 13 to 24 km, consistent with observations of seismicity in the Zagros Mountains and in the southern Apennines at depths where carbonate rocks are inferred to be present.

Appendix 5.A. Construction of deformation mechanism maps for calcite

To investigate the deformation mechanisms that might have operated in our samples we constructed deformation mechanism maps, using flow equations derived from experiments on dense calcite polycrystals (broadly following Herwegh et al., 2005). Maps of flow stress vs. grain size were constructed for constant temperatures of 400°, 500°, and 600°C (see Fig. 5.15), ignoring the role of water. Water is unlikely to affect GSI processes in calcite in a significant way (Rutter, 1974), but its presence can substantially enhance diffusive mass transfer processes (e.g. Rutter, 1983; Spiers et al., 2004). We infer that these processes will be slow in the case of our experiments, i.e. specifically, in the presence of low density, supercritical pore fluid water, at temperatures of 400° to 600°C (cf. Rutter, 1983).

To represent the grain size insensitive (GSI) creep field, we used an exponential flow equation of the form (Rutter, 1974; Schmid et al., 1980)

$$\dot{\varepsilon} = A \cdot \exp\left(\frac{\sigma}{B}\right) \cdot \exp\left(\frac{-Q}{RT}\right) \qquad (5.A1)$$

where A and B are empirical constants, σ is the flow stress, Q is the activation energy for flow, R is the gas constant and T is the absolute temperature. We fitted eq. 5.A1 to experimental data from triaxial compression tests on Carrara marble (see De Bresser, 2002). For grain size sensitive (GSS) flow, we used creep equations from Walker et al. (1990) and from Herwegh et al. (2003). Both GSS equations are based on experimental deformation of synthetic calcite aggregates, and were fitted to a creep equation of the form (e.g. Herwegh et al., 2005)

$$\dot{\varepsilon} = A \cdot \frac{\sigma^n}{d^p} \cdot \exp\left(\frac{-Q}{RT}\right) \qquad (5.A2)$$

where A, n, and p are empirical constants. To estimate the flow stress from an imposed

strain rate, we have reorganized eqs. 5.A1 and 5.A2, and used strain rates ranging from 10^{-6}-10^{1} s^{-1}. The lower rates (10^{-6}-10^{-4} s^{-1}) correspond with the order of magnitude strain rates used in the experiments by Walker et al. (1990), De Bresser (2002), and Herwegh et al. (2003), while the higher rates correspond with a range representative of that imposed in our experiments, allowing for varying degrees of localization. All empirical constants used are listed in Table 5.A1.

Flow equation	**Parameter used**	**Type**	**Reference**
Eq. 5.A1	B = 2.431	GSI, exponential type flow (regime 1 of Schmid et al., 1987)	De Bresser (2002)[1)]
	Log(A) = 16.65		
	Q = 584 kJ/mol		
Eq. 5.A2	Log(A) = -6.04	GSS + GSI, grain boundary sliding accommodated by volume diffusion and dislocation processes.	Walker et al. (1990) Herwegh et al. (2003)
	n = 3.3		
	m = 1.3		
	Q = 190 kJ/mol		
Eq. 5.A2	Log(A) = -11.927	GSS, grain boundary diffusion / sliding	
	n = 1.1		
	m = 3.3		
	Q = 200 kJ/mol		

Table 5.A1. List of creep equations and parameters used for constructing Figure 5.15. [1)]The empirical parameters listed here were obtained by fitting eq. 5.A1 to data on Carrara Marble reported by De Bresser (2002).

Acknowledgements

Martyn Drury is acknowledged for his help with interpretation of the electron micrographs, and Philip Wehrens for discussions on comparison of our samples with natural mylonite microstructures. We thank the Penn State Rock Mechanics laboratory (esp. Chris Marone) for developing XLook, which was used for analysis of the mechanical data. Gert Kastelein, Tony van der Gon, and Eimert de Graaff are thanked for their technical support, and Otto Stiekema for making the thin sections.

Chapter VI

Strain rate dependent, frictional-to-viscous transition in simulated calcite fault gouge sheared at 550°C: Implications for the lower boundary of the seismogenic zone

After:
Verberne, B. A., De Bresser, J. H. P., and Niemeijer, A. R. Strain rate dependent frictional-to-viscous transition in simulated calcite fault gouge sheared at 550°C: Implications for the lower boundary of the seismogenic zone. *Manuscript in preparation*.

Abstract

The largest magnitude earthquakes nucleate at depths near the base of the seismogenic zone, near the transition from velocity weakening (frictional) slip to velocity strengthening ductile flow. However, the mechanisms controlling this transition, and relevant to earthquake nucleation, remain poorly understood. Here we investigate the effect of slip rate on the mechanical properties and microstructure development of simulated calcite fault gouge sheared at ~550°C, close to the transition from (unstable) velocity weakening to (stable) velocity strengthening behaviour. We conducted experiments at a constant effective normal stress (σ_n^{eff}) of 50 MPa, as well as σ_n^{eff}-stepping tests employing 20 MPa ≤ σ_n^{eff} ≤ 140 MPa, at constant sliding velocities (v) of 0.1, 1, 10, or 100 μm/s. Samples sheared at v ≥ 1 μm/s showed a microstructure characterized by a single, 30 to 40 μm wide boundary shear, as well as a linear correlation of shear strength (τ) with σ_n^{eff}. By contrast, samples sheared at 0.1 μm/s showed a microstructure characterized by evidence for homogeneous deformation and plastic flow, as well as a flattening-off of the τ-σ_n^{eff} curve. The implications is that in the experiments conducted at v ≥ 1 μm/s, deformation occurred via localized frictional slip, whereas in samples sheared at 0.1 μm/s, shear strain was mainly achieved by homogeneous, plastic flow. These results demonstrate a strain rate dependent frictional-to-viscous transition in simulated calcite fault gouge, and show that localization is crucial in controlling fault strength and stability at conditions close to the base of the seismogenic zone.

6.1. Introduction

The largest magnitude earthquakes frequently nucleate near the base of the seismogenic zone (Sibson, 1982, 1983, 1984; Scholz, 1988, 2002) at depths ranging from 10 to 25 km in Earth's crust, depending especially on tectonic setting and local geotherm (e.g. Ito, 1990, 1999; Hyndman et al., 1997; Chiarabba et al., 2005; Shibazaki et al., 2008). Within the seismogenic zone, shear displacement is believed to be achieved via localized, normal stress sensitive, frictional or frictional-viscous processes (e.g. Shimamoto, 1986; Chester & Higgs, 1992; Chester, 1994, 1995; Bos et al., 2000b; Holdsworth et al., 2001; Imber et al., 2008), whereas at depths beyond its lower limit this is believed to occur via dominantly ductile, normal stress-insensitive flow characterized by relatively distributed (i.e. non-localized), plastic deformation (e.g. Sibson, 1977, 1982, 1983; Brace & Kohlstedt, 1980; Shimamoto, 1989; Stewart et al., 2000; Rutter et al., 2001). Investigating the transition from frictional or frictional-viscous fault slip to fully ductile or plastic shear is important for delineating the lower boundary of the seismogenic zone, and for improving our understanding of the processes responsible for the nucleation of earthquakes.

Fault displacement associated with recurring earthquake ruptures occurs by periodic, sudden slip events instead of by continuous motion (see Nadeau & Johnson, 1998; Peng & Gomberg, 2010), similar to the jerky sliding motion or stick-slip behaviour that is commonplace in laboratory rock friction experiments (Brace & Byerlee, 1966). Using a spring-slider model to represent a fault and the surrounding elastic rock, Ruina (1983) showed that for a fault to produce periodic seismogenesis it must exhibit velocity weakening frictional properties, or decrease in strength with increasing displacement rate along the fault. In cases where fault strength increases with increasing displacement rate, the fault is velocity strengthening, and exhibits stable sliding without producing seismicity (Ruina, 1983; Rice & Ruina, 1983). In natural faults, the sliding medium consists of the granular wear material, or "fault gouge", present in the fault core, which is the product of cumulative slip along the fault (Sibson, 1977, 2003). This means that an understanding of the microphysical mechanisms controlling the frictional velocity dependence of fault gouge is key for understanding the processes that are responsible for the nucleation of earthquakes.

Recent experiments reported by Verberne et al. (2010, 2013a, b, 2014, in prep.) (i.e. Chapters II to V) on layers of simulated calcite(-rich) fault gouge demonstrated transitions from velocity strengthening to velocity weakening, and vice versa, with

increasing temperature in the range from room temperature (~18°C) to ~600°C. Employing an effective normal stress (σ_n^{eff}) of 50 MPa, and sequentially stepped sliding velocities (v) of 0.1 to 10 µm/s, a transition from stable velocity strengthening to (potentially) unstable velocity weakening slip occurred at around at 80° to 100°C (Verberne et al., 2010, 2013a ,b, 2014 or Chapters II to IV; see also Chen et al., 2015). A further transition from velocity weakening back to velocity strengthening slip, for v = 0.1 to 10 µm/s, was found at around 550° to 600°C (Verberne et al., in prep., or Chapter V). Tests performed within the velocity weakening regime, i.e. between 100° and 550°C, usually exhibited regular stick-slip, with stress drops that increased with increasing temperature and decreasing displacement rate (Figs. 6.1a, b). At 500° to 550°C, imposing a sufficiently low displacement rate in some cases led to stable slip (e.g. Fig. 6.1b).

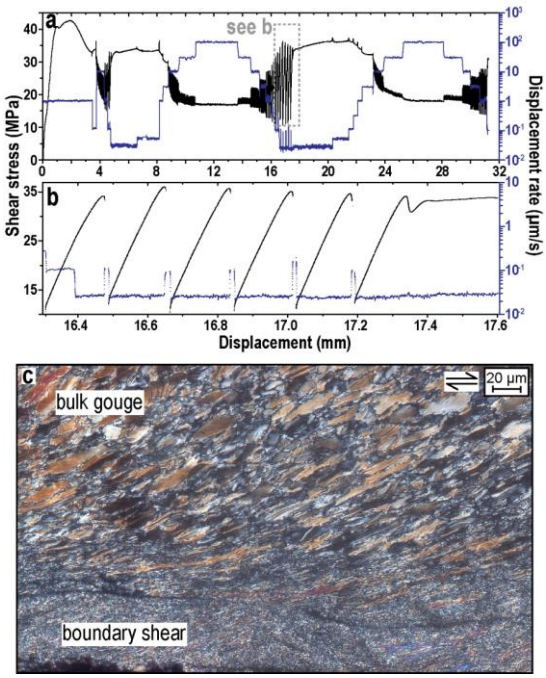

Figure 6.1. Mechanical data and microstructure from ring-shear velocity stepping tests (taken from Verberne et al., in prep., or Chapter V). a) Plot of shear stress against displacement from a ring-shear experiment on water-saturated simulated calcite gouge, conducted at a temperature (T) of 500°C at a fixed effective normal stress (σ_n^{eff}) of 50 MPa, employing sliding rates (v) ranging from 0.03 to 100 µm/s (plotted on the right axis). b) Highlight of (a) showing recurrent stick-slip, and then stable sliding, at v = 0.03 µm/s within the displacement interval from 16.3 to 17.6 mm. c). Cross-polarized light micrograph of sheared simulated calcite fault gouge, recovered from a velocity-stepping experiment performed under water-saturated conditions, at T = 550°C, at σ_n^{eff} = 50 MPa, employing sequentially stepping sliding velocities in the range $0.1 \leq v \leq 100$ µm/s.

The experiments by Verberne et al. (2013a, b, 2014, in prep.) mentioned above were coupled to a microstructure investigation of the recovered sheared gouge layers. For experiments conducted at relatively low temperatures (≤200°C), this consistently demonstrated the development of a localized microstructure, regardless of velocity strengthening or velocity weakening behaviour (Verberne et al., 2013a, b, 2014, in prep., or Chapters III to V), comprising the formation of ultra-fine grained, boundary-parallel and inclined shear bands, characterized by (CPO). The processes responsible for the observed mechanical behaviour were ascribed to the nanoscale processes active within the shear bands (see Verberne et al., 2013a, b, 2014, or Chapters III and IV). In the case of experiments performed at higher temperatures (400° to 600°C), the sheared gouges showed evidence for localized slip on a boundary shear involving granular flow, as well as for more distributed deformation, involving intracrystalline plasticity and/ or dynamic recrystallization of 10 to 30 μm sized, bulk gouge grains (Fig. 6.1c, Verberne et al., in prep., or Chapter V). The higher temperature transition from velocity strengthening to velocity weakening, at 550° to 600°C, was interpreted to correspond with a transition from potentially unstable, localized, frictional or frictional-viscous slip to (intrinsically) stable, more homogeneous, ductile flow involving dominant dislocation and/ or diffusion creep processes (Verberne et al., in prep., or Chapter V).

In detail, however, for the higher temperature (400° to 600°C) sheared gouges it is difficult to correlate the microstructures with the mechanical behaviour, since each of the sheared gouges recovered from these tests experienced a complex slip rate and displacement history (e.g. Fig. 6.1a, b). For example, it is unknown in what stage of the experiments the shear bands developed, whether they remained active thereafter, and how their presence affected subsequent mechanical behaviour of the samples. Significant effects can be expected, though, as it is well-known that shear localization can strongly affect gouge strength and stability (e.g. Marone & Kilgore, 1993; Beeler et al., 1996; Scruggs & Tullis, 1998; Mair & Abe, 2008; Hadizadeh et al., 2010, 2015). Specifically, at conditions close to the transition from frictional or frictional-viscous fault slip to dominantly ductile flow, localization will increase the effective shear strain rate ($\dot{\gamma} = v/L$, where L is the slip zone width) on a fault, which may lead to a transition from stable velocity strengthening to potentially unstable velocity weakening behaviour (Reinen et al., 1992; Sleep et al., 2000; Niemeijer & Spiers, 2007; Noda & Shimamoto, 2010, 2012; Den Hartog & Spiers, 2014; Shimamoto & Noda, 2014; Chen, 2015).

Against this background, the question arises as to whether localized or distributed

shear close the transition from frictional or frictional-viscous fault slip to dominantly ductile flow, such as in our previous tests conducted at around 500° to 600°C (Verberne et al., in prep., or Chapter V), corresponds to any of the specific mechanical behaviours observed. In particular, is localized deformation in these experiments associated with velocity weakening and stick-slip? Or conversely, is more homogeneous deformation specifically associated with stable velocity strengthening beyond the brittle-ductile transition? Answering these questions is important for the interpretation of velocity-stepping experiments at conditions close to the brittle-ductile transition, since a persistent shear band developed at low displacements may affect subsequent mechanical behaviour (for a discussion see Verberne et al., in prep. or Chapter V). Moreover, a microphysical understanding of the interplay of localization and the strain rate/ strength evolution in fault rocks, in both experiment and nature, may shed more light on the microphysical processes relevant to earthquake nucleation near the base of the seismogenic zone (cf. Shimamoto, 1986, 1989; Kawamato & Shimamoto, 1997, 1998).

In this study we report shear experiments on simulated calcite gouge, conducted at conditions close to the transition from frictional or frictional-viscous slip to ductile flow, i.e. at a ~550°C, at σ_n^{eff} = 50 MPa, while employing constant displacement rates of 0.1, 1, 10 or 100 μm/s. To investigate the gouge microstructure developed in "slow" and "fast" shear experiments, we recovered and then sectioned samples from tests conducted at 0.1 μm/s as well as from tests conducted at 100 μm/s. We also investigated the dependence of shear stress upon increasing effective normal stress at 550°C, within the range 20 MPa ≤ σ_n^{eff} ≤ 140 MPa, at displacement rates of 0.1, 1 and 10 μm/s.

6.2. Materials and Methods

6.2.1. Sample material

We used simulated calcite gouges prepared from crushed and sieved Iceland Spar single crystals. X-ray diffraction (XRD) analyses showed that this material consists for ~98% of calcite, with minor quartz (≤2%). Measurement using a Malvern laser particle sizer showed that the grain size (d) distribution of the starting sample powder falls in the range 0.2 ≤ d ≤ 400 μm, with median $\tilde{d}$ ≈ 6 μm (Fig. 6.2a). However, since we do not visually recognize relatively coarse, ~0.4 μm sized fragments in the starting sample powder we suspect that the small (<2%) fraction of grains with d > 100 μm (Fig. 6.2a) represent clumped aggregates instead. To investigate this, as well as the sample microstructure prior to applying shear strain in our experiments, we used a Matra

hydraulic press to compress ~1 g of water-saturated sample in a 10 mm-in-diameter steel cylinder, at a normal stress of 50 MPa, for ~1 hour. This produced a ~1 mm thick circular plate, which we recovered, and then impregnated with an epoxy resin before sectioning to a slice ~30 μm in thickness. Subsequent analysis with a polarizing light microscope showed the presence of ~10 to 30 μm sized grains embedded in a matrix of ~1 to 5 μm sized grains (Fig. 6.2b). When using cross-polarized light, the grain extinction orientations appear as randomly distributed. All grains are sub-rounded to angular in shape, and a distinctive shape fabric is absent.

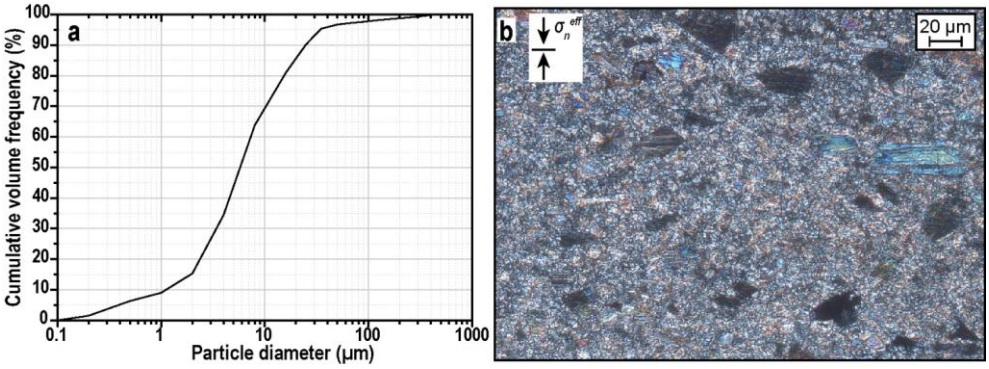

Figure 6.2. Simulated calcite gouge used in our experiments. a) Grain size distribution (cumulative volume frequency versus particle diameter) measured using a Malvern laser particle sizer. b) Cross-polarized light micrograph of a section prepared from a simulated gouge sample that was subject to uniaxial compression at room temperature at an effective normal stress of 50 MPa in the presence of demineralized water, for ~1 hour.

6.2.2. Experimental apparatus

All experiments were performed using the hydrothermal ring shear apparatus described by Niemeijer et al. (2008) and by Den Hartog et al. (2012, 2013). The apparatus consists of a pressure vessel plus internal ring shear assembly, located in an Instron loading frame with servo-controlled ram for applying normal load (Fig. 6.3a). Rotary shear is independently applied via a servo-controlled motor and gearbox system programmed via a digital interface.

In this machine, the annular sample is located in the centre of the pressure vessel, sandwiched between two, grooved René -41, "superalloy" pistons – the upper and lower internal pistons shown in Figures 3b and c. The lower internal piston is fixed to the vessel via a clamped, lower forcing block (Fig. 6.3b). The upper internal piston is fixed to a pressure-compensated, external piston, which is held stationary via a torque bar that

abuts against the 100 kN Instron load cell (Fig. 6.3a). Axial load is transmitted from the Instron ram to the sample and Instron frame via the lower forcing block (Figs. 6.3a, b), and measured using the 100 kN Instron load cell. This allows for normal stress-control to within 0.02 MPa of a desired value. Displacement of the Instron ram is measured in the Instron drive unit using a Linear Variable Differential Transformer (LVDT) of 100 mm full-scale and 5 μm resolution (see Den Hartog et al., 2012). When the motor for applying rotation is switched on, the vessel plus lower internal piston rotate with respect to the upper piston assembly and stationary torque bar, i.e. around the central axis of the machine (Fig. 6.3b). This imposes a shear displacement on the ring-shaped sample, resulting in a shear stress that is measured as a moment via the torque bar, using two load cells of 1.2 kN (or ~60 MPa) full-scale each, located at either end of the torque bar (Fig. 6.3a). Shear displacement imposed on the sample is measured externally with an accuracy of 1 μm, using a potentiometer attached to the forcing block. Pore fluid pressure is applied and adjusted as needed to within 0.1 MPa using a 5 mL hand pump. Each experiment reported here was performed wet, using demineralized water as the pore fluid. In the case of experiments at elevated temperatures, heating is achieved using a Thermocoax internal furnace (Fig. 6.3b) and temperature controlled using a three-term Eurotherm industrial controller, enabling control to within 0.1°C of any set-point value up to 700°C. Sample temperatures quoted here were measured by a thermocouple close (~5 mm) to the sample layer (Fig. 6.3c), and are mean values taken over the duration of each test.

To minimize sample extrusion upon axial loading and shearing, we confined our samples using an inner (diameter Ø = 22 mm) and an outer confining ring (Ø = 28 mm) composed of René-41 superalloy (Fig. 6.3c). To reduce wall friction between the sample and the confining rings, we lubricated the rings using Molykote D-321R anti-friction coating, applied using an aerosol spray. Following Den Hartog et al. (2012), the lubricated confining rings have negligible effect on the measured torque. Note that active piston faces were roughened with ~0.2 mm deep, cross cut grooves to ensure good grip between the piston and the sample layer.

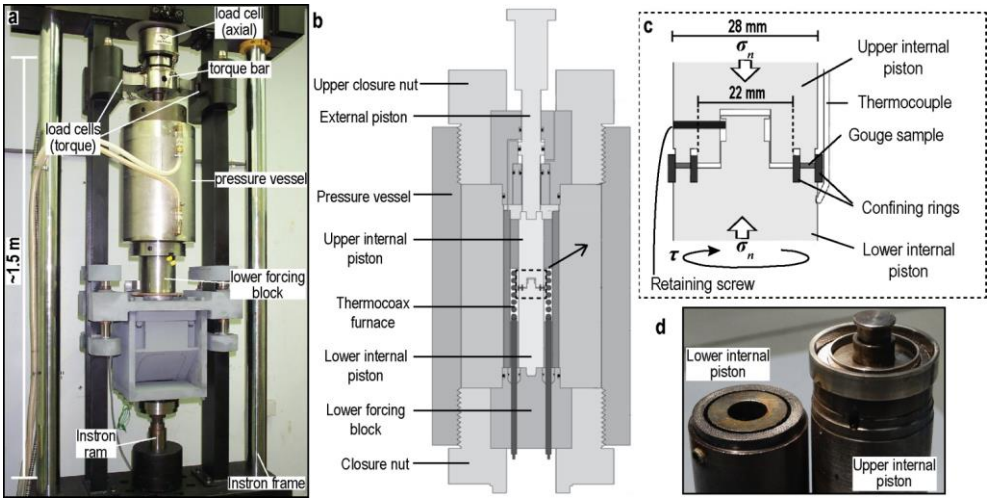

Figure 6.3. The ring-shear deformation apparatus. a) Photo, after Niemeijer et al. (2008). The rotation drive plus gearbox system are installed behind the pressure vessel. b and c) Schematic cross-sections, showing the pressure vessel (b) and a highlight of the sample-internal piston assembly (c) (after Den Hartog et al., 2013). d) Photo of the (disassembled) internal ring shear pistons, displaying the sample-piston interfaces as well as the confining rings on the upper internal piston.

6.2.3. Experimental conditions and procedure

In preparing each experiment, the confining rings were coated with Molykote D-321R using an aerosol sprayer, and then left to dry for ~2 hours in a hot air oven at 120°C. After emplacing the dried rings on one of the internal ring shear pistons, ~0.6 g of the sample powder was distributed in the annular space, i.e. covering the grooved piston face (Fig. 6.3d). To avoid an uneven distribution of the powder, we used the remaining piston to gently compress and rotate the sample. After securing the pistons plus sample layer with a retaining screw (Figs. 6.3c, d), the completed assembly was attached to the upper external piston, and loaded into the water-filled pressure vessel (ref. Figs. 6.3a, b). The vessel was then sealed using a closure nut and mounted into the Instron frame, followed by emplacement of the torque bar, and then application of the desired normal load. We continued by adding fluid to the pressure chamber including sample using the hand pump, until a stable fluid pressure of ~0.1 MPa was reached. The internal furnace was then switched on for heating to the desired testing temperature, in steps of ~100°C, to avoid overpressurization of the sample. By bleeding the vessel intermittently using the hand pump, the pore pressure was as far as possible maintained below that used during the test (= 100 MPa), adjusting to the desired final value when the system stabilized.

Upon reaching the desired testing temperature and pore water pressure, for each experiment the apparatus and sample assembly were left to equilibrate for ~1 hour.

Individual experiments were initiated by switching on the rotation drive system and by setting the shear displacement rate to the desired value. Each run was performed using a furnace setpoint temperature of 550°C and a pore fluid pressure (P_f) of 100 MPa – see Table 6.1 for a list of all experiments and their conditions. As the upper ring shear piston is pressure-compensated (Fig. 6.3b), the effective normal stress equals the applied normal stress (σ_n) acting on the sample layer, minus a contribution from seal friction. Thus, for each test, changes in effective normal stress were achieved by changing the axial load on the sample accordingly. We ran two types of experiments: i) Constant σ_n^{eff} tests. These consisted of constant velocity shear tests performed at a fixed effective normal stress of 50 MPa, one at v = 0.1 µm/s (experiment 550-slow) and one at v = 100 µm/s (550-fast – see Table 6.1), and ii) σ_n^{eff}-stepping tests. These consisted of constant velocity shear tests, performed at sequentially increased σ_n^{eff}-values in the range from 20 to 140 MPa, at v = 0.1 µm/s (experiments NS-slow_A and _B) and at v = 10 µm/s (NS-fast_A and _B – see Table 6.1). Each step in effective normal stress used a difference in σ_n^{eff} of 15 to 30 MPa, and was executed by a) stopping the rotation drive, b) increasing the axial load to the desired value, and c) re-starting rotation hence sample shear. In total this took around 1 minute. For each of the shear rates used, we conducted two σ_n^{eff}-stepping tests, using different initial values of the effective normal stress (i.e. 30 or 50 MPa, see Table 6.1). In σ_n^{eff}-stepping tests conducted at v = 0.1 µm/s we only applied upward-steps, to σ_n^{eff} = 140 MPa, while for σ_n^{eff}-stepping tests conducted at v = 10 µm/s we first applied upward-steps to σ_n^{eff} = 100 MPa, followed by downward-steps to 20 MPa.

Two additional σ_n^{eff}-stepping runs were conducted to investigate the effect of an interval of (relatively) high displacement rate on the shear stress dependence upon effective normal stress (experiments NS_mix_1 and _2, see Table 6.1). In these experiments, we first sequentially increased σ_n^{eff} from 50 to 120 MPa in steps of 15 to 20 MPa, while using a sliding velocity of 1 µm/s in run NS_mix_1 and of 0.1 µm/s in run NS_mix_2. For both runs, upon reaching a steady-state shear strength at σ_n^{eff} = 120 MPa, we stopped rotation of the vessel followed by unloading of the sample to σ_n^{eff} = 50 MPa. We then restarted rotation at a displacement rate of 100 to 300 µm/s for a total of 4 to 5 mm of slip, before re-setting v = 0.1 µm/s. We continued by repeating a σ_n^{eff}-stepping sequence to σ_n^{eff} = 100-120 MPa. In this way, we obtained shear strength data before ("pré $v\uparrow$") and after ("post $v\uparrow$") an interval of slip at relatively high v (Table 6.1).

Experiment	v (µm/s)	σ_n^{eff} (MPa)	P_f (MPa)	T (°C)[1]	x_{fnl} (mm)[2]	l_{fnl} (mm)[3]	γ_{fnl}[4]
550-slow	0.1	50	100	541±2.3	7.90	0.80	9.9
550-fast	100	50	100	552±0.6	10.4	1.0	10
NS-slow_A	0.1	30 | 50 | 80	100	542±1.3	6.75	0.29	23
NS-slow_B	0.1	50 | 65 | 80 | 100 | 120 | 140	100	548±3.7	12.6	0.44	29
NS-fast_A	10	30 | 50 | 80 | 100 | 75 | 65 | 40 | 20	100	544±0.6	12.4	0.33	38
NS-fast_B	10	50 | 65 | 80 | 100 | 90 | 75 | 60 | 40 | 20	100	540±0.5	13.3	0.25	53
NS-mix_1[5]	1-100-10-1	*pre v↑ :* 50 | 65 | 80 | 100 | 120 *post v↑ :* 50 | 65 | 80 | 100	100	*pre v↑ :* 547.2±0.7 *post v↑ :* 45.9±0.8	26.2	0.36	73
NS-mix_2[5]	0.1-300-100-0.1	*pre v↑ :* 50 | 65 | 80 | 100 | 120 *post v↑ :* 50 | 65 | 80 | 100 | 120	100	*pre v↑ :* 549.1±3.5 *post v↑ :* 550.2±3.4	29.7	0.47	63

Table 6.1. List of experiments and conditions. [1]Mean temperature measured over the duration of a test, with its standard deviation. In each test the furnace set point value was 550°C. [2]Total shear displacement. [3]Thickness of the sample measured after the experiment. [4]Maximum finite bulk strain (= x_{fnl} / l_{fnl}). [5]This test used two series of sequential steps in σ_n^{eff} (as indicated); one before (pre v↑), and one after (post v↑) sliding at v = 300 and 100 µm/s.

In terminating each experiment, we first switched off the rotational drive system and then the furnace. After cooling, the vessel was depressurized to atmospheric pressure, the normal load was removed, and the sample assembly was removed from the pressure vessel. This whole procedure took around 30 minutes. The total shear displacement (x_{fnl}) imposed in the constant-σ_n^{eff} tests was ~8 mm in experiment 550-slow (performed at 0.1 μm/s), and ~10 mm in experiment 550-fast (performed at 100 μm/s) (Table 6.1). In the σ_n^{eff} -stepping tests this ranged from ~12 to 13 mm (Table 6.1), with the exception of experiments NS_mix_1 & _2, which achieved a total of ~26 to 30 mm of slip. From the difference in length of the sample-internal piston assembly before and after a test (see Fig. 6.3b), measured using a calliper, we determined the thickness of the gouge layer after each experiment (l_{fnl}) (Table 6.1). Assuming that the total imposed shear displacement (x_{fnl}) in each test was distributed over the entire sample layer, and that the thickness of the sample layer (l) is constant and equal to l_{fnl} in each test, the final bulk imposed shear strain ($\gamma_{fnl} = l/x_{fnl}$) measured ~10 in the experiments conducted using constant σ_n^{eff}, ~23 to 29 in the σ_n^{eff} -stepping tests performed at 0.1 μm/s, and ~38 to 53 in the σ_n^{eff}-stepping tests performed at 10 μm/s (Table 6.1). In the experiments that used an interval of high displacement rate, i.e. NS_mix_1 and _2, the total bulk shear strain was estimated to be ~63 to 73 (Table 6.1).

6.2.4. Data processing and analyses

Voltage signals corresponding to shear displacement, torque, temperature, axial displacement and load, pore fluid pressure, and rotational drive velocity ($\dot{x}$), were recorded using a 16 bit A/D converter. The logging frequency (f) used was $10\dot{x}/x_r$, where x_r = 1 μm, except for a rotational drive velocity of 100 μm/s in which case f was set to be 300 Hz. Because elastic twist of the apparatus during shear loading of our samples was small (<1%) compared with the total imposed shear displacement, we ignored machine distortion in processing shear displacement of the sample. The effective normal stress was calculated by dividing the applied axial load by the area A of the ring-shaped sample, given $A = \pi(r_0^2 - r_i^2) = 75\pi$ mm² (Fig. 6.3c), and subtracting the contribution of friction of the water-cooled O-ring seals against the upper external piston. From calibrations using an internal axial load cell, the seal friction was determined to be equivalent to ~2.8 MPa normal stress when using a pore fluid pressure of 100 MPa. In processing our data, the effective normal stress was calculated by subtracting this value from the applied axial stress; the values listed in Table 6.1 are the targeted values for each experiment. The

externally measured torque was corrected for dynamic seal friction using displacement-dependent and pore-pressure-dependent calibrations following Den Hartog et al. (2012). The shear stress (τ) supported by the sample was determined assuming it to be uniform over the width of the annular sample (3 mm). Standard error analysis showed that error propagation in the measured shear stress is ≤0.1%.

All strength data obtained are presented as plots of shear stress (τ) against displacement (x) , which we used to pick values of the peak strength (τ_{pk}) achieved just after (apparent) yielding as well as the steady-state shear strength (τ_{ss}). In the case of stick-slip we determined the average value of the strength prior to failure (τ_{fail}). We chose to plot shear stress instead of the apparent coefficient of friction ($\mu = \tau/\sigma_n^{eff}$) to avoid an implicit treatment of the data in terms of frictional (i.e. normal stress dependent) processes. However, for comparison with previous studies on frictional sliding or shear of (simulated) calcite gouges we also report corresponding values of the peak and steady-state or failure strengths in terms of a apparent coefficient of friction (resp. μ_{pk}, μ_{ss}, μ_{fail}).

6.2.5. Sample recovery and microstructural analyses

Samples retrieved from the experiments performed at constant σ_n^{eff} (i.e. runs 550-slow and 550-fast – see Table 6.1) were used for investigation of the sheared gouge microstructure. The recovered, arc-shaped sample fragments were first impregnated using Araldite 2020 epoxy resin. After hardening for several days the samples were sectioned using a diamond watering saw, in a plane cut normal to the shear plane of the sample and tangential to a centrally inscribed circle with radius ~12.5 mm (see also Chapter V). In this way, the central portion of the section is oriented parallel to the imposed shear direction, whereas near the outer ends of the section the shear direction plunges at $\cos^{-1}(12.5/14) \approx 27^{\circ}$ into the section. All cut sections were used to prepare polished sections ~5 to 30 μm in thickness.

Transmitted light analysis was conducted using a Leica DMR polarizing light microscope. Selected thin sections were imaged further using an FEI Nova Nanolab 600 scanning electron microscope (SEM), operated in backscatter electron (BSE) mode using an acceleration voltage of 10 kV, except where otherwise indicated. A selection of BSE micrographs were analyzed using an image processing tool in ESRI ArcGIS, v. 10.1. In doing this, we manually delineated each visually distinctive grain with a polygon tracing tool. The resulting dataset was processed using the PolyLX toolbox in Matlab (see *http://petrol.natur.cuni.cz/~ondro/polylx:home*; e.g. Lexa et al., 2005). From the area

of each traced grain, we calculated the equivalent circular diameter as a proxy for the grain size, which we then used for computing grain size distributions (GSD's).

6.3. Mechanical results

We plot shear stress (τ) against displacement (x) for the experiments conducted at a constant effective normal stress (σ_n^{eff}) in Figure 6.4, and for the σ_n^{eff}-stepping experiments in Figures 6.5 and 6.6. A list of characteristic shear stress values (τ_{pk} and τ_{ss} or else τ_{fail}) as well as values of the apparent coefficient of friction (μ_{pk}, μ_{ss} or μ_{fail}), for each interval of constant effective normal stress, for each experiment, is given in Table 6.2.

6.3.1. Experiments at constant effective normal stress

The two experiments conducted at a constant effective normal stress of 50 MPa (550-slow and 550-fast, resp. using v = 0.1 and 100 µm/s – see Table 6.1), showed near-linear loading in the first 0.5 mm of displacement (x) (Fig. 6.4). For experiment 550-slow, this was followed by apparent yield and subsequent hardening towards a broad, near constant peak strength (τ_{pk}) of ~46 MPa at $x \approx 2$ mm, followed by gradual displacement-weakening to a steady-state shear strength (τ_{ss}) of ~38 MPa achieved after ~6 mm of displacement (Fig. 6.4, Table 6.2). By contrast, in experiment 550-fast, near-linear loading continued until a sharply-defined, peak strength of ~52 MPa was reached at $x \approx$ 0.7 mm (Fig. 6.4, Table 6.2). This was followed by a more or less exponential decay of shear strength, until a steady state value of ~23 MPa was reached after ~5 mm of displacement (Fig. 6.4, Table 6.2).

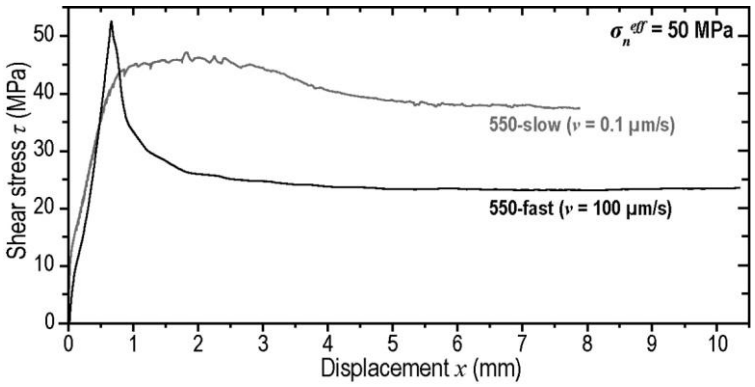

Figure 6.4. Plots of shear stress (τ) against displacement (x) for the experiments conducted at a constant effective normal stress of 50 MPa (Table 6.1).

6.3.2. Effective normal stress stepping experiments

6.3.2.1. Runs at constant displacement rate (0.1 and 10 μm/s)

The effective normal stress stepping experiments conducted at a sliding velocity of 0.1 μm/s (runs NS-slow_A and _B, see Table 6.1) showed near-linear loading in the first 0.6 to 0.9 mm of displacement (Figs. 6.5a, b). For experiment NS-slow_A, in which the first value of σ_n^{eff} used was 30 MPa, initial near-linear loading was followed by gradual displacement-hardening towards a broad, near-constant peak strength (τ_{pk}) of ~33 MPa, at $x \approx 2.3$-2.6 mm, followed by gradual slip-weakening until a steady-state shear strength (τ_{ss}) of ~26 MPa was achieved after ~4.3 to 4.5 mm of displacement (Fig. 6.5a). For experiment NS-slow_B, in which the first value of σ_n^{eff} used was 50 MPa, initial near-linear loading was followed by sliding at a near-constant average strength, until $\tau_{pk} \approx 46$ MPa at $x \approx 3$ mm, beyond which displacement-weakening occurred until $\tau_{ss} \approx 42$ MPa at $x \approx 4.4$-4.6 mm (Fig. 6.5b). After applying steps in the effective normal stress, beyond the initial value used, both experiments NS-slow_A and _B showed sliding at steady-state, or else a near-constant average strength, achieved ~0.5 to 0.7 mm after applying the step (Figs. 6.5a, b).

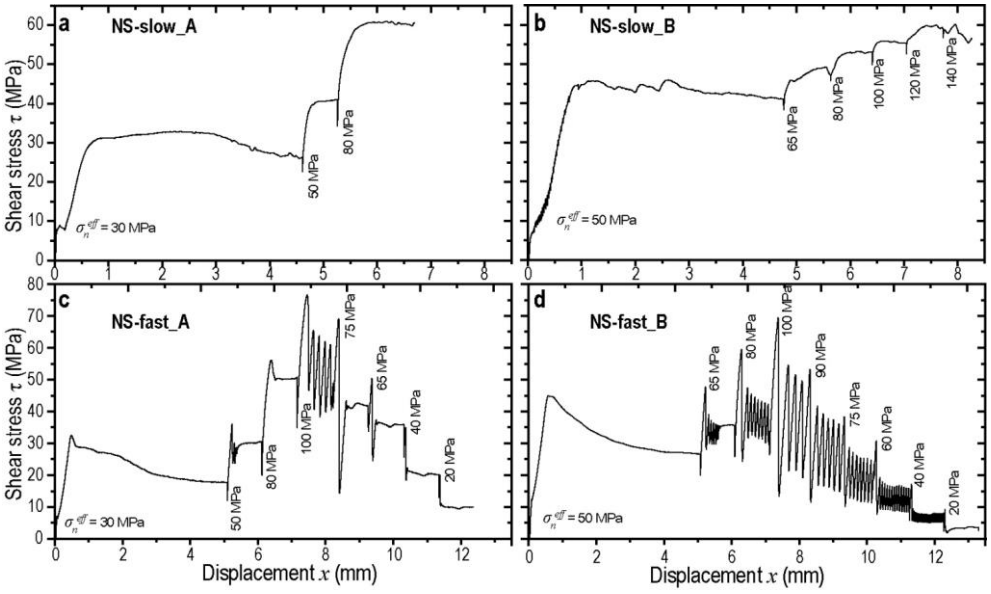

Figure 6.5. Plots of shear stress (τ) against displacement (x) for effective normal stress (σ_n^{eff}) stepping experiments performed at fixed displacement rate (v) (see Table 6.1). a and b) Experiments performed at 0.1 μm/s, using a starting σ_n^{eff}-value of 30 MPa (a) and of 50 MPa (b). c and d) Experiments performed at 10 μm/s, using a starting σ_n^{eff}-value of 30 MPa (c) and of 50 MPa (d).

The effective normal stress stepping experiments conducted at a sliding velocity of 10 μm/s (runs NS-fast_A and _B, see Table 6.1) showed near-linear loading in the first 0.5-0.6 mm of displacement. For experiment NS-fast_A, in which the first value of σ_n^{eff} used was 30 MPa, this was followed by a sharply-defined peak strength of ~32 MPa at $x \approx 0.5$ mm, followed by slip-weakening until $\tau_{ss} \approx 18$ MPa after ~4.3 mm of displacement (Fig. 6.5c). Upon all subsequent steps in effective normal stress, steady-state sliding was achieved some 0.5 to 0.7 mm after applying the step, except for $\sigma_n^{eff} = 100$ MPa, which showed regular stick-slip (Fig. 6.5c). For experiment NS-fast_B, in which the first value of σ_n^{eff} used was 50 MPa, initial near-linear loading continued until $\tau_{pk} \approx 45$ MPa at $x \approx 3$ mm, beyond which slip-weakening occurred until $\tau_{ss} \approx 27$ MPa after ~4.2 mm of displacement (Fig. 6.5d). In this experiment, all subsequent steps in effective normal stress showed regular stick-slip, except for the final downward step to $\sigma_n^{eff} = 20$ MPa, which achieved steady-state sliding ~0.5 mm after applying the step.

Experiment	v (µm/s)	σ_n^{eff} (MPa)	P_f (MPa)	T (°C)	τ_{pk} [1] (MPa)	μ_{pk} [1]	τ_{ss} or τ_{fail} [2] (MPa)	μ_{ss} or μ_{fail} [2]
550-slow	0.1	50	100	541±2.3	46.4	0.93	37.8	0.76
550-fast	100	50	100	552±0.6	52.4	1.05	23.4	0.47
NS-slow_A	0.1	50	100	542±1.3	32.8	1.09	26.2	0.87
		80			41.0	0.82	40.9	0.82
		100			60.7	0.76	60.2	0.75
NS-slow_B	0.1	50	100	548±3.7	45.4	0.92	41.3	0.83
		65			49.2	0.76	49.2	0.76
		80			53.1	0.66	53.1	0.66
		100			55.9	0.60	55.5	0.55
		120			59.8	0.50	59.3	0.49
		140			60.0	0.43	n/a[3]	n/a[3]
NS-fast_A	10	30	100	544±0.6	32.3	1.08	17.6	0.59
		50			35.8	0.72	30.2	0.60
		80			55.8	0.70	50.1	0.63
		100			76.2	0.76	60.6	0.61
		75			68.7	0.92	41.7	0.56
		65			49.7	0.76	35.6	0.55
		40			34.2	0.85	20.2	0.51
		20			19.9	0.99	9.9	0.49
NS-fast_B	10	50	100	540±0.5	44.6	0.89	26.6	0.53
		65			47.3	0.73	35.5	0.55
		80			59.2	0.74	41.9	0.52
		100			68.9	0.69	48.9	0.49
		90			52.7	0.59	36.4	0.40
		75			38.0	0.51	24.2	0.32
		60			30.4	0.51	15.8	0.26
		40			17.2	0.43	7.91	0.20
		20			9.20	0.46	3.60	0.18
NS-mix_1 [pre $v\uparrow$][4]	1	50	100	547.2±0.7	44.4	0.89	30.4	0.61
		65			42.7	0.66	39.8	0.61
		80			52.3	0.65	49.5	0.62
		100			66.0	0.66	61.2	0.61
		120			76.5	0.64	72.8	0.61
NS-mix_1 [post $v\uparrow$][4]	1	50	100	545.9±0.8	28.2	0.56	27.9	0.56
		65			37.6	0.58	35.5	0.55
		80			45.6	0.57	44.6	0.56
		100			57.7	0.58	56.3	0.56
NS-mix_2 [pre $v\uparrow$][4]	0.1	50	100	549.1±3.5	42.7	0.85	36.3	0.73
		65			45.4	0.70	45.4	0.70
		80			54.9	0.69	54.2	0.68
		100			62.3	0.62	60.7	0.61
		120			64.5	0.54	64.5	0.54
NS-mix_2 [post $v\uparrow$][4]	0.1	50	100	550.2±3.4	36.7	0.73	37.3	0.75
		65			44.5	0.68	44.4	0.68
		80			50.0	0.63	50.0	0.62
		100			57.4	0.57	57.2	0.57
		120				0.50	60.5	0.50

Table 6.2. List of shear strength parameters. [1]Peak strength measured just after apparent yield, ~0.5 mm after (re)starting shear. [2]Steady-state strength or, in the case of stick slip, average strength at failure. Values picked from experiments showing stick-slip (i.e. τ_{fail} or μ_{fail}) are shaded grey. [3]Steady-state sliding was not reached in this interval due to mechanical failure of the furnace. [4]This test used two series of sequential steps in σ_n^{eff} (as indicated); one before (pre $v\uparrow$), and one after (post $v\uparrow$) sliding at v = 300 and 100 µm/s.

6.3.2.2. Experiments employing an interval of slip at v = 100 to 300 μm/s

The effective normal stress stepping tests which employed an interval of slip at v = 100 to 300 μm/s (runs NS_mix_1 and _2, see Table 6.1) showed the same general trends of shear strength with displacement for the first sequence of σ_n^{eff}-steps, i.e. to σ_n^{eff} = 120 MPa or pré-v↑, as in the σ_n^{eff}-stepping experiments described above (Table 6.2, Figs. 6.6a, b, cf. Figs. 6.5a-d). Upon setting the displacement rate to v = 100 μm/s, both runs showed a sharply-defined peak strength of ~31 to 34 MPa, followed by slip weakening to a steady-state shear stress of ~20 to 23 MPa achieved ~1 to 1.5 mm after setting v to 100 μm/s (Figs. 6a, b). For run NS_mix_1, when using σ_n^{eff} = 50 MPa after the interval at high displacement rate (i.e. post-v↑), a sharply-defined peak strength (τ_{pk}) of 27 MPa was reached ~0.1 mm after re-setting v to 1 μm/s, followed by a stress drop and subsequent hardening to a (near-)steady-state shear stress (τ_{ss}) value of ~25 MPa, achieved ~9 mm after re-setting v (Fig. 6.6a, Table 6.2). For run NS_mix_2, at σ_n^{eff} = 50 MPa post-v↑, a broad peak strength of ~36 MPa was reached ~2.1-2.3 mm after re-setting v to 0.1 μm/s, followed first by net slip hardening to $\tau_{ss} \approx$ 37 MPa, achieved ~5 mm after re-setting v (Fig. 6.6b, Table 6.2). For both tests, subsequent steps in effective normal stress showed similar trends of shear stress with displacement as seen before the interval at high slip rate (Figs. 6.6a, b).

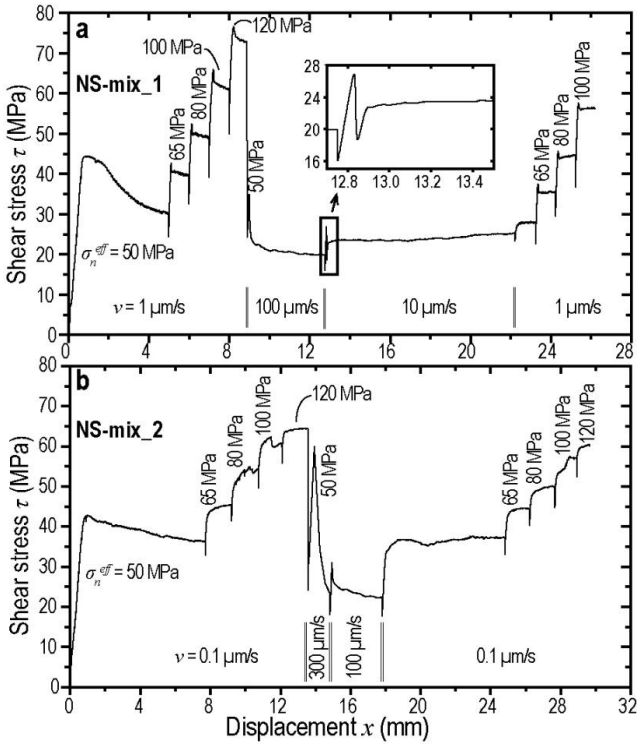

Figure 6.6. Plots of shear stress (τ) against displacement (x) for effective normal stress (σ_n^{eff}) stepping experiments which used an interval of relatively high displacement rate ($v \geq 10$ μm/s) (see Table 6.1). a) Experiment NS-mix_A, employing $v = 1$ μm/s before and after an interval of slip at 100 and then 10 μm/s. b) Experiment NS-mix_B, employing $v = 0.1$ μm/s before and after an interval of slip at 300 and then 100 μm/s.

6.3.2.3. Shear stress - effective normal stress data

We plot the values of steady-state shear strength (τ_{ss}), or in the case of stick-slip the failure stress (τ_{fail}), against the corresponding value of σ_n^{eff}, in Figure 6.7 for each effective normal stress stepping experiment. For tests performed at $v = 0.1$ μm/s, a plot of shear stress (τ_{ss} or else τ_{fail}) against effective normal stress (σ_n^{eff}) of data from run NS-slow_A shows a linear correlation, but from run NS-slow_B this shows a progressively decreasing slope (Fig. 6.7a). For the effective normal stress stepping experiments performed at $v \geq 1$ μm/s, all plots show a linear correlation between shear stress and effective normal stress (Figs. 6.7b, c), with the exception of data from downward steps in σ_n^{eff} in experiment NS-fast_B, for which the τ - σ_n^{eff} curve has a concave shape (Fig. 6.7b). For the experiments that used an interval at relatively high displacement rate ($v = 100$ to 300 μm/s), the pré- and post-$v\uparrow$ shear stress data show similar trends. That is, for

experiment NS_mix_1 both plots of τ_{ss} against σ_n^{eff} show linear correlations (Fig. 6.7c), whereas for experiment NS_mix_2, both plots show a progressively decreasing slope with increasing effective normal stress (Fig. 6.7d).

To investigate the linear correlation between shear stress and effective normal stress, for each experiment we performed linear regression to data from upward steps in effective normal stress, using $\tau = S_0 + \mu_0 \sigma_n^{eff}$. In this analysis we omitted shear stress data from downward steps in effective normal stress, as applied in experiments NS-fast_A and _B, because the majority of these steps showed regular stick-slip (Figs. 6.5c, d), preventing comparison of steady-state data. Values of the apparent coefficient of friction μ_0, the apparent cohesion S_o, and the goodness-of-fit R^2 are listed in Table 6.3. The shear stress-effective normal stress data from experiments NS-slow_A, NS-fast_A and _B, and NS_mix_1 (both pré- and post-$v\uparrow$), is well described by a straight line ($R^2 \approx 1$) of slope (μ_o) 0.6 to 0.7, with an intercept to the vertical axis (S_o) of ~0.4 to ~7.6 MPa (Table 6.3). By contrast, for experiment NS-slow_B, linear regression yielded $R^2 = 0.881$, $\mu_o \approx 0.26$, and $S_o \approx 32$ MPa, whereas for run NS_mix_2, $R^2 = 0.922$, $\mu_o \approx 0.40$, and $S_o \approx 20$ MPa for the pré-$v\uparrow$ data, but $R^2 = 0.960$, $\mu_o \approx 0.33$, and $S_o \approx 23$ MPa for the post-$v\uparrow$ data (Table 6.3).

Experiment	**Fitting range (MPa)**	**v (µm/s)**	**$\tau = S_o + \mu_o \cdot \sigma_n^{eff}$**		
			S_o	μ_o	R^2
NS-slow_A	$30 \le \sigma_n^{eff} \le 80$	0.1	7.6 ± 1.3	0.68 ± 0.02	0.997
NS-slow_B	$50 \le \sigma_n^{eff} \le 120$	0.1	32 ± 3.6	0.24 ± 0.04	0.881
NS-fast_A [1)]	$30 \le \sigma_n^{eff} \le 100$	10	0.4 ± 1.3	0.62 ± 0.04	0.997
NS-fast_B [1)]	$50 \le \sigma_n^{eff} \le 100$	10	6.7 ± 2.7	0.45 ± 0.04	0.979
NS-mix_1 [pre v↑]	$50 \le \sigma_n^{eff} \le 120$	1	2.1 ± 0.7	0.61 ± 0.01	0.999
NS-mix_1 [post v↑]	$50 \le \sigma_n^{eff} \le 100$	1	0.5 ± 1.0	0.57 ± 0.01	0.998
NS-mix_2 [pre v↑]	$50 \le \sigma_n^{eff} \le 120$	0.1	20 ± 4.8	0.40 ± 0.06	0.922
NS-mix_2 [post v↑]	$50 \le \sigma_n^{eff} \le 120$	0.1	23 ± 2.9	0.33 ± 0.03	0.960

Table 6.3. List of regression parameters. [1)] Regression applied to upward steps in σ_n^{eff} only.

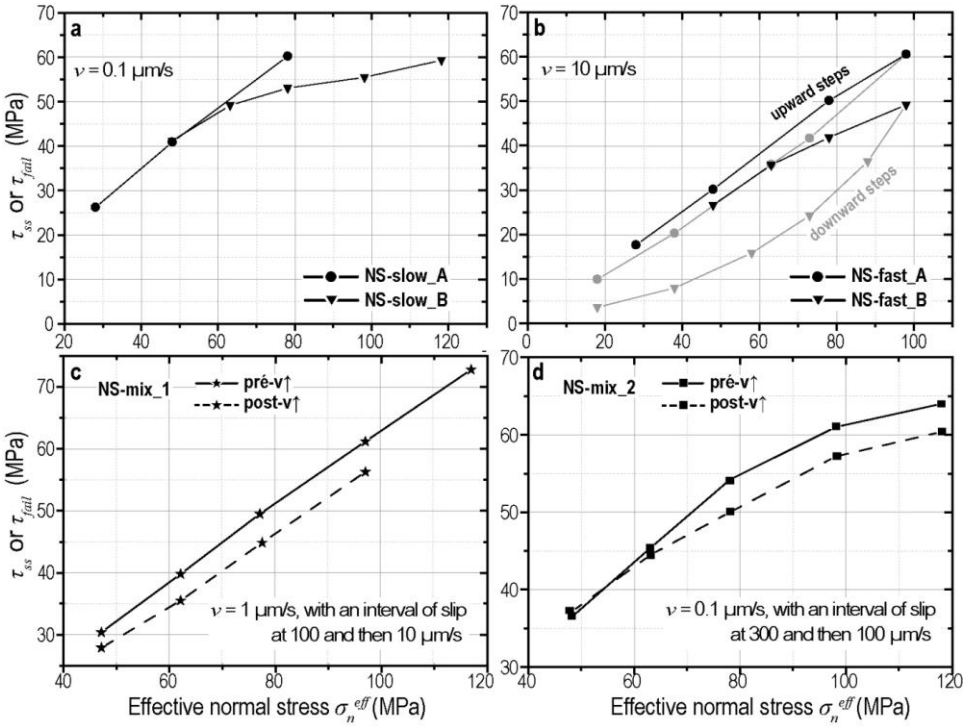

Figure 6.7. Plots of shear stress (τ_{ss} or else τ_{fail}) against effective normal stress. a and b) Experiments conducted at a constant displacement rate (v) of 0.1 µm/s (a) and 10 µm/s (b) (see Fig. 6.5). c and d) Experiments which used an interval of slip at high displacement rate, between sequences of steps in effective normal stress performed while using v = 1 µm/s (c) and 0.1 µm/s (d) (see Fig. 6.6).

6.4. Microstructures

6.4.1. Inspection of samples upon retrieval

Upon separation of the internal ring shear pistons and removal of the outer confining ring, all samples split along a shear-induced fabric consisting of inclined fractures oblique to the sample-piston interface (R_1 Riedel orientation, see Fig. 6.8a), as well as at least partially along a single fracture running parallel, close to this interface. The resulting arc-shaped sample fragments measured 0.3 to 1 mm thick (Table 6.1) by 3 mm wide by up to 10 mm long (Figs. 6.8b to d), and have a greyish colour, revealing the presence of the anti-friction coating used to lubricate the confining rings, as well as possible decarbonisation of the furnace coil or other internal components of the pressure vessel. In cases where the sample split along a boundary-parallel fracture, the exposed boundary-parallel planes of samples sheared at constant displacement rates of 0.1 µm/s

showed little visible internal structure (Fig. 6.8b). By contrast, in samples recovered from tests run at v > 10 μm/s, exposed boundary-parallel planes display specular light reflection and slip-parallel striations (Fig. 6.8c). When exposed, these striated surfaces are seen as continuous shiny surfaces (Fig. 6.8d – cf. Verberne et al., 2013b, 2014).

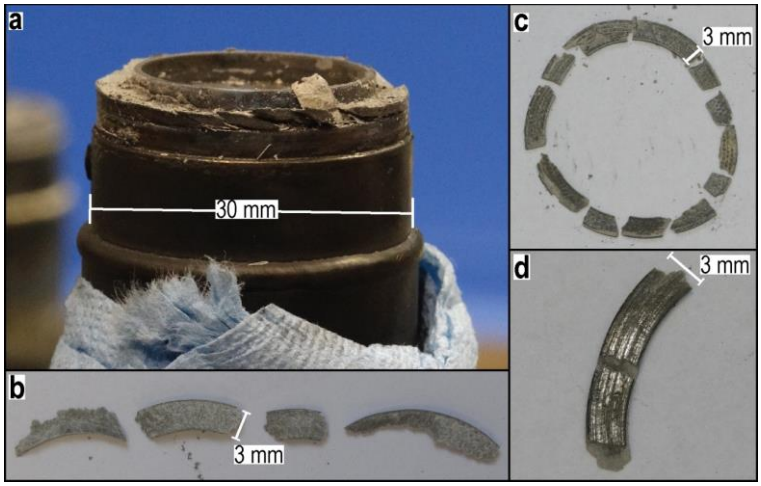

Figure 6.8. Visual inspection of our samples after an experiment. a) Lower internal ring shear piston, after removal of the outer confining ring. Notice the fractures at a Riedel (R_1) angle to the shear plane. b to d) Arc-shaped gouge fragments recovered from experiments conducted at a constant effective normal stress (σ_n^{eff}) of 50 MPa using a fixed displacement rate (v) of 0.1 μm/s (b – 550-slow) and of 100 μm/s (c – 550-fast), plus from a σ_n^{eff} stepping experiment performed at constant v = 10 μm/s (d) (NS-fast_B). The photo in d) was taken at an angle such to display the continuous shiny surface marking the shear plane (cf. Verberne et al., 2013b, 2014, or Chapters III and IV). See Table 6.1 for a list of the experiments.

6.4.2. Optical and electron microscopy results

6.4.2.1. Microstructure developed at σ_n^{eff} = 50 MPa at v = 0.1 μm/s

Sectioned samples from experiment 550-slow (Table 6.1) showed a microstructure that consists mainly of 10 to 20 μm-sized, rounded to elongated grains, which are supported by a much finer-grained matrix that, from visual inspection of the micrographs, appears to consist of grains ~1 to 5 μm in size (Fig. 6.9a). At some locations close to the sample-piston interface, the long axes of elongated grains appear to progressively rotate towards the sample boundary, consistent with a gradient in shear strain from the boundary towards the bulk gouge underneath, or with drag along the piston face (Fig. 6.9b). The extinction orientations of individual grains, as observed using cross-polarized light, appear to be random, hence there is no first order indication of a

CPO of the type observed by Verberne et al. (2013a, b) (or Chapter III).

SEM imaging revealed that the finer grains in the bulk gouge as well as those close to the sample boundary are rounded to polygonal in shape, and indeed of the order of ~1 to 5 μm in size (Fig. 6.9c, d). Close to the sample boundary, grain boundaries are frequently straight, and sometimes exhibit cavitations (Fig. 6.9e). On the basis of line-intercept analysis of visible void-space in SEM micrographs (Figs. 6.9c-e), the apparent porosity ϕ measured ~30% in the middle of the sectioned sample, but ~11% in regions close to the sample boundary. Away from the sample-piston boundary, void space in the recovered gouge sample is frequently present as 20 to 40 μm long by 5 to 10 μm wide, gash-like cracks, which are aligned with their long axis in boundary-parallel or Riedel orientations (Y, R_1, R_2, etc., see Logan et al., 1979).

6.4.2.2. Microstructure developed at σ_n^{eff} = 50 MPa at v = 100 μm/s

Samples from experiment 550-fast (Table 6.1) showed a microstructure consisting of a fine-grained, boundary-parallel shear band cutting a coarser-grained bulk sample. The bulk sample consists of ~10 to 30 μm sized angular clasts surrounded by much finer grains (Fig. 6.10a). The boundary-parallel shear band has a near-constant thickness of ~30 to 40 μm, shows an abrupt reduction in grain size with respect to the coarser-grained bulk sample (Fig. 6.10b), and uniform birefringence colours (Fig. 6.10a) and optical extinction.

SEM imaging revealed that the finer grains in the bulk sample are rounded to angular in shape, and range from ~1 to 10 μm in size (Figs. 6.10c, d). By contrast, grains within the boundary shear are polygonal, ~0.3 to 1 μm in diameter, and frequently arranged in linear, cavitated arrays (Fig. 6.10e). On the basis of line-intercept analysis of visible void-space in SEM micrographs, the bulk sample has an apparent porosity (ϕ) of ~6 to 8%, whereas in the boundary shear band this is ~10 to 15%.

►**Figure 6.9.** Sectioned gouge fragments recovered from an experiment conducted at a constant effective normal stress of 50 MPa, at a fixed displacement rate of 0.1 μm/s (experiment 550-slow, see Table 6.1). a) Crossed-polarized light micrograph. The wavy pattern at the bottom of the sample represents the imprint of the piston grooves. The inset highlights a zone where larger grains appear to progressively rotate towards the upper sample boundary. b) Plane polarized light micrograph. The dark, ring-like feature is an artefact from section preparation. c) Mosaic of backscatter electron (BSE) micrographs of the area highlighted in (a). d and e) BSE micrographs of the areas highlighted in c). Inset in (e) shows polygonal grains with cavitated boundaries.

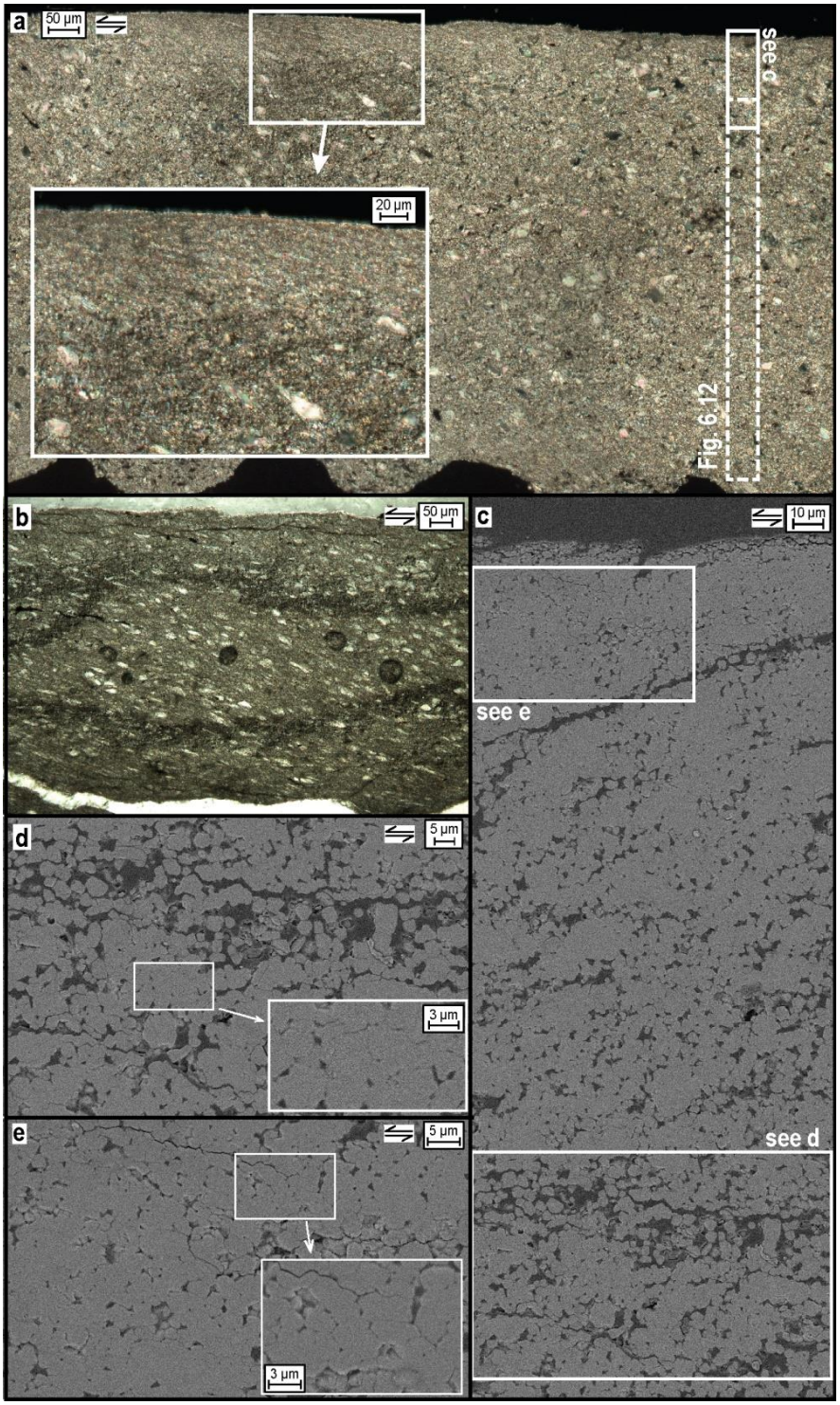
a
50 µm
20 µm
see d
Fig. 6.12
b
50 µm
c
10 µm
see e
see d
d
5 µm
3 µm
e
5 µm
3 µm

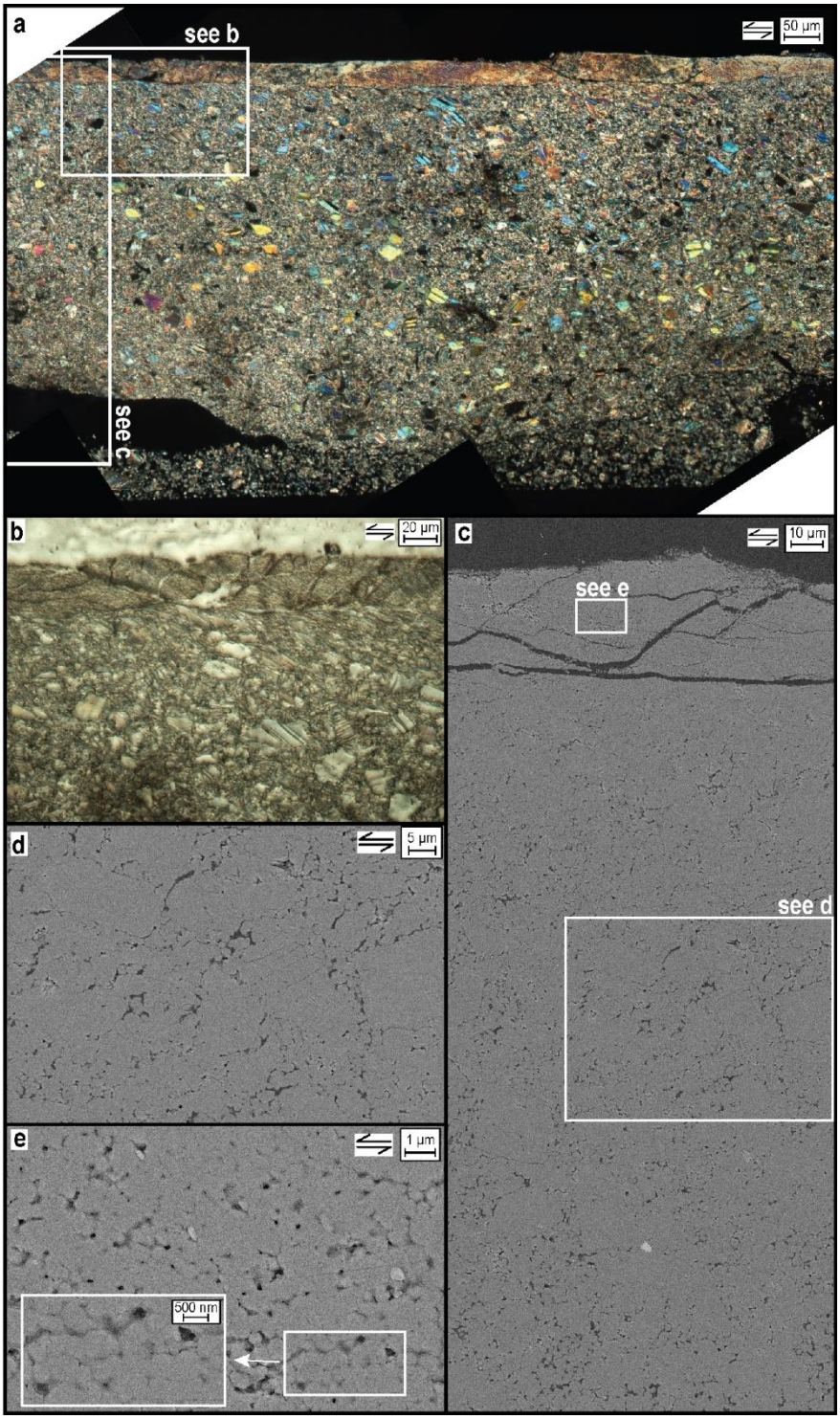
a
see b
see c
50 µm
b
20 µm
c
10 µm
see e
see d
d
5 µm
e
1 µm
500 nm

◄**Figure 6.10.** Sectioned gouge fragment recovered from an experiment conducted at a constant effective normal stress of 50 MPa, at a fixed displacement rate of 100 μm/s (experiment 550-fast, see Table 6.1). a). Crossed-polarized light micrograph. b) Plane polarized light micrograph of the area highlighted in (a). Notice the sharp contact between the shear band and the bulk sample underneath. c). Mosaic of backscatter electron (BSE) micrographs of the area highlighted in (a). d and e). BSE micrographs of the areas highlighted in c).

6.4.3. Grain size data

Micrographs from experiments 550-slow and 550-fast, taken away from the sample-piston boundaries towards the centre or bulk of the sectioned samples, were used for interpretation with ESRI ArcGIS mapping software, and then processed to obtain the grain size distribution (GSD). For examples see Figures 6.11a and b. In areas of micrographs where the grain boundaries could not be identified with sufficient certainty, we left the area open, i.e. uninterpreted. For both samples we chose not to use micrographs that were taken from areas close to or at the sample-piston boundary, because individual grains are (too) often too difficult to distinguish in these parts of the present sections (see e.g. Figs. 6.9e, 6.10e). For micrographs of samples from experiment 550-slow we traced a total of 4550 grains in 6 images with a pixel size of 62 nm^2 (e.g. Fig. 6.11a), which comprise a mosaic normal to the shear plane and – direction (see dashed box in Figure 6.9a). For micrographs of samples from experiment 550-fast we traced a total of 2802 grains, in 2 images with a pixel size of 60 nm^2 (Fig. 6.11b), plus in 6 with a pixel size of 19 nm^2.

The GSDs of all traced grains, for each sample investigated, are plotted as frequency histograms in Figure 6.11c. This shows that for experiment 550-slow, the GSD of the bulk sample has a lognormal distribution, characterized by a range $0.64 < d < 11$ μm, median $\tilde{d}$ = 2.96 μm, and mean $\bar{d}$ = 2.94 μm, with a standard deviation (*sd*) of 1.54 μm. By comparison, the GSD of the bulk sample recovered from experiment 550-fast is characterized by $0.67 < d < 11$ μm, $\tilde{d}$ = 2.85 μm, $\bar{d}$ = 2.65 μm, with *sd* = 1.87 μm (Fig. 6.11c). To investigate possible trends in GSDs normal to the shear plane and –direction in the sample recovered from experiment 550-slow, we compared the GSD of each micrograph in the mosaic (Fig. 6.12). This showed that the median grain size shifts from $\tilde{d}$ = 2.84 μm in the center of the bulk sample (OV-008 in Fig. 6.12) to values ranging from $\tilde{d}$ = 2.94 to 3.06 μm in the 4 images above, and to $\tilde{d}$ = 2.77 μm closest to the sample boundary (OV-013 in Fig. 6.12). At the same time, the mean grain size shifts from $\bar{d}$ = 2.85 μm in the center of the bulk sample to values ranging from 3.00 to 3.08 in the 4

images above, and to $\bar{d}$ = 2.80 µm closest to the sample boundary (Fig. 6.12). Thus, the median and mean grain sizes are 0.05 to 0.07 µm lower closest to the sample-piston boundary, compared with in the centre of the bulk sample. However, a clear trend within the mosaic, i.e. with respect to the shear plane, is lacking.

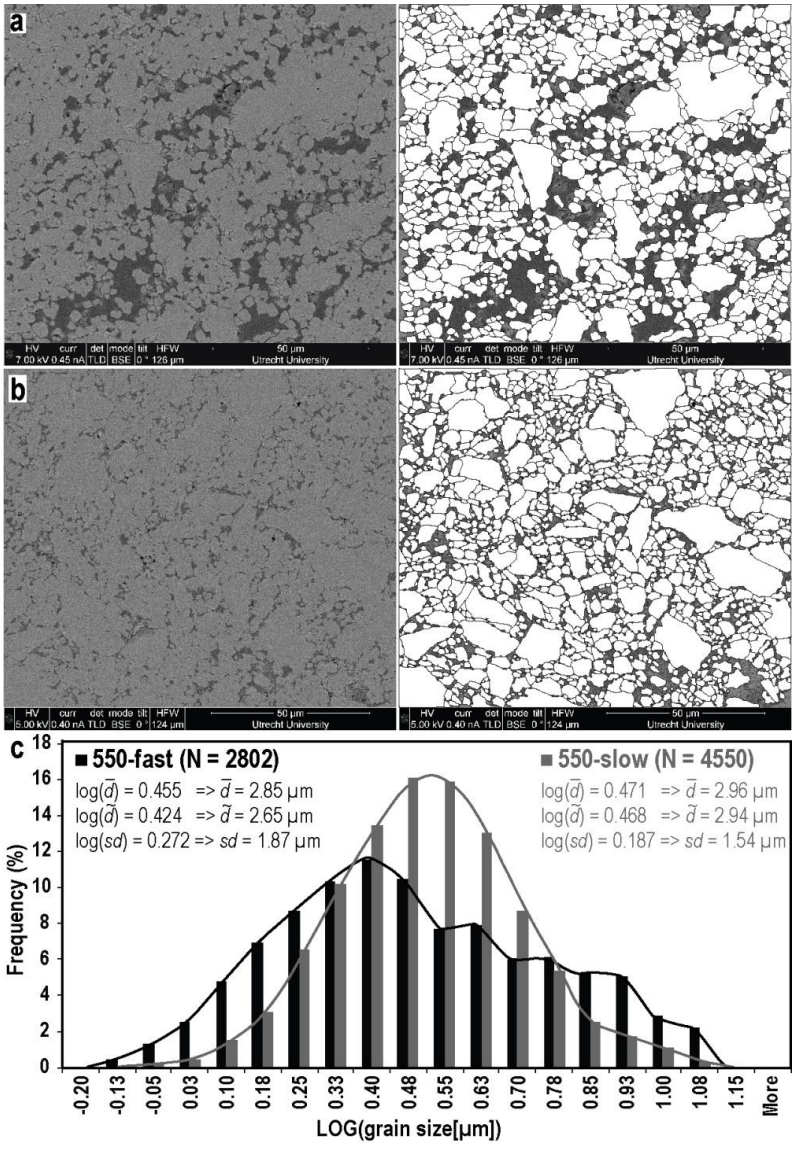

Figure 6.11. Grain mapping and subsequent size distribution analysis. a and b). Examples of backscatter electron micrographs (left) interpreted using ESRI ArcGIS (right), taken from gouge fragments recovered from experiments 550-slow (a) and 550-fast (b) (see Table 6.1). c). Size distributions of all mapped grains.

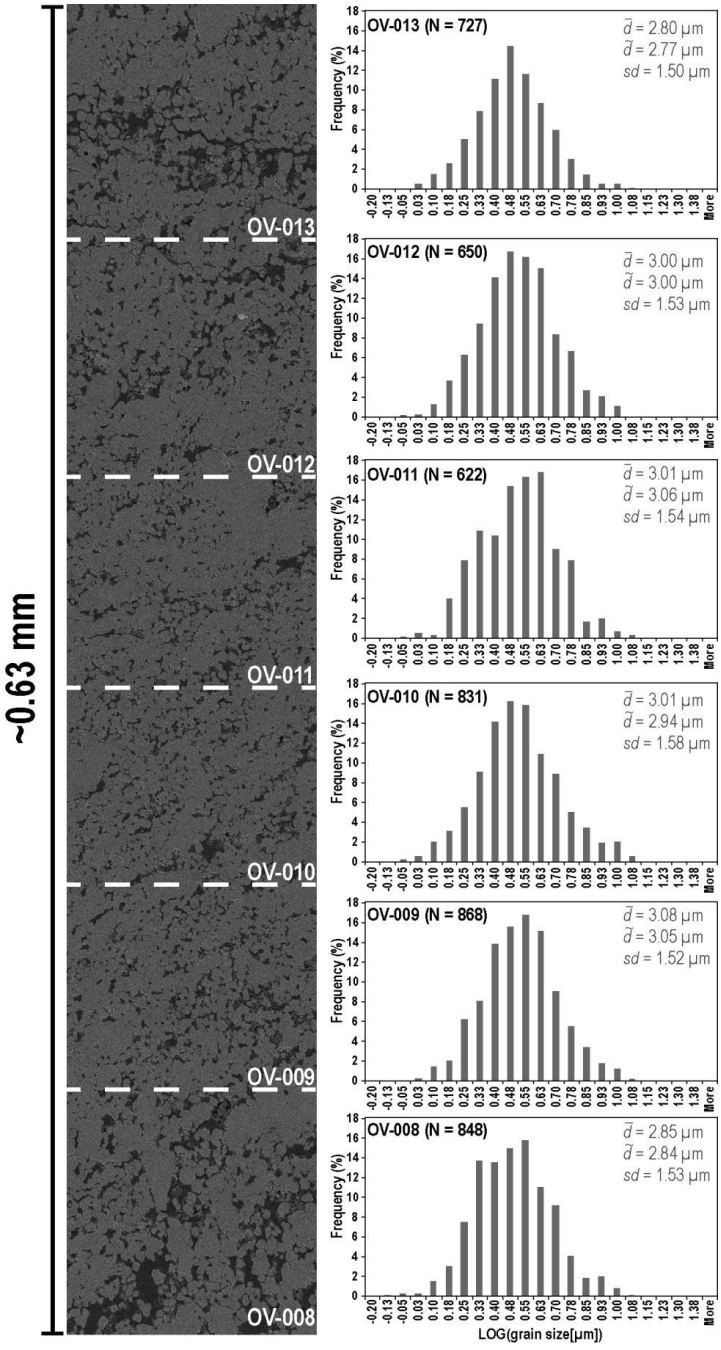

Figure 6.12. Mosaic of backscatter electron (BSE) micrographs (left) of a transect through the matrix of sample 550-slow (see Fig. 6.9a). On the right the size distributions corresponding to each BSE micrograph in the transect.

6.5. Discussion

The shear behaviour and microstructures reported in this study showed striking differences between experiments conducted at different sliding velocities (v). Firstly, the steady state shear strength (τ_{ss}) measured 23 MPa at a displacement rate (v) of 100 μm/s, but 39 MPa at 0.1 μm/s, corresponding to an apparent friction coefficient ($\mu = \tau/\sigma_n^{eff}$) of respectively 0.46 and 0.78. Secondly, samples sheared at v = 100 μm/s showed a much stronger localized microstructure compared with samples sheared at 0.1 μm/s (Fig. 6.9 cf. Fig. 6.10). Thirdly, effective normal stress stepping experiments performed at $v \geq 1$ μm/s showed linear dependence of shear stress (τ) upon increasing effective normal-stress (σ_n^{eff}), whereas in similar tests at v = 0.1 μm/s, using a starting value of σ_n^{eff} of 50 MPa, plots of τ vs σ_n^{eff} showed a flattening-off towards higher values of the effective normal stress (Figs. 6.7a, d). In the following, we first put constraints on the deformation mechanisms that may have played a role in our experiments, comparing our tests with empirical laws describing the rheology of dense, polycrystalline calcite aggregates. We continue by discussing the role of strain localization in our samples, and the role this may play in controlling fault strength and stability, rounding off with a discussion on the geological implications of our results.

6.5.1. Deformation mechanisms

From experiments on dense calcite polycrystals, axi-symmetrically compressed or sheared at temperatures of 300° to 1000°C and strain rates of 10^{-8} to 10^{-3} s^{-1}, it is well established that diffusion and/ or dislocation creep processes play a role in accommodating strain (e.g. Heard, 1960; Rutter, 1974; Schmid et al., 1987; Walker et al., 1990; De Bresser & Spiers, 1993; Barnhoorn et al., 2004, 2005; Renner et al., 2002; De Bresser et al., 2002; Herwegh et al., 2003, 2005; De Raadt et al., 2014). Since our experiments were conducted at ~550°C, the shear strain rates imposed on our samples may have been sufficiently low for ductile, grain size sensitive (GSS, diffusion creep) and/ or grain size insensitive (GSI, dislocation creep) deformation processes to have played a significant role. To investigate this, we used existing data on the rheology of dense calcite polycrystals to construct a deformation mechanism map (DMM) at T = 550°C (Fig. 6.13). Despite the important differences in experiments and sample character between our tests and those used to determine the flow equations on which the DMM is based (shear tests on water-saturated gouge vs. compression tests on dry, dense polycrystals), a comparison may help to elucidate which processes, at which strain rates, may have been relevant in

our experiments.

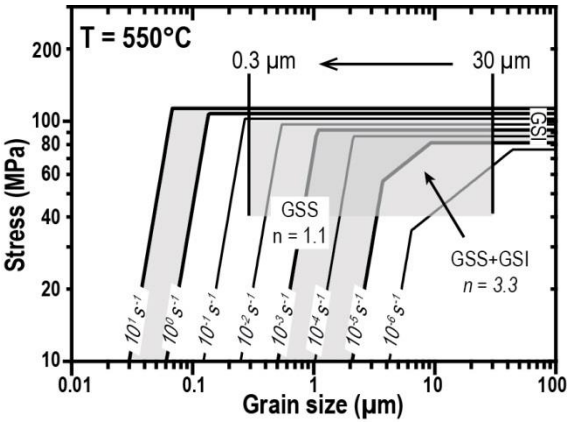

Figure 6.13. Deformation mechanism maps for calcite, drawn for a temperature of 550°C, using the creep equations fitted by Herwegh et al. (2003) (grain size sensitive (GSS), n = 1.1) and Walker et al. (1990) (grain size insensitive (GSI) + GSS, n = 3.3) on data from axi-symmetric compression tests on synthetic calcite aggregates, and using an exponential-type, GSI creep equation fitted to data from triaxial compression tests on Carrara marble by De Bresser (2002). Strain rate contours are shown for $\dot{\varepsilon}$ = 10^{-6}-10^{1} s^{-1}. The shaded area plots the conditions that are believed to be relevant for our experiments, based on estimates of the grain size and equivalent compressive stress. For details on construction of this map, see Verberne et al., in prep. (or Chapter V).

To construct the DMM, we used empirical flow equations determined by Herwegh et al. (2003) for the GSS field, by Walker et al. (1990) for the GSS + GSI field, and using the experimental data of De Bresser (2002) fitted to an exponential-type flow equation for the GSI field (refer Verberne et al., in prep., or Chapter V). These flow laws were determined for axi-symmetric compression of dense calcite polycrystals at elevated pressure. In order to compare our shear stress (τ) – shear strain rate ($\dot{\gamma}$) values with these flow laws, we converted τ and $\dot{\gamma}$ into equivalent flow stress (σ) and strain rate $\dot{\varepsilon}$ for compression tests, using the relations $\sigma = \tau\sqrt{3}$ and $\dot{\varepsilon} = \dot{\gamma}/\sqrt{3}$ (Schmid et al., 1987; Barnhoorn et al., 2004). Taking $\tau \approx$ 23-53 MPa as a broad range that represents the peak and steady-state shear stresses measured in our experiments performed at a constant effective normal stress of 50 MPa (Table 6.2), this resulted in an equivalent flow stress of $\sigma \approx$ 40-90 MPa representing our samples in the DMM (Fig. 6.13). As for the equivalent compressive strain rate ($\dot{\varepsilon}$), we estimated the shear strain rate in our experiments by dividing the imposed sliding velocity over the slip zone width, which was in turn determined from microstructure analysis. For experiment 550-slow, we assumed that the

imposed displacement was either distributed over the entire ~0.8 mm thick layer (Table 6.1), or that it was localized in a 50 to 100 μm wide boundary shear (Figs. 6.9a, b). This yielded an end-member range for the true shear strain rate in this test of $\dot{\gamma} \approx 1 \cdot 10^{-4}$ s^{-1} to $2 \cdot 10^{-3}$ s^{-1}, so that $\dot{\varepsilon} = 6 \cdot 10^{-5}$ to $1 \cdot 10^{-3}$ s^{-1} $\approx 10^{-5}$ to 10^{-3} s^{-1}. For experiment 550-fast, the boundary shear was very sharply-defined (Fig. 6.10a), leaving little doubt that the bulk of the imposed displacement was accommodated within this 30 to 40 μm wide zone. Therefore, for this experiment, $\dot{\gamma} \approx 2.5$ to 3.3 s^{-1}, so that $\dot{\varepsilon} = 1.4$ to 1.9 s^{-1} $\approx 10^{0}$ to 10^{1} s^{-1}. To represent these values of $\dot{\varepsilon}$ in the DMM, we plotted lines of constant strain rate using the range $\dot{\varepsilon} \approx 10^{-6}$ to 10^{1} s^{-1} (Fig. 6.13). We included $\dot{\varepsilon} = 10^{-6}$ s^{-1} because this more closely approximates the strain rates used in the experiments on which the flow equations are based (Walker et al., 1990; De Bresser, 2002; Herwegh et al., 2003).

Before we determine a representative grain size range for the gouge during shear, hence before we can plot our samples on the DMM, we must consider whether grain growth after termination of our shear experiments may have played a role *(*cf. e.g. Barnhoorn et al., 2005). After all, grain growth due to static recrystallization is characterized by the presence of grains with straight boundaries and a polygonal foam fabric (Bestmann et al., 2005), not dissimilar from (parts of) the microstructure recovered from experiments 550-slow and 550-fast (see Figs. 6.8e, 6.9e). Static grain growth of grains of initial size d_o to a new size d is frequently described using a generalized Arrhenius expression given by (e.g. Covey-Crump, 1997; Evans et al., 2001)

$$d^{1/n} - d_0^{1/n} = k_0 t \exp\left(\frac{-Q_g}{RT}\right) \qquad (6.1)$$

where k_o is a constant, t is the duration of the growth period, Q_g is the (apparent) activation energy for the process controlling the grain growth rate, R is the gas constant, and T is the temperature during grain growth. Covey-Crump (1997) reported on the kinetics parameters appearing in equation 6.1, for grain growth in porous (ϕ up to 40%), polycrystalline calcite aggregates (grain size ~3 to 5 μm), at 550° to 700°C, under hydrostatic conditions. In the present case, post-test, static recrystallization of our samples may have occurred upon termination of a test, during cooling from the testing temperature to room temperature conditions. Measurement of part of this temperature decay upon termination of experiment 550-fast showed a decrease from 550°C to 280°C

in 115 s. Taking Newton's law of cooling, or $\dot{T} = -c \cdot (T - T_a)$, where $T(0)$ = 550°C, $T(115)$ = 280°C, and T_a = 20°C, the decay rate can be approximated by

$$T(t) \approx 20 + (550 - 20)\exp(-ct) \quad , \quad \text{with } c = \frac{1}{115}\ln\left(\frac{280 - 20}{550 - 20}\right) \qquad (6.2)$$

Using equations 6.1 and 6.2, plus kinetics parameters for surface-diffusion controlled, static growth of calcite grains (Covey-Crump, 1997), we simulated the grain size that may have developed in the first 110 s of cooling of our samples, for initial grain sizes ranging from d_o = 0.01 μm to 0.6 μm in size (Fig. 6.14). This shows that regardless of the initial size d_o, the bulk of grain growth will have been achieved within the first ~20 to 25 s of cooling. Also, for grains with an initial size smaller than ~0.25 μm, the final size is more or less constant at $d \approx$ 0.4 μm (Fig. 6.14), whereas for grains with d_o exceeding 0.25 μm the total growth in size (d-d_o) will be limited to <0.1 μm. We recall that SEM micrographs of the sheared samples showed that the smallest particles present are ~0.3 μm in diameter (Figs. 6.9d, e, 6.10d, e). Allowing for differences in the detailed diffusion mechanisms (cf. Covey-Crump, 1997), the minimum grain size found in our samples thus roughly corresponds with the 'minimum' grain size as predicted by diffusion-controlled grain growth (~0.4 μm – Fig. 6.14). For our experiments this means that we cannot rule out the presence, during shear, of grains smaller than 0.3 μm, which have then become obliterated due to (limited) post-test, static grain growth. However, analysis of the post-shear grain size distribution (GSD) of the bulk part of our samples (Figs. 6.11c, 6.12), as well as visual inspection of micrographs from boundary shears (Figs. 6.9e, 6.10e), showed that the vast majority of grains is greater than 0.6 μm in size, suggesting little post-test grain growth (i.e. d-d_o <0.05 μm, see Fig. 6.14). Therefore, we suggest that to use a size range $0.3 \leq d \leq 30$ μm for plotting our samples in the DMM, i.e. based on the smallest and largest grains found in the bulk of the sheared samples, is reasonable (Fig. 6.13).

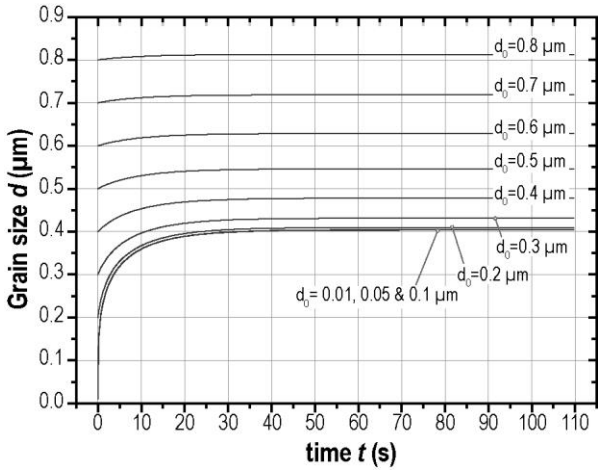

Figure 6.14. Static grain growth during cooling from 550°C to room temperature upon termination of our experiments, as predicted by a generalized grain growth model (e.g. Covey-Crump, 1997; Evans et al., 2001), using the kinetics parameters for grain growth in porous (ϕ up to 40%), polycrystalline calcite aggregates (grain size ~3 to 5 μm), at 550° to 700°C, under hydrostatic conditions (Covey-Crump, 1997). The plot shows the predicted evolution of grain size (d) with time (t), for different initial grain sizes d0.

6.5.1.1. Mechanisms operating at v = 0.1 μm/s

The stress and strain rate conditions applying to the calcite gouges as deformed at a slip rate (v) of 0.1 μm/s are in reasonable agreement with the conditions needed for ductile flow of calcite polycrystals in compression. The shear stresses (τ) in experiment 550-slow measured 38 to 46 MPa (Table 6.2), so that $\sigma \approx$ 65 to 80 MPa. Since the compressive strain rates ($\dot{\varepsilon}$) are ~10^{-5} to 10^{-3} s^{-1}, this implies that the experimental conditions at v = 0.1 μm/s are close to the conditions needed for ductile flow in dense calcite polycrystals at T = 550°C (Fig. 6.13). For all relevant values of $\dot{\varepsilon}$, 10 to 30 μm sized grains plot in the GSI + GSS field, close to the boundary with the GSI field, suggesting they may have deformed by dislocation creep. This is consistent with the 10 to 30 μm sized, elongated grains seen in the matrix of samples recovered from experiment 550-slow (Figs. 6.9a, b). The ~1 to 5 μm sized grains that are present in this sample (Figs. 6.8c-e) plot well within the GSS + GSI field for $\dot{\varepsilon} \approx 10^{-5}$ s^{-1}, and within the GSS field for $\dot{\varepsilon} \approx 10^{-3}$ and 10^{-4} s^{-1}. This suggests that these grains have been deformed by mechanisms such as diffusion creep or grain boundary sliding (GBS). For the effective normal stress stepping experiments performed at 0.1 μm/s, for 50 MPa < $\sigma_n^{eff} \leq$ 120 MPa, the shear stresses measured ~50 to 80 MPa (Table 6.2), hence $\sigma \approx$ 87 to 140 MPa, implying that the experimental conditions used fall well within the GSI field (Fig. 6.13). This is

consistent with the progressively decreasing slope seen in plots of (steady-state) shear stress against effective normal stress for these experiments (Fig. 6.7a), which suggest effective normal stress insensitive behaviour characteristic for ductile flow by GSI or GSS processes (cf. e.g. Shimamoto, 1986; Kawamoto & Shimamoto, 1997, 1998).

The microstructure from experiment 550-slow lacks the presence of one or more, sharply-defined shear bands as for example seen in the microstructure recovered from experiment 550-fast (Fig. 6.9 cf. Fig. 6.10). The uniform reduction in grain size over the entire width of the recovered sample layer (Figs. 6.9c-e, 6.12), suggests that the imposed displacement was accommodated (relatively) homogeneously. Moreover, the bulk of grains present are polygonal, and sometimes show cavitated grain boundaries (Fig. 6.9e), consisted with grain boundary sliding type shear (e.g. Fliervoet et al., 1997). Adding to that the above-mentioned consistency of the experimental conditions with the DMM (Fig. 6.13), we suggest that in the tests that used v = 0.1 μm/s and $\sigma_n^{eff} \geq 120$ MPa, the imposed displacement was mainly accommodated by GSI + GSS or viscous processes, in a distributed manner. The lack of a (strong) CPO suggests that GSS processes were dominant, although more detailed crystallographic orientation measurements (such as performed by e.g. Valcke et al., 2006) are needed to conclude on this. We note that the relatively high apparent porosity (ϕ) of 11 to 30%, measured using linear intercept analysis on micrographs of the sectioned sample recovered from experiment 550-slow (Fig. 6.9), is likely caused by cracks that were introduced upon depressurization and cooling after the experiment.

6.5.1.2. Mechanisms operating at v = 10 and 100 μm/s

The stress and strain rate conditions applying to the calcite gouges as deformed at a slip rate (v) of 100 μm/s do not match with the conditions needed for ductile flow in dense calcite polycrystals at T = 550°C (Fig. 6.13). The shear stresses (τ) in experiment 550-fast measured 23 to 52 MPa (Table 6.2), so that $\sigma \approx$ 40 to 90 MPa. For corresponding values of $\dot{\varepsilon}$ of 10^0 to 10^1 s^{-1}, GSI creep is only expected to occur at very high equivalent compressive stresses (i.e. σ > 100 MPa), while GSS creep would theoretically only occur in the case of ultra-fine grain sizes (<< 0.1 μm). Assuming that such ultrafine particles were not present during the experiment (ref. Fig. 6.14), this suggests that we can ignore the role of GSS or GSI mechanisms in controlling shear strength in experiment 550-fast. All effective normal stress stepping experiments conducted at $v \geq 1$ μm/s showed a proportional increase of (steady-state) shear strength upon increasing effective

normal stress (Table 6.3, Figs. 6.7b, c), strongly suggesting that the imposed shear strain in these tests was accommodated by linearly effective normal stress dependent, frictional sliding. For experiment 550-fast, the high porosity ($\phi \approx$ 10-15%) in the shear band suggests that (dilatant) granular flow has occurred, which is consistent with frictional slip (e.g. Paterson, 1995). However, the shear band developed in experiment 550-fast showed a strong, uniform optical interference and extinction (Fig. 6.10a), suggestive of a strong CPO (cf. Verberne et al., 2013a, b or Chapter III; Smith et al., 2015*)*. This means that dislocation/GSI mechanisms were active in the material without controlling shear strength, or that some other mechanism resulted in the development of the preferred crystallographic orientation, i.e. alongside granular flow. We infer that grain contact scale mechanisms must have played a role.

In the case of localized granular flow within the shear band, local grain contact stresses within force chains may have been much higher than the average measured (shear) stress (e.g. Aharonov & Sparks, 2002; Daniels & Hayman, 2008). Specifically, the intergranular equivalent compressive stress (σ) may have been sufficient for intergranular GSI processes to become active (Fig. 6.13). This suggests that dislocation-creep accommodated grain boundary sliding (GBS) may have played a role, which is known to be able to produce a CPO *(*e.g. Hansen et al., 2011; Miyazaki et al., 2013*)*. However, to our knowledge this mechanism has only been shown to operate in dry, dense polycrystalline olivine aggregates (ϕ < 3%, $d \approx$ 2 μm) that were relatively slowly deformed ($\dot{\varepsilon}$ = 10^{-3} to 10^{-5} s^{-1}) at temperatures as high as 1100° to 1300°C (Hansen et al., 2011, 2012a, b). Because the shear band developed in the water-saturated, porous ($\phi \approx$ 15-30%) calcite gouge was characterized by equivalent compressive strain rates that were 3 to 6 orders of magnitude faster (i.e. $\dot{\varepsilon}$ = 10^{0} to 10^{1} s^{-1}), it seems unlikely that dislocation creep accommodated GBS has played a role in experiment 550-fast.

In microstructures recovered from direct-shear experiments on simulated calcite gouge conducted at temperatures of 20 to 150°C at an effective normal stress of 50 MPa, under dry and water-saturated conditions using sliding velocities ranging from 0.1 to 10 μm/s, Verberne et al. (2013a, b, 2014) reported a CPO in nanocrystalline shear bands (see Chapters III and IV). To explain this, Verberne et al. (2014) argued that the strong anisotropy in surface energy of calcite produced preferred sintering (neck growth) via oriented attachment of coherent nanoparticle interfaces (cf. Penn & Banfield, 1998, 1999; for reviews see Niederberger & Cölfen, 2006; Zhang et al., 2009). Interestingly, in the shear band that developed in experiment 550-fast, the presence of polygonal grain

aggregates suggests that diffusion has played at least some role, while the linear cavitated grain arrays (Fig. 6.10e) may be interpreted as being due to linear chaining through diffusion of the 0.3 to 1 μm sized grains. On this basis, we speculate that oriented grain attachment by intergranular, water-assisted diffusive mass transfer was responsible for the shear band CPO developed in experiment 550-fast, similar to the mechanism proposed by Verberne et al. (2014) (i.e. in Chapter IV), and very much different from the commonly assumed dislocation-mechanism related CPO development in sheared polycrystals.

6.5.2. Role of localization in controlling strength and slip stability

Laboratory and numerical modelling studies of sheared granular materials show that, in general, shear localization occurs due to the presence of local heterogeneities, such as density fluctuations (Nübel & Huang, 2004; Aranson & Tsimring, 2006; Hadizadeh et al., 2010, 2015), introduced by for example a distribution in particle size (Marone & Scholz, 1989; Mair & Abe, 2008). Therefore, localization of shear strain is implicit for any polydisperse granular medium that undergoes dilatant granular flow, thus including the present calcite gouge sheared at 100 μm/s in experiment 550-fast (Fig. 6.9). The location of the shear band right at the sample boundary (Fig. 6.9a) may be due to the contrasts in strength and stiffness between piston and sample, leading to focused grain comminution in a narrow band close to the piston face (Niemeijer et al., 2010). For experiment 550-slow, which used a displacement rate of only 0.1 μm/s, time-dependent, inter- and/ or intragranular creep processes were fast enough to accommodate the imposed displacement, preventing sufficient dilatation and subsequent localization.

The localization of shear strain has important consequences for fault strength and stability. Verberne et al. (2014, in prep.) (i.e. Chapters IV and V) showed that the shear deformation of simulated calcite gouge is in a qualitative sense consistent with predictions of model involving a competition between dilatation by granular flow versus intergranular compaction (Niemeijer & Spiers, 2006, 2007; Den Hartog & Spiers, 2013, 2014). This model predicts that, at constant temperature, a transition from non-seismogenic, velocity strengthening viscous flow to potentially seismogenic, velocity weakening frictional slip will occur upon the onset of intergranular dilatation with increasing shear strain rate (Niemeijer & Spiers, 2007; Den Hartog & Spiers, 2014; Chen, 2015). The present experiments were performed at temperature and effective normal stress conditions close to this transition (Verberne et al. in prep., or Chapter V), and, on

the basis of the observed shear behaviours and microstructures, we suggest that the samples sheared at v = 0.1 μm/s have deformed in the stable, velocity strengthening flow regime, whereas those sheared at $v \geq 1$ μm/s have deformed in the (potentially) unstable, frictional velocity weakening regime.

Because the effective shear strain rate is key in controlling the microphysical processes achieving the imposed strain, the development of a shear band may affect the slip behaviour at higher displacements, specifically for velocity stepping experiments at conditions close to the upper temperature transition from velocity weakening to velocity strengthening slip. In the case that a shear band develops early on in the experiment, for example when using high slip rates, and the shear band is persistent and does not heal, upon subsequent steps in sliding velocity the effective shear strain rate will be higher compared with in a non-localized microstructure. If the change in shear strain rate is sufficient, at constant temperature, a transition from velocity strengthening viscous flow to frictional velocity weakening slip may occur.

We have investigated this in experiments NS_mix_1 & _2 (Table 6.1), in which a sequence of steps in effective normal stress were applied, before and after an interval of sliding at relatively high displacement rate ($v \geq 10$ μm/s). In experiment NS_mix_1 the steps in σ_n^{eff} were conducted at v =1 μm/s, and we only found linear correlations between shear stress and effective normal stress (Fig. 6.7c), suggesting that frictional sliding occurred both before and after the interval at high slip rate. In experiment NS_mix_2, in which the steps in σ_n^{eff} were conducted at v = 0.1 μm/s, the shear stress-effective normal stress curves of data from before and after the interval at high slip rate suggested effective normal stress insensitive behaviour (Fig. 6.7d), although linear regression showed a slightly better fit to data from after the high slip rate interval (Table 6.3). We suggest that a persistent shear band developed in experiment NS_mix_2, which facilitated dilatant granular flow hence frictional sliding, even before the interval at high slip rate. For experiment NS_mix_2, upon sliding at v = 300 and then 100 μm/s a shear band must have been introduced (cf. Fig. 6.9). We speculate that, at a temperature of 550°C, the shear rate of 0.1 μm/s was low enough for this shear band to have healed upon restarting shear after the interval of high slip rate. In this case, shear strain will be redistributed over a wider area, and the sample may deform in the stable, viscous flow regime.

6.5.3. Geological implications

From the foregoing it is clear that the effective fault shear strain rate is key in controlling the pressure-temperature conditions of the transition from frictional sliding to ductile flow, hence in controlling the depth window of the seismogenic zone. Taking a geothermal gradient of 25 to 30°/km, such as in the southern Apennines (Doglioni et al., 1996), a temperature of 550°C corresponds with a depth of ~18 to 22 km. For tectonic shear loading rates (~10^{-9} m s^{-1}, Marone, 1998b), our results imply that an earthquake is unlikely to nucleate on a fault cutting limestones at this depth, i.e. as long as shear is not localized in an extremely narrow zone (<1 nm). However, if the shear strain rate is increased, for example due to an earthquake propagating downward (e.g. Tse & Rice, 1986; Scholz, 1988; Shaw & Wesnousky, 2008) or due to ongoing localization of a sheared rock volume (e.g. Regenauer-Lieb & Yuen, 2003; Kaus & Podlachikov, 2006), the fault slip mechanism may transition from a regime of stable ductile shear to one of frictional velocity weakening, potentially leading to runaway slip at depths below that what is considered to be the lower limit of the seismogenic zone. For carbonate rocks in particular this may explain seismicity at depths of 15 to 18 km in respectively the Zagros mountains (Nissen et al., 2014) and the southern Apennines (Boncio et al., 2007), whereas in a more general sense this may explain the presence of syn-tectonic pseudotachylytes in nominally ductile shear zones (cf. e.g. Sibson, 1980; Hobbs et al., 1986; Toy et al., 2011).

6.6. Conclusions

We have investigated the effect of displacement rate on the mechanical properties and microstructure development of water-saturated, simulated calcite fault gouge, sheared at conditions close to the transition from frictional or frictional-viscous fault slip to dominantly ductile flow. Our aim was to unravel whether a “slow” versus a “fast” displacement rate, as applied in the experiments, corresponds to localized versus more homogeneous deformation of the gouge layer, and to determine how this may affect the mechanical properties. To this end, ring shear experiments were conducted at a fixed temperature of 550°C, at an effective normal stress (σ_n^{eff}) of 50 MPa, using constant displacement rates (v) of 0.1 and 100 μm/s, coupled with a microstructural analysis of the recovered sheared gouge layers. We also conducted ring shear effective normal stress stepping experiments, at 550°C, at sliding velocities of 0.1, 1 and 10 μm/s using sequentially increased σ_n^{eff} values within the range from 20 to 140 MPa. Our conclusions

are summarized as follows:

1. In the experiments conducted at a constant effective normal stress of 50 MPa, at v = 0.1 μm/s the imposed displacement was accommodated by distributed ductile flow, whereas at v = 100 μm/s this occurred by localized slip in a 30 to 40 μm wide shear band. Since the width of the actively slipping zone controls the effective shear strain rate, this can strongly affect the strength and stability of a gouge-filled fault. Specifically, at constant temperature, higher shear strain rates may lead to potentially unstable, velocity weakening slip as opposed to stable, viscous flow at lower shear strain rates.
2. Effective normal stress stepping experiments conducted at v = 0.1 μm/s, which used a starting σ_n^{eff}-value of 50 MPa, showed effective normal stress insensitive behaviour, characteristic for ductile deformation processes. Conversely, effective normal stress stepping experiments conducted at $v \geq 1$ μm/s, plus at 0.1 μm/s when using a starting σ_n^{eff} value of 30 MPa, showed linear effective normal stress dependent behaviour characteristic for frictional sliding.
3. Effective normal stress stepping experiments which employed an interval of displacement at relatively high rates (v = 100 or 300 μm/s) showed essentially the same type of shear behaviour before and after the high slip rate interval. For v = 1 μm/s, in both cases we observed linearly effective normal stress dependent, frictional slip, whereas for v = 0.1 μm/s in both cases we found effective normal stress insensitive behaviour. We suggest that a persistent shear band existed in the experiment conducted at 1 μm/s, whereas at 0.1 μm/s, a shear band formed at high slip rates, however which healed during subsequent sliding at v = 0.1 μm/s. However, in the case that shear band healing would be too slow, shear strain following the interval at high slip rate may become localized, increasing the shear strain rate, which in turn may significantly affect fault strength and stability.
4. When the shear strain rate is increased on faults cutting rocks at pressure-temperature conditions pertaining to the base of the seismogenic zone, the fault slip mechanism may change from a regime of stable ductile shear (such as in our experiments at v = 0.1 μm/s) to one of frictional velocity weakening (as in our experiments at $v \geq 1$ μm/s). This may explain the nucleation as well as propagation of runaway slip at depths below that what is considered to be the lower limit of the seismogenic zone.

Acknowledgements

Martyn Drury and Jianye Chen are thanked for insightful discussions. Maartje Houben is thanked for helping with the ArcGIS and PolyLX grain analysis software, Otto Stiekema for making the thin sections, and Peter van Krieken for conducting particle size and XRD analysis. Thony van der Gon-Netscher, Gert Kastelein and Eimert de Graaff are acknowledged for technical support.

Chapter VII

General conclusions and suggestions for further research

This thesis has reported an experimentally-based study aimed at determining the shear strength and sliding stability of (simulated) calcite fault gouges, deformed under conditions pertaining to earthquake nucleation in the upper and middle crust. Using observations of the micro- and nanostructure of samples that were retrieved from our experiments as a basis, an attempt was made to explain the physical processes controlling shear. The work is relevant not only to understanding the seismic cycle in tectonically-active limestone terrains, but to the processes responsible for earthquake nucleation in general, providing new insights into the multi-scale character of slip of gouge-filled faults. On the basis of the methods employed and results obtained, I reach the main conclusions outlined below. I also present a summary of the most important implications for natural faulting in limestone terrains. Unsolved problems and remaining data needs are then identified, and suggestions are made for future research.

7.1. The methods used

An extensive series of frictional shearing experiments was performed on ~1 mm thick layers of simulated calcite fault gouge, prepared from intact natural limestone (Xujiahe Limestone, 98% pure), pure $CaCO_3$ single crystals (Iceland Spar), or else from industrial grade pure calcite powder (MERCK). The experiments employed the saw-cut (Chapter II), the direct-shear (Chapter III & IV), as well as the ring-shear geometry (Chapter V & VI), and were designed to investigate the mechanical properties of calcite gouge, at conditions relevant to earthquake nucleation on faults in the seismogenic zone in tectonically-active carbonate terrains. The approach adopted included load point displacement rate- and effective normal stress-stepping experiments, as well as experiments that used a constant load point displacement rate, conducted at temperatures within the range from room temperature to ~600°C.

The saw-cut and direct-shear tests employed a constant load point displacement rate or sliding velocity (v) of 1 μm/s, or else sequentially stepped values within the range from 0.1 to 10 μm/s, and were performed under (lab-)dry or water-saturated conditions, at temperatures (T) of ~18° to 150°C, at an effective normal stress (σ_n^{eff}) of 50 to 53 MPa. In the case of water-saturated experiments, the pore fluid consisted of deionized water, which was pressurized to 10 MPa when using the direct-shear assembly, and to 20 MPa when using the saw-cut assembly. The total displacement achieved in the saw-cut tests typically measured ~1.5 to 3 mm, and in the direct-shear tests 4 to 6 mm, corresponding to final bulk shear strains imposed on the gouge layers of approximately 2 to 10.

Constant-v and v-stepping experiments in the ring shear machine were conducted in the range $0.03 \leq v \leq 300$ μm/s, at $\sigma_n^{eff} = 50$ MPa, at constant temperatures of 20° to 600°C. Effective normal stress-stepping experiments were also performed in this temperature range, employing $20 \leq \sigma_n^{eff} \leq 140$ MPa, at fixed or else stepped sliding velocities within the range $0.1 \leq v \leq 100$ μm/s. All ring shear tests were performed under water-saturated conditions, using deionized water, and pore fluid pressures ranging from 10 to 100 MPa. The total displacement in these experiments typically measured ~20 to 30 mm, corresponding to bulk shear strains of 25 to 60, depending on the degree of sample thinning during shear.

Sheared gouge layers from in particular the direct-shear but also the ring-shear experiments were recovered, and subjected to extensive micro- and nanostructural investigations using both light and electron microscopy. Recovered samples were resin-impregnated and then sectioned after hardening (Chapters III, V, VI), and/ or examined as loose fragments, collected fresh from the sample-piston interface after an experiment (Chapters IV, V, VI). In the case of sectioning, thin slices ~5 to 30 μm in thickness were prepared in an orientation normal to the shear plane, and normal and/ or parallel to the shear direction

7.2. Main findings

7.2.1. Effect of temperature on the shear behaviour of calcite(-rich) fault gouges

Regardless of the shear geometry employed, all experiments conducted at an effective normal stress of 50 MPa and sliding velocities (v) of 0.1 to 10 μm/s showed a transition from stable, velocity strengthening slip to potentially unstable, velocity weakening slip at temperatures above 80° to 100°C (Chapters II to V). Corresponding values of the apparent coefficient of friction at steady-state (μ = shear stress/ effective normal stress, or τ/σ_n^{eff}), determined at v = 1 μm/s, measured ~0.6 to 0.8. Experiments performed under water-saturated conditions generally showed somewhat lower μ-values (~0.6-0.7) compared with those conducted under nominally dry conditions ($\mu \approx 0.7$-0.8). However, the presence of pressurized pore fluid water did not affect the transition from velocity strengthening to velocity weakening at ~80° to 100°C (Chapters II to IV). Experiments conducted up to 550°C continued to display frequently unstable, velocity weakening behaviour, until a transition to stable velocity strengthening slip occurred at ~600°C (for v = 0.1 to 10 μm/s, see Chapter V). The shear strength or apparent coefficient of friction showed a maximum at 550° to 600°C ($\mu \approx 0.7$-1.0). Meanwhile, all effective normal

stress-stepping experiments, conducted in the range T = 20° to 600°C and employing a constant sliding velocity of 1 or 10 μm/s, or else velocity steps in the range from 1 to 100 μm/s, showed a linear dependence of the shear strength (τ) upon increasing effective normal stress (Chapters V, VI). However, in tests conducted at 550°C, and at the lowest sliding velocity explored (0.1 μm/s), a breakdown in linearity (i.e. a flattening-off of the τ vs. σ_n^{eff} curve) was seen at σ_n^{eff} –values above 65 to 80 MPa (Chapter VI).

7.2.2. Microstructure of calcite gouge sheared at sub-seismic sliding velocities

All sections prepared from experiments conducted in the temperature range from 20° to 200°C consistently show a pattern of shear strain localization into ultra-fine grained, boundary-parallel and inclined shear bands, corresponding to mainly boundary and R_1 shears in the terminology of Logan et al. (1979) (Chapters III, V). This includes samples recovered from direct-shear as well as ring-shear tests, regardless of whether conducted under velocity strengthening (T < 80°-100°C) or velocity weakening (T ≥ 80°-100°C) conditions. Surrounding the shear bands, coarser angular grains are present, resembling the undeformed starting sample powder. This suggests that the bulk of the imposed shear displacement was accommodated within the shear-plane-parallel boundary shears, which therefore represent the principal slip zone (PSZ). Importantly, the shear bands display a strong, uniform, optical birefringence, and optical extinction, indicative of a crystallographic preferred orientation (CPO) (Chapter III). Internally split, loose sheared gouge fragments recovered from the PSZ display aligned, striated, highly-reflective (shiny), surface patches marking the shear plane of the boundary shear band. Investigation of the PSZ using scanning as well as transmission electron microscopy (resp. SEM and TEM) demonstrated that they comprise porous (ϕ = 20-30%), sheet-like volumes composed of partially sintered, ~100 nm nanocrystalline spherules, with embedded dense, planar patches of aligned, ~100 nm-wide nanospherule chains or fibres that constitute the shiny slip surfaces (Chapter IV). The nanospherules and -fibres were shown to consist of crystallites ~5 to 20 nm in size, with a CPO of the (104)[$\bar{2}$01] calcite slip system (hexagonal structural cell) aligned parallel to the shear plane and direction.

Towards higher temperatures, i.e. in gouge layers recovered from experiments performed at 400° to 600°C, localized slip in a single boundary shear band was accompanied by more distributed deformation, involving grain size sensitive (diffusion creep) and/ or grain size insensitive (dislocation creep) processes (Chapter V). In these samples the shear bands are characterized by linear, cavitated arrays of ~1 to 5 μm sized

polygonal grains. Away from the sample boundary, i.e. in the bulk gouge or 'matrix', elongated porphyroclasts with a long axis ~10 to 30 μm in size display a foliation that sweeps into parallelism with the shear plane and direction as the boundary shear is approached. In other words, while the mechanical data for the temperature range of 400° to 600°C showed brittle/ frictional behaviour (e.g. stick-slip), the microstructure resembled that of a mylonite. However, the recovered microstructure reflects the complex slip rate and displacement history that was imposed in each experiment, so that for these tests it is difficult to couple the microstructure to any of the specific experimental conditions applied or mechanical behaviours observed. On this note, samples recovered from experiments performed at conditions close to the higher temperature transition from velocity weakening to velocity strengthening behaviour (i.e. at ~550°C), which employed constant v = 0.1 μm/s, showed a microstructure indicating distributed or homogeneous deformation (Chapter VI). By contrast, samples recovered from experiments conducted under the same conditions, but using v = 100 μm/s, showed the development of a ~30 to 40 μm wide shear band. Interestingly, this shear band is composed of linear, cavitated, arrays of ~0.3 to 1 μm-sized polygonal grains, and shows a strong, uniform, optical interference suggestive of a CPO, similar to samples sheared at low rates (0.1 to 10 μm/s) and much lower temperatures (18° to 150°C) as reported in Chapter III.

7.2.3. Microphysical processes controlling (the velocity dependence of) shear strength

The transition from velocity strengthening to velocity weakening slip around 80° to 100°C occurs in lab-dry as well as in water-saturated experiments, implying that the presence of (pressurized) pore fluid water is not crucial to this transition (Chapters II, III). However, in a nanocrystalline boundary shear band of the type observed in samples deformed at 18 to 200°C, only small quantities of water (2 to 3 wt.%) are sufficient to facilitate intergranular diffusive mass transport (Chapter IV). Ubiquitous evidence of sintering and/ or neck growth between nanospherules and within nanofibers present in boundary shears attests to significant diffusive mass transfer. At the same time, the high porosity in the shear band (~20 to 30%) points to the role of (dilatant) granular flow. A mechanism of dilatant, athermal granular flow, operating in competition with thermally-activated compaction creep processes was proposed to explain the observed behaviour, following the microphysical model originally put forward by *Niemeijer & Spiers (2007)*. Several variants of this model were progressively considered in Chapters II to IV.

Ultimately, however, a mechanism of nanogranular flow with partial accommodation by diffusive mass transport is proposed to have controlled shear deformation in experiments performed at temperatures of ~20° to 200°C. This is in effect analogous to Ashby-Verrall superplastic flow with incomplete accommodation of grain boundary sliding by diffusive mass transfer. The transition from velocity strengthening to – weakening slip, then, occurs due to enhanced diffusive mass transfer rates at elevated temperatures. Under these conditions, and at low sliding velocities, creep-controlled compaction is fast enough for pores to compact and grain contacts to spread or possibly "bond", ultimately imparting higher strength at lower sliding velocities, thus producing velocity weakening behaviour. Although the solubility of calcite decreases with increasing temperature, the net intergranular creep rate is shown to accelerate for $T \geq$ 80°-100°C for realistic values of the activation energy characterizing diffusion ($Q_d \geq$ 25 kJ/mol). The CPO observed in the shear bands was explained by positing a mechanism of oriented nanoparticle attachment as a consequence of the strong anisotropy in surface energy of calcite.

At temperatures of 400° to 600°C, as summarized above, intracrystalline plasticity and dynamic recrystallization of the bulk gouge material start to a play a significant role, especially at the lower slip velocities employed (Chapters V, VI). This was evident from the recovered microstructures, as well as from comparison of our experimental results with deformation mechanism maps constructed for axial compression of dense, polycrystalline calcite aggregates at similar temperatures. Nonetheless, the simultaneous presence of linear, cavitated arrays of polygonal grains in boundary shear bands suggest that incompletely accommodated grain boundary sliding (GBS), hence dilatant flow, is still important, in particular when shear strain rates are relatively high. This explains the velocity weakening behaviour in our experiments conducted at temperatures of 400° to 550°C, once again as due to competition between dilatant granular flow and creep-controlled compaction involving either diffusional or dislocation creep mechanisms (cf. Niemeijer & Spiers, 2007). The transition from velocity weakening to velocity strengthening behaviour observed at 600°C is accordingly interpreted as a transition from (localized) frictional sliding, involving balanced dilatant granular flow and creep-controlled compaction, to (more distributed) viscous/ plastic shear flow involving grain-size sensitive (diffusion creep) and/ or grain-size insensitive (dislocation creep) deformation processes.

In general, the micromechanical mechanism proposed by Niemeijer & Spiers (2007)

(see also Bos & Spiers, 2002a; Den Hartog & Spiers, 2014), which involves competition between dilatation by granular flow vs. creep-controlled compaction, predicts qualitatively remarkably similar trends in frictional behaviour to the observed trends in the present mechanical data (Chapters II to VI). This suggests that the principles of the model are more widely applicable than to just granular halite-phyllosillicate mixtures, on which the model was originally based. Indeed, the present results show that the principles of the Niemeijer-Spiers model appear to apply also to shear of monomineralic fault gouges composed of calcite.

7.3. Geological implications

7.3.1. Implications for seismicity in tectonically-active limestone terrains

The mechanical data reported in this thesis have important implications for understanding faulting and seismicity in tectonically-active limestone terrains, such as those commonly found in rifts and the external zones of orogenic belts. If we (crudely) extrapolate the measured effects of temperature on the velocity dependence of calcite gouge, then, using a geothermal gradient of 25 to 30°C/km, the lower temperature transition from velocity strengthening to –weakening (at 80° to 100°C) occurs at a depth of ~2 to 4 km, consistent with seismological observations of the depth of the upper boundary of the seismogenic zone in tectonically-active limestone terrains (see Chapter III). For the higher temperature transition, from velocity weakening back to velocity strengthening slip at around 550-600°C, the depth would be ~18 to 24 km, implying similar depths for the base of the seismogenic zone in carbonates. This transition may depend on slip rate, effective normal stress, and displacement history in a complex way. However, seismological observations indeed suggest that seismicity in limestones occurs at depths up to 18 km (see Chapters V, VI).

Despite the present experimentally-based depth estimates being only rough estimates, the three-regime behaviour of velocity strengthening, velocity weakening, and velocity strengthening, observed with increasing temperature, bears a striking parallel to that seen in shear experiments on simulated fault rocks prepared from other rock types, such phyllosillicates, gabbro, or granite gouge (see Chapter I), and with the concept of the seismogenic zone in limestone terrains and in seismogenic terrains in general. By contrast with other rock types, though, the tendency for faults in limestones to be velocity weakening at relatively shallow depths, coupled with their high frictional strength at the corresponding conditions, suggests that tectonically-active limestone terrains may be

particularly prone to shallow-focus seismicity characterized by large stress drops. The present results accordingly offer an explanation of why orogenic carbonate terrains have such high seismic hazard.

7.3.2. Implications for the interpretation of natural fault rock microstructures

The microstructural observations reported in this thesis, coupled with the insights into the associated mechanical behaviour, have important implications for the interpretation of natural (limestone) fault rocks. The most important microstructural findings in this context are: i). The nanocrystalline PSZs with internal shiny or 'mirror-like' slip surface patches, and ii). The mylonitic microstructures of samples derived from experiments that showed brittle/ frictional deformation features. I address the implications of these findings in turn below.

i). Shiny vs. mirror slip surfaces and the significance of nanogranular fault rocks

Simulated calcite fault gouge sheared here at low sliding velocities ($0.03 \leq v \leq 100$ μm/s) at effective normal stresses of 50 MPa demonstrated the development of striated, highly-reflective or shiny slip surfaces up to temperatures of 550°C. The roughness characteristics of a shiny patch developed at room temperature was shown to be essentially the same as that of the so-called "mirror-like" slip surfaces or "fault mirrors" reported to form in high-velocity friction (HVF) experiments (e.g. Han et al., 2007b; Smith et al., 2013; Fondriest et al., 2013) and observed in nature (Siman-Tov et al., 2013; Fondriest et al., 2013). By contrast with our experiments, HVF tests typically employ co-seismic sliding velocities in excess of 0.1 m/s, imposed at relatively low values of the effective normal stress (σ_n^{eff} = 0.25 – 26 MPa). Despite claims that mirror-slip surfaces are indicators of co-seismic slip in carbonate rocks (Fondriest et al., 2013; Siman-Tov et al., 2013), we infer that mirror-like slip surfaces are not restricted to form at coseismic slip rates, and that natural exposures of highly-reflective fault surfaces must be interpreted with caution. In addition, the principal reason that velocity weakening occurred in the present experiments on simulated calcite gouge at relatively low temperatures (80°-200°C) is because intergranular diffusive mass transfer is dramatically accelerated by the nanogranular nature of the shear bands. Because of this, intergranular diffusion creep can proceed at high rates at relatively low temperatures, which, alongside dilatant flow, may lead to velocity weakening hence earthquake nucleation at relatively shallow crustal conditions – as mentioned above. Given the

abundant observations of nanogranular fault surfaces increasingly reported in fault rocks of all types (e.g. Chester et al., 2005; Ma et al., 2006; Kirkpatrick et al., 2013; Evans et al., 2014), in differing tectonically-active terrains, the inferred mechanism of competition between dilatation by granular flow and creep-controlled compaction may be generally widespread in the upper-crust.

ii). Brittle/ frictional vs. ductile microstructures

The present experiments performed at 400° to 600°C have important implications for microstructural studies of natural calcite tectonites. Despite the occurrence of stick-slip events with huge stress drops in these experiments, the associated microstructure predominately showed evidence for crystal plastic deformation of ~10 to 30 μm sized grains in the sample body, as well as for dynamic recrystallization and grain boundary sliding in fine-grained (~0.3-1 μm) boundary shears, accommodated by diffusion and/ or dislocation creep processes. Thus, while our samples exhibited essentially brittle/ frictional mechanical behaviour, the corresponding microstructure resembled that of a mylonite. With only the very narrow, fine-grained boundary shear bands possibly recording the observed brittle/ frictional behaviour. This implies that microstructures from natural exposures of shear zones cutting calcite rocks, which are apparently formed by plastic flow, can potentially represent seismogenic faults, especially if they contain narrow, fine-grained ultra-mylonitic bands. The question then comes to mind as to whether this may apply more generally to other mylonitic rocks.

7.4. Remaining questions and suggestions for further research

7.4.1. Unsolved problems

Effects of (pressurized) pore water on the frictional behaviour of calcite fault gouge

In the experiments reported in this thesis, the presence of (pressurized) pore water does not affect the transition from velocity strengthening to velocity weakening slip at ~80°C in a substantial way. However, compared with tests vented to lab air, significant reduction of the absolute value of shear strength was seen in wet samples, specifically with increasing displacement beyond macroscopic (apparent) yield in experiments performed at temperatures ~20-50°C to 150°C (Chapter III). Also, peculiarities in the sample response to velocity stepping, such as a transient strength *increase* after a static strength increase due to an *upward* perturbation in sliding velocity (i.e. the so-called "positive *b*" -effect), were only observed in experiments performed under water-saturated

conditions (Chapters II to V). The data obtained here does not provide an unambiguous explanation for these effects. In view of the extreme, localized grain size reduction in shear bands that was observed to occur in all tests, the presence of (pressurized) pore water has been suggested in Chapter III to cause various effects, each of which can potentially influence the bulk frictional behaviour. This includes pre-test, over-consolidation of the gouge layers in the presence of water, as well as dynamic mechanical and/ or chemical effects of water, such as intergranular lubrication, pressure solution, or a reduction of fracture surface energy (see discussion in Chapter III). To solve this, more research is needed on the chemical effects of (pressurized) pore water and the role of gouge impurities herein, as well as on the mechanical effects of perturbations in the fluid pressure distribution in the gouge during localized slip. Such an investigation could have significant impact on studies of the frictional behaviour of water-saturated gouge-filled faults, as well as on the physical meaning of fitted rate-and-state-friction parameters (a, b, D_c, and θ).

Mechanism of shear band formation/ localization

The results of this thesis clearly demonstrated that localization of shear strain is crucial in controlling fault sliding properties. The present investigation focused mainly on the processes that occur within the shear bands, i.e. those that are believed to be responsible for accommodating the bulk of the imposed displacement during a test, and therefore the observed mechanical behaviour. However, the results do not explain why localization occurred, or why all samples showing localization contained at least one through-going shear band located immediately adjacent to the apices of the grooved piston interface. I speculated that it may be related to the contrast in stiffness between the piston and the sample. However, this does not provide a microphysical understanding of the formation mechanism. A possible reason is that R-shears developed in the early stages of deformation (e.g. Gu & Wong, 1994) create strain compatibility problems at the piston interface, which are accommodated by local dilatation, hence porosity increase and weakening of the gouge at its margins. This whole localization question requires further research, especially in view of the key role of localization in controlling fault strength and stability at conditions close to the base of the seismogenic zone and in friction experiments in general (as discussed in Chapters V and VI).

Mechanism(s) of nanocrystallite, nanospherule, and nanofibre formation

The shear bands developed at low temperatures (20° to 200°C) showed the presence of nanofibres (chains of sintered nanospherules), nanospherules, and, apparently within the nanospherules, polycrystalline arrays of ~5-20 nm-sized calcite nanocrystallites. The formation of nanocrystallites of this size within the nanospherules and fibres, in experiments with displacements of only ~4-5 mm, at displacement rates of just microns-per-second, was unexpected beforehand, and is not straightforward to unravel. The nanocrystallite clusters reported showed striking similarities with nanostructures reported to form in metals, i.e. with the development of cellular equiaxed nanograins from dense dislocation networks and tangles at high strain rates (10^0-10^3 s^{-1}) at room temperature (Umemoto, 2003; Yang et al., 2010; Tao et al., 2002). However, due to the relatively large strains accommodated by the shear bands, any relation between parent grains and the nanocrystallites, -spherules, and fibres, was obscured, complicating investigation of their respective formation mechanisms. More research is needed to investigate this further.

Mechanism of shear band CPO formation

All shear bands developed at low temperatures (20° to 200°C), plus that developed in an experiment performed at 550°C at v = 100 μm/s, showed uniform birefringence colours and uniform optical extinction, suggestive of a very strong crystallographic preferred orientation (CPO). Indeed, in selected samples from experiments performed at 20° to 200°C, this was proven to be present. However, the operation of granular flow in the shear bands, and its presumably randomizing nature, renders the formation of a CPO enigmatic. Hypotheses were established on the basis of parallels with well-known nanocrystallization mechanisms from the geochemistry and materials science literature, with the preferred orientation being one of crystallographically controlled sintering of nanospherules to form nanofibres, at least at 20° to 200°C. However, more research is needed to investigate whether these mechanisms are even remotely applicable to the present experiments.

7.4.2. Remaining data needs

Shear behaviour over a wider scope of (effective) normal stress and pore pressure

Most of the experiments reported in this thesis focussed on the effect of temperature on the shear behaviour of simulated calcite gouge, maintaining a constant effective

normal stress (σ_n^{eff}) of ~50 MPa. Possible effects of varying the normal stress, or pore fluid pressure (P_f), through ranges expected in the upper to middle crust have not been investigated in a systematic way. This is a potential problem for extrapolation of the results to natural conditions, i.e. assuming a hydrostatic state of stress in the seismogenic zone. Although recent literature emphasizes that substantial fluid overpressures can exist in faults at depth, dramatically lowering the effective normal stress (see Sibson, 2014; Suppe, 2014), it is useful to understand the mechanical behaviour of gouge-filled limestone faults over a wider range of in-situ fluid conditions, including hydrostatic. In this way, a more complete understanding of the range of the seismogenic zone in limestone terrains can be obtained. This, combined with precise information regarding the thermal and lithological structure of the crust, should allow a better basis to be developed for predictions of the depth of seismicity in tectonically-active limestone terrains. An experimental programme focused on this aim could make use of the ring shear deformation apparatus installed at the HPT lab of Utrecht University, which, when used in the set-up employed in Chapters V and VI, allows for simulated gouges to be tested to practically unlimited shear strains at normal stresses up to ~400 MPa, fluid pressures up to ~300 MPa, and temperatures up to ~700°C.

Shear behaviour over a wider range of sliding velocities

All experiments reported in this thesis were limited to sub-seismic sliding velocities, of the order of 10^{-8} to 10^{-4} m/s. The lowest end of this range is close to tectonic loading rates (~10^{-9} m/s), and may be considered representative for fault sliding rates relevant to earthquake rupture nucleation in the upper crust. However, for an earthquake to develop, an initial rupture must accelerate over a wide range of slip velocities before achieving co-seismic displacement rates of meters per second. In other words, to fully grasp the properties of faults cutting limestones, experiments over the full range of sliding velocities (10^{-9} to 10^{1} m/s) are needed, preferably at in-situ conditions of effective normal stress. This challenging task would require a low-to-high velocity (rotary) shear apparatus, such as that installed at the State Key Laboratory for Earthquake Dynamics of the China Earthquake Administration in Beijing, and currently under development at the HPT lab at Utrecht University (ERC SEISMIC project, A. R. Niemeijer).

7.4.3. Broader challenges

Investigation of impure carbonate gouges and associated rock types

The experimental data and microstructures reported here clearly show evidence that calcite gouge tends to exhibit unstable frictional behaviour with increasing temperature, i.e. above ~80°C. To understand the general implication of this to faults cutting calcite-rich rocks, besides relatively pure calcite limestones, an investigation of the frictional behaviour of gouge mixtures composed of calcite plus another phase or phases is needed. In addition, the present results are mainly relevant to faults cutting limestones, but do not necessarily apply to other carbonate rocks like dolomites. Limestones frequently show dolomitization, and are commonly associated with the presence of primary dolomites, and/ or evaporites such as anhydrite (e.g. in parts of the Apennines, Italy – see De Paola et al., 2008*)*. A study of seismogenesis in tectonically-active carbonate terrains, such as those widespread in the Mediterranean region, should therefore also include a study of the frictional sliding properties of these other, associated rock types. Calcite-bearing fault rocks are also often rich in clay minerals, especially if the protolith limestone is clay-rich. An investigation of the effect of clay content is therefore needed too (such as in a recent paper by Bullock et al., 2015).

The rheology of nanocrystalline aggregates

This study has provided strong evidence that nanogranular fault rocks are of major importance in controlling fault sliding behaviours in both experiment and in nature. In spite of the unusual physical properties that nanocrystalline materials are known to display compared with their coarser-grained counterparts, so far only few studies have focussed on the rheology or frictional behaviour of nanogouge (Hochella Jr., 2008; Han et al., 2011). In view of the present results, and that of recent field and drilling studies on the nanogranular character of natural fault PSZs (e.g. Chester et al., 2005; Ma et al., 2006), it is important to better constrain the role of nanogranular media in the seismic cycle. As a start, this could be approached by a systematic experimental study of the (static and dynamic) frictional properties of simulated 'nanogouge' of different compositions (cf. Han et al., 2011), followed by an investigation of (the rate of) compaction creep processes operating in nanogranular powders. Additional, potentially rewarding challenges include the in-situ imaging of deformation of nanogranular media relevant to the geosciences (cf. Ma, 2004; Shan et al., 2004).

Microphysical modelling of fault gouge friction

To extrapolate friction data generated in the laboratory to natural conditions, a microphysically based model is needed, for example that developed by Niemeijer & Spiers (2007) and Den Hartog & Spiers (2014), and applied in this thesis to qualitatively explain the behaviour seen in the experiments reported. Chen (2015) has recently expanded the Niemeijer-Spiers model to incorporate transients in frictional strength, describing the behaviour of mono-crystalline, granular calcite aggregates in a microphysical modelling framework that has the potential to replace empirical rate-and-state-friction models. A broad future challenge would be to expand this model to incorporate quantitatively the full microstructural evolution shown in the present work, and to then test this to examine the implications for the seismic cycle in tectonically-active carbonate terrains.

References

Abad, I. (2007). Physical meaning and applications of the illite Kübler index: measuring reaction progress in low-grade metamorphism, *In:* Diagenesis and Low-Temperature Metamorphism, Theory, Methods and Regional Aspects (eds. Nieto, F. and Millán, J. J.). *Seminarios, Sociedad Espanola Mineralogia* **3,** 53-64.

Aharonov, E., and Sparks, D. (2002). Shear profiles and localization in simulations of granular materials. *Phys. Rev. E.* **65,** 051302, doi:10.1103/PhysRevE.65.051302.

Alcantar, N., Israelachvili, J., and Boles, J. (2003). Forces and ionic transport between mica surfaces: Implications for pressure solution. *Geochim. Cosmochim. Ac.* **67,** 1289-1304.

Ampuero, J.-P., and Rubin, A. M. (2008). Earthquake nucleation on rate and state faults - Aging and slip laws. *J. Geophys. Res.* **113,** B01302, doi:10.1029/2007JB005082.

Aranson, I. S., and Tsimring, L.S. (2006). Patterns and collective behavior in granular media: Theoretical concepts. *Rev. Mod. Phys.* **78,** 641-692.

Ashby, M. F., and Verrall, R. A. (1973). Diffusion-accommodated flow and superplasticity. *Acta Metall. Mater.* **21,** 149-163.

Atkinson, B. K. (1984). Subcritical crack growth in geologic materials, *J. Geophys. Res.* **89,** 4077-4114.

Barnhoorn, A., Bystricky, M., Burlini, L., and Kunze, K. (2004). The role of recrystallization on the deformation behaviour of calcite rocks: large strain torsion experiments on Carrara marble. *J. Struct. Geol.* **26**, 885-903.

Barnhoorn, A., Bystricky, M., Burlini, L., and Kunze, K. (2005). Post-deformational annealing of calcite rocks. *Tectonophysics* **403,** 167-191.

Barth, N. C., Boulton, C., Carpenter, B. M., Batt, G. E., and Toy, V. G. Slip localization on the southern Alpine Fault, New Zealand. *Tectonics* **32,** 620-640.

Barton, N. (1976). The shear strength of rock and rock joints. *Int. J. Rock Mech. Min. Sci.* **13,** 255-279.

Baumberger, T., Bethoud, P., and Caroli, C. (1999). Physical analysis of the state-and rate-dependent friction law: II. Dynamic friction. *Phys. Rev. B.* **60,** 3928-3939.

Baumberger, T., Heslot, F., and Perrin, B. (1994). Crossover from creep to intertial motion in friction dynamics. *Nature* **367,** 544-546.

Beckmann, P., and Spizzichino, A. (1963). The scattering of electromagnetic waves from rough surfaces. International Series of Monographs on Electromagnetic Waves, **4** (Oxford, UK, Pergamon Press) 503 p.

Beeler, N. M., Tullis, T. E., Blanpied, M. L., and Weeks, J. D. (1996). Frictional behavior of large displacement experimental faults. *J. Geophys. Res.* **101,** B4, 8697-8715.

Bernard, P., and 19 others (2006). Seismicity, deformation and seismic hazard in the western rift of Corinth: New insights from the Corinth Rift Laboratory (CRL). *Tectonophysics* **426,** 7-30, doi:10.1016/j.tecto.2006.02.012.

Berthoud, P., Baumberger, T., G'Sell, C., and Hiver, J.-M. (1999). Physical analysis of the state-and rate-dependent friction law: Static friction. *Phys. Rev. B.* **59,** 14313-14327.

Bestmann, M., and Prior, D. J. (2003). Intragranular dynamic recrystallization in naturally deformed calcite marble: diffusion accommodated grain boundary sliding as a result of subgrain rotation recrystallization. *J. Struct. Geol.* **25**, 1597-1603.

Bestmann, M., Piazolo, S., Spiers, C. J., and Prior, D. J. (2005). Microstructural evolution during initial stages of static recovery and recrystallization: new insights from in-situ heating experiments combined with electron backscatter diffraction analysis. *J. Struct. Geol.* **27**, 447-457.

Bhushan, B. (2005). Nanotribology and nanomechanics. *Wear* **259,** 1507-1531.

Biegel, R. L., C. G. Sammis and J. H. Dieterich (1989). The frictional properties of a simulated gouge having a fractal particle distribution, *J. Struct. Geol.* **11,** 827-846.

Blanpied, M. L., Lockner, D. A., and Byerlee, J. D. (1991). Fault stability infereed from granite sliding experiments at hydrothermal conditions. *Geophys. Res. Lett.* **18,** 609-612.

Blanpied, M. L., Lockner, D. A., and Byerlee, J. D. (1995). Frictional slip of granite at hydrothermal conditions. *J. Geophys. Res.* **100,** 13045-13064.

Blanpied, M. L., Marone, C. J., Lockner, D. A., Byerlee, J. D., and King, D. P. (1998). Quantitative measure of the variation in fault rheology due to fluid-rock interactions. *J. Geophys. Res.***103,** 9691-9712.

Boatwright, J., and Choy, G. L. (1986). Teleseismic estimates of the energy radiated by shallow earthquakes. *J. Geophys. Res.* **91,** B2, 2095-2112.

Boatwright, J., and Cocco, M. (1996). Frictional constraints on crustal faulting, *J. Geophys. Res.* **101,** 13895 - 13909.

Bohr, J., Wogelius, R. A., Morris, P. M., and Stipp, S. L. S. (2010). Thickness and structure of the water film deposited from vapour on calcite surfaces. *Geochim. Cosmochim. Ac.* **74,** 5985-5999.

Boncio, P., Mancini, T., Lavecchia, G., and Selvaggi, G. (2007). Seismotectonics of strike-slip earthquakes within the deep crust of southern Italy: Geometry, kinematics, stress field and crustal rheology of the Potenza 1990-1991 seismic sequences (M_{max} 5.7). *Tectonophysics* **445,** 281-300.

Boneh, Y., Sagy, A., and Reches, Z. (2013). Frictional strength and wear-rate of carbonate faults during high-velocity, steady-state sliding. *Earth Planet. Sci. Lett.* **381,** 127-137.

Bos, B. (2000). Faults, fluids, friction. *Geologica Ultraiectina*, No. 197. [Ph.D. Thesis, 157 pp., Utrecht, The Netherlands].

Bos, B. and C. J. Spiers (2000). Effect of phyllosilicates on fluid-assisted healing of gouge-bearing faults, *Earth Planet. Sci. Lett.* **184** 199-210.

Bos, B., and Spiers, C. J. (2001). Experimental investigation into the microstructural and mechanical evolution of phyllosillicate-bearing fault rock under conditions favouring pressure solution. *J. Struct. Geol.* **23,** 1187-1202.

Bos, B., and Spiers, C. J. (2002a). Frictional-viscous flow of phyllosillicate-bearing fault rock: Microphysical model and implications for crustal strength profiles. *J. Geophys. Res.* **107,** B2, 2028, doi:10.1029/2001JB000301.

Bos, B., and Spiers, C. J. (2002b). Fluid-assisted healing processes in gouge-bearing faults: Insights from experiments on a rock analogue system. *Pure Appl. Geophys.* **159,** 2537-2566.

Bos, B., Peach, C. J., and Spiers, C. J. (2000a). Slip behavior of simulated gouge-bearing faults under conditions favoring pressure solution. *J. Geophys. Res.* **105,** B7, 16699-16717.

Bos, B., Peach, C. J., and Spiers, C. J. (2000b). Frictional-viscous flow of simulated fault gouge caused by the combined effects of phyllosillicates and pressure solution. *Tectonophysics* **327,** 173-194.

Bowden, F. P. and Tabor, D. (1950). The Friction and Lubrication of Solids, Part I (Clarendon Press, Oxford, UK).

Brace, W. F. (1972). Pore pressure in geophysics. *In*: Flow and fracture of rocks (eds. Heard, H. C., Borg, I. Y., Carter, N. L., Raleigh, C. B.). *Am. Geophys. Union*, Washington D. C., Geophys. Monogr. **16,** 265-273.

Brace, W. F., and Byerlee, J. D. (1966). Stick slip as a mechanism for earthquakes. *Science* **153,** 990-992.

Brace, W. F., and Kohlstedt, D. L. (1980). Limits on lithospheric stress imposed by laboratory experiments. *J. Geophys. Res.* **85,** 6248-6252.

Brown, K. M., Kopf, A., Underwood, M. B., and Weinberger, J. L. (2003). Compositional and fluid pressure controls on the state of stress on the Nankai subduction thrust: A weak plate boundary. *Earth Planet Sci. Lett.* **214,** 589-603.

Bullock, R. J., De Paola, N., and Holdsworth, R. E. (2015). An experimental investigation into the role of phyllosillicate content on earthquake propagation during seismic slip in carbonate faults. *J. Geophys. Res.* **120,** 3187-3207.

Bullock, R. J., De Paola, N., Holdsworth, R. E., and Trabucho-Alexandre, J. (2014). Lithological controls on the deformation mechanisms operating within carbonate-hosted faults during the seismic cycle. *J. Struc. Geol.* **58,** 22-42.

Burkhard, M. (1990). Ductile deformation mechanisms in micritic limestones naturally deformed at low temperatures (150-350°C). *In:* Deformation mechanisms, rheology and tectonics (eds. Knipe, R. J., and Rutter, E. H.). *Geological Society, London, Spec. Publ.* **54,** 241-257.

Burkhard, M. (1993), Calcite twins, their geometry, appearance and significance as stress-strain markers and indicators of tectonic regime; a review, J. Struct. Geol. 15, 351-368.

Byerlee, J. D. (1967). Frictional characteristics of granite under high confining pressure. *J. Geophys. Res.* **72,** 3639-3648.

Byerlee, J. D. (1978). Friction of rocks. *Pure Appl. Geophys.* **116,** 615-626.

Carpenter, B. M., Marone, C., and Saffer, D. M. (2011). Weakness of the San Andreas Fault revealed by samples from the active fault zone. *Nat. Geosci.* **4,** 251-254.

Carpenter, B. M., Scuderi, M. M., Collettini, C., and Marone, C. (2014). Frictional heterogeneities on carbonate-bearing normal faults: Insights from the Monte Maggio Fault, Italy. *J. Geophys. Res.* **119,** 1-15, doi:10.1002/2014JB011337.

Chen, J. (2015). Compositional, mechanical, and transport properties of carbonate fault rocks and the seismic cycle in limestone terrains. *Utrecht Studies in Earth Sciences,* No. 76. [Ph.D. Thesis, 274 pp., Utrecht, The Netherlands].

Chen, J., Verberne, B. A., and Spiers, C. J. (2015). Interseismic re-strengthening and stabilization of carbonate faults by "non-Dieterich-type" healing under hydrothermal conditions. *Earth Planet. Sci. Lett.* **423,** 1-12.

Chen, J., Yang, X., Lu, Y., Ma, S., and Shimamoto, T. (2013b). Frictional and transport properties of the 2008 Wenchuan Earthquake fault zone: Implications for coseismic slip-weakening mechanisms. *Tectonophysics* **603,** 237-256.

Chen, J., Yang, X., Ma, S., and Spiers, C. J. (2013a). Mass removal and clay mineral dehydration/ rehydration in carbonate-rich surface exposures of the 2008 Wenchuan earthquake fault: geochemical evidence and implications for fault zone evolution and coseismic slip. *J. Geophys. Res.* **118,** 1-23, doi:10.1002/jgrb.50089.

Chen, X., Madden, A. S., Bickmore, B. R., and Reches, Z. (2013c). Dynamic weakening by nanoscale smoothing during high-velocity fault slip. *Geology* **41,** 739-742.

Chester, F. M. (1994). Effects of temperature on friction: Constitutive equations and experiments with quartz gouge. *J. Geophys. Res.* **99,** 7247-7261.

Chester, F. M. (1995). A rheologic model for wet crust applied to strike-slip faults. *J. Geophys. Res.* **100,** B7, 13033-13044.

Chester, F. M., and Chester, J. S. (1998). Ultracataclasite structure and friction processes of the Punchbowl fault, San Andreas system, California. *Tectonophysics* **295,** 199-221.

Chester, F. M., and Higgs, N. G. (1992). Multimechanism friction model for ultrafine quartz gouge at hypocentral conditions. *J. Geophys. Res.* **97,** 1859-1870.

Chester, J. S., Chester, F. M., and Kronenberg, A. K. (2005). Fracture surface energy of the Punchbowl fault, San Andreas system. *Nature* **437,** 133-136.

Chiarabba, C., De Gori, P., and Mele, F. M. (2014). Recent seismicity of Italy: Active tectonics of the central Mediterranean region and seismicity rate changes after the Mw 6.3 L'Aquila earthquake. *Tectonophysics* **638,** 82-93.

Chiarabba, C., Jovane, K., and Di Stefano, R. (2005). A new view of Italian seismicity using 20 years of instrumental recordings. *Tectonophysics* **395,** 251-268.

Chiaraluce, L. (2012). Unravelling the complexity of Apenninic extensional fault systems: A review of the 2009 L'Aquila earthquake (Central Apennines, Italy). *J. Struct. Geol.* **42,** 2-18.

Chokshi, A. H., Mukherjee, A. K., and Langdon, T. G. (1993). Superplasticity in advanced materials. *Mat. Scie. Eng. R.* **10,** 237-274.

Cicerone, D. S., Regazzoni, A. E., and Blesa, M. A. (1992). Elektrokinetic properties of the calcite/water interface in the presence of Magnesium and organic matter. *J. Colloid Interf. Sci.* **154,** 423-433.

Collettini, C., and Barchi, M. R. (2002). A low-angle normal fault in the Umbria region (Central Italy): a mechanical model for the related microseismicity. *Tectonophysics* **359,** 97-115.

Collettini, C., Carpenter, B. M., Viti, C., Cruciani, F., Mollo, S., Tesei, T., Trippetta, F., Valoroso, L., and Chiaraluce, L. (2014). Fault structure and slip localization in carbonate-bearing normal faults: An example from the Northern Apennines of Italy. *J. Struct. Geol.* **67,** 154-166.

Collettini, C., Niemeijer, A. R., Viti, C., Smith, S. A. F., and Marone, C. (2011). Fault structure, frictional properties and mixed-mode fault slip behavior. *Earth Planet. Sc. Lett.* **311,** 316-327, doi:10.1016/j.epsl.2011.09.020.

Covey-Crump, S. J. (1997). The normal grain growth behaviour of nominally pure calcitic aggregates. *Contrib. Mineral. Petrol.* **129,** 239-254,

Crawford, B. R., Faulkner, D. R., and Rutter, E. H. (2008). Strength, porosity, and permeability development during hydrostatic and shear loading of synthetic quartz-clay fault gouge. *J. Geophys. Res.* **113,** B03207, doi:10.1029/2006JB004634.

Daniels, K. E., and Hayman, N. W. (2008). Force chains in seismogenic faults visualized with photoelastic granular shear experiments. *J. Geophys. Res.* **113,** B11411, doi:10.1029/2008JB005781.

De Bresser, J. H. P. (1991). Intracrystalline deformation of calcite. *Geologica Ultraiectina*, No. 79. [Ph.D. Thesis, 191 pp., Utrecht, The Netherlands].

De Bresser, J. H. P. (2002). On the mechanisms of dislocation creep of calcite at high temperature: Inferences from experimentally measured pressure sensitivity and strain rate sensitivity of flow stress. *J. Geophys. Res.* **107**, B12, doi:10.1029/2002JB001812.

De Bresser, J. H. P., and Spiers, C. J. (1993). Slip systems in calcite single crystals deformed at 300-800°C. *J. Geophys. Res.* **98,** 6397-6409.

De Bresser, J. H. P., and Spiers, C. J. (1997). Strength characteristics of the r, f, and c slip systems in calcite. *Tectonophysics* **272,** 1-23.

De Bresser, J. H. P., Evans, B., and Renner, J. (2002). On estimating the strength of calcite rocks under natural conditions. *In:* Deformation mechanisms, Rheology and Tectonics: Current status and future perspectives (eds. De Meer, S., Drury, M. R., De Bresser, J. H. P., and Pennock, G. M.). Geological Society, London, Spec. Pub. **200**, 309-329.

De Bresser, J. H. P., Ter Heege, J. H., and Spiers, C. J. (2001). Grain size reduction by dynamic recrystallization: can it result in major rheological weakening? *Int. J. Earth. Sci.* **90,** 28-45.

De Bresser, J. H. P., Urai, J. L., and Olgaard, D. L. (2005). Effect of water on the strength and microstructure of Carrara marble axially compressed at high temperature. *J. Struct. Geol.* **27,** 265-281.

De Leeuw, N. H., and Parker, S. C (1997). Atomistic simulation of the effect of molecular adsorption of water on the surface structure and energies of calcite surfaces. *J. Chem. Soc. Faraday T.* **93,** 467-475.

De Raadt, W. S., Burlini, L., Kunze, K., and Spiers, C. J. (2014). Effect of pre-existing crystallographic preferred orientation on the rheology of Carrara marble. *J. Struct. Geol.* **68,** 44-57.

Den Hartog, S. A. M. (2013). Frictional behaviour of megathrust fault gouges under in-situ subduction zone conditions. *Utrecht Studies in Earth Sciences,* No. 33. [Ph.D. Thesis, 192 pp., Utrecht, The Netherlands].

Den Hartog, S. A. M., and Spiers, C. J. (2013). Influence of subduction zone conditions and gouge composition on frictional slip stability of megathrust faults. *Tectonophysics* **600,** 75-90.

Den Hartog, S. A. M., and Spiers, C. J. (2014). A microphysical model for fault gouge friction applied to subduction megathrusts. *J. Geophys. Res.-Sol. Ea.* **119,** 1510-1529.

Den Hartog, S. A. M., Niemeijer, A. R., and Spiers, C. J. (2013). Friction on subduction megathrust faults: Beyond the illite-muscovite transition. *Earth Planet. Sci. Lett.* **373,** 8-19.

Den Hartog, S. A. M., Peach, C. J., de Winter, D. A. M., Spiers, C. J., and Shimamoto, T. (2012). Frictional properties of megathrust fault gouges at low sliding velocities: New data on effects of normal stress and temperature. *J. Struct. Geol.* **38,** SI, 156-171.

Densmore, A. L., Ellis, M. A., Li, Y., Zhou, R., Hancock, G. S., and Richardson, N. (2007). Active tectonics of the Beichuan and Pengguan faults at the eastern margin of the Tibetan plateau. *Tectonics* **26,** TC4005, doi: 10.1029/2006TC001987.

Di Toro, G., Han, R., Hirose, T., De Paola, N., Nielsen, S., Mizoguchi, K., Ferri, F., Cocco, M., and Shimamoto, T. (2011). Fault lubrication during earthquakes. *Nature* **471,** 494-498.

Dieterich, J. H. (1972). Time-dependent friction in rocks. *J. Geophys. Res.* **77,** 3690-3697.

Dieterich, J. H. (1978). Time-dependent friction and the mechanics of stick-slip. *Pure Appl. Geophys.* **116,** 791-806.

Dieterich, J. H. (1979a). Modelling of rock friction 1. Experimental results and constitutive equations. *J. Geophys. Res.* **84,** B5, 2161-2168.

Dieterich, J. H. (1979b). Modelling of rock friction: 2. Simulation of preseismic slip. *J. Geophys. Res.* **84,** 2169-2175.

Dieterich, J. H. (1981). Constitutive properties of faults with simulated gouge. *In:* Mechanical behavior of crustal rocks, The Handin Volume (eds. Carter, N. L., Friedman, F., Logan, J. M., and Stearns, D. W.). *AGU Geophys. Mon. Ser.* **24,** 103-120 (Washington D.C., USA).

Dieterich, J. H. (1986). A model for the nucleation of earthquake slip. *In:* Earthquake source mechanics (eds. Das, S., Boatwright, J., and Scholz, C. H.). *AGU Geophys. Mon. Ser.* **37,** 36-49 (Washington D.C., USA).

Dieterich, J. H. (1992). Earthquake nucleation on faults with rate- and state-dependent strength. *Tectonophysics* **211,** 149-178.

Dieterich, J. H. (1994). A constitutive law for rate of earthquake production and its application to earthquake clustering. *J. Geophys. Res.* **99,** B2, 2601-2618.

Dieterich, J. H., and Conrad, G. (1984). Effect of humidity on time- and velocity-dependent friction in rocks. *J. Geophys. Res.* **89,** 4196-4202.

Dieterich, J. H., and Kilgore, B. D. (1994). Direct Observation of Frictional Contacts: New Insights for State-dependent Properties. *Pure Appl. Geophys.* **143,** 283-302.

Dieterich, J. H., and Kilgore, B. D. (1996). Imaging surface contacts: power law contact distributions and contact stresses in quartz, calcite, glass and acrylic plastic. *Tectonophysics* **256,** 219-239.

Doglioni, C., Harabaglia, P., Martinelli, G., Mongelli, F., and Zito, G. (1996). A geodynamic model of the Southern Apennines accretionary prism. *Terra Nova* **8,** 540-547.

Drennon, C. B., and Handy, R. L. (1972). Stick-slip of lightly loaded limestone. *Int. J. Rock Mech. Min. Sci.* **9,** 603-615.

Dunning, J., Douglas, B., Miller, M., and McDonald, S. (1994). The role of the chemical environment in frictional deformation: Stress corrosion cracking and comminution. *Pure Appl. Geophys.* **143,** 151-178.

Evans, B., Renner, J., and Hirth, G. (2001). A few remarks on the kinetics of static grain growth in rocks. *Int. J. Earth Sci.* **90,** 88-103.

Evans, J. P., Prante, M. R., Janecke, S. U., Ault, A. K., and Newell, D. L. (2014). Hot faults: Iridescent slip surfaces with metallic luster document high-temperature ancient seismicity in the Wasatch fault zone, Utah, USA. *Geology* **42,** 623-626.

Fagereng, Å., and Toy. V. G. (2011). Geology of the earthquake source: an introduction. *In:* Geology of the earthquake source: A volume in honour of Rick Sibson (eds. Fagereng, Å, Toy, V. G., and Rowland, J. V.). Geological Society, London, Spec. Publ. **359,** 1-16, doi:10.1144/SP359.1.

Farver, J. R., and Yund, R. A. (1996). Volume and grain boundary diffusion of calcium in natural and hot-pressed calcite aggregates. *Contrib. Mineral. Petrol.* **123,** 77-91.

Fliervoet, T. F., White, S. H., and Drury, M. R. (1997). Evidence for dominant grain boundary sliding deformation in greenschist- and amphibolites grade polymineralic ultramylonites from the Redbank Deformed Zone, Central Australia. *J. Struct. Geol.* **19,** 1495-1520.

Fondriest, M., Smith, S. A. F., Candela, T., Nielsen, S. B., Mair, K., and Di Toro, G. (2013). Mirror-like faults and power dissipation during earthquakes. *Geology* **41,** 1175-1178.

Forbes, T. Z., Radha, A. V., and Navrotsky, A. (2011). The energetics of nanophase calcite. *Geochem. Cosmochem. Ac.* **75,** 7893-7905.

Fusseis, F., Regenauer-Lieb, K., Liu, J., Hough, R. M., and De Carlo, F. (2009). Creep cavitation can establish a dynamic granular fluid pump in ductile shear zones. *Nature* **459,** 974-977.

Gehrke, N., Cölfen, H., Pinna, N., Antonietti, M., and Nassif, N. (2005). Superstructures of calcium carbonate crystals by oriented attachment. *Cryst. Growth. Des.* **5,** 1317-1319.

Gilotti, J. A., and Hull, J. M. (1990). Phenomenological superplasticity in rocks *In:* Deformation mechanisms, Rheology and Tectonics (eds. Rutter, E. H., and Knipe, R. J.). *Geological Society, London, Spec. Publ.* **54,** 229-240.

Graf, D. L. (1961). Crystallographic tables for the rhombohedral carbonates. *Am. Miner.* **46,** 1283-1316.

Gratier, J.-P., Dysthe, D. K., and Renard, F. (2013). The role of pressure solution creep in the ductility of the Earth's upper crust. *Adv. Geophys.* **54,** 47-179.

Gu, J.-C., Rice, J. R., Ruina, A. L., and Tse, S. T. (1984). Slip motion and stability of a single degree of freedom elastic system with rate and state dependent friction. *J. Mech. Phys. Solid* **32,** 167-196.

Gu, Y., and Wong, T.-f. (1991). Effects of loading velocity, stiffness, and inertia on the dynamics of a single degree of freedom spring-slider system. *J. Geophys. Res.* **96,** B13, 21677-21691.

Gu, Y., and Wong, T.-F. (1994). Development of shear localization in simulated quartz gouge: effect of cumulative slip and gouge particle size. *Pure Appl. Geophys.* **143,** 387-423.

Gudehus, G. (2011). Physical soil mechanics. *Springer-Verlag*, Berlin Heidelberg, Germany, 840 pp.

Hadizadeh, J., Sehhati, R., and Tullis, T. (2010). Porosity and particle shape changes leading to shear localization in small-displacement faults. *J. Struct. Geol.* **32,** 1712-1720.

Hadizadeh, J., Tullis, T. E., White, J. C., and Konkachbaev, A. I. (2015). Shear localization, velocity weakening behavior, and development of cataclastic foliation in experimental granite gouge. *J. Struct. Geol* **71,** 86-99.

Han, R., Hirose, T., and Shimamoto, T. (2010). Strong velocity weakening and powder lubrication of simulated faults at seismic slip rates. *J. Geophys. Res.* **115**, B03412, doi:10.1029/2008JB006136.

Han, R., Hirose, T., Shimamoto, T., Lee, Y., and Ando, J.-i. (2011). Granular nanoparticles lubricate faults during seismic slip. *Geology* **39,** 599-602.

Han, R., Shimamoto, T., Ando, J.-i., and Ree, J.-H. (2007b). Seismic slip record in carbonate-bearing fault zones: An insight from high-velocity friction experiments on siderite gouge. *Geology* **35,** 1131-1134.

Han, R., Shimamoto, T., Hirose, T., Ree, J.-H., and Ando, J.-i. (2007a). Ultralow friction of carbonate faults caused by thermal decomposition. *Science* **316**, 878-881.

Hansen, L. N., Zimmerman, M. E., and Kohlstedt, D. L. (2011). Grain boundary sliding in San Carlos olivine: Flow law parameters and crystallographic-preferred orientation. *J. Geophys. Res.* **116,** B08201, doi:10.1029/2011JB008220.

Hansen, L. N., Zimmerman, M. E., and Kohlstedt, D. L. (2012a). The influence of microstructure on deformation of olivine in the grain-boundary sliding regime. *J. Geophys. Res.* **117,** B09201, doi:10.1029/2011JB009305.

Hansen, L. N., Zimmerman, M. E., and Kohlstedt, D. L. (2012b). Laboratory measurements of the viscous anisotropy of olivine aggregates. *Nature* **492,** 415-418.

He, C., and Ma, S. (1997). Dynamic fault motion under variable normal stress condition with rate and state dependent friction. *In:* Proceedings of 30th International Geological Congress (ed. Zheng, Y.). VSP **14,** 41-52, Utrecht, The Netherlands.

He, C., Luo, L., Hao, Q.-H., and Zhou, Y. (2013). Velocity-weakening behavior of plagioclase and pyroxene gouges and stabilizing effect of small amounts of quartz under hydrothermal conditions. *J. Geophys. Res.* **118,** 3408-3430.

He, C., Ma, S., and Huang, J. (1998). Transition between stable sliding and stick-slip due to variation in slip rate under variable normal stress conditions. *Geophys. Res. Lett.* **25,** 3235-3238.

He, C., Wang. Z., and Yao, W. (2007). Frictional sliding of gabbro gouge under hydrothermal conditions. *Tectonophysics* **445,** 353-362.

He, C., Wong, T.-f., and Beeler, N. M. (2003). Scaling of stress drop with recurrence interval and loading velocity for laboratory derived fault strength relations. *J. Geophys. Res.* **108,** 2037 doi:10.1029/2002JB001890.

He, C., Yao, W., Wang, Z., and Zhou, Y. (2006). Strength and stability of frictional sliding of gabbro gouge at elevated temperatures. *Tectonophysics* **427,** 217-229.

Heard, H. C. (1960). Transition from brittile fracture to ductile flow in solenhofen limestone as a function of temperature, confining pressure, and interstitial fluid pressure. *Geol. Soc. Am. Mem.* **79,** 1, 193-226.

Heitzmann, P. (1987). Calcite mylonites in the Central Alpine "root zone". *Tectonophysics* **135,** 207-215.

Herwegh, M., De Bresser, J. H. P., and Ter Heege, J. H. (2005). Combining natural microstructure with composite flow laws: improved approach for the extrapolation of lab data to nature. *J. Struct. Geol.* **27,** 503-521.

Herwegh, M., Xiao, X., and Evans, B. (2003). The effect of dissolved magnesium on diffusion creep in calcite. *Earth Planet. Sci. Lett.* **212,** 457-470.

Hettema, M. H. H., Schutjens, P. M. T. M., Verboom, B. J. M., and Gussinklo, H. J. (2000). Production-induced compaction of a sandstone reservoir: The strong influence of a stress path. *SPEREE* (August), 342-347.

Hilgers, C., Kirschner, D. L., Breton, J.-P., and Urai, J. L. (2006). Fracture sealing and fluid overpressures in limestones of the Jabal Akhdar dome, Oman mountains. *Geofluids* **6,** 168-184.

Hiraga, T., Miyazaki, T., Tasaka, M., and Yoshida, H. (2010). Mantle superplasticity and its self-made demise. *Nature* **468,** 1091-1094.

Hirth, G., and Kohlstedt, D. L. (1995a). Experimental constraints on the dynamics of the partially molten upper mantle: Deformation in the diffusion creep regime. *J. Geophys. Res.* **100,** B2, 1981-2001.

Hirth, G., and Kohlstedt, D. L. (1995b). Experimental constraints on the dynamics of the partially molten upper mantle 2. Deformation in the dislocation creep regime. *J. Geophys. Res.* **100,** B8, 15441-15449.

Hobbs, B. E., Ord, A., and Teyssier, C. (1986). Earthquakes in the ductile regime? *Pure Appl. Geophys.* **124,** 309-336.

Hochella Jr., M. F. (2008). Nanogeoscience: From origins to cutting-edge applications. *Elements* **4,** 373-379.

Holdsworth, R., Stewart, M., Imber, J., and Strachan, R. A. (2001). The structure and rheological evolution of reactivated continental shear zones: a review and case study. *In:* Continental reactivation and reworking (eds. Miller, J. A., Holdsworth, R. E., Buick, I. S., and Hand, M.). *Geological Society, London, Spec. Publ.* **184,** 115-137.

Holzapfel, C., Soldera, F., Vollmer, C., Hoppe, P., and Mücklich, F. (2009). TEM foil preparation of sub-micrometre sized individual grains by focused ion beam technique. *J. Microsc.* **235,** 59-66.

Hoskins, E. R., Jaeger, J. C., and Rosengren, K. J. (1968). A medium-scale direct friction experiment. *Int. J. Rock Mech. Min. Sci.* **5,** 143-154.

Huang, Y., Wu, J., Zhang, T., and Zhang, D. (2008). Relocation of the M8.0 Wenchuan earthquake and aftershock sequence. *Sci. China Earth Sci.* **51,** 1703-1711.

Hubbard, J., and Shaw, J. H. (2009). Uplift of the Longmen Shan and Tibetan plateau, and the 2008 Wenchuan (M = 7.9) earthquake. *Nature* **458,** 194-197.

Hubbert, M. K., and Rubey, W. W. (1959). Role of fluid pressure in mechanics of overthrust faulting. I. Mechanics of fluid-filled porous solids and its application to overthrust faulting. *Geol. Soc. Am. Bull.* **70,** 115-166.

Hussain, A., Yeats, R. S., and MonaLisa (2009). Geological setting of the 8 october 2005 Kashmir earthquake. *J. Seismol.* **13,** 315-325.

Hyndman, R. D., Yamano, M., and Oleskevich, D. A. (1997). The seismogenic zone of subduction thrust faults. *Isl. Arc* **6,** 244-260.

Ide, S. (2014). Modeling fast and slow earthquakes at various scales. *Proc. Jpn. Acad. Ser. B.* **90,** 259-277.

Ikari, M. J., Marone, C., and Saffer, D. M. (2011). On the relation between fault strength and frictional stability. *Geology* **39,** 83-86.

Ikari, M. J., Niemeijer, A. R., Spiers, C. J., Kopf, A., and Saffer, D. (2013). Experimental evidence linking slip stability with seafloor lithology and topography at the Costa Rica convergent margin. *Geology* **41,** 891-894.

Ikari, M. J., Saffer, D. M., and Marone, C. (2007). Effect of hydration state on the frictional properties of montmorillonite-based fault gouge. *J. Geophys. Res.* **112,** B06423, doi:10.1029/2006JB004748.

Ikari, M. J., Saffer, D. M., and Marone, C. (2009). Frictional and hydrologic properties of clay-rich fault gouge. *J. Geophys. Res.* **114,** B05409, doi:10.1029/2008JB006089.

Imber, J., Holdsworth, R. E., Smith, S. A. F., Jefferies, S. P., and Collettini, C. (2008). Frictional-viscous flow, seismicity and the geology of weak faults: a review and future directions. *In:* The internal structure of fault zones: Implications for mechanical and fluid-flow properties (eds. Wibberley, C. A. J., Kurz, W., Imber, J., Holdsworth, R., and Collettini, C.). *Geological Society, London, Spec. Publ.* **299,** 151-173, doi:10.1144/SP299.10.

Ito, K. (1990). Regional variations of the cutoff depth of seismicity in the crust and their relation to heat flow and large inland-earthquakes. *J. Phys. Earth* **38,** 223-250.

Ito, K. (1999). Seismogenic layer, reflective lower crust, surface heat flow and large inland earthquakes. *Tectonophysics* **306,** 423-433.

Jaeger, J. C., Cook, N. G. W., and Zimmerman, R. (2007). Fundamentals of rock mechanics. *Blackwell publishing,* Singapore, Singapore, 475 pp.

Jiang, X., and Jin, Y. (2005). Mapping the deep lithospheric structure beneath the eastern margin of the Tibetan Plateau from gravity anomalies. *J. Geophys. Res.* **110,** B07407, doi:10.1029/2004JB003394.

Kanamori, H. (1981). The nature of seismicity patterns before large earthquakes. *In:* Earthquake prediction, An International review. (eds. Simpson, D., and Richards, P. G.). American Geophysical Union, Washington D.C., 1-19.

Kaproth, B. M., and Marone, C. (2013). Slow earthquakes, preseismic velocity changes, and the origin of slow frictional stick-slip. *Science* **341,** 1229-1232.

Kassner, M. E., and Hayes, T. A. (2003). Creep cavitation in metals. *Int. J. Plasticity* **19**, 1715-1748.

Kato, N., and Tullis, T. E. (2003). Numerical simulation of seismic cycles with a composite rate and state-dependent friction law. *Bull. Seismol. Soc. Am.* **93,** 841-853.

Kaus, B. J. P., and Podlachikov, Y. (2006). Initiation of localized shear zones in viscoplastic rocks. *J. Geophys. Res.* **111,** B04412, doi:10.1029:2005JB003652.

Kawamoto, E., and Shimamoto, T. (1997). Mechanical behavior of halite and calcite shear zones from brittle to fully-plastic deformation and a revised fault model. *In:* Proceedings of the 30th international geological congress, Beijing, China (ed. Zheng, Y.). *VSP* **14,** 89-105, Utrecht, The Netherlands.

Kawamoto, E., and Shimamoto, T. (1998). The strength profile for bimineralic shear zones: an insight from high-temperature shearing experiments on calcite-halite mixtures. *Tectonophysics* **295,** 1-14.

Kennedy, L. A., and White, J. C. (2001). Low-temperature recrystallization in calcite: Mechanisms and consequences. *Geology* **29,** 1027-1030.

Kilgore, B. D., Blanpied, M. L., and Dieterich, J. H. (1993). Velocity dependent friction of granite over a wide range of conditions. *Geophys. Res. Lett.* **20,** 903-906.

King, G. (1983). The accommodation of large strains in the upper lithosphere of the earth and other solids by self-similar fault systems: the geometrical origin of the b-value. *Pure. Appl. Geophys.* **121,** 761-815.

Kirkpatrick, J. D., Rowe, C. D., White, J. C., and Brodsky, E. E. (2013). Silica gel formation during fault slip: Evidence from the rock record. *Geology* **41,** 1015-1018.

Koelemeijer, P. J., Peach, C. J., and Spiers, C. J. (2012). Surface diffusivity of cleaved NaCl crystals as a function of humidity: Impedance spectroscopy measurements and implications for crack healing in rock salt. *J. Geophys. Res* **117,** doi:10.1029/2011JB008627.

Kohlstedt, D. L., Evans, B., and Mackwell, S. J. (1995). Strength of the lithosphere: Constraints imposed by laboratory experiments. *J. Geophys. Res.* **100,** B9, 17857-17602.

Kukla, P. A., Reuning, L., Becker, S., Urai, J. L., and Schoenherr, J. (2011). Distribution and mechanisms of overpressure generation and deflation in the late Neoproterozoic to early Cambrian South Oman Salt Basin. *Geofluids* **11,** 349-361.

Kuo, L.-W., Hsiao, H.-C., Song, S.-R., Sheu, H.-S., and Suppe, J. (2014). Coseismic thickness of principal slip zone from the Taiwan Chelungpu fault Drilling Project-A (TCDP-A) and correlated fracture energy. *Tectonophysics* **619-620,** 29-35.

Lapusta, N, and Rice, J. R. (2003). Nucleation and early seismic propagation of small and large events in a crustal earthquake model. *J. Geophys. Res.* **108,** doi:10.1029/2001JB000793.

Lasaga, A. C. (1984). Chemical kinetics of water-rock interactions. *J. Geophys. Res.* **89,** 4009-4025.

Lasaga, A. C. (1998). Kinetic theory in the Earth Sciences. *Princeton University Press*, Princeton, New Jersey, USA, 811 pp.

Lee, S.-J., Komatitsch, D., Huang, B.-S., and Tromp, J. (2009). Effects of topography on seismic-wave propagation: An example from Northern Taiwan. *Bull. Seismol. Soc. Am.* **1,** 314-325.

Lexa, O., Štípská, P., Schulmann, K., Baratoux, L., and Kröner, A. (2005). Contrasting textural record of two distinct metamorphic events of similar P-T conditions and different durations. *J. Metamorphic. Geol.* **23,** 649-666.

Li, H., and 11 others. (2013). Characteristics of the fault-related rocks, fault zones and the principal slip zone in the Wenchuan Earthquake Fault Scientific Drilling Project Hole-1 (WFSD-1). *Tectonophysics* **584,** 23-42.

Li, Y. S., Tao, N. R., and Lu, K. (2008). Microstructural evolution and nanostructure in copper during dynamic plastic deformation at cryogenic temperatures. *Acta Mater.* **56,** 230-241.

Linker, M. F., and Dieterich, J. H. (1992). Effects of Variable Normal Stress on Rock Friction: Observations and Constitutive Equations. *J. Geophys. Res.* **97,** 4923-4940.

Liteanu, E., and Spiers, C. J. (2009). Influence of pore fluid salt content on compaction creep of calcite aggregates in the presence of supercritical CO_2. *Chem. Geol.* **265,** 134-147.

Liteanu, E., Niemeijer, A. R., Spiers, C. J., Peach, C. J., and De Bresser, J. H. P. (2012). The effect of CO_2 on creep of wet calcite aggregates. *J. Geophys. Res.* **117,** B03211, doi:10.1029/2011JB008789.

Liu, Y. and Rice, J. R. (2005). Aseismic slip transients emerge spontaneously in three-dimensional rate and state modeling of subduction earthquake sequences. *J. Geophys. Res.* **110,** B083037, doi:10.1029/2004JB003424.

Liu, Y. and Rice, J. R. (2007). Slow slip predictions based on granite and gabbro friction data compared to GPS measurements in northern Cascadia. *J. Geophys. Res.* **114,** B09407, doi:10.1029/2008JB006142.

Liu, Y. and Rice, J. R. (2009). Spontaneous and triggered aseismic deformation transients in a subduction model. *J. Geophys. Res.* **112,** B09404, doi:10.1029/2007JB004930.

Liu, Y. H., Wang, G., Wang, R. J., Zhao, D. Q., Pan, M. X., and Wang, W. H. (2007). Super plastic bulk metallic glasses at room temperature. *Science* **315,** 1385-1388.

Liu-Zeng, J., Zhang, Z., Wen, L., Tapponnier, P., Sun, J., Xing, X., Hu, G., Xu, Q., Zeng, L., Ding, L., Ji, C., Hudnut, K. W., and Van der Woerd, J. (2009). Co-seismic ruptures of the 12 May 2008, Ms 8.0 Wenchuan earthquake, Sichuan: East-west crustal shortening on oblique, parallel thrusts along the eastern edge of Tibet. *Earth Planet. Sci. Lett.* **286,** 355-370.

Lockner, D. A., Summers, R., and Byerlee, J. D. (1986). Effects of temperature and sliding rate on frictional strength of granite. *Pure Appl. Geophys.* **124,** 3, 445-469.

Logan, J. M., and Rauenzahn, K. A. (1987). Frictional dependence of gouge mixtures of quartz and montmorillonite on velocity, composition and fabric. *Tectonophysics* **144,** 87-108.

Logan, J. M., Friedman, M., Higgs, N., Dengo, C. A., and Shimamoto, T. (1979). Experimental studies of simulated gouge and their application to studies of natural fault zones. *In:* Proceedings of Conference VIII - Analysis of Actual Fault Zones in Bedrock (eds. Speed., R., and Sharp., R.). *United States Geological Survey*, Menlo Park, 305-343.

Lu, L., Sui, M. L., and Lu, K. (2000). Superplastic extensibility of nanocrystalline copper at room temperature. *Science* **287,** 1463-1466.

Lu, Z., and He, C. (2014). Frictional behaviour of simulated biotite fault gouge under hydrothermal conditions. *Tectonophysics* **622,** 62-80.

Ma, E. (2004). Watching the nanograins roll. *Science* **305,** 623-624.

Ma, K.-F., and 12 others. (2006). Slip zone and energetics of a large earthquake from the Taiwan Chelungpu-fault Drilling Project. *Nature* **444,** 473-476.

Ma., S. (2008). A physical model for widespread near-surface and fault zone damage induced by earthquakes. *Geochem. Geophy. Geosy.* **9,** Q11009, doi:10.1029/2008GC002231.

Machel, H. G. (2004). Concepts and models of dolomitization: a critical reappraisal. *In:* The geometry and petrogenesis of dolomite hydrocarbon reservoirs (eds. Braithwaite, C. J. R., Rizzi, R., and Darke, G.). *Geological Society, London, Spec. Publ.* **235,** 7-63.

Maillot, B., and Koyi, H. (2006). Thrust dip and thrust refraction in fault-bend folds: analogue models and theoretical predictions, *J. Struct. Geol.* **28,** 36-49.

Mair, K., and Abe, S. (2008). 3D numerical simulations of fault gouge evolution during shear: Grain size reduction and strain localization. *Earth Planet. Sci. Lett.* **274,** 72-81.

Marone, C. (1998a). Laboratory-derived friction laws and their application to seismic faulting, *Annu. Rev. Earth Planet. Sci.* **26,** 643-696.

Marone, C. (1998b). The effect of loading rate on static friction and the rate of fault healing during the earthquake cycle. *Nature* **391,** 69-72.

Marone, C., and Kilgore, B. (1993). Scaling of the critical slip distance for seismic faulting with shear strain in fault zones. *Nature* **362,** 618-621.

Marone, C., and Scholz, C. H. (1988). The depth of seismic faulting and the upper transition from stable to unstable slip regimes. *Geophys. Res. Lett.* **15,** 6, 621-624.

Marone, C., and Scholz, C. H. (1989). Particle-size distribution and microstructures within simulated fault gouge. *J. Struct. Geol.* **7,** 799-814.

Marone, C., Raleigh, C. B., and Scholz, C. H. (1990). Frictional behavior and constitutive modeling of simulated fault gouge. *J. Geophys. Res.* **95,** 7007-7026.

McClure, M. W., and Horne, R. N. (2011). Investigation of injection-induced seismicity using a coupled fluid flow and rate/ state friction model. *Geophysics* **76,** WC181-WC198.

McLaskey, G. C., Thomas, A. M., Glaser, S. D., and Nadeau, R. M. (2012). Fault healing promotes high-frequency earthquakes in laboratory experiments on natural faults. *Nature* **491,** 101-105.

Meissner, R., and Strehlau, J. (1982). Limits of stresses in continental crusts and their relation to the depth-frequency distribution of shallow earthquakes. *Tectonics* **1,** 73-89.

Meyers, M. A., Mishra, A., and Benson, D. J. (2006). Mechanical properties of nanocrystalline materials. *Prog. Mater. Sci.* **51,** 427-556.

Mirabella, F., Barchi, M., Lupattelli, A., Stucchi, E., and Ciaccio, M. G. (2008). Insights on the seismogenic layer thickness from the upper crust structure of the Umbria-Marche Apennines (central Italy). *Tectonics* **27,** TC1010, doi:10.1029/2007TC002134.

Miyazaki, T., Sueyoshi, K., and Hiraga, T. (2013). Olivine crystals align during diffusion creep of Earth's upper mantle. *Nature* **502,** 321-326.

Mizoguchi, K., Takahashi, M., Tanikawa, W., Masuda, K., Song, S.-R., and Soh, W. (2008). Frictional strength of fault gouge in Taiwan Chelungpu fault obtained from TCDP Hole B, *Tectonophysics* **460,** 198-205.

Moore, D. E., and Lockner, D. A. (2004). Crystallographic controls on the frictional behavior of dry and water-saturated sheet structured minerals. *J. Geophys. Res.* **109,** B03401, doi:10.1029/2003JB002582.

Moore, D. E., Lockner, D. A., Ma, S., Summers, R., and Byerlee, J. D. (1997). Strengths of serpentinite gouges at elevated temperatures. *J. Geophys. Res.* **102,** B7, 14787-14801.

Moore, J. C., and Saffer, D. M. (2001). Updip limit of the seismogenic zone beneath the accretionary prism of southwest Japan: An effect of diagenetic to low-grade metamorphic processes and increasing effective stress. *Geology* **29,** 183-186.

Morrow, C. A., and Byerlee, J. D. (1989). Experimental studies of compaction and dilatancy during frictional sliding on faults containing gouge. *J. Struct. Geol.* **7,** 815-825.

Morrow, C. A., Moore, D. E., and Lockner, D. A. (2000). The effect of mineral bond strength and adsorbed water on fault gouge frictional strength. *Geophys. Res. Lett.* **27,** 815-818.

Morrow, C. A., Radney, B., and Byerlee, J. D. (1992). Frictional strength and the effective pressure law of montmorillonite and illite clays. *In:* Fault mechanics and transport properties of rocks (eds. Evans, B., and Wong, T. F.). *Academic Press,* pp. 33–67 (London, UK).

Nadeau, R. M., and Johnson, L. R. (1998). Seismological studies at Parkfield VI: Moment release and estimates of source parameters of small repeating earthquakes. *Bull. Seismol. Soc. Am.* **88,** 790-814.

Nadeau, R. M., Foxall, W., and McEvilly, T. V. (1995). Clustering and periodic recurrence of microearthquakes on the San Andreas Fault at Parkfield, California. *Science* **267,** 503-507.

Nakashima, S. (1995). Diffusivity of ions in pore water as a quantitative basis for rock deformation rate estimates. *Tectonophysics* **245,** 185-203.

Nakatani, M. (2001). Conceptual and physical clarification of rate and state friction: Frictional sliding as a thermally activated rheology. *J. Geophys. Res.* **106,** B7, 13347-13380.

Nakatani, M., and Scholz, C. H. (2004). Frictional healing of quartz gouge under hydrothermal conditions: 1. Experimental evidence for solution transfer healing mechanism. *J. Geophys. Res.* **109,** B07201, doi:10.1029/2001JB001522.

Nichols, G. (2004). Sedimentology and stratigraphy. *Blackwell science,* Padstow, UK, 355 pp.

Niederberger, M., and Cölfen, H. (2006). Oriented attachment and mesocrystals: Non-classical crystallization mechanisms based on nanoparticle assembly. *Phys. Chem. Chem. Phys.* **8,** 3271-3287.

Nieh, T. G., Wadsworth, J., and Sherby, O. D. (1997). Superplasticity in metals and ceramics. *Cambridge Univ. Press,* Cambridge, UK, 273 pp.

Niemeijer, A. R. (2006). Effects of pressure solution and phyllosilicates on the slip and compaction behaviour of crustal faults. *Geologica Ultraiectina,* No. 255. [Ph.D. Thesis, 213 pp., Utrecht, Netherlands].

Niemeijer, A. R., and Spiers, C. J. (2005). Influence of phyllosilicates on fault strength in the brittle-ductile transition: insights from rock-analogue experiments. *In:* High-strain zones: Structure and physical properties (eds. Bruhn, D., and Burlini, L.). *Geol. Soc. London Spec. Publ.* **245,** London, p. 303-327.

Niemeijer, A. R., and Spiers, C. J. (2006). Velocity dependence of strength and healing behaviour in simulated phyllosilicate-bearing fault gouge. *Tectonophysics* **427,** 231-253.

Niemeijer, A. R., and Spiers, C. J. (2007). A microphysical model for strong velocity weakening in phyllosilicate-bearing fault gouges. *J. Geophys. Res.* **112,** B10405, doi:10.1029/2007JB005008.

Niemeijer, A. R., Marone, C., and Elsworth, D. (2010). Frictional strength and strain weakening in simulated fault gouge: Competition between geometrical weakening and chemical strengthening. *J. Geophys. Res.* **115,** B10207, doi:10.1029/2009JB00838.

Niemeijer, A. R., Spiers, C. J., and Peach, C. J. (2008). Frictional behaviour of simulated quartz fault gouges under hydrothermal conditions: Results from ultra-high strain rotary shear experiments. *Tectonophysics* **460,** 288-303.

Nissen, E., Tatar, M., Jackson, J. A., and Allen, M. B. (2011). New views on earthquake faulting in the Zagros fold-and-thrust belt or Iran. *Geophys. J. Int.* **186,** 928-944.

Nissen, E., Jackson, J., Jahani, S., and Tatar, M. (2014). Zagros "phantom earthquakes" reassessed – The interplay of seismicity and deep salt flow in the Simply Folded Belt? *J. Geophys. Res.* **119,** 3561-3583.

Noda, H., and Lapusta, N. (2013). Stable creeping fault segments can become destructive as a results of dynamic weakening. *Nature* **493,** 518-521.

Noda, H., and Shimamoto, T. (2010). A rate- and state-dependent ductile flow law of polycrystalline halite under large shear strain and implication for transition to brittle deformation. *Geophys. Res. Lett.* **37,** L09310, doi:10.1029/2010GL042512.

Noda, H., and Shimamoto, T. (2012). Transient behavior and stability analyses of halite shear zones with an empirical rate-and-state friction to flow law. *J. Struct. Geol.* **38,** 234-242.

Noda, H., Dunham, E. M., and Rice, J. R. (2009). Earthquake ruptures with thermal weakening and the operation of major faults at low overall stress levels. *J. Geophys. Res.* **114,** B07302, doi:10.1029.2008JB006143.

Nübel, K., and Huang, W. (2004). A study of localized deformation pattern in granular media. *Comput. Method Appl. M.* **193,** 2719-2743.

Nur, A., and Byerlee, J. D. (1971). An exact effective stress law for elastic deformation of rock with fluids. *J. Geophys. Res.* **76,** 6414-6419.

Ohnaka, M. (1973). Experimental studies of stick-slip and their application to the earthquake source mechanism. *J. Phys. Earth.* **21,** 285-303.

Ohnaka, M. (1975). Frictional characteristics of typical rocks. *J. Phys. Earth.* **23,** 87-112.

Ohnaka, M. (2013). The physics of rock failure and earthquakes. *Cambridge Univ. Press*, Cambridge, UK, 279 pp.

Olsson, W. A. (1974). Effects of temperature, pressure and displacement rate on the frictional characteristics of a limestone. *Int. J. Rock Mech. Min.* **11,** 267-278.

Oohashi, K., Han, R., Hirose, T., Shimamoto, T., Omura, K., and Matsuda, T. (2014). Carbon-forming reactions under a reducing atmosphere during seismic fault slip. *Geology* **42,** 787-790.

Passelègue, F. X., Schubnel, A., Nielsen, S., Bhat, H. S., and Madariaga, R. (2013). From sub-Rayleigh to supershear ruptures during stick-slip experiments on crustal rocks. *Science* **340,** 1208-1211.

Paterson, M. S. (1995). A theory for granular flow accommodated by material transfer via an intergranular fluid. *Tectonophysics* **245,** 135-151.

Paterson, M. S., and Wong, T.-f. (2005). Experimental rock deformation; the brittle field. *Springer*, Berlin Heidelberg, Germany, 347 pp.

Pei, S., Su, J., Zhang, H., Sun, Y., Nafi Toksöz, M., Wang, Z., Gao, X., Liu-Zeng, J., and He, J. (2010). Three-dimensional seismic velocity structure across the 2008 Wenchuan earthquake, Sichuan, China. *Tectonophysics* **491,** 211-217, doi: 10.1016/j.tecto.2009.08.039.

Peng, Z., and Gomberg, J. (2010). An integrated perspective of the continuum between earthquakes and slow-slip phenomena. *Nat. Geosci.* **3,** 599-607.

Penn, R. L., and Banfield, J. F. (1998). Imperfect oriented attachment: Dislocation generation in defect-free nanocrystals. *Science* **281,** 969-971.

Penn, R. L., and Banfield, J. F. (1999). Morphology development and crystal growth in nanocrystalline aggregates under hydrothermal conditions: Insights from titania. *Geochim. Cosmochim. Ac.* **63,** 1549-1557.

Perrin, G., Rice, J. R., and Zheng, G. (1995). Self-healing slip pulse on a frictional surface. *J. Mech. Phys. Solids* **43,** 1461-1495.

Pizzi, A., and Scisciani, V. (2012). The May 2012 Emilia (Italy) earthquakes: preliminary interpretations on the seismogenic source and the origin of the coseismic ground effects. *Ann Geophys-Italy* **55,** 751-757.

Plummer, L. N., and Busenberg, E. (1982). The solubilities of calcite, aragonite and vaterite in CO_2-H_2O solutions between 0 and 90°C, and an evaluation of the aqueous model for the system $CaCO_3$-CO_2-H_2O. *Geochim. Cosmochim. Ac.* **46**, 1011-1040.

Pluymakers, A. M. H., and Spiers, C. J. (2014). Compaction creep of simulated anhydrite fault gouge by pressure solution: Theory v. experiments and implications for fault sealing. *In:*

Rock deformation from field, experiments and theory: A volume in honour of Ernie Rutter (eds. Faulkner, D. R., Mariani, E., and Mecklenburg, J.). *Geol. Soc. London Spec. Publ.* **409,** *doi:10.1144/SP409.6*.

Power, W. L., and Tullis, T. E. (1989). The relationship between slickenside surfaces in fine-grained quartz and the seismic cycle. *J. Struct. Geol.* **11,** 879-893.

Raj, R., and Ashby, M. F. (1971). On grain boundary sliding and diffusion creep. *Metall. Trans.* **2,** 1113-1127.

Rathbun, A. P., and Marone, C. (2013). Symmetry and critical slip distance in rate and state friction laws. *J. Geophys. Res.* **118,** 3728-3741.

Rebetskii, Y. L. (2002). Development of the Method of Cataclastic Analysis of Shear Fractures for Tectonic Stress Estimation. *Dokl. Earth Sci.* **388,** 72-76.

Ree, J.-H., Ando, J.-i., Han, R., and Shimamoto, T. (2014). Coseismic microstructures of experimental fault zones in Carrara marble. *J. Struct. Geol.* **66,** 75-83.

Regenauer-Lieb, K., and Yuen, D. (2003). Modeling shear zones in geological and planetary sciences: solid and fluid-thermal-mechanical approaches. *Earth-Sci. Rev.* **63,** 295-349.

Reinen, L. A., and Weeks, J. D. (1993). Determination of rock friction constitutive parameters using an iterative least squares inversion method. *J. Geophys. Res.* **98,** B9, 15937-15950.

Reinen, L. A., Tullis, T. E., and Weeks, J. D. (1992). Two-mechanism model for frictional sliding of serpentinite. *Geophys. Res. Lett.* **19,** 1535-1538.

Renner, J., Evans, B., and Siddiqi, G. (2002). Dislocation creep of calcite. *J. Geophys. Res.* **107,** B12, doi:10.1029/2001JB001680.

Rice, J. R. (1978). Thermodynamics of the quasi-static growth of Griffith cracks. *J. Mech. Phys. Solids* **26,** 61-78.

Rice, J. R., and Ruina, A. (1983). Stability of steady frictional slipping. *J. Appl. Mech.* **50,** 343-349.

Rice, J. R., Lapusta, N., and Ranjith, K. (2001). Rate and state dependent friction and the stability of sliding between elastically deformable solids. *J. Mech. Phys. Solids* **49,** 1865-1898.

Rodríguez, K., and Araujo, M. (2006). Temperature and pressure effects on zeta potentials of reservoir minerals. *J. Colloid Interf. Sci.* **300,** 788-794.

Rogowitz, A., Grasemann, B., Huet, B., and Habler, G. (2014). Strain rate dependent calcite microfabric evolution – An experiment carried out by nature. *J. Struct. Geol.* **69,** 1-17.

Røyne, A., Bisschop, J., and Dysthe, D. K. (2011). Experimental investigation of surface energy and subcritical crack growth in calcite. *J. Geophys. Res.* **116,** B024204, doi:10.1029/2010JB008033.

Rubin, A. M. (2008). Episodic slow slip events and rate-and-state friction. *J. Geophys. Res.* **113,** B11414, doi:10.1029/2008JB005642.

Rudnicki, J. W. (1988). Physical Models of Earthquake Instability and Precursory Processes, *Pure Appl. Geophys.* **126,** 531-554.

Ruina, A. L. (1983). Slip instability and state variable friction laws. *J. Geophys. Res.* **88,** B12, doi:10.1029/JB088iB12p10359.

Rutter, E. H. (1972). The influence of interstitial water on the rheological behaviour of calcite rocks. *Tectonophysics* **14,** 13-33.

Rutter, E. H. (1974). The influence of temperature, strain rate and interstitial water in the experimental deformation of calcite rocks. *Tectonophysics* **22,** 311-334.

Rutter, E. H. (1983). Pressure solution in nature, theory, and experiment. *J. Geol. Soc. London* **140,** 725-740.

Rutter, E. H., Casey, M., and Burlini, L. (1994). Preferred crystallographic orientation development during the plastic and superplastic flow of calcite rocks. *J. Struct. Geol.* **16,** 1431-1446.

Rutter, E. H., Holdsworth, R. E., and Knipe, R. J. (2001). The nature and tectonic significance of fault-zone weakening: an introduction. *In:* The nature and tectonic significance of fault-zone weakening (eds. Holdsworth, R. E., Strachan, R. A., Magloughlin, J. F., and Knipe, R. J.). *Geological Society, London, Spec. Publ.* **186,** 1-11.

Saffer, D. M., and Marone, C. (2003). Comparison of smectite- and illite-rich gouge frictional properties: application to the updip limit of the seismogenic zone along subduction megathrusts. *Earth Planet. Sci. Lett.* **215,** 219-235.

Samuelson, J. E., and Spiers, C. J. (2012). Fault friction and slip stability not affected by CO_2: Evidence from short-term laboratory experiments on North Sea reservoir sandstones and caprocks. *Int. J. Greenh. Gas Con.* **11,** S78-S90, doi:10.1016/j.ijggc.2012.09.018.

Samuelson, J. E., Elsworth, D., and Marone, C. (2009). Shear-induced dilatancy of fluid-saturated faults: Experiment and theory. *J. Geophys. Res.* **114,** B12404, doi:10.1029/2008JB006273.

Schmid, S. M., Panozzo, R., and Bauer, S. (1987). Simple shear experiments on calcite rocks: rheology and microfabric. *J. Struct. Geol.* **9,** 5/6, 747-778.

Schmid, S. M., Paterson, M. S., and Boland, J. N. (1980). High temperature flow and dynamic recrystallization in Carrara Marble. *Tectonophysics* **65,** 245-280.

Schofield, A., and Wroth, P. (1968). Critical State Soil Mechanics. *McGraw-Hill*, London, 218 pp.

Scholz, C. H. (1988). The brittle-plastic transition and the depth of seismic faulting. *Geol. Rund.* **77,** 1, 319-328.

Scholz, C. H. (1998). Earthquakes and friction laws. *Nature* **391,** 37-42.

Scholz, C. H. (2002). The mechanics of earthquakes and faulting. *Cambridge University Press*, Cambridge, 504 pp.

Scholz, C. H., and Engelder, J. T. (1976). The role of asperity indentation and ploughing in rock friction. I. Asperity creep and stick-slip. *Int. J. Rock Mech. Min. Sci. & Geomech. Abstr.* **13,** 149-154.

Schubnel, A., Brunet, F., Hilairet, N., Gasc, J., Wang, Y., and Green II, H. W. (2013). Deep-focus earthquak analogs recorded at high pressure and temperature in the laboratory. *Science* **341,** 1377-1380.

Schutjens, P. M. T. M., Hanssen, T. H., Hettema, M. H. H., Merour, J., De Bree, P., Coremans, J. W. A., and Hellesen, G. (2004). Compaction-inducted porosity/ permeability reduction in sandstone reservoirs: Data and model for elasticity-dominated deformation. *SPEREE* (June), 202-216.

Schwartz, D. P., and Coppersmith, K. J. (1984). Fault behaviour and characteristic earthquakes: Examples from the Wasatch and San Andreas fault zones. *J. Geophys. Res.* **89,** 5681-5698.

Scruggs, V. J., & Tullis, T. E. (1998). Correlation between velocity dependence of friction and strain localization in large displacement experiments on feldspar, muscovite and biotite gouge. *Tectonophysics* **295,** 15-40.

Scuderi, M. M., Niemeijer, A. R., Collettini, C., and Marone, C. (2013). Frictional properties and slip stability of active faults within carbonate-evaporite sequences: The role of dolomite and anhydrite. *Earth Planet. Sci. Lett.* **369-370,** 220-232.

Segall, P. (1989). Earthquakes triggered by fluid extraction. *Geology* **17,** 942-946.

Segall, P., and Rice, J. R. (1995). Dilatancy, compaction, and slip instability of a fluid-infiltrated fault. *J. Geophys. Res.* **100,** B11, 22155-22171.

Shan, Z., Stach, E. A., Wiezorek, J. M. K., Knapp, J. A., Follstaedt, D. M., and Mao, S. X. (2004). Grain boundary-mediated plasticity in nanocrystalline nickel. *Science* **305,** 654-657.

Shaw, B. E., and Wesnousky, S. G. (2008). Slip-length scaling in large earthquakes: The role of deep-penetrating slip below the seismogenic layer. *Bull. Seismol. Soc. Am.* **98,** 1633-1641.

Shibazaki, B., Garatani, K., Iwasaki, T., Tanaka, A., and Iio, Y. (2008). Faulting processes controlled by the nonuniform thermal structure of the crust and uppermost mantle beneath the northeastern Japanese island arc. *J. Geophys. Res.* **113,** B08415, doi:10.1029/2007JB005361.

Shimamoto, T. (1986). Transition between frictional slip and ductile flow for halite shear zones at room temperature. *Science* **231,** 4739, 711-714.

Shimamoto, T. (1989). The origin of *S-C* mylonites and a new fault zone model. *J. Struct. Geol.* **11,** 51-64.

Shimamoto, T., and Logan, J. M. (1981). Effects of simulated fault gouge on the sliding behavior of Tennessee sandstone: nonclay gouges. *J. Geophys. Res.* **86,** 2902-2914.

Shimamoto, T., and Noda, H. (2014). A friction to flow constitutive law and its application to a 2-D modelling of earthquakes. *J. Geophys. Res.* **119,** 8089-8106, doi:10.1002/2014JB011170.

Sibson, R. H. (1977). Fault rocks and fault mechanisms. *J. Geol. Soc. London* **133,** 191-213.

Sibson, R. H. (1980). Transient discontinuities in ductile shear zones. *J. Struct. Geol.* **2,** 165-171.

Sibson, R. H. (1982). Fault zone models, heat flow, and the depth distribution of earthquakes in the continental crust of the united states. *Bull. Seismol. Soc. Am.* **72,** 1, 151-163.

Sibson, R. H. (1983). Continental fault structure and the shallow earthquake source. *J. Geol. Soc. London* **140,** 741-767.

Sibson, R. H. (1984). Roughness at the base of the seismogenic zone: Contributing factors. *J. Geophys. Res.* **89,** B7, 5791-5799.

Sibson, R. H. (1986). Earthquakes and rock deformation in crustal fault zones. *Annu. Rev. Earth Pl. Sc.* **14,** 149-175.

Sibson, R. H. (2000). Fluid involvement in normal faulting. *J. Geodyn.* **29,** 469-499.

Sibson, R. H. (2003). Thickness of the seismic slip zone. *B. Seismol. Soc. Am.* **93,** 1169-1178.

Sibson, R. H. (2014). Earthquake rupturing in fluid-overpressured crust: How common? *Pure Appl. Geophys.* **171,** 2867-2885.

Sieh, K. (1996). The repetition of large-earthquake ruptures. *Proc. Nat. Acad. Sci.* **93,** 3764-3771.

Siman-Tov, S., Aharonov, E., Sagy, A., and Emmanuel, S. (2013). Nanograins from carbonate "fault mirrors". *Geology* **41,** 703-706.

Sjöberg, E. L., and Rickard, D. T. (1984). Temperature dependence of calcite dissolution kinetics between 1 and 62°C at pH 2.7 to 8.4 in aqueous solutions. *Geochim. Cosmochim. Ac.* **48,** 485-493.

Sleep, N. H. (1997). Application of a unified rate and state friction theory to the mechanics of fault zones with strain localization. *J. Geophys. Res.* **102,** B2, 2875-2895.

Sleep, N. H. (2005). Physical basis of evolution laws for rate and state friction. *Geochem. Geophy. Geosy.* **6,** Q11008, doi:10.1029/2005GC000991.

Sleep, N. H., Richardson, E., and Marone, C. (2000). Physics of friction and strain rate localization in synthetic fault gouge. *J. Geophys. Res.* **105,** B11, 25875-25890.

Smith, S. A. F., Billi, A., Di Toro, G., and Spiess, R. (2011). Principal slip zones in limestone: Microstructural characterization and implications for the seismic cycle (Tre Monti Fault, Central Apennines, Italy). *Pure Appl. Geophys.* **168,** 2365-2393.

Smith, S. A. F., Di Toro, G., Kim, S., Ree, J.-H., Nielsen, S., Billi, A., and Spiess, R. (2013). Coseismic recrystallization during shallow earthquake slip. *Geology* **41,** 63-66.

Smith, S. A. F., Nielsen, S., and Di Toro, G. (2015). Strain localization and the onset of dynamic weakening in calcite fault gouge. *Earth Planet. Sci. Lett.* **413,** 25-36.

Snoke, A. W., Tullis, J., and Todd, V. R. (1998). Fault-related rocks: A photographic atlas. *Princeton Univ. Press.,* Princeton, NJ, USA, 629 pp.

Solberg, P., and Byerlee, J. D. (1984). A note on the rate sensitivity of Westerly granite. *J. Geophys. Res.* **89,** 4203-4206.

Solum, J. G., and Van der Pluijm, B. A. (2009). Quantification of fabrics in clay gouge from the Carboneras fault, Spain and implications for fault behavior. *Tectonophysics* **475,** 554–562.

Solum, J. G., Van der Pluijm, B. A., and Peacor, D. R. (2005). Neocrystallization, fabrics and age of clay minerals from an exposure of the Moab Fault, Utah. *J. Struct. Geol.* **27,** 1563–1576.

Spiers, C. J., de Meer, S., Niemeijer, A. R., and Zhang, X. (2004). Kinetics of rock deformation by pressure solution and the role of thin aqueous films. *In:* Physicochemistry of water in geological and biological systems - structures and properties of thin aqueous films (eds. Nakashima, S., Spiers, C. J., Mercury, L., Fenter, P. A. and Hochella Jr., M. F.). *Universal Academy Press*, p. 129-158 (Tokyo, Japan).

Spiers, C. J., Schutjens, P. M. T. M., Brzesowsky, R. H., Peach, C. J., Liezenberg, J. L., and Zwart, H. J. (1990). Experimental determination of constitutive parameters governing creep of rocksalt by pressure solution. *In:* Deformation mechanisms, Rheology and Tectonics (eds. Knipe, R. J., and Rutter, E. H.). *Geological Society, London, Spec. Publ.* **54,** 215-227.

Stesky, R. M. (1978). Rock friction – effect of confining pressure, temperature and pore pressure. *Pure Appl. Geophys.* **116,** 690-704.

Stesky, R. M., Brace, W. F., Riley, D. K., and Robin, P.-Y. F. (1974). Friction in faulted rock at high temperature and pressure. *Tectonophysics* **23,** 177-203.

Stewart, M., Holdsworth, R. E., and Strachan, R. A. (2000). Deformation processes and weakening mechanisms within the frictional-viscous transition zone of major crustal-scale faults: insights from the Great Glen Fault Zone, Scotland. *J. Struct. Geol.* **22,** 543-560.

Stipp, S. L. (1999). Toward a conceptual model of the calcite surface: Hydration, hydrolysis and surface potential. *Geochim. Cosmochim. Ac.* **63,** 3121-3131.

Summers, R., and Byerlee, J. D. (1977). A note on the effects of fault gouge composition on the stability of frictional sliding. *Int. J. Rock Mech. Min. Sci.* **14,** 155-160.

Suppe, J. (2014). Fluid overpressures and strength of the sedimentary upper crust. *J. Struct. Geol.* **69,** 481-492.

Sykes, L. R., Shaw, B. E., and Scholz, C. H. (1999). Rethinking earthquake prediction. *Pure Appl. Geophys.* **155,** 207-232.

Takahashi, M., Mizoguchi, K., Kitamura, K., and Masuda, K. (2007). Effects of clay content on the frictional strength and fluid transport property of faults. *J. Geophys. Res.* **112,** B08206, doi:10.1029/2006JB004678.

Talwani, P. (1997). On the nature of reservoir-induced seismicity. *Pure. Appl. Geophys.* **150,** 473-792.

Tang, L., Yang, K., Jin, W., Lü, Z., and Yu, Y. (2008). Multi-level decollement zones and detachment deformation of Longmenshan thrust belt, Sichuan Basin, southwest China. *Sci. China Earth Sci.* **51,** 32-43.

Tao, N. R., Wang, Z. B., Tong, W. P., Sui, M. L., Lu, J., and Lu, K. (2002). An investigation of surface nanocrystallization mechanism in Fe induced by surface mechanical attrition treatment. *Acta Mater.* **50,** 4603-4616.

Tchalenko, J. S. (1970). Similarities between shear zones of different magnitudes. *Geol. Soc. Am. Bull.* **81,** 1625-1640.

Tembe, S., Lockner, D. A., and Wong, T.-f. (2010). Effect of clay content and mineralogy on frictional sliding behavior of simulated gouges: Binary and ternary mixtures of quartz, illite and montmorillonite. *J. Geophys. Res.* **115,** B3, doi: 10.1029/2009JB006383.

Terakawa, T., Zoporowski, A., Galvan, B., and Miller, S. A. (2010). High-pressure fluid at hypocentral depths in the L'Aquila region inferred from earthquake focal mechanisms. *Geology* **38,** 995-998.

Tesei, T., Collettini, C., Barchi, M. R., Carpenter, B. M., and Di Stefano, G. (2014). Heterogeneous strength and fault zone complexity of carbonate-bearing thrusts with possible implications for seismicity. *Earth Planet. Sci. Lett.* **408,** 307-318.

Tinti, E., Bizarri, A., and Cocco, M. (2005). Modelling the dynamic rupture propagation on heterogeneous faults with rate- and state-dependent friction. *Ann. Geophys.* **48,** 327-345.

Tisato, N., Di Toro, G., De Rossi, N., Quaresimin, M., and Candela, T. (2012). Experimental investigation of flash weakening in limestone. *J. Struct. Geol.* **38,** 183-199.

Tjong, S. C., and Chen, H. (2004). Nanocrystalline materials and coatings. *Mat. Sci. Eng. R.* **45,** 1-88.

Toy, V. G., Ritchie, S., and Sibson, R. H. (2011). Diverse habitats of pseudotachylytes in the Alpine Fault Zone and relationships to current seismicity. *In:* Geology of the earthquake source: A volume in honour of Rick Sibson (eds. Fagereng, Å, Toy, V. G., and Rowland, J. V.). *Geological Society, London, Spec. Publ.* **359**, 115-133, doi:10.1144/SP359.7.

Tse, S. T. and Rice, J. R. (1986). Crustal earthquake instability in relation to the depth variation of frictional slip properties, *J. Geophys. Res.* **91,** 9452-9472.

Tullis, T. E. (1988). Rock friction constitutive behavior from laboratory experiments and its implications for an earthquake prediction field monitoring program. *Pure Appl. Geophys.* **126,** 555-588.

Tullis, T. E., and Weeks, J. D. (1986). Constitutive behavior and stability of frictional sliding of granite. *Pure Appl. Geophys.* **124,** 383-414.

Twiss, R. J., and Moores, E. M. (2007). Structural geology. *W.H. Freeman and company*, New York, USA, 736 pp.

U.S. Geological Survey Earthquake Hazards Program (2008). USGS Central Moment Tensor Solution, from *http://neic.usgs.gov/neis/FM/neic_ryan_cmt.html* (last accessed Dec. 2, 2009).

Umemoto, M. (2003). Nanocrystallization of steels by severe plastic deformation. *Mater. Trans.* **44,** 1900-1911.

Urai, J. L., Means, W. D., and Lister, G. S. (1986). Dynamic recrystallization of minerals. *In:* Mineral and rock deformation: Laboratory studies - The Paterson Volume (eds. Hobbs, B. E., and Heard, H. C.). *Geophys. Monogr. Ser.* **36,** AGU, Washington D. C, p. 161-199.

Valcke, S. L. A., De Bresser, J. H. P., Pennock, G. M., and Drury, M. R. (2014). Influence of deformation conditions on the development of heterogeneous recrystallization microstructures in experimentally deformed Carrara marble. *In:* Rock deformation from field, experiments and theory: A volume in honour of Ernie Rutter (eds. Faulkner, D. R., Mariani, E., and Mecklenburg, J.). *Geological Society, London, Spec. Pub.* **409**, doi:10.1144/SP409.4.

Valoroso, L., Chiaraluce, L., Piccinini, D., Di Stefano, R., Schaff, D., and Waldhauser, F. (2013). Radiography of a normal fault system by 64,000 high-precision earthquake locations: The 2009 L'Aquila (central Italy) case study. *J. Geophys. Res.* **118**, doi:10.1002/jgrb.50130.

Verberne, B. A., De Bresser, J. H. P., Niemeijer, A. R., Spiers, C. J., De Winter, D. A. M., and Plümper, O. (2013a). Nanocrystalline slip zones in calcite fault gouge show intense crystallographic preferred orientation: Crystal plasticity at sub-seismic slip rates at 18-150°C. *Geology* **41,** 863-866.

Verberne, B. A., De Bresser, J. H. P., Niemeijer, A. R., and Spiers, C. J. Frictional-viscous transition in simulated calcite fault gouge sheared at 20-600°C and implications for seismogenesis in limestones. *Manuscript in preparation* (in revision, 10-08-2015).

Verberne, B. A., De Bresser, J. H. P., and Niemeijer, A. R. Strain rate dependent frictional-to-viscous transition in simulated calcite fault gouge sheared at 550°C: Implications for the lower boundary of the seismogenic zone. *Manuscript in preparation* (as of 10-08-2015).

Verberne, B. A., He, C., and Spiers, C. J. (2010). Frictional properties of sedimentary rocks and natural fault gouge from the Longmenshan Fault Zone, Sichuan, China. *B. Seismol. Soc. Am.* **100,** 2767-2790.

Verberne, B. A., Plümper, O., De Winter, D. A. M., and Spiers, C. J. (2014). Superplastic nanofibrous slip zones control seismogenic fault friction. *Science* **346,** 1342-1344.

Verberne, B. A., Spiers, C. J., Niemeijer, A. R., De Bresser, J. H. P., De Winter, D. A. M., and Plümper, O. (2013b). Frictional properties and microstructure of calcite-rich fault gouges sheared at sub-seismic sliding velocities. *Pure Appl. Geophys.* **171,** 2617-2640.

Vrolijk, P., and Van der Pluijm, B. A. (1999). Clay gouge. *J. Struct. Geol.* **21,** 1039-1048.

Walker, A. N., Rutter, E. H., and Brodie, K. H. (1990). Experimental study of grain-size sensitive flow of synthetic, hot-pressed calcite rocks. *In:* Deformation mechanisms, Rheology and Tectonics (eds. Knipe, R. J., and Rutter, E. H.). *Geological Society, London, Spec. Publ.* **54,** 259-284.

Wang, J. Y. (1996). Geothermics in China. *Seismological Press*, Beijing, 299 pp.

Wang, Z., Fukao, Y., and Pei, S. (2009). Structural control of rupturing of the M_w 7.9 2008 Wenchuan Earthquake, China, *Earth Planet. Sci. Lett.* **279,** 131-138.

White, J. C., and White, S. H. (1981). On the structure of grain boundaries in tectonites. *Tectonophysics* **78**, 613-628.

Wibberley, C. A. J., and Shimamoto, T. (2003). Internal structure and permeability of major strike-slip zones: the Median Tectonic Line in Mie Prefecture, Southwest Japan. *J. Struct. Geol.* **25,** 59-78.

Wilson, J. T. (1975). Carbonate facies in geological history. *Springer-Verlag*, Heidelberg, Germany, 471 pp.

Wintsch, R. P., Christofferson, R., and Kronenberg, A. K. (1995). Fluid-rock reaction weakening of fault zones. *J. Geophys. Res.* **100,** B7, 13021-13032.

Wong, T.-f., and Zhao, Y. (1990). Effects of load point velocity on frictional instability behavior. *Tectonophysics* **175,** 177-195.

Wong, T.-f., Gu, Y., Yanagidani, T., and Zhao, Y. (1992). Stabilization of faulting by cumulative slip. *In:* Fault mechanics and transport properties of rocks (eds. Evans, B., and Wong, T.-f.). *Academic Press*, pp. 119–143 (London, UK).

Wu, C., Gomberg, J., Ben-Naim, E., and Johnson, P. (2014). Triggering of repeating earthquakes in central California. *Geophys. Res. Lett.* **41,** 1499-1505.

Wu, F., Blatter, T. L., and Roberson, H. (1975). Clay gouges in the San Andreas Fault System and their possible implications. *Pure Appl. Geophys.* **113,** 87-95.

Würschum, R., Herth, S., and Brossmann, U. (2003). Diffusion in nanocrystalline metals and alloys – a status report. *Adv. Eng. Mater.* **5,** 365-372.

Xu, X. W., Wen, X. Z., Yu, G. H., Chen, G. H., Klinger, Y., Hubbard, J., and Shaw, J. (2009). Coseismic reverse- and oblique-slip surface faulting generated by the 2008 M_w 7.9 Wenchuan earthquake, China. *Geology* **37,** 515-518.

Xu, Z., Ji, S., Li, H., Hou, L., Fu, X., and Cai, Z. (2008). Uplift of the Longmen Shan range and the Wenchuan earthquake. *Episodes* **31,** 291-301.

Yang, D. K., Cizek, P., Hodgson, P.D., and Wen, C. E. (2010). Microstructure evolution and nanograin formation during shear localization in cold-rolled titanium. *Acta Mater.* **58,** 4536-4548.

Yong, R. N., Nakano, M., and Pusch, R. (2012). Environmental soil properties and behaviour. *CRC press Taylor & Francis Group*, Boca Raton, 446 pp.

Yund, R. A., Blanpied, M. L., Tullis, T. E., and Weeks, J. D. (1990). Amorphous material in high strain experimental fault gouges. *J. Geophys. Res.* **95,** 15589-15602.

Zhang, H., and Banfield, J. F. (2012). Energy calculations predict nanoparticle attachment orientations and asymmetric crystal formation. *J. Phys. Chem. Lett.* **3,** 2882-2886.

Zhang, H., and Banfield, J. F. (2014). Interatomic Coulombic interactions as the driving force for oriented attachment. *CrystEngComm* **16,** 1568-1578.

Zhang, J., Huang, F., and Lin, Z. (2010a). Progress of nanocrystalline growth kinetics based on oriented attachment. *Nanoscale* **2,** 18-34.

Zhang, L., and He, C. (2013). Frictional properties of natural gouges from Longmenshan fault zone ruptured during the Wenchuan Mw 7.9 earthquake. *Tectonophysics* **594,** 149-164.

Zhang, P.-Z., Shen, Z., Wang, M., Gan, W., Bürgmann, R., Molnar, P., Wang, Q., Niu, Z., Sun, J. Wu, J., Sun, H., and You, X. (2004). Continuous deformation of the Tibetan Plateau from global positioning system data. *Geology* **32,** 809-812.

Zhang, Q., Liu, S.-J., and Yu, S.-H. (2009). Recent advances in oriented attachment growth and synthesis of functional materials: concept, evidence, mechanism, and future. *J. Mater. Chem.* **19,** 191-207.

Zhang, X., and Spiers, C. J. (2005). Compaction of granular calcite by pressure solution at room temperature and effects of pore fluid chemistry. *Int. J. Rock Mech. Min. Sci.* **42,** 950-960.

Zhang, X., Salemans, J., Peach, C. J., and Spiers, C. J. (2002). Compaction experiments on wet calcite powder at room temperature: evidence for operation of intergranular pressure solution. *In:* Deformation mechanisms, Rheology and Tectonics: Current Status and Future Perspectives (eds. De Meer, S., Drury, M. R., De Bresser, J. H. P., and Pennock, G. M.). *Geological Society, London, Spec. Pub.* **200,** 29-39.

Zhang, X., Spiers, C. J., and Peach, C. J. (2010b). Compaction creep of wet granular calcite by pressure solution at 28°C to 150°C. *J. Geophys. Res.* **115,** B09217, doi:10.1029/2008JB005853.

Zhu, R., Zhao, X., Liu, L., Wang, X., Zhang, N., Guo, H., and Song, L. (2009). Depositional system and favorable reservoir distribution of Xujiahe Formation in Sichuan Basin. *Petrol. Explor. Dev.* **36,** 46-55.

Ziv, A., and Rubin, A. M. (2003). Implications of rate-and-state friction for properties of aftershock sequence: Quasi-static inherently discrete simulations. *J. Geophys. Res.* **108,** B1, doi:10.1029/2001JB001219.

Afterword/ Acknowledgements

Eén van de persoonlijke doelen die ik had toen ik aan mijn promotieonderzoek begon was om, door middel van kennisvergaring, naast een inkomen te generen, een soort verrijkende, gnostische wijsheid op te doen. Vier-en-een-half jaar later kan ik concluderen dat ik in aanraking ben gekomen met een schat aan specialistische kennis, waarvan ik veel heb kunnen leren, maar dat gnostiek er weinig mee te maken heeft. Om met de niet onomstreden G. B. Shaw te spreken, *'Science never solves a problem without creating ten more'*. Ondanks dit weerzinwekkende lot heb ik zonder twijfel unieke kennis en ervaringen opgedaan, en ben ik talloze vaardigheden rijker. Hiervoor ben ik mijn promotor, co-promotoren, en andere directe collega's/ mensen in mijn omgeving, erg dankbaar!!

Hoe het dan ook gesteld word, ik had dit onderzoek nooit kunnen voltooien zonder de kunde, inzet, steun, en discipline van mijn promotor, **Chris Spiers**. My sincerest thanks for all your efforts, Chris. I learned a lot from you on countless aspects, including geology, materials science, proper scientific methods and writing, but also on how to attain a professional attitude. Your perfectionist drive is truly inspirational, and it was (is) an honour to learn from you. I also appreciate your sense of humor, the occasional uncanny joke, which made working under pressure much easier for me. It can also not be left unmentioned how you have always supported me with my Asian affiliations, i.e. in being generally interested, welcoming my wife, and so on. A huge thanks for everything!

Dan heb ik ook erg veel te danken aan mijn co-promotor, **André Niemeijer**. Jouw interesse in en ondersteuning tijdens het onderzoek waren van vitaal belang voor de voltooiing ervan. Tijdens de introductie Aardwetenschappen, ergens in 2003, heb je mij als eerste op een uiterst overtuigende manier uitgelegd wat er boeiend is aan aardbevingen. Misschien vormt dat gesprek wel de onderliggende motivatie voor dit werk! Ik vond het fantastisch dat je erbij was in Vietnam, bij mijn bruiloft, en ik zal ook niet vergeten dat je altijd voor me hebt klaargestaan wanneer het nodig was, zowel op het werk als daarbuiten. Heel erg bedankt. Ik hoop dat er nog vele biertjes (en flatliners,

embryos…☺☺😐☹…) volgen!

Mijn andere co-promotor, **Hans de Bresser**, heeft me ook veel geholpen in het verloop van mijn onderzoek, en in het bijzonder met het inzichtelijk maken van deformatie van calciet. Na iedere sessie was ik op positieve wijze enorm verbaasd over hoe verhelderend de gesprekken met jou wel niet zijn. Je hebt een bijzonder talent om op subtiele wijze iedere keer de vinger op de zere plek te leggen, zodat het vervolgens aangepakt en gerepareerd kan worden. Conclusie: als je meer tijd had gehad was ik waarschijnlijk vorig jaar al klaar geweest ☺… (dat laatste was natuurlijk een geintje!). Heel erg bedankt voor je inzet en voor je gezelligheid!

Before I continue, I want to mention that, although **Jon Samuelson** has by comparison not participated in my research that much, we have spent a lot of precious time drinking (coffee), while talking/ discussing/ bitching a lot. Much obliged for your friendship and moral support, it really made it worthwhile. Hopefully we can maintain contact, even now that you have returned to the, godforsaken, western hemisphere.

Thanks also to my paranymphs, **Wouter Smit** and **Tim Wolterbeek**. Wouter, ik waardeer het heel erg dat je me na al die jaren altijd bent blijven opzoeken in Utrecht. Je vormt daardoor een niet te verwaarlozen deel van dit proefschrift. Bedankt voor een goede vriendschap! Tim, we hebben elkaar vooral in de laatste fasen van ons onderzoek goed leren kennen, maar des te waardevoller. Het is heel prettig om een collega te hebben die de onoverkomelijke frustraties van het promoveren begrijpt, en die het ook op prijs steld om dat te uiten onder het genot van een kopje liefst niet-verse koffie.

I then want to acknowledge **Colin Peach**. Your profound knowledge of rock physics and experiments helped to solve problems more than once when it was really necessary. I also appreciate that you are a very friendly person who's always in for a good laugh. I also owe thanks to **Chen Jianye**, for being an inspiring colleague of the same generation. You can also cook Chinese food very well, which is awesome.

Zonder twijfel, de sterkhouders, ruggengraat, etc., van het HPT lab, zonder wie enig onderzoek inclusief het huidige absoluut niet mogelijk zou zijn, word gevormd door onze secretaresse, **Magda Martens**, en onze technici, **Eimert de Graaff**, **Gert Kastelein**, **Peter van Krieken**, en **Thony van der Gon**. Elk van jullie is een zeer bekwaam professional van wie menig promovendus/ postdoc - onderdeurtje enorm veel kan leren!

Of course I'd also like to thank my other colleagues at the lab, past and present, including **Nawaz, Anne, Elisenda, Jinfeng, Miao, Maartje[2nd], Annelies, Ken, Michiyo, Nino, Reinier, Giorgios,** and **Suzanne.** It was good to be able to talk with fellow victims of Ph.D. serfdom. I wish the present generation, including **Luuk, Martijn, Ayumi, Evangelos, Loes, Zahra, Yu, Mariska,** and **Ronald**, the best of luck with their research!

Next I want to thank all people present at the State Key Laboratory for Earthquake Dynamics (at the CEA) when I spent my time there in early 2009. In particular, **Prof. He** and **Prof. Ma**, you have walked the extra mile to make it possible for me to visit your state-of-the-art lab in Beijing. This basically provided a kick-start to my research. Thanks also to **Prof. Zhou, Prof. Ning, Ji Yuntao, Dang Jiaxiang, Yun Long, Zhen Lu**, and **Lan Caiyun**, for welcoming me and sharing such a nice time (and the food!!....oh, alas, all that food...).

All people from Structural Geology & Tectonics at the UU, past and present, including **Gill, Martyn, Herman, Reinoud, Oli, Maartje[1st],** and **Ernst,** are thanked for always being ready to help. I was lucky enough to enjoy many post-SRS science meetings with you (ahum...), on the second floor of our old building. **Matthijs**, even though your affiliation is with Biomolecular Imaging, I still really appreciated our collaborations! ☺ I hope we may continue them in the future.

Of course I owe a lot, if not the most, of gratitude to my parents, **Cees & Bep Verberne**. Jullie hebben het mogelijk gemaakt dat ik überhaupt kon gaan studeren. Heel erg veel dank dat jullie altijd voor me klaar staan! Ook veel dank aan **Benny & Marita Visser** voor de gezelligheid naast de studie, en de interesse in mijn voortgang. Jullie zijn allemaal top!

Als laatste wil ik bedanken mijn echtgenote, **Vũ Hoài An**. Ik ben heel gelukkig met jou, met jouw zorg, zachtaardigheid, en fantastische kookkunst. Ook wil ik je familie bedanken, in het bijzonder **Vũ Hải**, **Nguyễn An Vinh**, **Vũ Hoàng Trung**, and **Vũ Hoài Thu**. Het kan niet makkelijk voor jullie zijn geweest om jullie dochter of zusje te zien vertrekken naar Nederland. Jullie zijn enorm lief, en bedankt dat jullie mij geaccepteerd hebben in de familie. [Sau cùng, tôi muốn gửi lời cảm ơn đến vợ tôi, Vũ Hoài An. Anh rất hạnh phúc khi có em, sự chăm sóc, dịu dàng, và những món ăn ngon của em. Anh cũng xin cảm ơn đến gia đình em, **bố Vũ Hải**, **mẹ Vinh**, **anh Trung**, và **chị Thu**.

Cũng không dễ dàng để gặp được con gái, em gái ở Hà Lan. Mọi người thật tuyệt, cảm ơn mọi người đã đón nhận con, em đến với gia đình của mình.]

List of publications

As of 10 August 2015.

Manuscripts in preparation:

Verberne, B. A., De Bresser, J. H. P., and Niemeijer, A. R. Strain rate dependent, frictional-to-viscous transition in simulated calcite fault gouge sheared at 550°C: Implications for the lower boundary of the seismogenic zone

Manuscripts submitted:

Verberne, B. A., De Bresser, J. H. P., Niemeijer, A. R., and Spiers, C. J. Frictional-to-viscous transition in simulated calcite fault gouge sheared at 20-600°C: Implications for seismogenesis in limestones. *Submitted to J. Geophys. Res.*

Verberne, B. A., Plümper, O., De Winter, D. A. M., King, H. E., Thieulot, C., and Spiers, C. J. Nanocrystalline principal slip zones in simulated calcite fault gouge sheared at 1 μm/s. *Submitted to J. Geophys. Res.*

Papers in press/ published:

Chen, J., **Verberne, B. A.**, and Spiers, C. J. Effects of healing on the seismogenic potential of carbonate fault rocks: Experiments on samples from the Longmenshan Fault, Sichuan, China. *J. Geophys. Res.*, in press, doi:10.1002/2015JB012051.

Chen, J., **Verberne, B. A.**, and Spiers, C. J. (2015). Interseismic re-strengthening and stabilization of carbonate faults by "non-Dieterich" healing under hydrothermal conditions. *Earth Planet. Sci. Lett.* **423,** 1-12.

Verberne, B. A., Plümper, O., De Winter, D.A.M., and Spiers, C. J. (2014). Superplastic nanofibrous slip zones control seismogenic fault friction. *Science* **346,** 1342-1344.

Verberne, B. A., Spiers, C. J., Niemeijer, A. R., De Bresser, J. H. P., De Winter, D. A. M., and Plümper, O. (2013). Frictional properties and microstructure of calcite-rich fault gouges sheared at sub-seismic sliding velocities. *Pure Appl. Geophys.* **171,** 2617-2640.

Verberne, B. A., De Bresser, J. H. P., Niemeijer, A. R., Spiers, C. J., De Winter, D. A. M., and Plümper, O. (2013). Nanocrystalline slip zones in calcite fault gouge show intense crystallographic preferred orientation: Crystal plasticity at sub-seismic slip rates at 18-150°C. *Geology* **41,** 863-866.

He, C., **Verberne, B. A.**, and Spiers, C. J. (2011). Frictional properties of sedimentary rocks and natural fault gouges from the Longmenshan fault zone and their implications (in Chinese). *Chin. J. Rock Mech. Eng.* **30,** 113-131.

Verberne, B. A., He, C., and Spiers, C. J. (2010). Frictional properties of sedimentary rocks and natural fault gouge from the Longmenshan Fault Zone, Sichuan, China. *B. Seismol. Soc. Am.* **100,** 2767-2790.

Curriculum Vitae

Sept 1996 to Aug 2003	Atheneum. Profiel: Natuur & Techniek. Roncalli Sg., Bergen op Zoom
Sept 2003 to Aug 2006	Bachelor of Science (B.Sc.). Track: GGG *(With distinction)*. Dept. of Geosciences, Utrecht University
Sept 2007 to Aug 2009	Master of Science (M.Sc.). Track: Earth Materials *(Cum Laude)* Dept. of Geosciences, Utrecht University
March 2008 to May 2010	Course mandarin Chinese, ~3 hrs/ week. James Boswell Institute, Utrecht University
Nov 2010 to Sept 2011	Jr. researcher, CATO2, w.p. 3.3 and 3.4 High Pressure and Temperature (HPT) laboratory, Utrecht University
Sept 2011 - ??	Ph.D. candidate HPT laboratory, Utrecht University
Feb 2015 - ??	Postdoctoral researcher HPT laboratory, Utrecht University

Berend Antonie (Bart) Verberne was born on the 18th of July 1984 in Halsteren, Noord-Brabant, The Netherlands. He completed his Athenaeum at the Roncalli Sg., Bergen op Zoom, in 2003, after which he moved to Utrecht to study Earth Sciences at Utrecht University. He completed his B.Sc. degree in 2006, on a thesis entitled *"The Duality of Orogenic Belts"*, supervised by Prof. Dr. Reinoud Vissers. This included a fieldwork in the Mérida Andes of Venezuela, co-organized with M.Sc. E. Praagman. In the following year he left to New-Zealand, and later to South-East Asia, where he met his future wife Vũ Hoài An. Upon his return to The Netherlands he continued a M.Sc. programme in Earth Sciences, specifically focussing on "Earth Materials", and reaching a M.Sc. degree in 2009. His M.Sc. thesis was entitled *"Structural analysis, geothermobarometry and geochronology of rocks from Gossa Island, Western Gneiss Region, Norway"*, supervised by Dr. Herman van Roermund. This included a fieldwork on Gossa island in western Norway, co-organized with M.Sc. W. Dabekaussen. In 2010 he started as a Jr. Researcher at the HPT laboratory, and a Ph.D. research in the following year, culminating in the present thesis.

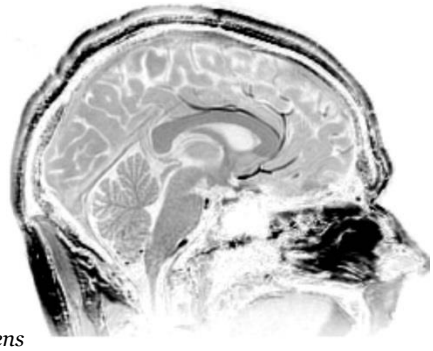

Courtesy: Dr. W. Schellekens